

**New Insights into the Coronal Heating Problem: Analysis of Spectral Line
Widths in the Solar Corona**

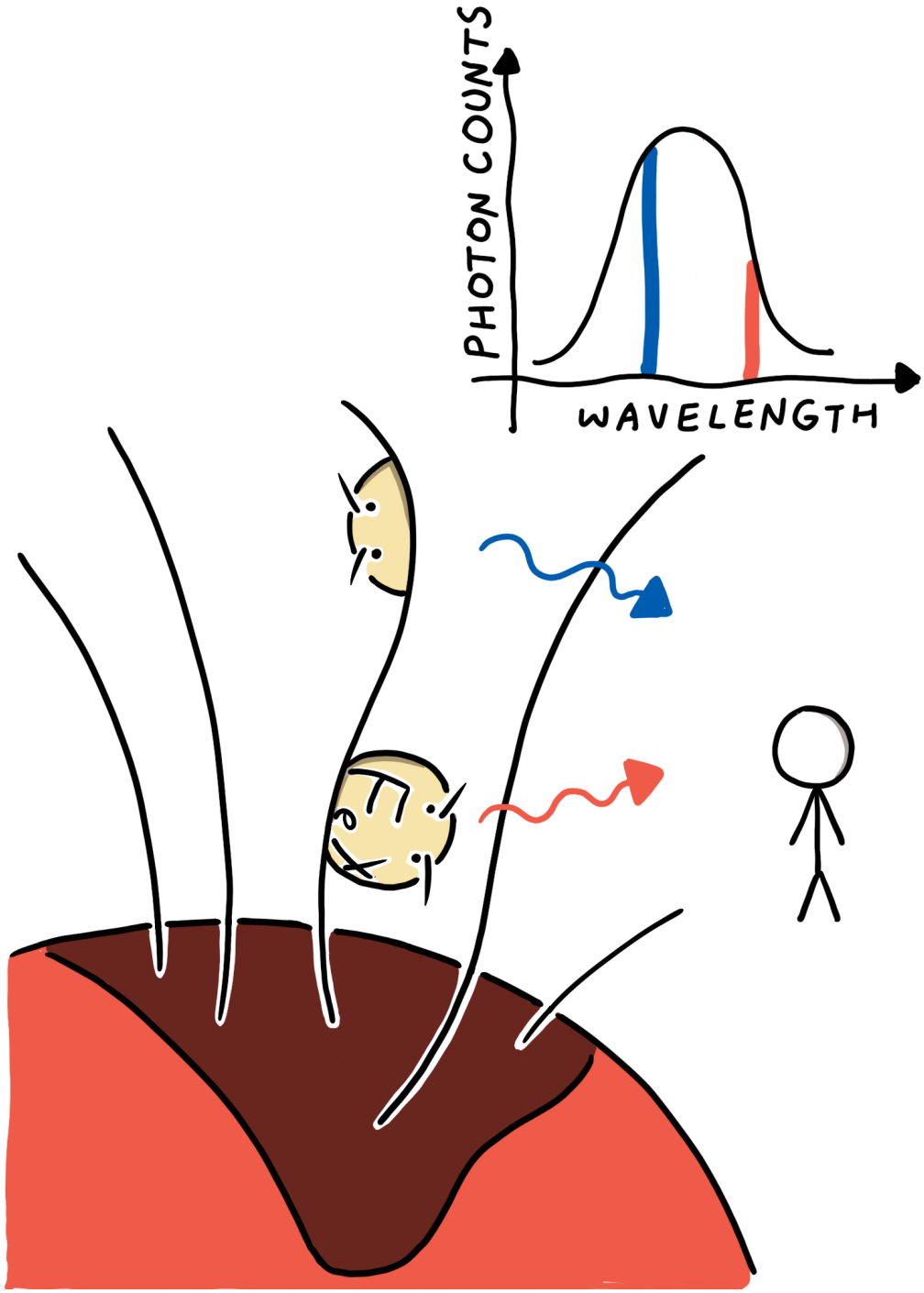
by

Yingjie Zhu

A dissertation submitted in partial fulfillment
of the requirements for the degree of
Doctor of Philosophy
(Climate and Space Sciences and Engineering)
in the University of Michigan
2024

Doctoral Committee:

Professor Enrico Landi, Chair
Astronomer Shadia R. Habbal, Institute for Astronomy, University of Hawaii
Research Professor Ward B. Manchester IV
Associate Professor Jim Raines
Research Scientist Judit Szente



Yingjie Zhu

yjzhu@umich.edu

ORCID iD: 0000-0003-3908-1330

© Yingjie Zhu 2024

DEDICATION

To my mother, grandmother, and the rest of my family,
for their love and support.
To my grandfather and father,
in loving memory.

ACKNOWLEDGEMENTS

I am profoundly thankful to everyone who accompanied me throughout this journey. First, I would like to express my deepest gratitude to my advisor, Prof. Enrico Landi, who guided me into the world of spectroscopy and introduced the data calibration and CHIANTI database to me meticulously. He patiently addressed my naive questions with his vast knowledge of atomic physics and spectroscopic diagnostics. Prof. Landi provided invaluable support in presenting my work at conferences, getting me involved in the research community, and applying for potential postdoc positions.

I sincerely appreciate Dr. Judit Szente, a key collaborator in my PhD research and a dissertation committee member. Without her development of the pivotal SPECTRUM module and non-equilibrium ionization calculation in AWSoM, I could not have easily made spectrum synthesis and simulation-observation comparison. Dr. Szente also contributed her AWSoM, and AWSoM-R runs for my papers and the dissertation.

In particular, I am immensely grateful to Prof. Shadia Habbal and Prof. Adalbert Ding. Their invitation to visit the Institute of Astronomy at the University of Hawaii and generous sharing of their spectroscopic observations during the 2017 total solar eclipse offered the foundation for my research into the widths of coronal forbidden lines in visible. Prof. Habbal also thoroughly reviewed my paper manuscript and provided many constructive suggestions. I am honored to have Prof. Habbal as a cognate member of my dissertation committee.

Many gratitudes to all who collaborated with me and helped me with my PhD research. I am pleased to work with the rest of my committee members, Prof. Jim Raines and Prof. Chip Manchester IV, for their insights to enrich my dissertation. Special thanks to Bryan Yamashiro for sharing his experiences processing the eclipse observations and Dr. Benjamin Boe for his expert feedback on my manuscript. Thanks should also go to Zihao Yang, who is always supportive as a friend and an expert in coronal seismology and CoMP data analysis, and Prof. Michael Hahn for valuable discussions on line width measurements and the EIS instrumental broadening. I also appreciated Dr. Yeimy Rivera, Dr. Akiko Tei, Prof. Xudong Sun, and many others for their discussions to inspire me and refine my research papers.

I am also grateful to the faculty of the CSEM group, notably Dr. Bart van der Holst, Dr. Zhenguang Huang, Prof. Gábor Tóth, Dr. Nishtha Sachdeva, Dr. Lulu Zhao, Prof. Tamas

Gombosi, Dr. Igor Sokolov, and Prof. Spiro Antiochos for their invaluable development and support in AWSoM, and bring me to the coffee break. I also wish to acknowledge the faculty from SHRG, including Prof. Sue Lerpi, Dr. Liang Zhao, and Dr. Sarah Spitzer, for bridging me and my remote-sensing observations to the in-situ measurements of heavy ion charge states.

My journey became more vibrant thanks to other friends and colleagues, especially at CLaSP. Special thanks to Tim Keebler, who shared the windowless office with me for almost five years, Elizabeth Wraback, Xiantong Wang, Tong Shi, Xianyu Liu, Daniel Muccio, Yingxiao Zhang, Alex Lojko, Yan Xie, Natasha Dacic, Tristan Rendfrey, Erika Hathaway, Weihao Liu, Stephanie Colón Rodríguez, Yifan Guan, Charles Powell, Weiping Li, Ananyo Bhattacharya, Daniel Carpenter, Tyler Eddy, Michael Hackett, Austin Glass, and all others who made this journey memorable.

Words cannot express my gratitude to all my family members, especially my grandmother and mother. I could not have undertaken this journey without their unwavering love and support.

Lastly, a special mention to Prof. Hui Tian and Prof. Adam Kowalski, for introducing me to the field of solar physics and paving my way to this incredible adventure. And great applause to the CLaSP AAs and IT staff for their dedication and hard work.

Funding for the DKIST Ambassadors program is provided by the National Solar Observatory, a facility of the National Science Foundation, operated under Cooperative Support Agreement number AST-1400405. YJ also acknowledges support from the University of Michigan. EL acknowledges support from NASA grants NNX16AH01G, NNX17AD37G, 80NSSC18K0645, 80NSSC20K0185, 80NSSC22K0750, 80NSSC21K0579, 80NSSC18K1553, 80NSSC18K0647, and 80NSSC22K1015, and NSF grants AGS 1408789, 1460170, and 2229138. JS acknowledges support from NASA grant 80NSSC18K0645. The 2017 total solar eclipse observations were supported by NASA grant NNX17AH69G and NSF grants AGS-1358239, AGS-1255894, and AST-1733542 to the Institute for Astronomy of the University of Hawaii.

Hinode is a Japanese mission developed and launched by ISAS/JAXA, collaborating with NAOJ as a domestic partner, NASA and UKSA as international partners. Scientific operation of the Hinode mission is conducted by the Hinode science team organized at ISAS/JAXA. This team mainly consists of scientists from institutes in the partner countries. Support for the post-launch operation is provided by JAXA and NAOJ (Japan), UKSA (U.K.), NASA, ESA, and NSC (Norway). SOHO is a project of international cooperation between ESA and NASA. The SUMER project is financially supported by DLR, CNES, NASA, and the ESA PRODEX Program (Swiss contribution). The SDO data are

courtesy of NASA/SDO and the AIA, EVE, and HMI science teams. The CoMP data are courtesy of the Mauna Loa Solar Observatory, operated by the High Altitude Observatory, as part of the National Center for Atmospheric Research (NCAR). NCAR is supported by the National Science Foundation. CHIANTI is a collaborative project involving George Mason University, the University of Michigan (USA), the University of Cambridge (UK), and NASA Goddard Space Flight Center (USA). This work utilizes data obtained by the Global Oscillation Network Group (GONG) program, managed by the National Solar Observatory, which is operated by AURA, Inc. under a cooperative agreement with the National Science Foundation. The data were acquired by instruments operated by the Big Bear Solar Observatory, High Altitude Observatory, Learmonth Solar Observatory, Udaipur Solar Observatory, Instituto de Astrofísica de Canarias, and Cerro Tololo Interamerican Observatory. YZ and JZ also acknowledge high-performance computing support from Pleiades, operated by NASA's Advanced Supercomputing Division.

TABLE OF CONTENTS

DEDICATION	ii
ACKNOWLEDGEMENTS	iii
LIST OF FIGURES	ix
LIST OF TABLES	xviii
LIST OF APPENDICES	xix
LIST OF ACRONYMS	xx
ABSTRACT	xxii

CHAPTER

1 Introduction	1
1.1 Solar Interior and Lower Atmosphere	2
1.2 Solar Corona and its Heating	8
1.2.1 The Solar Corona	8
1.2.2 The Coronal Heating Problem	12
1.2.3 Direct Current (DC) Models	14
1.2.4 Alternating Current (AC) Models	17
1.3 Line Widths and Coronal Heating	23
1.3.1 Total or Nonthermal Widths	24
1.3.2 Thermal Broadening and Ion Temperature	26
1.4 Global Modeling of the Solar Corona	27
1.5 Dissertation Overview	28
2 Methodology	30
2.1 Instruments to Observe Coronal Emission Lines	30
2.1.1 Hinode/EIS	30
2.1.2 SOHO/SUMER	32
2.1.3 3PAMIS	35
2.1.4 Instrument Design	35
2.1.5 CoMP	44
2.2 Spectroscopic Diagnostics	44






2.2.1	Formation of Optically thin emission	44
2.2.2	Electron Density Diagnostics	49
2.2.3	Electron Temperature Diagnostics	50
2.2.4	Line Widths, Ion Temperature, and Nonthermal Motions	51
2.3	Simulations	52
2.3.1	AWSoM	52
2.3.2	AWSoM-R	56
2.3.3	Spectrum Synthesis	56
3	Line Width Variation in the CHs	59
3.1	Preface	59
3.2	Introduction	59
3.3	Methodology	60
3.3.1	Data Reduction	60
3.3.2	Stray-light Correction	61
3.3.3	Fitting	62
3.3.4	AWSoM Simulations and Line Synthesis	64
3.4	Results	64
3.5	Discussion	70
3.5.1	Streamer Contamination	70
3.5.2	Ion Temperature in AWSoM	72
3.5.3	Spatial Binning and FOV	74
3.5.4	Stray-light Level	75
3.5.5	Photoexcitation	75
3.5.6	Instrumental Effect	77
4	Ion Temperature in Coronal Holes	80
4.1	Preface	80
4.2	Introduction	80
4.3	Methodology	81
4.3.1	Observation and Data Reduction	81
4.3.2	Data Fitting	82
4.3.3	Ion Temperature Estimation	83
4.3.4	Electron Density and Temperature Diagnostics	84
4.3.5	AWSoM-R Simulation	85
4.4	Results	87
4.4.1	Observations	87
4.4.2	Simulations	92
4.5	Discussion	94
4.5.1	Uncertainty in Instrumental Broadening	94
4.5.2	Wavelength Dependence of the EIS instrumental Widths	96
4.5.3	Validation of the Technique	97
4.5.4	Non-Gaussian Profiles	98
4.5.5	Preferentially Heated Ions	101
5	Line Widths Observed during the 2017 Total Solar Eclipse	105



5.1	Preface	105
5.2	Introduction	105
5.3	3PAMIS Observations and Results	106
5.3.1	Operation and Data Acquisition	106
5.3.2	Data Analysis and Results	108
5.4	Comparison with Ancillary Space-based and Ground-based Data	113
5.4.1	Hinode/EIS	113
5.4.2	Data Analysis and Results	114
5.4.3	CoMP	118
5.4.4	Comparison with Other Observations	119
5.5	Discussion	120
5.5.1	Line Widths and Their Variation with Height: Open and Closed Fields	120
5.5.2	Doppler Shifts in the Corona	128
6	Conclusion and Future Works	129
6.1	Summary	129
6.2	Ongoing and Future Plans	131
6.2.1	AWSoM Simulation of the 2017 TSE	131
6.2.2	Ion Temperature in Post-flare Active Regions	133
6.2.3	Line Widths in the Coronal Rain	134
6.2.4	Magnetic Field Diagnostics in the Solar Corona	135
6.2.5	Material Upflows in the Lower Corona	137
	APPENDICES	140
	BIBLIOGRAPHY	150

LIST OF FIGURES






FIGURE









1.1	A schematic of the solar interior and its atmosphere from https://www.mps.mpg.de/phd/solar-physics-lecture-2008-introduction.pdf	2
1.2	Left: Temperature structure of the famous 1-D semi-empirical VAL solar atmosphere from the photosphere to the upper chromosphere. Image taken from Vernazza et al. (1981) . Right: The structure of the solar atmosphere. Credit: Solar-C mission proposal, NAOJ/JAXA, and NASA.	4
1.3	Quiet Sun granules (left) and a sunspot (right) captured by the Visible Broadband Imager (VBI) of the Daniel Inouye K. Solar Telescope (DKIST). Credits: NSO/AURA/NSF.	4
1.4	The dynamic chromosphere and lower transition region. Top: Spicules observed by Solar Optical Telescope (SOT) on the Hinode spacecraft in Ca II H 396.8 nm at the solar limb from De Pontieu et al. (2007b) . Middle: Hot UV bursts observed in an AR by the Atmospheric Imaging Assembly (AIA) on the Solar Dynamics Observatory (SDO) from Peter et al. (2014) . Bottom: Network jets observed in the Slit-jaw Imager (SJI) on the Interface Region Imaging Spectrograph (IRIS) 1330 and Si II 1394 Å line intensity and width from Tian et al. (2014)	6
1.5	Intensity and Doppler shifts of spectral lines forming in the lower transition region (C IV, 0.1 MK) and higher transition region (Ne VIII 0.6 MK) in the quiet Sun and coronal hole. Image from Tian et al. (2021) , data from Hassler et al. (1999) and Damasch et al. (1999)	7
1.6	A schematic representation of the lower quiet Sun solar atmosphere from Wedemeyer-Böhm et al. (2009)	8
1.7	Cranmer & Winebarger (2019) composite image of the solar corona. Left: 17.4 nm broadband image of the solar corona on July 25, 2014 taken by SWAP (Sun Watcher using Active-pixel-system detector and image Processing) telescope onboard the PROBA spacecraft (Seaton et al., 2013). Right: White-light image of the solar corona during the 2017 TSE obtained and processed by M. Druckmüller, P. Aniol, and S. Habbal.	10
1.8	Different coronal structures observed by the High Resolution Imager (HRI) as a part of the Extreme Ultraviolet Imager (EUI) on board Solar Orbiter. Top: NOAA active region (AR) 12957 and an enhanced zoom-in image of the closed loop systems. S1, S2, and S3 are manual slits to study loop oscillations. Bottom left: A polar coronal hole (CH). Bottom right: quiet Sun (QS) corona with small EUV brightenings (campfires). Images are taken from Berghmans et al. (2021) and Berghmans et al. (2023)	11








1.9	Observations of various small-scale heating events in the corona. Top left: Reconnection nanojets in coronal loops observed by IRIS (Antolin et al., 2021). Top right: EUV bright dots at the edge of an AR observed by Hi-C (Régnier et al., 2014). Bottom left: Braided coronal loops observed by Hi-C (Cirtain et al., 2013). Bottom right: Picoflare jets observed by SolO/EUI (Chitta et al., 2023).	15
1.10	Observations of diverse wave modes in the solar corona. Top left: Decaying kink oscillations in coronal loops observed by SDO/AIA (Nechaeva et al., 2019). Top right: Doppler shifts of slow modes in flaring loops observed by SOHO/SUMER (Wang, 2011). Bottom left: Phase speed of kink waves observed by CoMP (Yang et al., 2020). Bottom right: Torsional Alfvén waves in an AR prominence (Kohutova et al., 2020).	19
1.11	Left: Line width variation in a polar coronal hole reported by Hahn et al. (2012). Right: Possible ion temperature T_i intervals vs. the heavy ion charge-to-mass ratios in a polar coronal hole (Landi & Cranmer, 2009).	25
2.1	Young et al. (2007) example of QS spectrum observed by Hinode/EIS.	31
2.2	Culhane et al. (2007) Optical layout of Hinode/EIS.	32
2.3	Wilhelm et al. (1995) collection of emission lines observed by SUMER.	33
2.4	Wilhelm et al. (1995) layout of the SUMER optical system.	34
2.5	An example of curvature correction: (a) A CCD image showing curved neutral helium spectral lines on the detector. The red rectangle outlines the region shown in panel (c) where the curvature is corrected. (b) Fitting of curved neutral hydrogen and helium lines. (c) Curvature-corrected helium lines from the red rectangle in panel (a). Link to the Jupyter notebook creating this figure:  .	37
2.6	1-D flat field function of the red detector for 52nd-order Fe x 637.4 nm line. (a) Curvature-corrected sky flat image. (b) Zoom-in sky flat image. (c) The 1-D flat-field function averaged between the two green vertical lines. Link to the Jupyter notebook creating this figure:  .	38
2.7	CCD x -pixel positions of various-order spectral lines and the relative wavelength calibration of the green (left) and red (right) detectors. The neutral hydrogen and helium lines are used in the wavelength calibration. The dashed curves show the quadratic fittings of wavelengths. The locations of the observed Fe x and Fe XIV lines during the eclipse are also shown. Links to Jupyter notebooks creating this figure:  (green) and  (red).	39
2.8	Absolute wavelength calibration of the green detector. (a) Chromospheric H β (green arrow) and He I (red arrow) emissions between the lunar disk and corona. (b) The average chromospheric spectrum (grey curve) between the two red ticks in panel (a). The vertical green and red lines indicate the line centroids of laboratory H β and He I. (c) The shift between the chromospheric lines and the laboratory lines at different orders. The horizontal grey line indicates the average pixel shift for the absolute wavelength calibration. Link to the Jupyter notebook creating this figure:  .	40



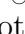




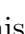
2.9	Line widths of the narrow neutral hydrogen and helium lines as a function of CCD y -pixel position in the green (a) and red (b) detectors. The blue diamonds represent the curvature-corrected widths, and the red dots are for the uncorrected widths. The dashed horizontal lines indicate the instrumental widths used in this study. Link to the Jupyter notebook creating this figure: 	41
2.10	Determining the spectrograph pointing: (a) Fitting the lunar limb on context images. The red cycle highlights the lunar limb, and the red vertical line represents the position of the slit. (b) and (c) Linear fitting of the motion of the disk center on context images. (d) Variation of the fitted disk radius. (e) An off-limb CCD image. The blue and green arrows indicate limb emission leaking from the slit mirror. (f) CCD counts averaged along the x -axis, with the arrows being the same as Panel (e). The shaded pink area between the two arrows is used to calculate the spatial sampling of the detector. Link to the Jupyter notebook creating this figure: 	43
2.11	Intensity ratio of Mg IX 706/694 Å and Fe XII 186/195 Å at different electron density N_e	50
2.12	Intensity ratio of Fe X 184/6374 Å and Fe XI 188/257 Å at different electron density N_e	51
2.13	Meridional cuts of steady-state AWSoM simulation of the corona density, electron temperature, solar wind velocity (top three panels), and NEI heavy ion charge state ratios (middle and bottom rows). Figure taken from Szente et al. (2022)	54
2.14	Comparison between AWSoM synthetic line intensity and Doppler shift of an AR with Hinode/EIS observations from Shi et al. (2022)	58
3.1	The positions of the EIS Slit over SDO/AIA 193 Å observations during on-disk exposures on 2011 March 5, 6, and 11. On March 5 and 6, most of the slit was covered by the quiet-Sun plasma. On March 11, the slit was directed at the CH, which explains why the stray-light intensity estimated on March 11 is much lower.	62
3.2	2% stray-light intensity (dot-dashed) of Fe XII and Fe XIII lines vs. off-limb spectrum (solid) at $1.4 R_\odot$ on March 5 (left), 6 (middle), and 11 (right). The inferred stray-light contribution on March 11 is much lower than that on March 5 and 6.	63
3.3	Examples of fitting an observed Fe XII 195.1 Å line profile at $\sim 1.03, 1.26,$ and $1.49 R_\odot$ assuming a stray-light level of 2%. The pink histogram represents the observed line profiles. The dashed red profiles are the fitted off-limb true emission. The dot-dashed purple lines are the 2% stray-light profile. The solid black lines are the sum of the fitted off-limb spectrum and the stray-light profile. The fitting parameters and their 90% credible levels are listed as well (integrated intensity I_0 , line centroid wavelength λ_0 , FWHM $\Delta\lambda$, and background intensity I_{bg}).	65




3.4	A corner plot of the marginalized distribution of the posterior probability sampled by MCMC algorithms from the Fe XII 195 Å line profile in Figure 3.3 (b), corresponding to $1.26 R_{\odot}$: I_0 integrated intensity, λ_0 line centroid wavelength, $\Delta\lambda$ FWHM, and I_{bg} background intensity. The diagonal panels show the 1D distribution of the parameters. The vertical lines in each panel stand for the 5%, 50%, and 95% cumulative probability (i.e., 90% credible levels). The 2D posterior probability distribution between each of the two parameters is shown in the off-diagonal panels. This figure is generated using the python package <code>corner.py</code> (Foreman-Mackey, 2016).	66
3.5	The measured FWHMs and the effective temperature or the effective velocity of the Fe XII 192.4, 193.5, and 195.1 Å and Fe XIII 202.0 Å lines as a function of heliocentric distance using different stray-light levels. The data were spatially binned in every 16 pixels along the y-axis. The red, yellow, and green lines illustrate the FWHMs fitted using 2%, 4%, and 10% stray-light levels, respectively. The purple lines represent the line widths inferred from the SPECTRUM synthetic spectrum. The line widths caused by undamped (UD) waves are shown in blue and pink curves. The shaded blue and pink area indicates the uncertainty in estimating the undamped widths.	67
3.6	Physical quantities in AWSoM outputs in the meridional cuts of the solar corona taken in the plane corresponding to the LOS, perpendicular to the ecliptic: (a) electron temperature T_e ; (b) ion temperature T_i ; (c) particle number density n ; (d) total magnetic field strength B_{tot} ; (e) LOS velocity u_{LOS} ; (f) total velocity u_{tot} ; (g) local LOS nonthermal velocity ξ ; and (h) contribution function of the Fe XII 195 Å line $C_{I,195}$	68
3.7	(Upper left) Local total FWHM $\Delta\lambda$ distribution in the meridional cut of the AWSoM results. The contours show the levels of the Fe XII 195.1 Å contribution function normalized to its maximum $C_{I,195}/C_{I,195,max}$. The contour labels are in the logarithmic scale, i.e., -1 means 10^{-1} of the maximum value. (Upper right) Relative contribution of Fe XII 195.1 emission originated from the CH or the streamer at different heights in AWSoM simulations. (Middle) Relative contribution of Fe XII 195.1 emission per voxel along the LOS (dot-dashed blue) and local FWHM distribution along the LOS (solid red) at a heliocentric distance of $1.2 R_{\odot}$. The dashed horizontal line indicates the fitted emergent Fe XII line width at $1.2 R_{\odot}$. (Bottom) The same as the middle panel, but at a heliocentric distance of $1.5 R_{\odot}$	71
3.8	SECCHI EUVI 195 Å imaging of the streamer on 2011 March 11, when the STEREO-B spacecraft was in the quadrature with Earth and Sun. The red rectangle in the upper panel outlines the FOV of the lower panel. Note that the intensity in the lower panel has been rescaled.	73
3.9	(a) Modified Fe XII ion temperature distribution in the meridional cut of the solar corona taken in the plane corresponding to the LOS, where the green region stands for the streamer and the yellow region is treated as the CH. (b) Fe XII 195 Å line widths synthesized from the modified Fe XII ion temperature compared with the current AWSoM simulation and EIS observations.	74

3.10	FWHMs of Fe XII 192.4, 193.5, and 195.1 Å and Fe XIII 202.0 Å measured by different spatial binnings: every 2, 4, 8, 16, and 32 pixels along the slit using a 2% stray-light level. In order to save the computation time, the line profiles used in this figure are fit using a maximum likelihood optimization method. The error bars in this figure are from the diagonal components of the covariance metrics.	76
3.11	The variation in the Fe XII 195 Å line centroid wavelengths λ_0 as a function of height measured from EIS observations and AWSoM simulations. We show the differences between the line centroid wavelengths λ_0 and the line centroid wavelength $\lambda_{0,\text{initial}}$ of the pixel closest to the limb. The horizontal line indicates the line centroid wavelength of the fitted stray-light profile.	77
3.12	Fe XII 192.4, 193.5 and 195.1 Å line intensity ratios at different height using different radiometric calibration method: Warren et al. (2014) (solid) and Del Zanna (2013) (dashed). The dotted horizontal lines indicate the reference values given by the CHIANTI database.	78
3.13	The difference between the FWHM of the Fe XII 192.4, 193.5, and 195.1 Å lines at different heights.	79
4.1	Positions of SUMER and EIS slits on the EIT 195 context image. Left: EIT 195 image of the full solar disk on 2007 November 16 at 07:25:35 UT. The red rectangle displays the FOV of the right panel. Right: slit pointing at the coronal hole boundary. The red dashed line shows the location of the 300" slit of SUMER. The yellow dashed lines show the first and the last pointing location of the EIS slit during the seven-step raster. The solid blue line shows the region of the data analyzed in this paper. Link to the Jupyter notebook creating this figure:  .	82
4.2	Two in-flight radiometric corrections in the SW (top) and LW (bottom) detectors of EIS. Locations of the spectral lines used for electron temperature and density diagnostics are also displayed. Link to the Jupyter notebook creating this figure: 	86
4.3	Examples of the single and multi-Gaussian fitting. (a) Single-Gaussian fitting of the Na IX 681 Å line observed by SUMER. (b) Multi-Gaussian fitting of the blended lines near 192 Å observed by EIS, including the blended Fe VIII and Fe XI 192.021 Å, Fe XII 192.394 Å, and three other unidentified (u) lines. The top panel shows the observed spectrum (step line) and the fitting line profile (solid black line). The lower panel displays the fitting residual. Links to the Jupyter notebook creating panels (a)  and (b) 	88
4.4	The measured effective velocity v_{eff} of the Fe XII 192, 193, and 195 Å lines and the average effective velocity \bar{v}_{eff} of Fe XII. The horizontal dashed line indicates the average effective velocity \bar{v}_{eff} . The darker/lighter shaded regions show the $1\sigma/3\sigma$ uncertainty level, respectively. Link to the Jupyter notebook creating this figure: 	89

4.5	<p>Left: electron density n_e diagnostics of the coronal hole boundary region shown in Figure 4.1. Right: electron temperature T_e diagnostics in the same region. The colored data points in the right panel represent T_e at $\log n_e = 8.0$, while the gray ones stand for the T_e inferred at $\log n_e = 8.5$. The yellow-shaded area displays the chosen range of the electron temperature. The line ratios are sorted from left to right by the maximum formation temperature T_{\max} (see Tables 4.1 and 4.2). Link to the Jupyter notebook creating this figure: </p>	90
4.6	<p>Estimated ion temperatures T_i vs. ion charge-to-mass ratio Z/A. For each ion, the boxes show possible ion temperature intervals between $T_{i,\min}$ and $T_{i,\max}$, while the whiskers indicate the uncertainty in $T_{i,\min}$ and $T_{i,\max}$. The ion temperatures inferred from lines observed by EIS and SUMER are shown in dark green and orange, respectively. The horizontal shaded area displays the electron temperature measurement shown in Figure 4.5. The dashed gray line is arbitrarily drawn to illustrate the U-shaped dependence. * The S x 776.373 Å line is poorly fitted. †The Fe x 1028 Å line is self-blended, but still kept for comparison. Link to the Jupyter notebook creating this figure: </p>	91
4.7	<p>Physical parameters predicted by AWSoM-R along the LOS covering the entire SUMER slit. The dotted white lines show the region selected for analysis. (a) Electron temperature T_e, (b) proton temperature T_p, (c) electron density n_e, (d) total magnetic field B_{tot} and field lines, (e) LOS velocity v_{LOS}, (g) wave-induced nonthermal velocity ξ_w, (h) emissivity of the Fe VIII 186 Å line, (i) and emissivity of the Fe XII 192 Å line. Link to the Jupyter notebook creating this figure: </p>	92
4.8	<p>Fitting synthetic Fe VIII 186 Å and Fe XII 192 Å lines under different conditions. w v_{LOS}: synthetic profiles with the Doppler effect. w/o v_{LOS}: synthetic profiles without the Doppler effect. w $\Delta\lambda_{\text{inst}}$: synthetic profiles convolved with instrumental width $\Delta\lambda_{\text{inst}} = 70 \text{ mÅ}$ and rebinned to EIS spectral resolution. w/o $\Delta\lambda_{\text{inst}}$: synthetic profiles without instrumental effects. Link to the Jupyter notebook creating this figure: </p>	93
4.9	<p>Differences between the observed effective velocity $v_{\text{eff,obs}}$ and the synthetic effective velocity $v_{\text{eff,AWSoM}}$ of each spectral line used in ion temperature diagnostics. Red dots with error bars: EIS lines. Blue diamonds with error bars: SUMER lines. Link to the Jupyter notebook creating this figure: </p>	94
4.10	<p>Same as Figure 4.6 but using the cross-calibrated EIS instrumental width $\Delta\lambda'_{\text{inst,EIS}} = 62.7 \text{ mÅ}$. The dashed gray line is arbitrarily drawn to illustrate the U-shaped dependence. Link to the Jupyter notebook creating this figure: </p>	95
4.11	<p>Same as Figure 4.9 but using EIS instrumental broadening $\Delta\lambda'_{\text{inst,EIS}} = 62.7 \text{ mÅ}$ cross-calibrated with SUMER. Link to the Jupyter notebook creating this figure: </p>	96
4.12	<p>Fitted FWHM $\Delta\lambda_{\text{fit}}$ versus line centroid wavelength λ_0 of the Fe XI and Fe XII lines in off-limb quiet-Sun corona. The dashed line in the left panel shows the best fitting of $\Delta\lambda_{\text{fit}} = f(\lambda_0 \Delta\lambda_{\text{inst}}, v_{\text{eff}})$. Link to the Jupyter notebook creating this figure </p>	97

4.13	Same as Figure 4.6, but using line widths from AWSoM-R simulations. The colored horizontal area represents the range of average electron temperature T_e and proton temperature T_p along the LOS weighted by either Fe VIII 186 Å emissivity or Fe XII 192 Å emissivity. Link to the Jupyter notebook creating this figure: 	98
4.14	Single-Gaussian and double-Gaussian fitting to the (a) O VI 1032 and 1037 Å, (b) Ne VIII 770 and 780 Å, and (c) Mg X 609 and 624 Å lines, including the adjacent C II 1036 and 1037 Å and Si X 624 Å lines. The black solid curve shows the fitting result. The dashed curves show each Gaussian component. The single-Gaussian widths, the double-Gaussian widths, and relative intensities are also shown. The vertical gray areas in panel c indicate the masked pixels during the fitting. Note that we only fixed the line centroids in the double-Gaussian fitting of the Mg X 624 Å line. Link to the Jupyter notebook creating this figure: 	100
4.15	κ fitting of the brightest coronal lines observed by SUMER. The fitted κ and FWHM of the κ profile $\Delta\lambda_\kappa$ are shown as well. The weak blended or stray-light lines are still fitted with a Gaussian distribution. Link to the Jupyter notebook creating this figure: 	102
4.16	Comparison between the ion temperature T_i in the polar coronal hole measured by this study (gray box plot), Dolla & Solomon (2008) , (red error bars), and Landi & Cranmer (2009) , (blue error bars). Gray ion names represent ions that are not used in this study. Link to the Jupyter notebook creating this figure: 	103
5.1	Overview of the 3PAMIS observation during the 2017 TSE and two Hinode/EIS observations made on 2017 August 21. (a) 3PAMIS/Green FOV (Gray) overplotted on the Fe XIV 530.3 nm line-to-continuum ratio image. (b) 3PAMIS/Red FOV (Gray) overplotted on the Fe XI 789.2 nm line-to-continuum ratio image. (c) An example streamer spectrum showing Fe XIV 530.3 nm line at the 61st, 62nd, and 63rd orders. Link to the Jupyter notebook creating this figure: 	107
5.2	Overview of the Fe XIV 530.3 nm (left) and Fe X 637.4 nm (right) line intensities observed by 3PAMIS. The line-to-continuum ratios of the two lines are shown, along with the SDO/AIA images on the disk. To fill the data gaps, the intensity is interpolated using a 2-D Gaussian convolution kernel. The small zoom-in panels show Fe XIV 530.3 nm and Fe X 637.4 nm line profiles, which are binned over 5 pixels along the slit. Additionally, single-Gaussian fit results of these profiles are shown. v represents the Doppler velocity, and v_{eff} denotes the effective velocity, both of which are in units of km s^{-1} . Link to the Jupyter notebook creating this figure: 	109
5.3	(a) Fe XIV 530.3 nm line-to-continuum ratio measured by a narrow-bandpass imager from Boe et al. (2020) . (b) 3PAMIS Fe XIV 530.3 nm line intensity. (c) ambient continuum intensity. (d) line-to-continuum ratio. (e) Doppler velocity. (f) line width. (g) Fe XI 789.2 nm narrow-band image. (h-l) similar to panels (b-f) but for Fe X 637.4 nm. The red rectangles represent the FOVs of two complementary Hinode/EIS observations. Link to the Jupyter notebook: 	110

5.4	Fe xiv 530.3 nm line intensity I_{tot} (b) and line width (c) variation along four cuts: northern streamer and polar plumes (NS/PP), active region 1 (AR1), active region 2 (AR2), and southern streamer (SS). Fe x 637.4 nm line intensity I_{tot} (b) and line width (c) variation along four cuts: northern streamer and polar plumes (NS/PP), coronal hole (CH), active region (AR), and the quiet Sun (QS). Link to the Jupyter notebook creating this figure: 	112
5.5	Overview of EIS line intensity fitted by EISPAC. Top: <code>dhb_polar_scan</code> observation of the CH. Bottom: <code>Atlas_30</code> observation of the east limb QS region. The red curves highlight the regions where line profiles are averaged. Profiles in the green boxes are averaged to estimate the off-limb stray light for the CH observation. Link to the Jupyter notebook creating this figure: 	115
5.6	Effective temperature T_{eff} and effective velocity v_{eff} of different ions observed by 3PAMIS and EIS in the north pole coronal hole at three different heights: 1.03–1.08 R_{\odot} (top), 1.08–1.13 R_{\odot} (mid), and 1.13–1.18 R_{\odot} (bottom). Link to the Jupyter notebook creating this figure: 	116
5.7	Effective temperature T_{eff} of different ions observed by 3PAMIS and EIS in the off-limb QS region. Link to the Jupyter notebook creating this figure: 	117
5.8	Comparison between the Doppler velocity v_{LOS} and line width observed in Fe XIII 1074.7 nm by CoMP and Fe xiv 530.3 nm 3PAMIS. (a) CoMP Doppler velocity. (b) CoMP Doppler velocity resampled to match the 3PAMIS pixels. (c) 2D histogram and Pearson correlation coefficient of the Doppler velocity measured by 3PAMIS and CoMP. (d) CoMP Fe XIII line widths. (e) CoMP widths resampled at 3PAMIS pixels. (f) 2D histogram and Pearson correlation coefficient of the widths measured by 3PAMIS and CoMP. Link to the Jupyter notebook creating this figure: 	118
5.9	Comparison between the Fe xiv 530.3 nm line widths given as effective velocity v_{eff} in (b) and effective temperature T_{eff} (c) measured by Koutchmy et al. (2019) (red) and 3PAMIS along the slit position 1 (K19-1) and 4 (K19-4) shown in panel (a). Koutchmy et al. (2019) (blue, purple). Link to the Jupyter notebook creating this figure: 	120
5.10	Comparison of the line widths variation different structures observed by 3PAMIS and other instruments, along with the spectral lines and years of observation. Lithium-like ions are labeled by *. Data is digitized from the listed publications. Link to the Jupyter notebook creating this figure: 	121
5.11	Electron density n_e measured by CoMP and the excitation of the upper energy level of Fe xiv. (a) Fe XIII 1074.7 nm intensity enhanced by a radial intensity filter. (b) Electron density n_e inferred by Fe XIII 1074/1079 ratio. (c) Decrease in n_e along the three cuts shown in Panel a. (d) Population entering the upper energy level of Fe xiv 530.3 nm by different processes at various densities and heights. PE: photoexcitation; RD: radiative decay through cascades from higher levels; e^- : collisions with electrons; p^+ : collisions with protons. $*n_e$ is extrapolated, assuming an exponential drop with height. Link to the Jupyter notebook creating this figure: 	124

5.12	(a) Electron temperature T_e measured by Boe et al. (2020) using the Fe XI 789.2 nm and Fe XIV 530.3 nm ratio. (b) and (c) Nonthermal velocity ξ in Fe XIV 530.3 nm and Fe X 637.4 nm lines. (d) and (e) Nonthermal velocity along the cuts shown in Figure 5.4. Link to the Jupyter notebook creating this figure:  .	126
6.1	Synthetic intensity to continuum ratio, Doppler shifts, and line widths of Fe XIV 530.3 nm (top row) and Fe X 637.4 nm (bottom row).	132
6.2	Yohkoh/Soft X-ray Telescope (SXT; Tsuneta et al., 1991) and EIT images of the post-flare AR. The red vertical line represents the SUMER slit position. The sections of the slit used to study the ion temperature in post-flare AR (left two) and coronal rain (right two) are highlighted by two blue parallel lines.	133
6.3	Estimated ion temperatures T_i vs. charge-to-mass ratios Z/A in the post-flare AR loops observed by SUMER. For each ion, the boxes show possible ion temperature intervals between $T_{i,\min}$ and $T_{i,\max}$, while the whiskers indicate the uncertainty in $T_{i,\min}$ and $T_{i,\max}$. The horizontal shaded area displays the measured electron temperature.	134
6.4	A SUMER exposure recording both the warm emission from the coronal loop (e.g., Ne VIII) and cold emission indicative of the coronal rain (e.g., C IV). A free-free continuum enhancement is also highlighted at the location where coronal rain occurred.	135
6.5	Effective temperature T_{eff} and nonthermal velocity ξ in the warm loop (red) and cold coronal rain (blue).	136
6.6	A schematic diagram of the proposed FOV of DKIST/Cryo-NIRSP in the spectropolarimetric scan of an AR.	137
6.7	Emission originating from the chromosphere to solar corona in NOAA AR 12960 observed by IRIS, SoHO/SPICE, and Hinode/EIS.	138
A.1	Normalized intensity of the cooler stray light lines (O I, Ly β , C II, O IV, O V, N IV, and S V), and hotter lines (N V and Ne VIII) along the SUMER slit. The vertical shaded area represents the averaged 30 pixels. Link to the Jupyter notebook creating this figure  .	141
C.1	Comparison between Fe XIV 530.3 nm profiles at the 61st, 62nd, and 63rd orders in various coronal structures and heights: the QS, AR, and streamer (ST). The profiles in each structure are depicted in two rows of subplots: the first row shows the original profiles, while the second row displays the 5-pixel averaged profiles. The last row shows the sum of three different orders. The fit Doppler velocity v and effective velocity v_{eff} are measured in the units of km s^{-1} . Link to the Jupyter notebook creating this figure:  .	147

LIST OF TABLES

TABLE

4.1	Spectral lines ratios used for electron density diagnostics. T_{\max} is the temperature of the maximum line formation calculated by CHIANTI using the DEM derived from the average coronal hole spectra in Vernazza & Reeves (1978)	85
4.2	Spectral lines ratios used for electron temperature diagnostics. T_{\max} is the temperature of the maximum line formation calculated by CHIANTI using the DEM derived from the average coronal hole spectra in Vernazza & Reeves (1978)	87
5.1	Electron density n_e and electron temperature T_e diagnostics of regions 1 (1.035–1.06 R_\odot) and 2 (1.06–1.1 R_\odot). Fe XII 18.68 nm and Fe XI 25.75 nm lines are self-blended. Entries in the GDZ, HPW, and New columns utilize the radiometric corrections reported by Del Zanna (2013) , Warren et al. (2014) , and the latest Del Zanna et al. (2023) , respectively.	117
B.1	Estimated ranges of ion temperatures $T_{i,\min}$ and $T_{i,\max}$ from spectral line widths. The fitting of the individual spectral line can be found in the following Jupyter notebooks : EIS , SUMER window 1 , SUMER window 2 , SUMER window 3 , and SUMER window 4	143

LIST OF APPENDICES

A Spicules, stray light, and Opacity Effects in SUMER and EIS Observations	140
B Table of Ion Temperatures at the Coronal Hole Boundary	142
C Comparison between Different Spectral Orders in PaMIS	146
D Photon Redistributions of Constant Continuum	148

LIST OF ACRONYMS

AIA Atmospheric Imaging Assembly

AR Active Region

AWSOM Alfvén Wave Solar atmosphere Model

AWSOM-R Alfvén Wave Solar atmosphere Model-Realtime

BATS-R-US Block Adaptive Tree Solarwind Roe Upwind Scheme

CCD Charge-Coupled Device

CH Coronal Hole

CoMP COronal Multi-channel Polarimeter

Cyro-NIRSP Cryogenic Near-Infrared Imaging Spectropolarimeter

DKIST Daniel K. Inouye Solar Telescope

EIS Extreme Ultraviolet Imaging Spectrometer

EIT Extreme Ultraviolet Imaging Telescope

EUI Extreme Ultraviolet Imager

EUV Extreme Ultraviolet

GONG Global Oscillation Network Group

HCS Heliospheric Current Sheet

PaMIS Partially Multiplexed Imaging Spectrometer

PFSS Potential Field Source Surface

MCMC Markov chain Monte Carlo

MCP Microchannel Plate

MHD Magnetohydrodynamics

MLSO Manua Loa Solar Observatory
NRL Naval Research Lab
QS Quiet Sun
TSE Total Solar Eclipse
TR Transition region
SDO Solar Dynamics Observatory
SOHO SOLar and Heliospheric Observatory
Solo Solar Orbiter
SUMER Solar Ultraviolet Measurements of Emitted Radiation
SWAP Sun Watcher using APS and Imaging Processing
SWMF Space Weather Modeling Framework
UV Ultraviolet
VBI Visble Broadband Imager
VISP the Visible Spectro-Polarimeter
XDL cross delay-line

ABSTRACT

The coronal heating problem is the most challenging and enduring mystery in solar physics research: how does the corona, the outermost atmosphere, maintain a temperature exceeding one million kelvin, in contrast to the surface at 5,770 K? The past eight decades of research developed multiple coronal heating theories, classified into two major categories: the direct current (DC) models, commonly known as the "nanoflare" conjecture, and the alternating current (AC) models, promoting the wave heating scenarios.

This dissertation aims to advance our knowledge of the mysterious coronal heating problem by employing the broadening of spectral lines, which simultaneously reflects the heating of heavy ions and the unresolved motions in the solar corona. Together with the forward modeling of the line broadening from the Alfvén Wave Solar Model (AWSoM), the dissertation yields new constraints on coronal heating models.

The dissertation consists of three independent studies. The first part of the dissertation investigated the variation of line widths as a function of height in a coronal hole. The Fe XII and Fe XIII line widths start to increase below 1.2 solar radii and plateau beyond this height, which differs from the predictions made by AWSoM. In the second part, a non-monotonic, U-shape dependence of ion temperatures on their charge-to-mass ratio was disclosed at the coronal hole boundary, which challenges the classical ion-cyclotron resonance heating models. In the last part, distinct line width variations between the open- and closed-field regions were unveiled, taking advantage of the 2017 total solar eclipse (TSE) observations in the visible light with a large field-of-view (FOV). Ancillary extreme ultraviolet (EUV) and near-infrared observations further fortify the eclipse data. These discoveries shed light on the essential role of MHD waves and turbulence in coronal heating.

In summary, this dissertation presents a comprehensive study of spectral line widths and their variation in the dynamic and inhomogeneous solar corona. The dissertation finds that nonthermal velocity increases from 30 to 80 km s⁻¹, and heavy ions are heated 1.5 to 3 times more than electrons in open structures, while the line widths in closed structures are nearly constant, which provides essential limitations for wave heating models. The differences in the width of spectral lines between various coronal structures suggest that wave heating is more dominant in open structures, while localized heating occurs in closed structures.

CHAPTER 1

Introduction

The Sun is a unique G2V dwarf among the billions and trillions of stars in our universe. The star, now in its mid-life at approximately five billion years, hosts a remarkable planet called Earth, home to humans. The Sun endlessly radiates electromagnetic emission, commonly known as the sunlight, which warms our tiny planet into a habitable zone. Our ancestors, ranging from Sumerians, Egyptians, Greeks, and Romans to Incas and Chinese, all developed their worship of the powerful Sun. Total solar eclipses, when the Sun darkens, were frequently interpreted as a warning of incoming calamities in ancient civilizations.

Historically, studying the Sun shed the first light on the development of modern science. Over 2,500 years ago, Babylonian astronomers learned to predict the occurrence of total solar eclipses. In the early 19th century, Fraunhofer's finding of the dark lines in the solar spectrum paved the way for future exploration of atomic structures. During the 1868 total solar eclipse (TSE), an anomalous yellow spectral line sitting near the sodium yellow doublets led to the discovery of helium, named after the Sun. It was not until the last century that scientists realized nuclear fusion powers the Sun and other stars, which marked a significant achievement in understanding the stellar interiors. With the Sun being the sole star that can be well resolved by current telescopes, it still provides incomparable opportunities to investigate plasma physics and stellar astrophysics.

On the other hand, the Sun, with its frequent eruptions such as flares and coronal mass ejections (CMEs), endangers human activities. A huge amount of energy, previously stored in the magnetic fields and then released through eruptions, can significantly distort the terrestrial magnetic field and upper atmosphere. Such events can drive severe space weather phenomena, such as geomagnetic storms and radio blackouts. Therefore, understanding the behavior of this giant neighbor is essential for ensuring humans continue living with a star.

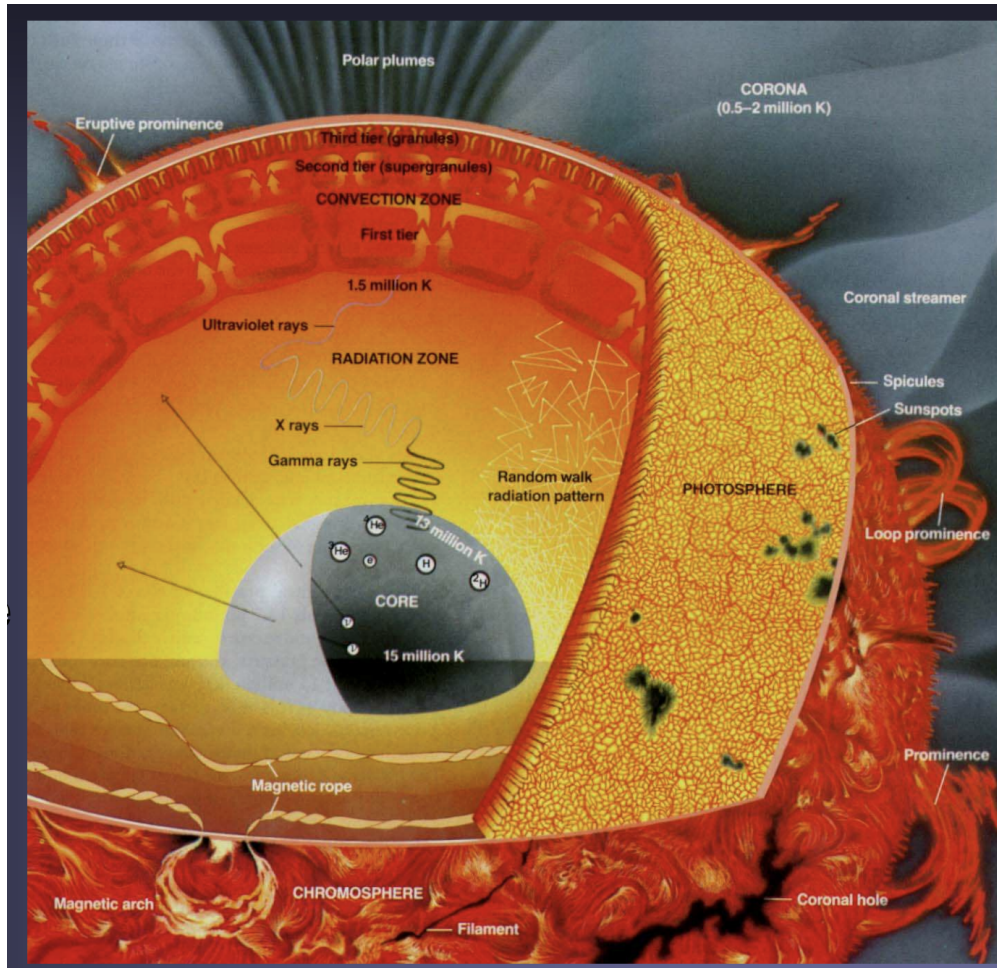


Figure 1.1: A schematic of the solar interior and its atmosphere from <https://www.mps.mpg.de/phd/solar-physics-lecture-2008-introduction.pdf>.

1.1 Solar Interior and Lower Atmosphere

The Sun can be conceptually divided into two primary regions: the interior and the atmosphere, as shown in Figure 1.1. The solar interior is sufficiently dense to prevent any photons from escaping. Above the interior lies a partially transparent atmosphere. The solar interior consists of the core, the radiative zone, and the convection zone. In contrast, the solar atmosphere comprises several layers characterized by plasma temperatures: the photosphere, chromosphere, transition region (TR), and the million-degree corona (Figure 1.2). The solar wind traveling in the interplanetary space originates from the supersonic outflows of the solar corona.

More than 99.999% of the solar mass resides in the solar interior. The interior determines the surface temperature, luminosity, and the evolution of the Sun. The solar interior is also the genesis of solar magnetism, which is the ultimate driver of the diverse activities in the

solar atmosphere, the 11-year sunspot cycle, and the 22-year solar magnetic cycle.

The core extends from the center of the Sun to approximately $0.25 R_{\odot}$. The temperature exceeds 15 MK and the density reaches 150 g cm^{-3} . Proton-proton chain reactions occur in the core as the quantum tunneling effect, enabling protons to overcome their Coulomb barriers, fuse into helium, and release energy.

The radiative zone spans from approximately $0.25 R_{\odot}$ to $0.7 R_{\odot}$, where the high density maintains a short mean free path for photons. The energy transportation is dominated by the absorption and re-emission of photons. In the radiative zone, density decreases from approximately 20 g cm^{-1} to 0.2 g cm^{-3} . The temperature drops from 10 MK to 2 MK between the bottom and the top (Stix, 2002).

The layer above the radiative zone witnesses the recombination of free electrons with heavy ions into various ionic species, significantly increasing the opacity. Therefore, energy transportation through radiation becomes more and more difficult. This further increases the temperature gradient, triggering convection instability by exceeding the adiabatic temperature gradient (Schwarzschild, 1906). Consequently, in the convection zone from $0.75 R_{\odot}$ to $1 R_{\odot}$, the energy is carried by both convective motions of plasma parcels and radiation.

Notably, the convection zone and the solar surface rotate differentially, where the rotation rate varies at different latitudes. The radiative zone and core rotate together as a single rigid body. According to the solar dynamo theory, the tachocline, an interface region between the differentially rotating convection zone and the radiative zone, may be crucial in generating and modulating solar magnetism.

The convection zone is capped by the photosphere, where the gas density is sufficiently low for continuum photons to escape. This layer spans 500-600 km above the surface, commonly defined by the unity optical depth at $5,000 \text{ \AA}$. Within the photosphere, the temperature gradually declines from 6,500 K at its base to 4,000 K, reaching the so-called temperature minimum region. The solar luminosity L_{\odot} is dominated by the photospheric radiation in the visible spectrum, commonly approximated by a blackbody curve at $T = 5778 \text{ K}$.

Observations disclosed that the quiet photosphere is filled with small convection cells, known as granules, with a typical size of 1 Mm (see Figure 1.3). The granule shows a bright central area due to the hot upflowing plasma from the top of the convection zone, contrasted by the dark boundary where the cooled downflow occurs. Large convection cells, with a typical size of 30 Mm called supergranules, can be identified in the horizontal motions in the photosphere (Hart, 1956). They are found to be associated with convective motions in the deeper solar interior.

Occasionally, large-scale (tens of Mm) magnetic fields with strength reaching thousands of Gauss emerge from the convection zone, forming a darker region called a sunspot (right

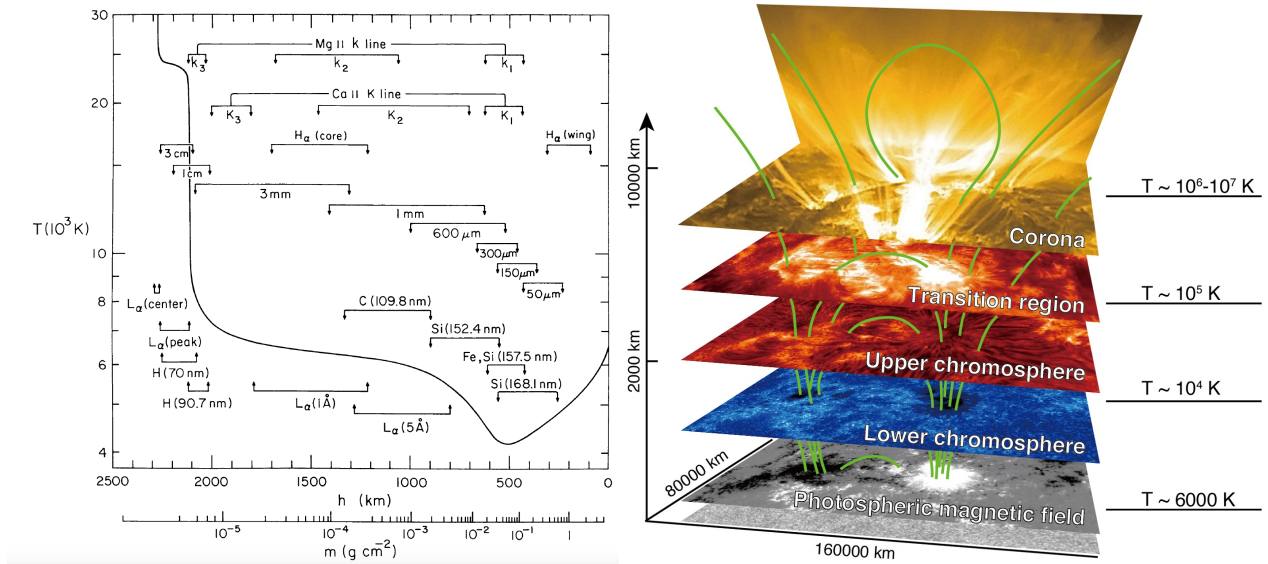


Figure 1.2: Left: Temperature structure of the famous 1-D semi-empirical VAL solar atmosphere from the photosphere to the upper chromosphere. Image taken from Vernazza et al. (1981). Right: The structure of the solar atmosphere. Credit: Solar-C mission proposal, NAOJ/JAXA, and NASA.

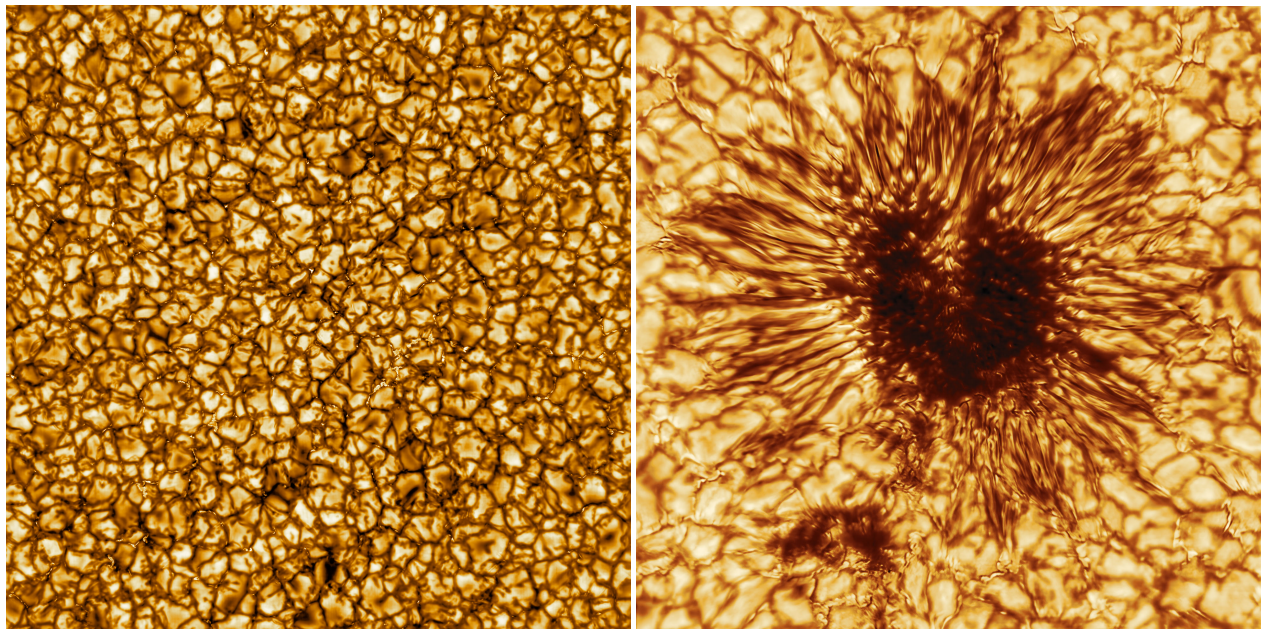


Figure 1.3: Quiet Sun granules (left) and a sunspot (right) captured by the Visible Broadband Imager (VBI) of the Daniel Inouye K. Solar Telescope (DKIST). Credits: NSO/AURA/NSF.

panel in Figure 1.3). The sunspots appear darker than the ambient, known as quiet Sun

(QS) regions. This is because the strong vertical magnetic field in the center (umbra) forbids the convection to transport energy to the surface.

In addition, the photosphere, along with the solar interior, oscillates globally. [Leighton \(1960\)](#) and [Leighton et al. \(1962\)](#) found the Doppler velocity in the photosphere shows a strong temporal correlation with a period of 296 ± 3 s, corresponding to five minutes. This phenomenon, known as five-minute oscillation, was successfully explained by [Ulrich \(1970\)](#) and [Leibacher & Stein \(1971\)](#) as the superposition of velocity fields of numerous nonradial acoustic wave modes (pressure modes, or p -modes) propagating in the solar interior. The observed oscillating patterns provide effective tools for investigating wave propagation and reflection in the solar interior ([Basu, 2016](#)) and may contribute to the generation of Alfvén waves in the higher solar atmosphere ([Morton et al., 2023](#)).

Above the temperature minimum region, the temperature of the solar atmosphere starts to rise. Hydrogen, the most abundant element, starts to ionize and becomes fully ionized at $2 - 5 \times 10^4$ K. As the density decreases, the behavior of plasma becomes dominated by magnetic fields (plasma $\beta < 1$) instead of gas dynamics in the photosphere (plasma $\beta \gg 1$). This region is known as the chromosphere, a name coined during the solar eclipse ([Lockyer, 1868](#)) when the red $H\alpha$ line dominates the chromospheric emission at the limb.

The chromosphere is very dynamic and inhomogeneous. It has an average thickness of 1,500–2,500 km. However, the thickness varies significantly across different regions and over time. The chromospheric network, shown in the bottom panels of Figure 1.4, is a web-like brightening structure, often observed in $H\alpha$ and Ca II H&K, contrasting to the dark internetwork regions. The brightening at the network boundary is caused by the interaction of magnetic fluxes driven to supergranulation boundaries by the convection flow ([Wang et al., 1996](#); [Schrijver et al., 1997](#)).

Other dynamic and small-scale structures in the chromosphere are shown in Figure 1.4, including spicules, UV bursts in active regions (e.g., [Peter et al., 2014](#)), Ellermann bombs ([Ellerman, 1917](#)), and jets in ARs (e.g., [Shibata et al., 2007](#)) or networks (e.g., [Tian et al., 2014](#)). Spicules, the ubiquitous needle-like features at the solar limb, often swing transversely. They appear like dynamic fibrils on the disk in $H\alpha$ ([De Pontieu et al., 2007a](#)).

The substantial radiative energy loss of $\sim 10^6$ erg cm⁻² s⁻¹ in the chromosphere ([Withbroe & Noyes, 1977](#)) necessitates additional heating mechanisms like acoustic (e.g., [Bello González et al., 2010](#)), Alfvén waves (e.g., [De Pontieu et al., 2007b](#)), or the direct Joule heating from the electric currents dissipating in the aforementioned fine structures. Much like the enigmatic coronal heating problem that will be discussed later, whether the wave or current dissipation adequately heat the chromosphere is still a topic of ongoing debate (e.g., [Molnar et al., 2021](#); [da Silva Santos et al., 2022](#)).

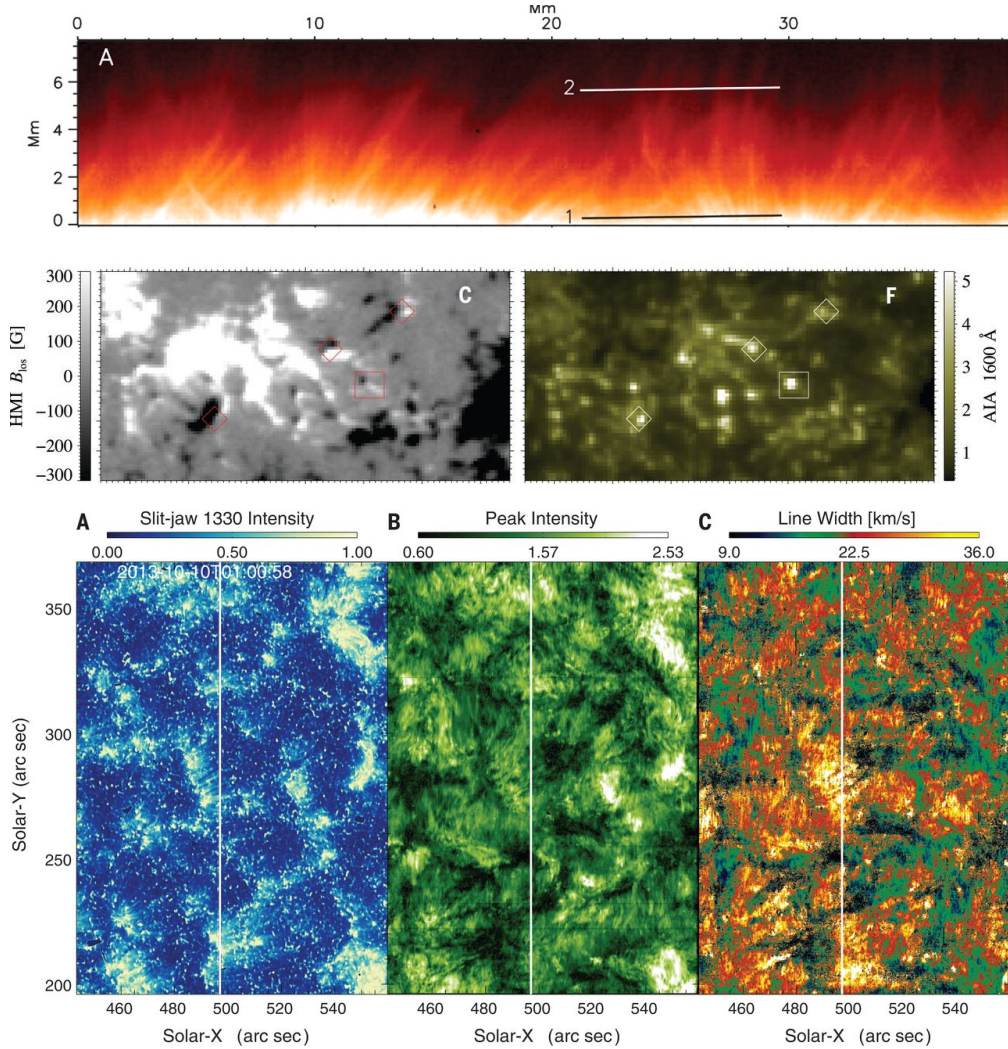


Figure 1.4: The dynamic chromosphere and lower transition region. Top: Spicules observed by Solar Optical Telescope (SOT) on the Hinode spacecraft in Ca II H 396.8 nm at the solar limb from [De Pontieu et al. \(2007b\)](#). Middle: Hot UV bursts observed in an AR by the Atmospheric Imaging Assembly (AIA) on the Solar Dynamics Observatory (SDO) from [Peter et al. \(2014\)](#). Bottom: Network jets observed in the Slit-jaw Imager (SJI) on the Interface Region Imaging Spectrograph (IRIS) 1330 and Si II 1394 Å line intensity and width from [Tian et al. \(2014\)](#).

The transition region (TR) is a critical interface connecting the lower atmosphere to the focus of this dissertation, the hot solar corona. Characterized by a drastic increase in temperature from approximately 5×10^4 K to millions of degrees, the density drops by more than one order of magnitude to maintain the pressure balance. The TR is primarily heated by thermal conduction from the solar corona facilitated by its steep temperature gradient.

The TR also shows a dynamic nature, unveiling network-like structures in the lower transition region and corona-like structures in the higher transition region (see Figure 1.5).

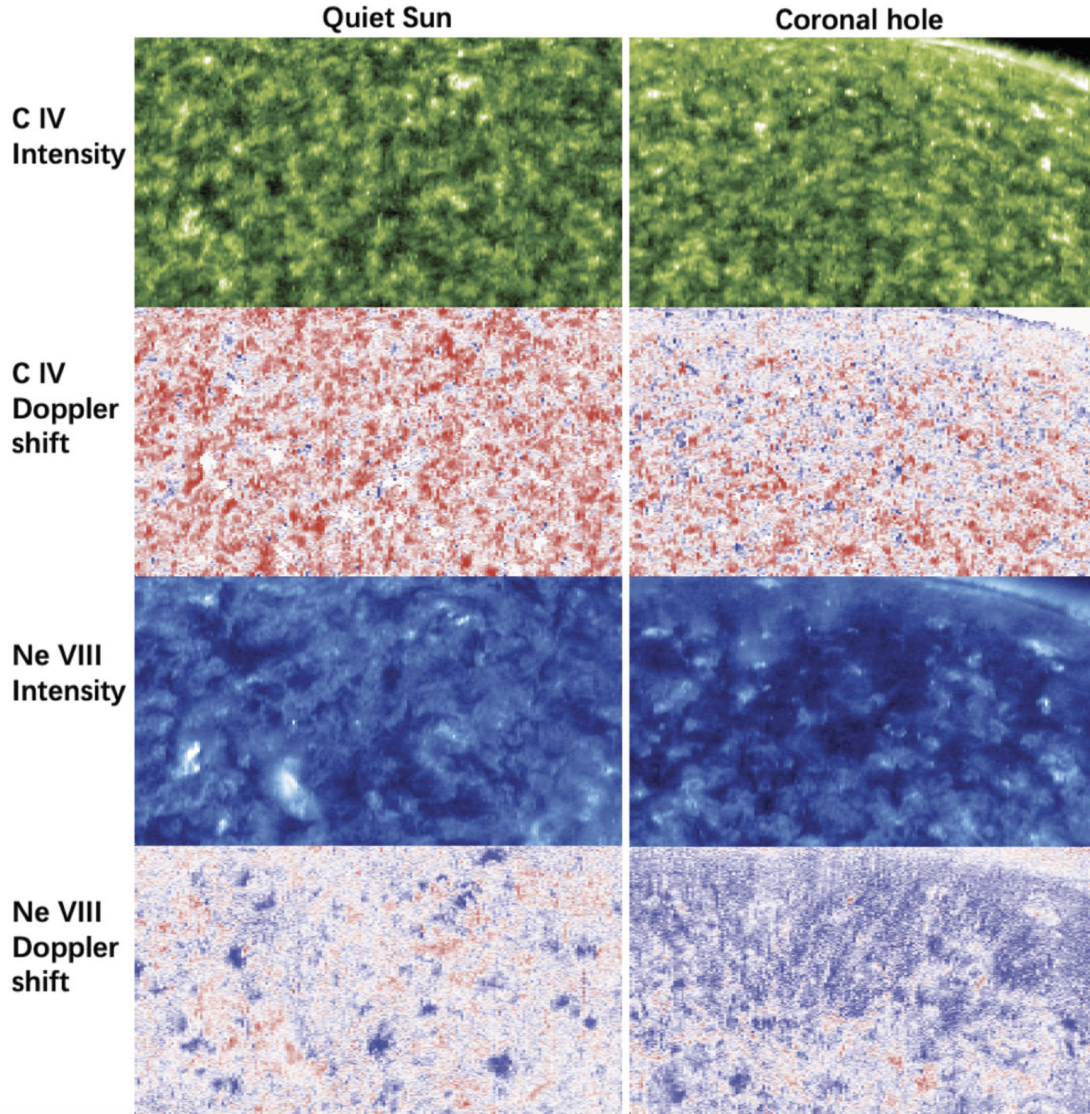


Figure 1.5: Intensity and Doppler shifts of spectral lines forming in the lower transition region (C IV, 0.1 MK) and higher transition region (Ne VIII 0.6 MK) in the quiet Sun and coronal hole. Image from Tian et al. (2021), data from Hassler et al. (1999) and Dammasch et al. (1999).

The temperature-dependent Doppler shifts of spectral lines forming in TR (Peter & Judge, 1999, also in Figure 1.5), together with the multi-component profiles (Peter, 2000, 2001) suggest a complex picture of mass circulation and waves transiting various physical regimes, including small closed loops and open funnels connecting to the corona. Furthermore, the TR is peppered with numerous small-scale heating events, such as explosive events (Dere et al., 1989) and blinkers (Harrison, 1997).

Decades of comprehensive studies of the lower solar atmosphere yielded a modern view of how the underlying layers couple with each other and become connected to the solar

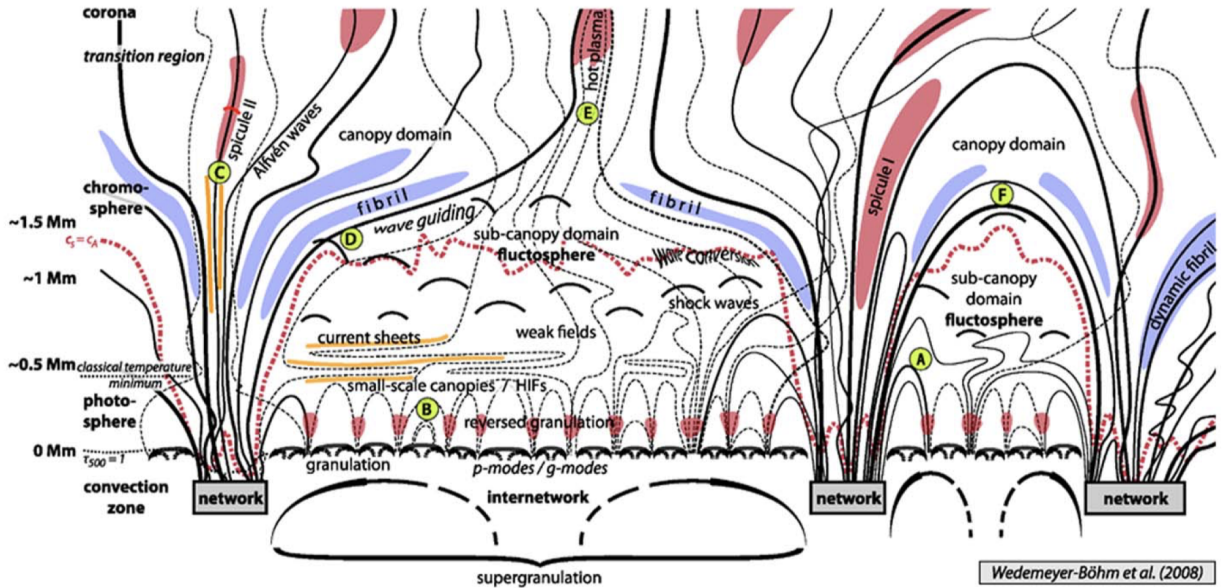


Figure 1.6: A schematic representation of the lower quiet Sun solar atmosphere from [Wedemeyer-Böhm et al. \(2009\)](#).

corona and solar wind ([Wedemeyer-Böhm et al., 2009](#)). As depicted in Figure 1.6, the lower atmosphere, on large scales, consists of the magnetized canopy regions in networks and weak-field sub-canopy regions. As the gas pressure decreases with height, the flux tubes constrained in the canopy domains undergo expansion, forming the open funnels directly connected to the TR and corona and loops connecting the network with opposite polarities. The aforementioned dynamic structures predominantly form in the canopy domain, driven by shocks converted from the leakage of p -mode oscillation ([Hansteen et al., 2006](#); [De Pontieu et al., 2007a](#), e.g., type I spicules and fibrils), magnetic reconnection in current sheets ([De Pontieu et al., 2007b](#), e.g., type II spicules), or the release of magnetic tension accumulated by ambipolar diffusion (e.g., type II spicules, [Martínez-Sykora et al., 2017](#)).

1.2 Solar Corona and its Heating

1.2.1 The Solar Corona

The solar corona is the outermost atmosphere of the Sun. The corona appears very faint compared to the photosphere in the visible light. Historically, the corona was only visible during total solar eclipses (TSEs) when the moon blocked the photospheric emission from the disk. The great astronomer Cassini vividly described the prominent off-limb structures during the 1706 TSE as “une couronne d’une lumière pâle,” translating to “a crown of pale

light” (Westfall & Sheehan, 2015; Cranmer & Winebarger, 2019). This extended layer of the solar atmosphere was aptly named “corona” by José Joaquín de Ferrer after he observed the 1806 TSE.

The invention of photography and regular eclipse expeditions enabled the early scientific observations, both imaging and spectroscopic, of the solar corona. Surprising discoveries include the faint continuum without Fraunhofer lines, known as K-corona, anomalous spectral lines or emission (E-corona). These lines include the D₃ line sitting in the vicinity of the Na I D doublets at 589.0 and 589.6 nm and another green line near the Fraunhofer E line (e.g., Young, 1870).

After the invention of the coronagraph by Bernard Lyot, an instrument that manually eclipses the bright solar disk. Routine observations of the solar corona became feasible. Lyot (1931a,b) first deduced a ion temperature of over 600,000 K from spectral line widths. This conjecture was quickly corroborated by identifying the unidentified green line as originating from the highly-ionized Fe XIV (Grotrian, 1939; Edlén, 1943), indicative of a two million-degree atmosphere.

The space age ushered in a new era of coronal observations, extending to the ultraviolet and X-ray wavelengths, which greatly advanced our knowledge of this hot and dynamic atmosphere. Figure 1.7 illustrates a composite image of the solar corona in EUV (left) and white light (right). The EUV corona reveals multiple structures in the solar corona: a bright active region on the disk, a less visible dark coronal hole (CH) close to the south pole, and the rest diffuse emission of the so-called quiet Sun (QS). Meanwhile, the off-limb part of the EUV and white-light images disclose more prominent closed and open magnetic field structures, including coronal loops, cusp-like streamers, pseudostreamers, and ray-like polar plumes.

Figure 1.8 shows detailed structures of AR, CH, and QS captured by the Extreme Ultraviolet Imager (EUI; Rochus et al., 2020) on board the Solar Orbiter (SolO; Müller et al., 2020) spacecraft. ARs are the most dynamic structures in the solar corona due to the strong magnetic fields, hosting explosive eruptions like flares and CMEs triggered by filament eruptions. The complicated magnetic field topology in ARs is accompanied by the multi-thermal plasmas, mostly ranging from 1–3 MK. During flares, the AR plasma can be heated to over 10 MK.

Coronal loops are among the most striking features in ARs, frequently interpreted as flux tubes filled with dense and hot plasma frozen to the magnetic fields. AR loops can be best identified in emission forming at approximately 1 MK and connecting opposite polarities in the underlying sunspots. At the edge of ARs, fan-like loop structures can be observed (e.g., Warren et al., 2011), which might be the cooler footpoints of hotter coronal loops. The

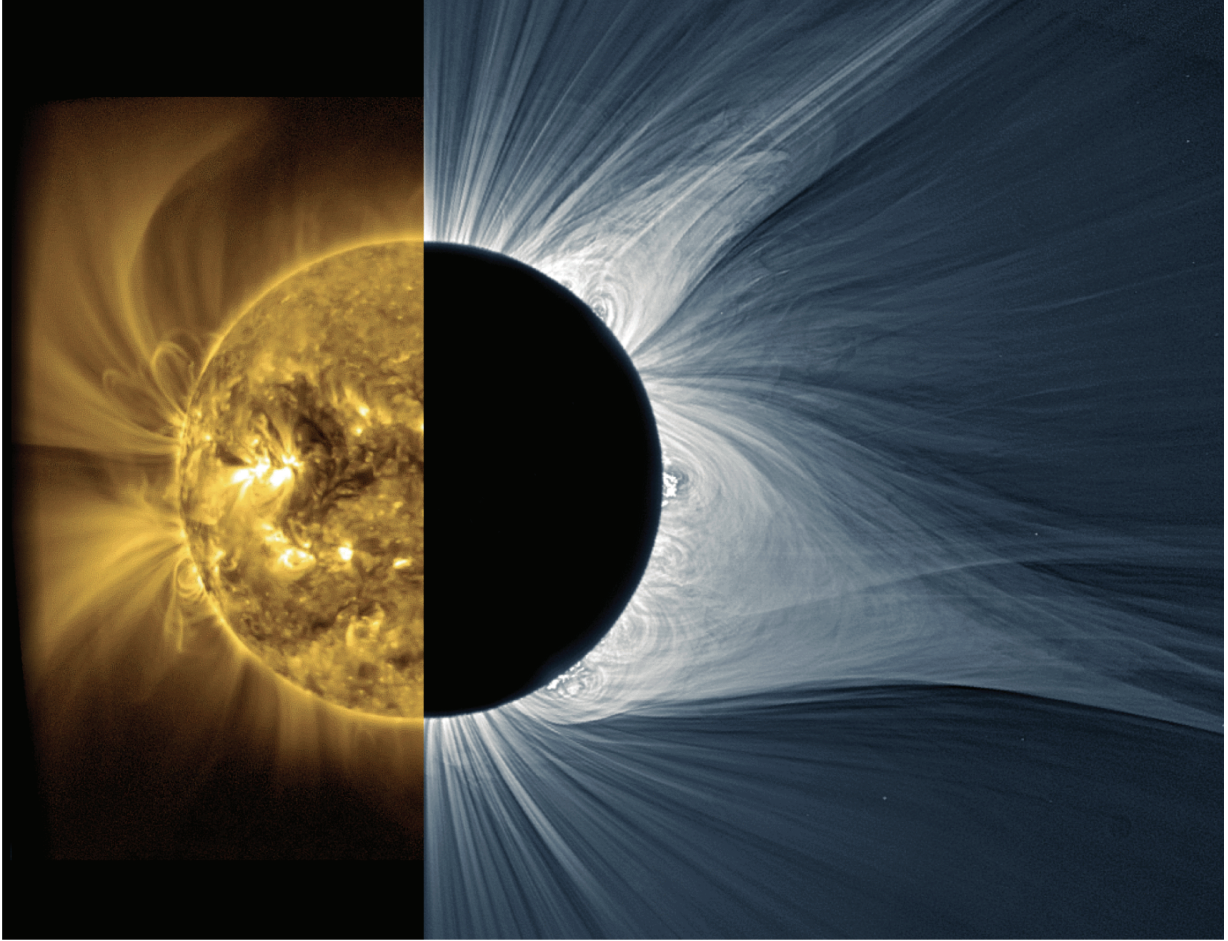


Figure 1.7: Cranmer & Winebarger (2019) composite image of the solar corona. Left: 17.4 nm broadband image of the solar corona on July 25, 2014 taken by SWAP (Sun Watcher using Active-pixel-system detector and image Processing) telescope onboard the PROBA spacecraft (Seaton et al., 2013). Right: White-light image of the solar corona during the 2017 TSE obtained and processed by M. Druckmüller, P. Aniol, and S. Habbal.

complex bright points below the overarching loops are known as the AR moss (Schrijver et al., 1999), which are transition region structures corresponding to the footprints of both warm and hot loops with substantial density increase (Tripathi et al., 2010).

Coronal holes (CHs) are the darkest areas on the solar disk or above the limb when observed in extreme ultraviolet (EUV) or X-ray images because of their low density (e.g., Fludra et al., 1999) and temperature (e.g., Habbal et al., 1993). They often mark the poles during solar minimum and can extend to lower altitudes during solar maximum. Coronal holes are widely accepted as the source regions of the fast solar wind ($\gtrsim 500 \text{ km s}^{-1}$) for the following reasons:

- On-disk CHs have high correlation with high-speed streams in the solar wind (Krieger

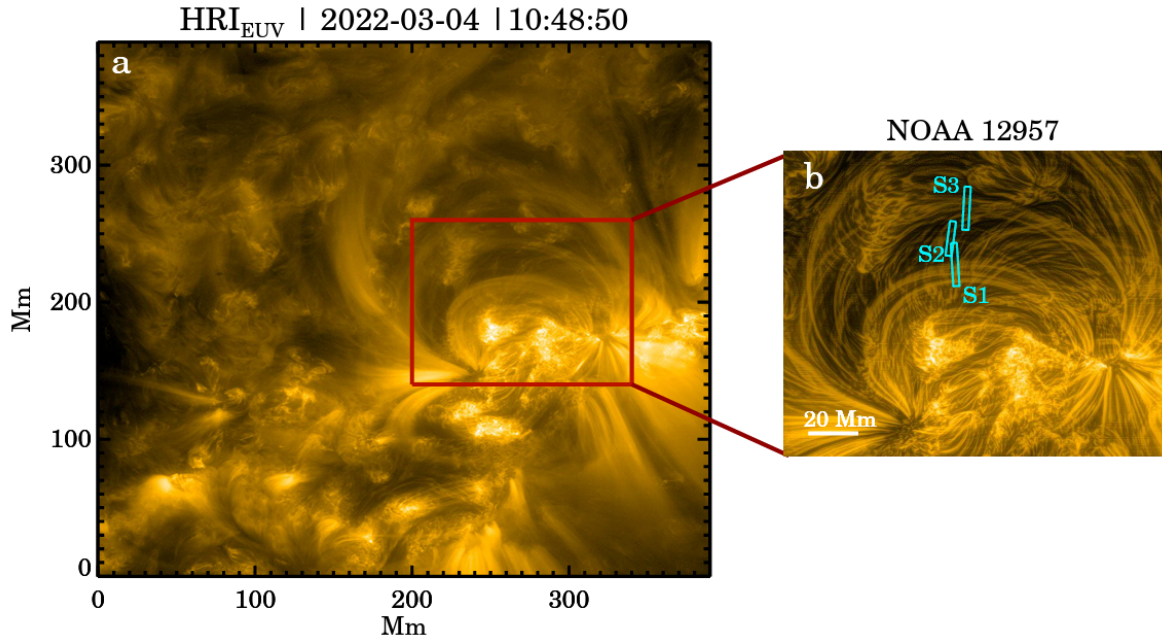


Figure 1.8: Different coronal structures observed by the High Resolution Imager (HRI) as a part of the Extreme Ultraviolet Imager (EUI) on board Solar Orbiter. Top: NOAA active region (AR) 12957 and an enhanced zoom-in image of the closed loop systems. S1, S2, and S3 are manual slits to study loop oscillations. Bottom left: A polar coronal hole (CH). Bottom right: quiet Sun (QS) corona with small EUV brightenings (campfires). Images are taken from [Berghmans et al. \(2021\)](#) and [Berghmans et al. \(2023\)](#).

[et al., 1973, e.g.,](#)).

- Association between CHs and open flux regions in the extrapolated coronal magnetic

field (e.g., Potential Field Source Surface, PFSS [Altschuler & Newkirk, 1969](#); [Schatten et al., 1969](#)).

- Outflows observed in CHs from on-disk TR observations (e.g., [Tu et al., 2005](#)) to a few solar radii (e.g., [Antonucci et al., 2000](#)).

The open magnetic field structure (best seen in the eclipse image in Figure 1.7) and the fast solar wind render the coronal hole an excellent laboratory to study the mechanisms of coronal heating and solar wind acceleration, especially the wave dissipation and turbulence models (e.g., [Hollweg & Isenberg, 2002](#); [Cranmer et al., 2007](#)).

CHs are not uniformly dark. The left bottom panel of Figure 1.8 unveils small brightenings, known as coronal bright points (CBPs). CBPs consist of shorter coronal loops similar to ARs but on smaller scales, associated with flux emergence in photospheric ephemeral regions ([Madjarska, 2019](#)). Polar plumes, characterized by ray-like features, are prominent in the off-limb CH regions to a few solar radii, outlining the flux tubes originating from the unipolar CHs. Plumes are filled with denser and cooler plasma compared to the ambient dark regions ([Wilhelm et al., 2000](#); [Del Zanna et al., 2003](#)). Additionally, CHs are also the site of dynamics processes like X-ray jets (e.g., [Cirtain et al., 2007](#)).

The quiet Sun (QS) represents closed-field regions besides ARs with a typical temperature of 1–2 MK. This diffuse region does not show distinct structures like coronal loops ([Gorman et al., 2023](#)). However, the QS is known to be not “quiet” when observed with high spatial and temporal resolution. CBPs also appear in the QS, alongside other transient brightenings, such as jets, mini-filament eruptions (e.g., [Panesar et al., 2023](#); [Schwanitz et al., 2023](#)), and localized EUV brightenings (campfires; e.g., [Berghmans et al., 2021](#); [Panesar et al., 2021](#)).

1.2.2 The Coronal Heating Problem

The ultimate and challenging question with the solar corona is how this outermost layer reaches over 1 MK, in contrast to the 5,770 K surface. The responsible mechanisms must accommodate the diversity in magnetic topology and plasma conditions in ARs, CHs, and QS. The energy flux required to balance the losses through radiation, thermal conduction, and solar wind (in CHs) is estimated to be 10^7 (AR), 8×10^5 (CH) and $3 \times 10^5 \text{ erg} \cdot \text{cm}^{-2} \cdot \text{s}^{-1}$ (CH, [Withbroe & Noyes, 1977](#)).

A comprehensive coronal heating theory would focus on how the energy and mass are transported and distributed in the solar corona from the coupled lower atmosphere. Numerous heating mechanisms have been proposed since the finding of million-degree plasma in 1940s, reaching a consensus is that the magnetic field plays an essential role in building up

energy in the solar corona, as the acoustic waves appear not to carry enough energy to heat the corona (Athay & White, 1978; Cranmer et al., 2007).

Most coronal heating theories are based on the following observational facts (De Moortel & Browning, 2015):

- The presence of small-scale reconnection in the corona (Cirtain et al., 2013; Panesar et al., 2021, e.g.).
- Various wave modes propagate in the corona (Thompson et al., 1998; Nakariakov et al., 1999, e.g.).
- The solar corona is coupled with the lower atmosphere.

Additionally, a coronal heating model should contain the following subprocesses (Aschwanden, 2005): the mechanical driver for the heating, the storage of energy in magnetic fields, the heating of plasma from the chromosphere to the corona, and the trapping of the heated plasma in the corona.

The coronal heating models can be broadly classified into two major categories: the direct current (DC) and alternating current (AC) models. The DC models represent the dissipation of direct currents in the solar corona when the photospheric boundary condition varies much slower than the Alfvén transit time through the coronal loops. On the other hand, the AC model is characterized by the rapid variation (typically 5–10 min, could be 1 min or less; Cranmer 2019) of photospheric footpoints generating the AC in the solar corona. Many DC models employ magnetic reconnection to dissipate the current. Therefore, they are also known as the “reconnection models.” On the other hand, most AC models rely on the propagation and dissipation of MHD waves in the solar corona, so they are often called “wave dissipation models.”

However, it is worth pointing out that the waves and reconnection are not mutually exclusive and could be interrelated. For example, the reconnection can generate waves, and the collective behavior of reconnection might be described as an expression of magnetically dominated MHD turbulence (Velli et al., 2015). Furthermore, with more observations of the existence of small-scale reconnection and wave propagation in the past two decades, the community realized the heating of different coronal structures might be related to multiple processes (Cranmer & Winebarger, 2019), and the answer to the coronal heating problem should quantify the contribution of each process, for instance, between DC and AC models (Parnell & De Moortel, 2012; Aschwanden, 2019). Readers are referred to extensive reviews like Cranmer & Winebarger (2019), for the detailed parameterized heating efficiency of the following models and theories.

1.2.3 Direct Current (DC) Models

First proposed by [Parker \(1972\)](#), most DC models postulate that the random motions of photospheric footpoints twist and braid the magnetic flux tubes with each other, creating a non-potential field to build up stress and additional free energy in the corona (e.g., [Sturrock & Uchida, 1981](#)). The stress can be released by several processes, such as reconnection (known as "nanoflares" [Parker, 1983, 1988](#)), current cascade (e.g., [van Ballegooijen, 1986](#)), and MHD turbulence (e.g., [Milano et al., 1997](#)).

In addition to the classic view of reconnection in braided loops, reconnection could potentially also occur in coronal separatrix layers, known as flux tectonics ([Priest et al., 2002](#)) or as a consequence of flux cancellations in the photosphere (e.g., [Priest et al., 2018](#)). Furthermore, the energy restored in large-scale twisted field lines can be released while conserving the total helicity through processes like hyperdiffusion ([van Ballegooijen & Cranmer, 2008](#)).

The benchmark evidence supporting the DC models is the spatially resolved imaging of braided loop systems in the corona ([Aschwanden, 2019](#)). With a few vague indications (e.g., [Schrijver et al., 1999](#)) from the Transition Region and Coronal Explorer (TRACE; [Handy et al., 1999](#)), the braided loop systems in an AR were finally observed by the High-resolution Coronal Imager (Hi-C; [Kobayashi et al., 2014](#)) mission with an unprecedented spatial resolution of 150 km ([Cirtain et al., 2013](#), see Figure 1.9). The twisted braids developed across a polarity inversion line (PIL) in photospheric magnetograms and finally resulted in a C1.7 flare observed by the Atmospheric Imaging Assembly (AIA; [Lemen et al., 2012](#)) on the Solar Dynamics Observatory (SDO; [Pesnell et al., 2012](#)), where the plasma was heated to a maximum temperature of 7 MK.

Recent observations by SolO/EUI further advanced our understanding by unveiling similar magnetic braids and intermittent heating during the untangling of the braided loop systems ([Chitta et al., 2022](#)). The individual thread evolved rapidly and developed the tangling on timescales of approximately 25 s, implying additional magnetic disturbances like flux cancellation. Furthermore, nanojets in coronal loops, a possible smoking gun of reconnection in magnetic braids, were observed by the Interface Region Imaging Spectrograph (IRIS; [De Pontieu et al., 2014](#)) and reproduced by 3D MHD simulations ([Antolin et al., 2021](#), see Figure 1.9).

Nevertheless, observation of magnetic braids has other challenges. Simulations show that the magnetic field relaxes before it becomes highly twisted (e.g., [Reid et al., 2018](#)). Furthermore, [Tiwari et al. \(2014\)](#) argued that the observed magnetic braids and C1.7 flare in [Cirtain et al. \(2013\)](#) might be initiated by external flux cancellation instead of internal reconnection in braids. In addition, [Peter et al. \(2022\)](#) reported the absence of braids between the warm loops observed by Hi-C and cool loops observed by IRIS in the AR.

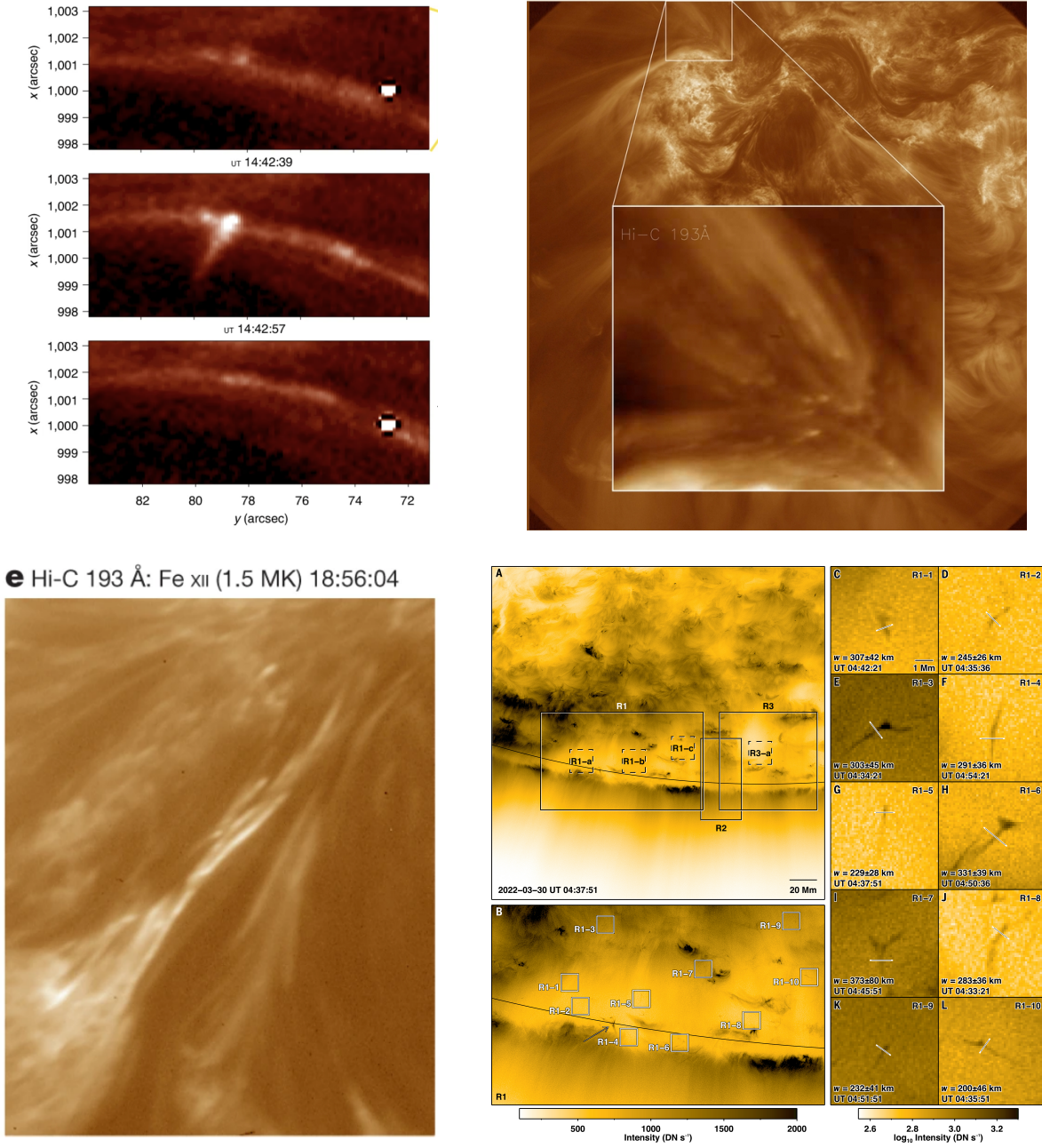


Figure 1.9: Observations of various small-scale heating events in the corona. Top left: Reconnection nanojets in coronal loops observed by IRIS (Antolin et al., 2021). Top right: EUV bright dots at the edge of an AR observed by Hi-C (R gnier et al., 2014). Bottom left: Braided coronal loops observed by Hi-C (Cirtain et al., 2013). Bottom right: Picoflare jets observed by SolO/EUI (Chitta et al., 2023).

Over the past 15 years, the observations of small-scale coronal heating events related to flux emergence, cancellation, or interchange reconnection were facilitated by high-resolution coronal imagers like AIA and EUI, photospheric magnetographs like the Helioseismic and

Magnetic Imager (HMI; Scherrer et al., 2012) and the Polarimetric and Helioseismic Imager (PHI; Solanki et al., 2020), ground-based telescopes. The heating events appear in different coronal structures with various morphology, such as bright dots at loop footpoints (e.g., Régnier et al., 2014; Tiwari et al., 2019b, 2022), jetlets at the based of CH plumes (e.g., Uritsky et al., 2021; Kumar et al., 2023), X-ray jets and transient brightenings at CH boundaries (e.g., Sterling et al., 2015), wide-spread picoflare jets in CHs (see Figure 1.9d Chitta et al., 2023), mini-flares and mini-filament eruption in CBPs (e.g., Madjarska et al., 2022), and transient brightenings in QS (campfire; e.g., Berghmans et al., 2021; Kahil et al., 2022). However, not all observed brightenings reach coronal temperatures >1 MK, for instance, campfires (e.g., Huang et al., 2023b; Dolliou et al., 2023), and jet materials (e.g., Long et al., 2023). Nevertheless, the collective impact of small-scale events may make a significant contribution to the coronal heating (e.g., Raouafi et al., 2023).

Beyond the spatially resolved small-scale heating events, the DC models can also be further assessed by the differential emission measure (DEM), which utilizes spectral lines forming at different temperatures to probe the temperature distribution of the multithermal plasma. The detection of hot plasma (> 5 MK) in non-flaring ARs corroborates the reconnection heating proposed by DC models (e.g., Schmelz et al., 2009, 2015; Ishikawa et al., 2017). Additionally, the DEM slope also provides constraints on the frequency of heating events (Guennou et al., 2013), as infrequent heating events allow plasma to cool to lower temperatures. Evidence supporting (e.g., Winebarger et al., 2011) or challenging the DC models (e.g., Warren et al., 2012) were both reported.

The actual heating rate from heating events across orders magnitudes can be estimated from a power-law distribution of event frequencies $dN(E) \sim E^{-\alpha}dE$, spanning large Hard X-ray flares at approximately 10^{32} erg down to EUV nanoflares at around 10^{24} erg (Aschwanden, 2005). If $\alpha > 2$, small-scale nanoflares dominate the total energy release compared to large flares (Hudson, 1991). Previous observations from TRACE and the Extreme Ultraviolet Telescope (EIT; Delaboudinière et al., 1995) on SOHO found both $\alpha > 2$ (Krucker & Benz, 1998; Parnell & Jupp, 2000) and $\alpha < 2$ (Aschwanden et al., 2000). The discrepancies can be caused by instrumental effects (e.g., Benz & Krucker, 2002) and the inherent temperature bias of various EUV channels (e.g., Aschwanden & Parnell, 2002). Recent studies utilizing SDO/AIA observations also drew conflicting conclusions on $\alpha > 2$ (Purkhart & Veronig, 2022) and $\alpha < 2$ (Joulin et al., 2016).

In addition to the DC models predicting heating events in the corona, it is suggested the heating events in the chromosphere and transition region may also offer significant energy input into the corona. These scenarios are inspired by various observations from the SOHO and TRACE era, which highlighted phenomena including the overdense, uniformly heated

coronal loops, elementary loop cross sections, and the complex Doppler shifts and magnetic structures in the TR (Aschwanden et al., 2007). Recent observations from Hinode, SDO, IRIS, and SolO unveiled more heating events in the lower atmosphere, such as type II spicules (De Pontieu et al., 2007b), UV bursts (Peter et al., 2014), and network jets (Tian et al., 2014), which further supported this scenario. A few studies advocated that type II spicules might be heated to coronal temperature, and could provide material to the solar corona (e.g., De Pontieu et al., 2009, 2011; Tian et al., 2011; Samanta et al., 2019). However, this view is still challenged by some observations and simulations arguing that the spicules or other chromospheric plasma cannot be directly heated to a million degrees (Madjarska et al., 2011; Klimchuk, 2012; Tripathi & Klimchuk, 2013; Klimchuk & Bradshaw, 2014). Meanwhile, the corresponding coronal emission to spicules may originate from the plasma heated by the shock-front driven by flows in spicules (Petrulia et al., 2014).

1.2.4 Alternating Current (AC) Models

The discovery of million-degree corona (Edlén, 1943) and Alfvén waves (Alfvén, 1942) was closely followed by Alfvén (1947), who first suggested that MHD waves, driven by the turbulent photosphere, can propagate upward to heat the chromosphere and corona. The past decades have seen AC models developed to explain the presence and dissipation of waves and oscillations to heat the solar corona and highlight their essential roles in the solar wind acceleration. For a comprehensive overview, please see recent reviews by Nakariakov & Kolotkov (2020); Van Doorselaere et al. (2020b); Nakariakov et al. (2021); Morton et al. (2023).

1.2.4.1 Basic MHD Wave Modes

The inhomogeneity of coronal density structures gives rise to a variety of MHD wave modes. These basic MHD wave modes can be analytically studied using the theoretical model of a 1-D cylinder (r, ϕ, z) (Zajtsev & Stepanov, 1975; Edwin & Roberts, 1983), which represents the overdense flux tubes, such as coronal loops, as an MHD waveguide. The dispersion relation of waves propagating in a 1-D cylinder reveals two major branches:

- **Fast-mode** branch with a phase speed v_{ph} that lies between the Alfvén speed inside v_A and outside v_{Ae} the cylinder: $v_A < v_{\text{ph}} < v_{Ae}$.
- **Slow-mode** or acoustic branch propagates at a phase speed that falls between the sound speed inside the tube c_s and the tube speed $c_T \equiv c_s v_a / \sqrt{c_s^2 + v_A^2}$: $c_T < v_{\text{ph}} < c_s$.

The fast modes can be further characterized by their azimuthal behaviors. If the velocity disturbances $\tilde{\mathbf{v}}$ can be expressed as a wave form:

$$\tilde{\mathbf{v}} \sim \exp [i(\omega t + m\phi - k_z z)] \quad (1.1)$$

then, the integer $m = 0, 1, 2, \dots$ describes the axial symmetry of the oscillating tube. For instance, $m = 0$ represents the symmetric sausage mode, whereas $m = 1$ describes the non-axial-symmetric kink mode.

The inhomogeneity of the corona might mix the properties of various wave modes, compared to the distinct fast and slow magnetoacoustic waves in the homogenous plasma (Goossens et al., 2019). For example, kink modes in thin flux tubes can be nearly incompressible and thus behave more like Alfvén waves instead of fast magnetoacoustic waves (Goossens et al., 2009). Therefore, these modes are also called Alfvénic waves to highlight the mixed properties (Morton et al., 2023), earlier introduced by Ionson (1978) to describe the surface Alfvén modes.

In addition to the fast and slow modes, when $m = 0$, the cylinder model also predicts the torsional Alfvén wave, manifesting independent twisted motions in individual shells of flux tubes propagating at the phase speed $v_{\text{ph}} = v_A$. It is challenging to detect torsional Alfvén waves in the solar corona directly because the twisted motion and incompressible nature result in no observable Doppler shifts and intensity variation (Van Doorselaere et al., 2008).

1.2.4.2 Wave Observations

The launch of SOHO, TRACE, Hinode, and SDO substantially revolutionized the observations of waves and oscillations in the solar corona. A great family of waves related to eruptions was observed, such as the global EIT (EUV) waves (e.g., Dere et al., 1997b; Thompson et al., 1998) and quasi-periodic fast propagating (QFP) wave trains (e.g., Liu et al., 2011). Except for these global disturbances, waves, and oscillations localized in single coronal structures are frequently observed (see Figure 1.10), in particular, the kink modes.

Kink modes represent the transverse swinging motions of overdense magnetic flux tubes in the solar corona. Kink modes were first directly observed by TRACE (Aschwanden et al., 1999; Nakariakov et al., 1999) in the transverse oscillations of coronal loops triggered by nearby eruptions and plasma ejections in the lower corona (Zimovets & Nakariakov, 2015). Recently, more kink oscillations were identified in SDO/AIA (e.g., Aschwanden & Schrijver, 2011; Nechaeva et al., 2019) and SolO/EUI (e.g., Zhong et al., 2023a), with a typical period of 2–10 minutes and an amplitude of 1–10 Mm (Nechaeva et al., 2019).

Spectroscopic observations have identified the counter-propagating oscillations in closed

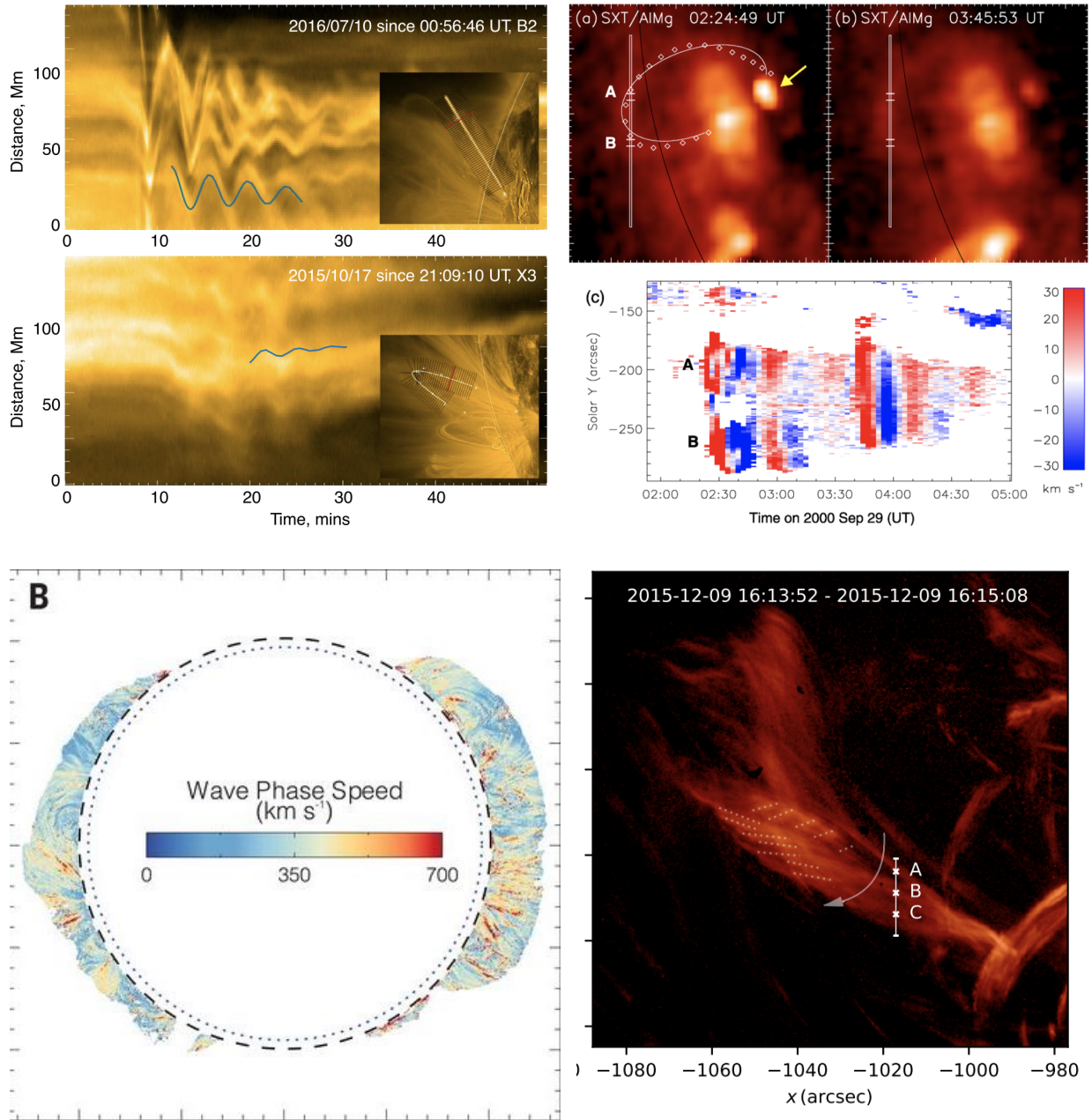


Figure 1.10: Observations of diverse wave modes in the solar corona. Top left: Decaying kink oscillations in coronal loops observed by SDO/AIA (Nechaeva et al., 2019). Top right: Doppler shifts of slow modes in flaring loops observed by SOHO/SUMER (Wang, 2011). Bottom left: Phase speed of kink waves observed by CoMP (Yang et al., 2020). Bottom right: Torsional Alfvén waves in an AR prominence (Kohutova et al., 2020).

fields from the Doppler shifts. Tomczyk et al. (2007) and Tomczyk & McIntosh (2009) identified both outward and inward propagating waves along field lines through Doppler shifts of Fe XIII 1074.7 nm line observed by the COronal Multi-channel Polarimeter (CoMP;

Tomczyk et al., 2008). The transverse waves show a power-law velocity spectrum with a power index of 1.5 and a peak between 3 and 4 mHz, which suggests that the wave energy might originate from the mode conversion of photospheric 5-min p -mode oscillations (e.g., Tomczyk & McIntosh, 2009; Morton et al., 2016). The velocity amplitude observed by CoMP is under 1 km s^{-1} , which is much lower than the transverse oscillation of approximately 15 km s^{-1} observed by SDO/AIA (Morton et al., 2015), potentially due to the limited spatial resolution of CoMP. Hence, the energy flux estimated from the transverse waves observed by CoMP is too low to heat the solar corona.

In particular, the nature of transverse waves observed by CoMP still remains uncertain. Tomczyk et al. (2007) suggested that these transverse oscillations are Alfvén waves propagating in the solar corona. However, Van Doorselaere et al. (2008) argued transverse oscillations in approximate cylindrical plasma structures are better interpreted as kink waves, as the torsional Alfvén waves in these structures cannot produce significant Doppler shifts. Still, McIntosh et al. (2011) argued both shear Alfvén waves in homogenous plasmas and kink waves in 1-D cylinders are over-simplified theoretical models, which cannot represent the complicated inhomogeneous structures in the solar corona.

A great family of decayless oscillations in the solar corona was found in the past decade, followed by the discovery of persistent oscillations in Doppler shifts at loop footpoints (Tian et al., 2012) and growing transverse oscillations in coronal loops (Wang et al., 2012). After that, the decayless oscillations were frequently observed in various coronal structures, including quiescent AR loops (e.g., Nisticò et al., 2013), flaring AR loops (e.g., Mandal et al., 2021), CBPs (e.g., Gao et al., 2022), with a low amplitude of less than 2 km s^{-1} (e.g., Anfinogentov et al., 2015). The oscillation periods were found to range from 10 seconds (e.g., Li & Long, 2023) to 30 minutes (e.g., Zhong et al., 2023b). The observed periods appear to scale linearly with the loop length (Anfinogentov et al., 2015), which supports the hypothesis that the standing kink mode might be responsible for decayless oscillations.

Decayless oscillations imply the existence of continuous energy input to excite transverse motions in the solar corona. However, a consensus on the triggering mechanism of the decayless oscillations is still under debate, for example, the Kelvin-Helmholtz vortices (Antolin et al., 2016, also see Section 1.2.4.3), random footprint driving (Nisticò et al., 2013), and self-oscillation (Nakariakov et al., 2016). Furthermore, the recent observations of decayless oscillations by SoLO/EUI revealed the existence of high-amplitude decayless oscillations up to 125 km s^{-1} (Petrova et al., 2023) and challenged all the commonly proposed excitation mechanisms (Mandal et al., 2022).

In addition to kink modes, other basic MHD modes were also observed in the solar corona. For instance, slow and fast sausage modes were detected in the overdense post-flare

loops (e.g., Wang et al., 2003b,a; Tian et al., 2016) via Doppler shifts and line intensity. Similar compressive oscillations were found in polar plumes (DeForest & Gurman, 1998). In particular, a significant number of the standing slow magnetoacoustic wave events were observed by the Solar Ultraviolet Measurements of Emitted Radiation (SUMER; Wilhelm et al., 1995) onboard SOHO. These standing oscillations appear in emission forming at 0.6–14 MK (Nakariakov & Kolotkov, 2020) and have a typical period of 10–20 minutes (Wang et al., 2003a). The rapid decay of the oscillations in one or two periods indicates additional suppression of thermal conductivity by a factor of 3 and enhancement in compressive viscosity by a factor of 15 (Wang et al., 2015). Most recently, the presence of torsional Alfvén waves was also found in AR prominences (Kohutova et al., 2020) and flare eruptions (Aschwanden & Wang, 2020).

1.2.4.3 Wave Dissipation

Once Alfvén (1947) suggested that Alfvén waves could heat the corona, it was soon realized that shear Alfvén waves are difficult to dissipate in the solar corona (Cowling, 1953) due to the low resistivity and viscosity there (Hollweg, 1991). Other MHD waves, such as fast magnetoacoustic waves, are found to be internally reflected in the chromosphere instead of transmitted into the corona like Alfvén waves (Hollweg, 1978, 1984; Hollweg & Sterling, 1984). To address this problem, AC models have proposed various mechanisms to dissipate the Alfvén wave energy in the corona, such as phase mixing (e.g., Heyvaerts & Priest, 1983), resonant absorption (e.g., Ionson, 1978), induced shocks (e.g., Hollweg et al., 1982), turbulence (e.g., Hollweg, 1983), and ion cyclotron resonance (e.g., Marsch et al., 1982).

The phase mixing model (Heyvaerts & Priest, 1983) suggested that the inhomogeneous corona allows Alfvén waves propagating along neighbor field lines to fall out of phase due to a perpendicular gradient in Alfvén speeds. This facilitates the resistivity and viscosity between two neighboring field lines by creating smaller length scales, substantially increasing the dissipation of Alfvén waves. The dissipation rate closely depends on the perpendicular gradient of Alfvén speed, which is determined by the density gradient, geometry, and scale heights (De Moortel et al., 1999, 2000). It is also challenged by recent 3-D MHD simulations of flux tubes that phase mixing does not provide enough energy to heat and maintain the overdense coronal loops (e.g., Cargill et al., 2016; Pagano et al., 2018).

Similar to phase mixing, resonant absorption (Chen & Hasegawa, 1974; Ionson, 1978) also relies on the Alfvén speed gradient perpendicular to field lines to create a continuum frequency spectrum ω_A of Alfvén waves in the corona. Waves dissipate where the Alfvén wave frequency resonates with the frequency of photospheric drivers. The observed damping of kink waves in coronal loops is frequently interpreted as evidence of resonant absorption of

MHD waves in the solar corona (e.g., Goossens et al., 2002; Aschwanden et al., 2003; Verth et al., 2010; Tiwari et al., 2019a).

MHD turbulence and Alfvén waves were first discovered in the solar wind in the late 1960s and early 1970s (Coleman, 1968; Belcher & Davis, 1971). Since then, turbulence has been suggested as a competitive mechanism to cascade and dissipate wave energy on small scales (e.g., Hollweg, 1983, 1986; Inverarity & Priest, 1995; Matthaeus et al., 1999), benefiting from the non-linear interaction of waves propagating parallel or anti-parallel to the field lines. The counter-propagating waves are frequently observed in closed fields (e.g., Morton et al., 2019; Tiwari et al., 2022), while in the open fields, outwardly propagating Alfvén waves are partially reflected due to the Alfvén speed gradient along the field lines (Heinemann & Olbert, 1980; Barkhudarov, 1991).

Various MHD turbulence models have been developed to study the heating in different coronal structures, including closed loops (e.g., van Ballegooijen et al., 2011; Downs et al., 2016), open fields in CHs (e.g., Cranmer et al., 2007; Lionello et al., 2014), and global models (e.g., van der Holst et al., 2014). The turbulence models show excellent capability in reproducing the plasma thermodynamics and emission in different coronal structures (e.g., Mikić et al., 2018; Shi et al., 2022). Nonetheless, van Ballegooijen et al. (2017) suggested that it is difficult to reproduce the hot emissions (> 5 MK) in ARs using turbulence models.

Recently, Magyar et al. (2017, 2019) introduced the concept of “uniturbulence”, suggesting that the density inhomogeneity perpendicular to the field lines can also develop turbulence-like behaviors through generalized phase mixing. Magyar et al. (2019) challenged the classical Elsässer variables z_{\pm} (Elsasser, 1950) cannot fully separate the parallel and anti-parallel components in the inhomogeneous and compressible plasma. The uniturbulence model has been used to study the energy cascade and wave damping in kink modes and surface Alfvén modes (Van Doorselaere et al., 2020a, 2021; Ismayilli et al., 2022).

Additionally, the 3-D MHD simulation of cylindrical flux tubes also unveiled Kelvin-Helmholtz instability (KHI) developed at the boundary layer of overdense flux tubes (e.g., Terradas et al., 2008; Antolin et al., 2014). The KHI deforms the flux tube and provokes a turbulent layer where both resistivity and viscosity substantially increase to dissipate kink modes and create additional heating (e.g., Magyar & Van Doorselaere, 2016; Karampelas & Van Doorselaere, 2018).

The ion-cyclotron resonance is one of the promising candidates for potentially explaining the preferential and anisotropic heating of heavy ions perpendicular to field lines (T_{\perp}) in the corona and solar wind (e.g., Marsch et al., 1982; Isenberg & Hollweg, 1983; Cranmer et al., 1999; Hu et al., 2000; Hollweg & Isenberg, 2002). The heating peaks when the wave frequency approaches the ion gyrofrequency of 10^2 – 10^4 Hz in the solar corona. The high-

frequency ion cyclotron waves might be generated by activity in the chromospheric network (e.g., Tu & Marsch, 1997), the local instability (e.g., Markovskii & Hollweg, 2004), or by turbulent cascade (e.g., Hu & Habbal, 1999), which complements the turbulence heating models (e.g., Cranmer, 2014).

The presence of high-frequency waves at the ion gyrofrequency in the inner heliosphere was found in in-situ solar wind measurements (e.g., Kasper et al., 2013; Bowen et al., 2020, 2022), and spectroscopic observations (e.g., Kohl et al., 1998, also see Section 1.3). As the wave-particle interaction efficiency is sensitive to the gyrofrequency of heavy ions, the ion charge-to-mass ratio (Z/A) plays an essential role in determining the heating efficiency of ion-cyclotron resonance (e.g., Patsourakos et al., 2002).

1.3 Line Widths and Coronal Heating

The widths of the coronal spectral lines, caused by the thermal and other unresolved non-thermal motions along the line of sight (LOS), allow the measurements of ion temperatures T_i and nonthermal velocities ξ in the solar corona. The presence of nonthermal broadening in UV emission lines above the limb has been observed since the 1970s (see Mariska et al., 1978, 1979). Alfvén waves or other acoustic and (MHD) waves propagating in the corona have been suggested as one of the nonthermal mechanisms that broaden spectral lines (Boland et al., 1975; Esser et al., 1987). In particular, Hassler et al. (1990) suggested that nonthermal widths of coronal lines caused by the undamped Alfvén wave should increase exponentially with altitude, which has led to a significant number of line width studies using spectroscopic observation in the past thirty years. Remarkably, the decrease in line widths is often interpreted as evidence for wave damping to heat the solar corona (e.g., Hahn et al., 2012; Gupta et al., 2019).

Investigations of spectral line widths can be characterized into three major categories: study the total line widths, nonthermal widths, or the thermal widths (ion temperature). Since the removal of thermal widths is trivial (usually by assuming T_i equals the maximum formation temperature of the ion T_{\max} or T_i equals the electron temperature T_e) the total line widths and nonthermal widths are often studied together. However, it has been suggested that the assumptions $T_i \approx T_{\max}$ or $T_i \approx T_e$ may fail in some low-density regimes like CHs (e.g., Tu et al., 1998).

1.3.1 Total or Nonthermal Widths

The most common measurements of coronal line widths have been obtained by spaceborne extreme ultraviolet (EUV) spectrographs since the late 1970s, revealing dissimilar behaviors of line widths with height in various coronal structures (e.g., Cheng et al., 1979; Mariska et al., 1979). Similar studies were significantly enhanced by the launch of SOHO/SUMER and Hinode/EIS. In open-field regions, EUV line widths have been observed to increase up to approximately $1.2 R_{\odot}$ (e.g., Banerjee et al., 1998, 2009), reach a plateau (e.g., Moran, 2003), or start to decrease (e.g., O’Shea et al., 2003; Hahn et al., 2012; Hara, 2019, also see Figure 1.11). On the other hand, EUV line widths in close-field regions appear to be narrower than those in open fields (e.g., Wilhelm et al., 2004) and show diverse variations. These variations include a decrease with height (e.g., Hahn & Savin, 2014; Lee et al., 2014), an initial increase followed by a decrease (e.g., Gupta, 2017), remaining relatively constant (e.g., Landi & Feldman, 2003; Wilhelm et al., 2005), or with significant variation (e.g., Del Zanna et al., 2019; Gupta et al., 2019). Additionally, the long-term variability of the line widths in one solar cycle was found in off-limb quiet-Sun (QS) regions (Landi, 2007) and on-disk ARs (Prabhakar & Raju, 2022).

Distinct behavior in spectral line widths can also be found in forbidden lines in the visible light, for instance, Fe XIV 530.3 nm, Fe X 637.4 nm and Fe XI 789.2 nm observed by ground-based coronagraph and during TSEs. During the 2001 TSE, Fe XIV line width was found to fluctuate or increase between 0.07 nm and 0.12 nm below $1.5 R_{\odot}$ (Koutchmy et al., 2005; Raju et al., 2011; Prabhakar et al., 2019). However, between 1.5 – $2.0 R_{\odot}$, a drastic decrease to 0.02 nm in Fe XIV widths was observed (Koutchmy et al., 2005). Spectroscopic observations during the 2009 TSE revealed that Fe XIV widths fluctuate or increase with height, while Fe X widths exhibited fluctuation or a decrease with height (Singh et al., 2011). During the 2012 TSE, Bazin (2013) found a variation in Fe XIV widths ranging from 0.08–0.12 nm in the corona below $1.6 R_{\odot}$. Koutchmy et al. (2019) compared the variation of Fe XIV line width in different structures obtained during the 2017 TSE and found a decrease in Fe XIV line widths above $1.3 R_{\odot}$ in a coronal hole but an increase in a streamer above 1.5 – $1.6 R_{\odot}$.

For coronagraph observations, Fe XIV line widths have been observed to decrease in both equatorial and high-latitude regions (e.g., Singh et al., 1999, 2002; Krishna Prasad et al., 2013), or reach a plateau up to $1.5 R_{\odot}$ above the equator (Contesse et al., 2004). On the other hand, the Fe X line widths tend to increase with height in the coronal hole and other closed-field regions (e.g., Hassler & Moran, 1994; Singh et al., 2002). Moreover, Fe XIV line widths were found to decrease, remain constant, or peak at approximately $1.3 R_{\odot}$ (Mierla et al., 2005, 2008) as observed by the Large Angle Spectroscopic Coronagraph (LASCO; Brueckner et al., 1995) C1 instrument. In contrast, the widths of Fe X kept increasing to

$1.3 R_{\odot}$ in LASCO C1 observations (Mierla et al., 2008).

Different types of observations have their strengths and weaknesses. Eclipses observations, although rare, provide measurements of line profiles and continuum at large heliospheric distances $> 2-3 R_{\odot}$, benefiting from low atmospheric scattering light (e.g., Habbal et al., 2013; Ding & Habbal, 2017; Boe et al., 2018). Moreover, the radiative excitation of upper energy levels of visible forbidden lines makes their intensity drop more slowly with height compared to the collisionally excited lines in EUV (e.g., Habbal et al., 2007).

Ground-based coronagraphs with tunable filters may perform routine observations during the day, but they may still be affected by weather and atmospheric scattering light (Landi et al., 2016).

EUV spectrographs offer the advantage of observing more spectral lines from different temperature regimes. However, they are also subject to limitations such as the fast drop in line intensity above the limb, instrumental stray light, and substantial instrumental broadening. For example, Dolla & Solomon (2008) suggested that the decrease of line widths above $1.1 - 1.2 R_{\odot}$ can be explained by the effect of the stray light, which hinders any convincing measurements of line widths above $1.2 R_{\odot}$ using SUMER.

Compared to observations made by ground-based coronagraphs and spaceborne EUV spectrographs, the large spatial extent of eclipse observations, in particular, benefits measuring variations of line widths with height in both open- and closed-field structures.

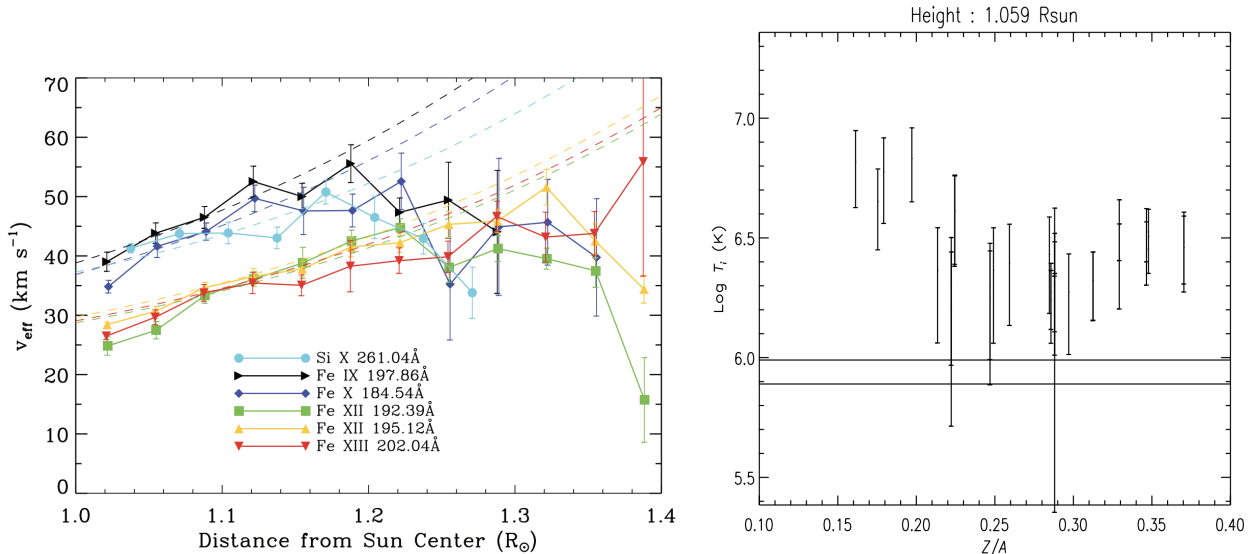


Figure 1.11: Left: Line width variation in a polar coronal hole reported by Hahn et al. (2012). Right: Possible ion temperature T_i intervals vs. the heavy ion charge-to-mass ratios in a polar coronal hole (Landi & Cranmer, 2009).

1.3.2 Thermal Broadening and Ion Temperature

The thermal width of a spectral line is the only remote-sensing measurement of ion temperatures T_i in a variety of coronal structures. Observations from SOHO/SUMER showed that the ion temperatures of Ne, Mg, Fe, and S are more than 2.5 times higher than their formation temperatures (Seely et al., 1997). In the darkest region of the coronal hole, Si VIII and Ne VIII show extreme effective temperatures of 10^7 and 2.3×10^7 K (Wilhelm et al., 1998; Wilhelm, 1999). Besides, observations from the Ultraviolet Coronagraph Spectrometer (UVCS; Kohl et al., 1995) on board SOHO indicated that O VI and Mg X ions are preferentially heated to 10^7 – 10^8 K compared to the protons above the polar coronal hole between 1.35 and $3 R_\odot$, where ion collisions become infrequent (e.g., Kohl et al., 1997; Esser et al., 1999; Doyle et al., 1999). Significant O VI temperature anisotropy perpendicular to the field lines is also found using the Doppler dimming or pumping of O VI 1032/1037 Å lines (e.g., Kohl et al., 1998; Li et al., 1998).

Fewer studies have focused on the dependence of T_i on Z/A using remote-sensing observations. Most of the studies used observations from SOHO/SUMER and yielded contradictory results. Tu et al. (1998, 1999) found that T_i remains constant or slightly decreases with increasing Z/A in a polar coronal hole. Dolla & Solomon (2008, 2009) also reported that T_i decreases with the increase in Z/A , but the low Z/A species (i.e., Fe VIII and Fe X) are significantly heated. Wilhelm et al. (2005) found a linear relation between T_i and Z/A in the quiet Sun only if the Ca XIII and Fe XVII widths are discarded. Landi (2007) investigated the SUMER quiet-Sun observations during different solar activity levels and concluded no correlation between T_i and Z/A . On the other hand, Landi & Cranmer (2009) suggested a nonmonotonic dependence of T_i on Z/A in a coronal hole.

A couple of studies used observations from Hinode/EIS to study the dependence of T_i on Z/A in different regions. Hahn et al. (2010) found that T_i decreases with Z/A in a off-limb polar coronal hole. However, in the quiet Sun, T_i of different ions appears to be constant (Hahn & Savin, 2014). Hahn & Savin (2013a) study the ion temperature anisotropy in an on-disk coronal hole and found that only the perpendicular ion temperature $T_{i,\perp}$ shows a dependence on Z/A . In contrast, the parallel ion temperature $T_{i,\parallel}$ is relatively constant.

The primary difficulty in measuring T_i is that it is challenging to estimate and remove the unresolved nonthermal motions from observed line widths. Scientists had to make additional assumptions to separate the thermal and nonthermal components in observations. The assumptions include T_i equals the line formation temperature (Hassler et al., 1990), the constant nonthermal widths for all ions (Tu et al., 1998), or more complicated assumptions based on the nature of waves (e.g., Dolla & Solomon, 2008; Hahn & Savin, 2013b).

1.4 Global Modeling of the Solar Corona

Attempts to model the million-degree solar corona and supersonic solar wind can be dated back to the early 1960s, including the conductive heating models (Noble & Scarf, 1963; Scarf & Noble, 1965) and the PFSS model (Altschuler & Newkirk, 1969; Schatten et al., 1969). The modern global modeling of the inner corona employs MHD frameworks and realistic coronal heating terms (e.g., Alfvén wave turbulence) to simulate the large-scale corona. The global corona models provide essential tools to study coronal heating and space weather.

This subsection focuses on the applications of two distinguished MHD models: the Magnetohydrodynamic Algorithm outside a Sphere (MAS; Mikić et al., 1999; Lionello et al., 2009; Mikić et al., 2018) developed at the Predictive Science, Inc (PSI) and the Alfvén Wave Solar atmosphere Model (AWSoM; van der Holst et al., 2014, 2022) developed at the University of Michigan. Complete reviews of the historical and modern developments of modeling the steady-state corona and solar wind can be found in Gombosi et al. (2018) and Feng (2020).

The MAS code solves the time-dependent resistive thermodynamic MHD equations to model the inner corona. The boundary condition is driven by a synoptic photospheric magnetogram of the radial magnetic field, as a standard approach for global simulations. The important coronal heating in the inner corona is addressed with either empirical heating (Lionello et al., 2009) or physical-based wave-turbulence-driven (WTD) models (Lionello et al., 2014; Downs et al., 2016). The MAS model can forward model a series of remote-sensing observations of the inner corona, from SXR to near-infrared. The comparison between synthetic multithermal emissivity and observations offers vital insights into coronal heating models (Lionello et al., 2009).

One of the major applications of MAS is the prediction of eclipse observations. Starting from the 1994 TSE (Mikić & Linker, 1996), PSI provided MHD simulations of tens of eclipses. In 2017, PSI predicted the white light and EUV images of the solar corona during the August 21 TSE one week before (Mikić et al., 2018). MAS successfully forecasted the large-scale coronal structures and unveiled small-scale features like the ray-like polar plume extending from a low-latitude CH at the far side. The introduction of shearing magnetic fields along the PIL (Yeates et al., 2018) further energized the solar corona and reproduced observed filament channels and dark cavities. Subsequent simulations of the following 2019 TSE were utilized to study the brightness of K- and F-corona (Boe et al., 2021), the intensity of coronal forbidden lines (Boe et al., 2022), and thermodynamic structures (Boe et al., 2023). Moreover, Schad et al. (2023) compared the off-limb Si x $1.4\mu\text{m}$ intensity synthesized by MAS to observations made by the latest Cryogenic Near-Infrared Spectropolarimeter (Cryo-NIRSP; Fehlmann et al., 2023) mounted on the Daniel K. Inouye Solar Telescope (DKIST);

Rimmele et al., 2020). Beyond the simulation of the steady-state corona, MAS can perform time-accurate simulations for solar eruptions (Titov et al., 2014; Török et al., 2018).

The Alfvén Wave Solar atmosphere Model (AWSoM; van der Holst et al., 2014, 2022) solves three-temperature MHD equations along with the low-frequency Alfvén wave turbulence equation to simulate the coronal heating caused by turbulence cascade. The coronal heating is fully realized by the dissipation of Alfvén wave energy through a turbulence cascade developed in counter-propagating waves. A detailed description of AWSoM can be found in Section 2.3.1. AWSoM has been widely used to simulate the solar wind background (e.g., Sachdeva et al., 2019, 2021), the charge-state evolution (Szente et al., 2022), and the initiation and propagation of CMEs (e.g., Manchester et al., 2014; Jin et al., 2017).

Benefiting from the solution of low-frequency Alfvén wave turbulence, AWSoM can synthesize the actual spectral line profiles, including the realistic treatment of thermal and non-thermal broadenings (also see Section 2.3.3). Oran et al. (2017) calculated the line profiles from AWSoM simulations and found that the line widths between 1.04 and 1.34 R_{\odot} show good consistency with SUMER observations, except for the Fe XII 1242 Å line at higher altitude. Shi et al. (2022) found the synthetic line broadening in an on-disk AR matches Hinode/EIS observations, albeit with the discrepancies at the loop footpoints. Szente et al. (2023) extended charge-state calculations into the synthesis of EUV emission and reported significant deviations caused by non-equilibrium ionization in particular regions like CHs.

Furthermore, AWSoM can provide constraints on the turbulence heating models. Huang et al. (2023a) found the correlation between the Alfvén wave Poynting flux input at the upper chromosphere and the open flux areas through the solar cycle. Shi et al. (submitted to ApJ) employed AWSoM to study the AR loop heating in 3-D configurations and found an exponential decrease in loop footpoints to the apex. In addition to studying the lower corona, the coupling of AWSoM with other modules in the Space Weather Modeling Framework (SWMF; Tóth et al., 2012; Gombosi et al., 2021) allows it to study the diverse physics processes and subsystems in the heliosphere, including the solar energetic particles (e.g., Zhao et al., 2023) and outer heliosphere.

1.5 Dissertation Overview

This dissertation aims to employ both the coronal line broadening and global MHD simulations as robust diagnostic tools to study the AC (wave dissipation) heating of the solar corona and advance the understanding of the following science questions:

1. How does the line width vary with height in open field regions? How do other factors like LOS integration and instrumental stray light affect this type of observation?

2. Does the preferential heating of heavy ions exist at the base of CH boundaries? If so, how do heavy ion temperatures T_i depend on the ion charge-to-mass ratios Z/A ?
3. What is the difference between line widths in closed and open fields and their variation with heights?
4. Are there any differences between line widths of allowed transitions in UV and forbidden transitions in the visible?

Chapter 2 introduces the spectrographs, plasma diagnostic techniques, and MHD simulations used in this dissertation to investigate the line width variation in the solar corona.

To explore the first question, Chapter 3 presented the measurements of line widths of the Fe XII 192.4, 193.5, and 195.1 Å and Fe XIII 202.0 Å lines in an off-limb southern coronal hole up to $1.5 R_{\odot}$ using Hinode/EIS. The measurements were then compared to the predictions from AWSoM and the SPECTRUM module.

The second question was addressed in Chapter 4 by analyzing coordinated observations of a polar CH made by SOHO/SUMER and Hinode/EIS. Temperatures of heavy ions with a Z/A between 0.12 and 0.37 were measured and compared with synthetic line width from AWSoM, which calculates the thermal line width using the proton temperature.

In Chapter 5, spectroscopic observations with a large field of view (FOV) acquired during the 2017 August 21 TSE were analyzed to tackle the third and fourth questions. Supplementary observations made by Hinode/EIS and CoMP were also presented to validate the eclipse observations.

Finally, Chapter 6 made the concluding remarks and discussed the ongoing and potential follow-up studies in the future.

CHAPTER 2

Methodology

2.1 Instruments to Observe Coronal Emission Lines

This section outlines the instruments employed in this dissertation. The data reduction, calibration, and processing procedures are also briefly summarized.

2.1.1 Hinode/EIS

The EUV Imaging Spectrograph (EIS; Culhane et al., 2007) on board the Hinode (Kosugi et al., 2007) mission is designed to measure the EUV emissions lines in two distinct spectral windows, 170–210 Å and 250–290 Å. These spectral lines originate in the plasma from 0.1 MK to 10 MK. The EUV line profiles provide unique diagnostics to the plasma kinematics (e.g., Harra et al., 2023), thermodynamics (e.g., Warren et al., 2018), chemical composition (e.g., Brooks & Warren, 2011), and even magnetic fields in the solar corona (e.g., Landi et al., 2020). Figure 2.1 shows a typical QS spectrum observed by EIS with a full-detector exposure. The brightest lines are from Fe VIII–XV, as well as S and Si.

Figure 2.2 presents the optical layout of EIS. EIS is equipped with two back-illuminated 2048×1024 CCDs, referred to as the short wavelength (SW) and long wavelength (LW) detectors. The EUV emission, after passing through one of the two narrow slits (1"×512" and 2"×512"), undergoes dispersion by the grating, is recorded by a designated portion (usually 2048×512) of the two detectors. This configuration results in a spatial scale of 1" per pixel along the slit. The wavelength scale of the detector is approximately 22 mÅ px⁻¹, providing a spectral resolution of 47 mÅ (FWHM) at 185 Å.

The calibration of level 0 EIS data to level 1 was performed using the SolarSoft routine `eis_prep` (Young, 2022). The 1 σ error in data numbers (DNs) was determined by the quadratic sum of Poisson statistics and dark-current (readout) noise (Young, 2022). The other standard data reduction procedures include correction for the offset along the y -axis

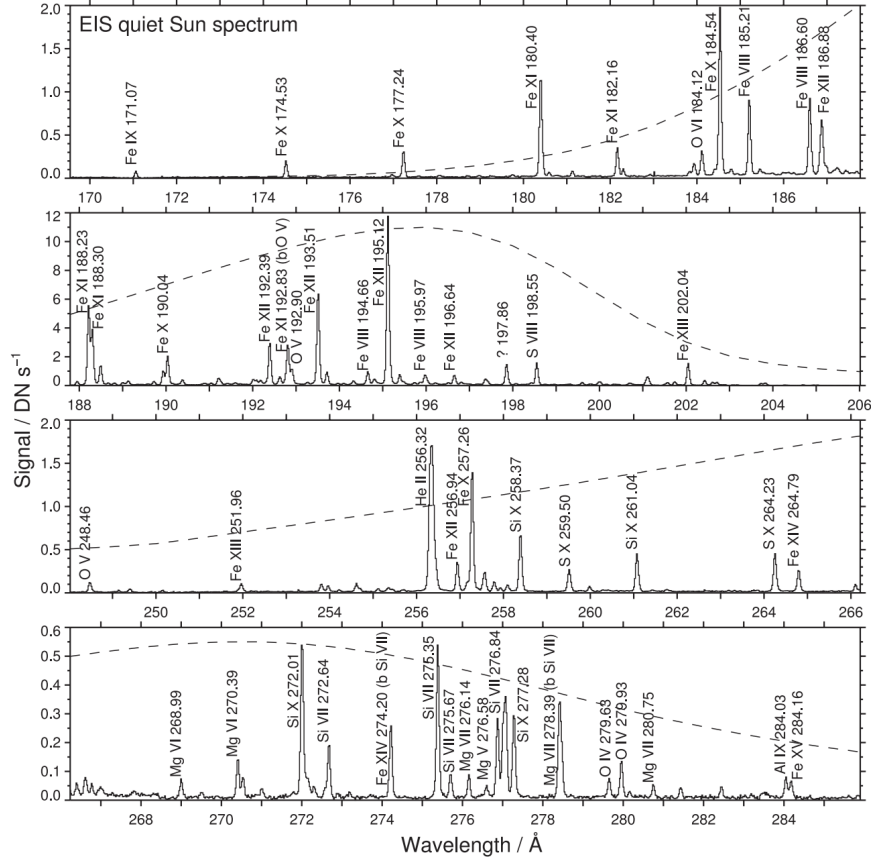


Figure 2.1: Young et al. (2007) example of QS spectrum observed by Hinode/EIS.

(`eis_ccd_offset`, Young, 2011a) between two detectors, slit tilt (Young, 2010) and the correction for the orbital drift of the wavelength scale (Kamio et al., 2019).

The radiometric calibration was conducted in two steps. First, the original laboratory calibration, as a part of `eis_prep`, was applied to convert the units from DN s^{-1} into physical units $\text{erg s}^{-1} \text{cm}^{-2} \text{sr}^{-1} \text{\AA}^{-1}$. Subsequently, a secondary radiometric correction was applied to account for the onboard variation, particularly the degradation in the EIS effective area. This correction factor has been measured through various methods, with previously reported values by Del Zanna (2013, hereafter, GDZ) and Warren et al. (2014, hereafter, HPW). Most recently, Del Zanna et al. (2023) released the latest in-flight radiometric correction with an accuracy of $\pm 20\%$, derived from QS and AR observations from 2007 to 2022.

Apart from the EIS Software in Solarsoft, a collection of level-1 EIS data files, restored in HDF5 format, is prepared and distributed by the Naval Research Lab (NRL)¹. These data files have been processed by the EIS Software to level-1 and are ready to be analyzed by the

¹<https://eis.nrl.navy.mil/>

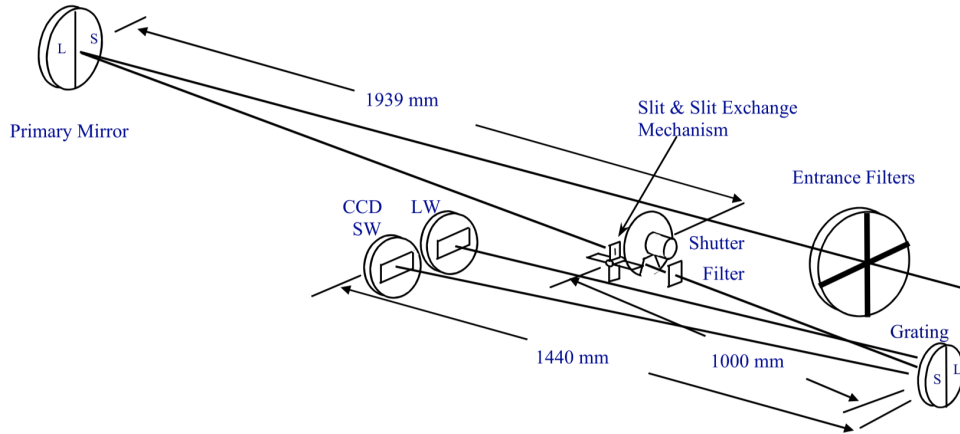


Figure 2.2: Culhane et al. (2007) Optical layout of Hinode/EIS.

EIS Python Analysis Code (EISPAC)², which imitates the EIS Software in SolarSoft.

2.1.2 SOHO/SUMER

The Solar Ultraviolet Measurements of Emitted Radiation (SUMER; Wilhelm et al., 1995) is a UV slit spectrograph on board the Solar and Heliospheric Observatory (SOHO; Domingo et al., 1995). SUMER offers an extensive wavelength coverage from 500–1610 Å to observe spectral lines originating from the chromosphere, transition region, and the solar corona. As illustrated in Figure 2.3, these spectral lines provide a wealth of diagnostics to plasma at temperatures ranging from 10^4 to 2×10^6 K, and even up to 10^7 K during flares.

The optical layout of SUMER is depicted in Figure 2.4. SUMER has four different slits for various observation targets. The $4 \times 300''$ slit is often used for off-limb observations, while the $1 \times 300''$ slit is optimized for high-resolution on-disk observations. Two shorter and narrower $1 \times 120''$ and $0.3 \times 120''$ slits are designed for intense lines from the lower atmosphere (e.g., Ly α) or high-continuum regimes. The slit image dispersed by the grating is recorded by one of the two 1024×360 -pixel cross delay-line (XDL) detectors (A or B), which consist of a Z stack of microchannel plates (MCPs) and XDL anodes.

The detectors simultaneously capture spectral lines at the first and second orders with an instantaneous wavelength coverage of around 40–45 Å at the first order. Occasionally, the detectors can also record a few intense third-order lines (e.g., Si XII 499 and 521 Å). The combined first-order wavelength coverages of detectors A and B extend from 780 to 1610 Å and 660 to 1500 Å, respectively. However, the second-order lines below 500 Å are difficult to

²<https://github.com/USNavalResearchLaboratory/eispac>

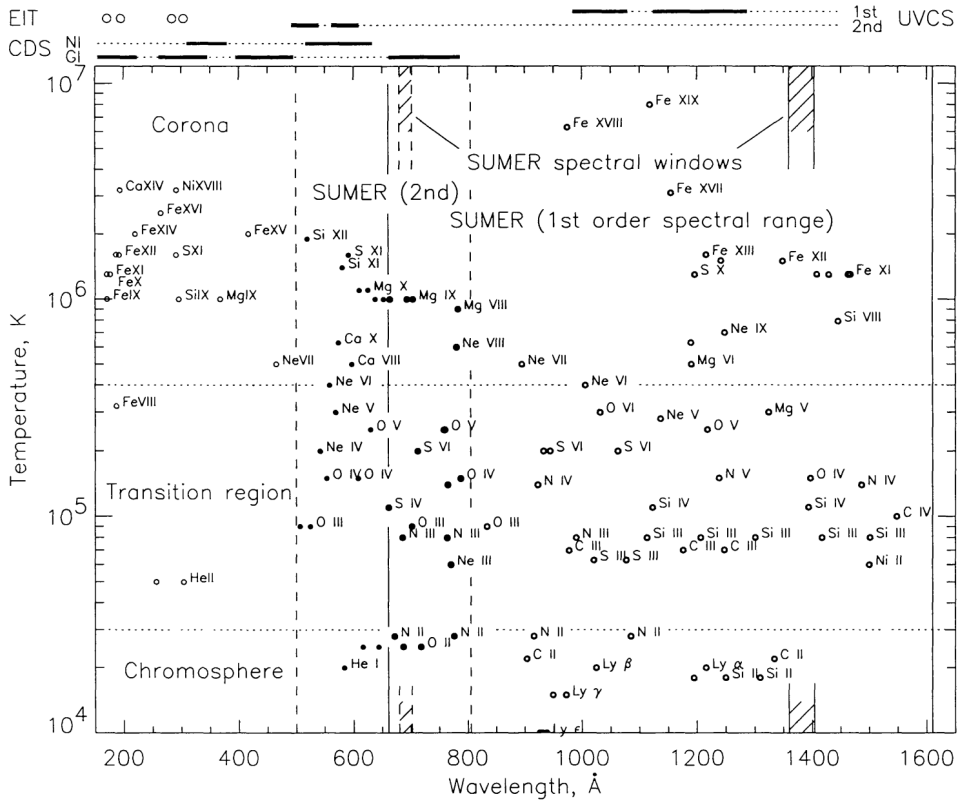


Figure 2.3: Wilhelm et al. (1995) collection of emission lines observed by SUMER.

observe due to the decreased reflectivity of UV photons on the mirrors and the grating.

The spectral scale of the detector varies between 45.0 \AA px^{-1} and 41.8 \AA px^{-1} from 800 \AA to 1600 \AA at the first order, whereas the spatial scale decreases from $1.03'' \text{ px}^{-1}$ to $0.95'' \text{ px}^{-1}$. Notably, the center halves of the detectors are coated with the KBr photocathode material, which enhances the quantum efficiency and aids in distinguishing the first and second-order lines.

We retrieved the SUMER data from the original telemetry through the SUMER Image Database. Then, we applied a series of standard data corrections and calibrations described in the SUMER Data Cookbook³. These procedures include decompression, reversion, dead-time correction, flat-field correction, local-gain correction, and geometric distortion correction.

To identify the illuminated portion of the 1024×360 SUMER detector, we manually examined the intensity distribution along the y direction in the four spectral windows. Subsequently, we resized the images to 1024×300 using the IDL `congrid` function.

We calculated the uncertainty of the SUMER intensity in each pixel, assuming that the

³<http://www2.mps.mpg.de/projects/soho/sumer/text/cookbook.html>

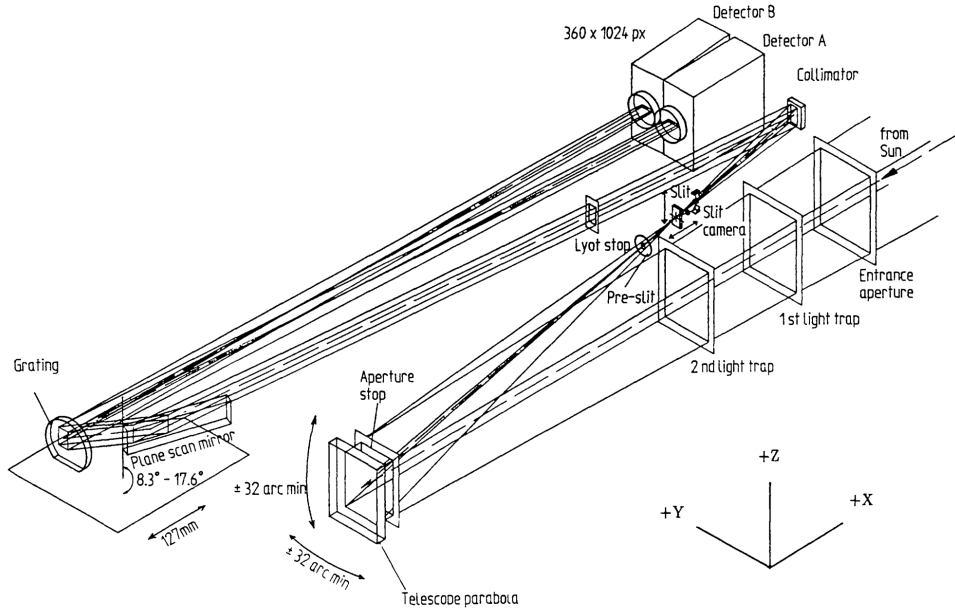


Figure 2.4: Wilhelm et al. (1995) layout of the SUMER optical system.

uncertainty is dominated by the photon shot noise following Poisson statistics (Peter & Judge, 1999), namely,

$$\sigma_P = \sqrt{P} \quad (2.1)$$

where P is the total photon counts per pixel and σ_P is the corresponding uncertainty. The uncertainty of the radiometrically calibrated intensity I is given by Young (2022):

$$\frac{\sigma_I}{I} = \frac{\sigma_P}{P} \quad (2.2)$$

Since SUMER does not provide an absolute wavelength calibration, we calibrated the wavelength across the detector by performing linear regression between line centroids (in detector pixels) and the wavelengths provided by the CHIANTI atomic database (Dere et al., 1997a; Del Zanna et al., 2021; Dere et al., 2023). The discrepancy between the calibrated pixel sizes and the pixel sizes given by the grating dispersion relation in the SUMER software is less than 0.5%. No absolute wavelength calibration was performed, as we only used the line width and intensity diagnostics in this dissertation. Finally, before fitting, we applied the latest (Epoch 9) SUMER radiometric calibration to individual spectral lines.

2.1.3 3PAMIS

2.1.4 Instrument Design

A three-channel Partially Multiplexed Imaging Spectrometer (3PAMIS) was used to obtain spectroscopic observations during the 2017 TSE. The 3PAMIS has a design similar to the dual-channel (2PAMIS) spectrometer used at the 2015 TSE (Ding & Habbal, 2017).

The eclipsed Sun is imaged onto a slit mirror using a tele lens (NIKON ED Nikkor $f = 300$ mm, F/2.8). The transmitted light is made parallel by a collimator lens (ASKANIA Askinar $f = 100$ mm, F/1.9), and then passes three dichroic mirrors which separate the spectrum into three wavelength regions: blue(400–500 nm), green(500–610 nm), and red(610–1100 nm). The light from each of these regions is dispersed by three diffraction gratings into different output angles, depending on the wavelength and the diffraction order. The diffracted light is focused onto a CCD camera (ATIK Infinity) with a lens system (NIKON Nikkor $f = 50$ mm, F/1.8). Schott color filters (cut-off and bandpass filters) are used to correct the deficiencies of the dichroic mirrors.

A monitor camera captures the solar image reflected by the slit mirror and determines the slit position with respect to the sun. Our analysis of the detector images found that the Chromium slit mirror coating is slightly transparent, resulting in ghost images of the solar limb and of bright prominences which are superimposed onto the coronal spectrum.

The green and red channels are designed specifically to observe the Fe XIV 530.3 nm line and Fe X 637.4 nm line at multiple orders (> 50). The green detector captures Fe XIV 530.3 nm lines from 60th to 64th orders, while the red detector records the Fe X 637.4 nm lines from 51st to 53rd orders. In addition to the spectral lines, the electron K-corona continuum was also observed. However, the stacking of multiple orders of the white light continuum on the detector made its interpretation challenging. The wavelength scale of the green detector is approximately 0.025 nm px⁻¹, and the red detector has a wavelength scale of around 0.030 nm px⁻¹, yielding a resolution power $R \sim 20,000$.

The 3PAMIS slit covered a region corresponding to $4 R_s$ along the slit direction. The pixel size is equivalent to $8''3$ in the spatial dimension. The spatial resolution perpendicular to the slit depends on the exposure time of each raster. This is because 3PAMIS made a sit-and-stare observation, with the Sun gradually moving across the slit as time went by.

2.1.4.1 Calibration and Coalignment

We performed data reduction and calibration of the raw CCD images through the following steps: (1) dark frame subtraction, (2) curvature correction, and (3) flat-fielding. Furthermore, we determined the instrument pointing, carried out the wavelength calibration, and

measured the instrumental broadening of the spectrometer.

We applied dark-frame subtraction to remove both the detector bias and dark current. We created master dark frames for each detector with exposure times of 1 s, 3 s, and 5 s, corresponding to the exposure times used during observations. Each master dark frame is obtained by averaging 10 dark frames with the same exposure time, after removing their hot pixels $> 5\sigma$. These master dark frames were subsequently utilized to correct the CCD images with identical or similar exposure times.

In addition, we corrected the curved spectral lines recorded by the detector. The correction of line curvature is crucial for various downstream calibrations, including flat-fielding, pixel binning along the y -axis, wavelength calibration, and fitting of line widths. To accomplish this, we employed neutral hydrogen and helium calibration lines taken in the laboratory to measure the curvature.

The measurement of the curvature was carried out in two steps: (1) We averaged every 5 pixels along the y -axis and fitted the line centroids at different CCD y -pixels using single-Gaussian fitting (see Figure 2.5b). The shift along the x -axis was measured with respect to the line centroid at $y = 400$. (2) To extrapolate the shift from where calibration lines were located to the entire detector, we utilized a 2-D Chebyshev polynomial. This polynomial is a first-order polynomial in the x -direction and second-order polynomial in the y -direction, and was used to fit the shift of all calibration lines at various parts of the detector. This approach was chosen to emulate the legacy Image Reduction and Analysis Facility (IRAF) and its user guide for slit spectroscopy (Massey et al., 1992). Then we interpolated each pixel along the x -axis to correct the curvature (Figure 2.5c). All the images used in this study, except for the dark frames, were subjected to the curvature correction procedure.

In this study, we performed flat-fielding correction only along the y -direction for several reasons. First, the spectral lines are recorded along the y -axis of the detector. Second, the laboratory/dome flat field images were not used as they were acquired when the slit was not evenly illuminated. Finally, the sky flat field images contain a considerable number of telluric lines (see Figure 2.6a). To obtain the 1-D flat-fielding function, we averaged the "clean" sky flat field images between telluric contamination. We carried out this procedure specifically at the regions of the detector where Fe X and Fe XIV lines are located. Figure 2.6c illustrates an example of the flat-fielding curve for the Fe X 637.4 nm line at the 52nd order. It is important to note that the 1-D flat-fielding primarily corrects optical effects, such as vignetting, but does not correct the response differences of individual CCD pixels.

We performed the wavelength calibration in two steps: (1) a relative wavelength calibration using laboratory hydrogen and helium calibration lines, followed by (2) an absolute wavelength calibration using chromospheric hydrogen and helium emission at the limb. Fig-

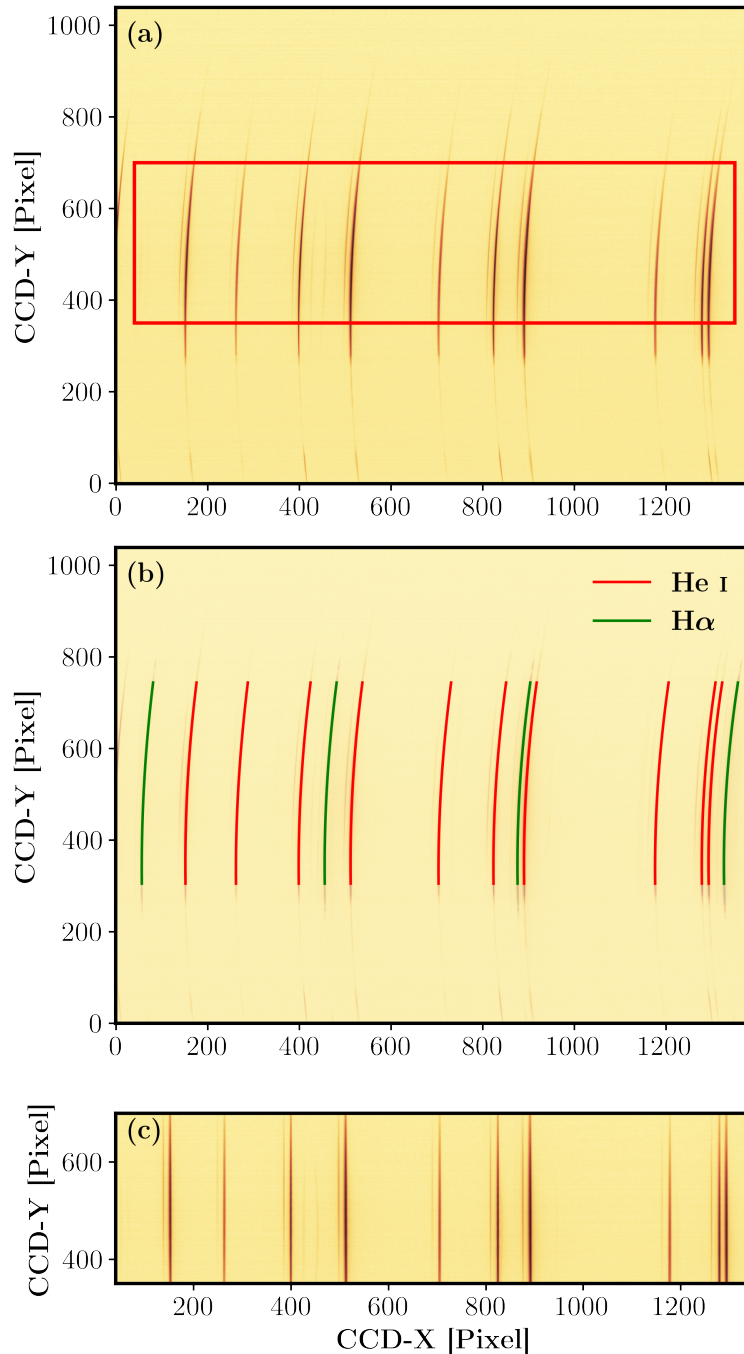


Figure 2.5: An example of curvature correction: (a) A CCD image showing curved neutral helium spectral lines on the detector. The red rectangle outlines the region shown in panel (c) where the curvature is corrected. (b) Fitting of curved neutral hydrogen and helium lines. (c) Curvature-corrected helium lines from the red rectangle in panel (a). Link to the [Jupyter notebook](#) creating this figure: [🔗](#).

ure 2.7 shows the relative wavelength calibration of the green and red detectors. Specifically,

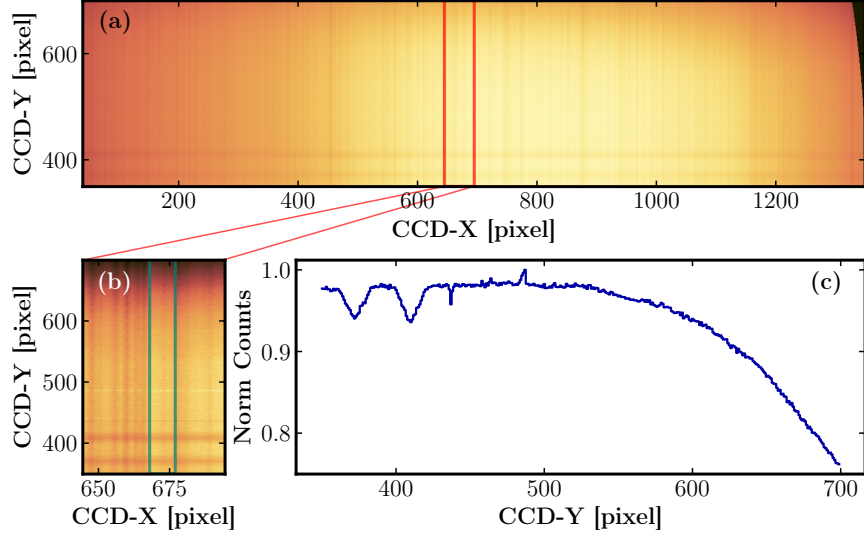


Figure 2.6: 1-D flat field function of the red detector for 52nd-order Fe x 637.4 nm line. (a) Curvature-corrected sky flat image. (b) Zoom-in sky flat image. (c) The 1-D flat-field function averaged between the two green vertical lines. Link to the `Jupyter` notebook creating this figure: [🔗](#).

$H\beta$, He I 501.6 nm, and He I D_3 are used for the green detector and $H\alpha$, He I D_3 , and He I 667.8 nm are used for the red detector. The He I D_3 line at 587.6 nm can be observed in both detectors because it is close to the wavelength limit of the dichroic mirror. To derive the wavelength scale, we adopted a second-order polynomial to fit the NIST air wavelengths of neutral hydrogen and helium lines. The wavelength scales at the detector center are approximately 0.025 nm px^{-1} (62nd order, green) and 0.030 nm px^{-1} (52nd order, red).

A significant deviation from the laboratory wavelength scale was found in the totality images, likely resulting from slight perturbations of the optics during transportation and deployment. Therefore, we carried out an additional absolute wavelength calibration using chromospheric lines at the limb to correct the reference wavelength.

Figure 2.8 displays the absolute wavelength calibration of the green detector. We found a shift of approximately 5 pixels along the x -direction between the chromospheric lines and the same lines measured in the laboratory. We utilized the average pixel shift at different orders to update the reference wavelength. The average shifts are found to be -5.56 pixels for the green detector and -1.17 pixels for the red detector. Moreover, the spread of the pixel shift in Figure 2.8c allowed an estimation of the uncertainty in wavelength calibration, which is about $1/3$ pixel ($\approx 0.008 \text{ nm}$ or 4.5 km s^{-1} at 530 nm). Additionally, we chose the median value of the Doppler shift measured at the east limb as the zero point velocity to remove the solar rotation.

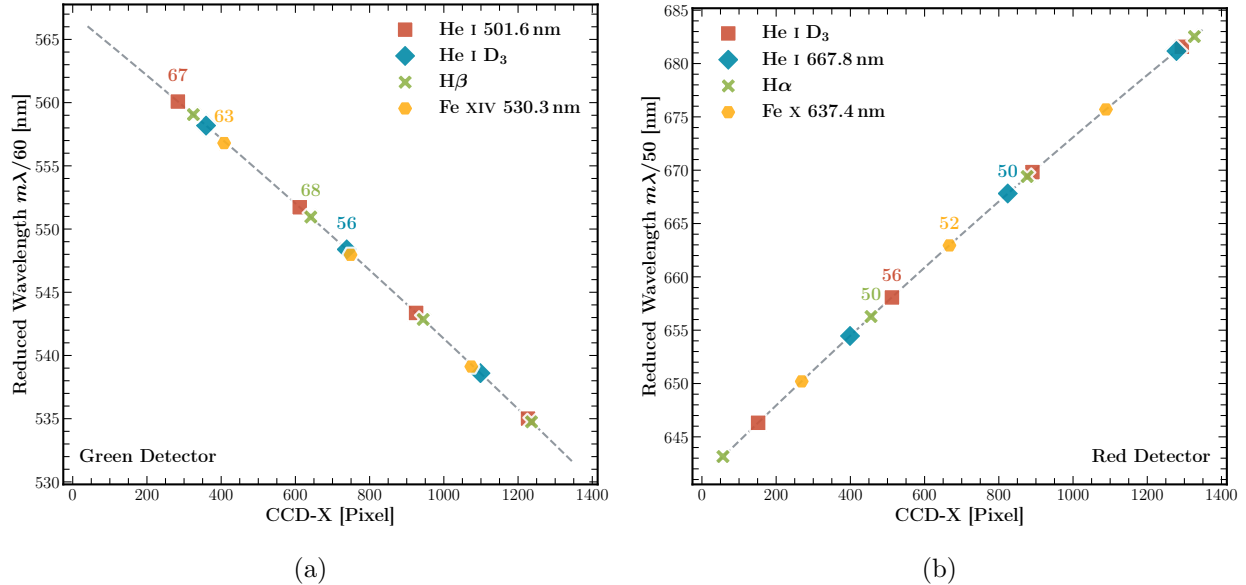


Figure 2.7: CCD x -pixel positions of various-order spectral lines and the relative wavelength calibration of the green (left) and red (right) detectors. The neutral hydrogen and helium lines are used in the wavelength calibration. The dashed curves show the quadratic fittings of wavelengths. The locations of the observed Fe x and Fe xiv lines during the eclipse are also shown. Links to [Jupyter](#) notebooks creating this figure: [🔗](#) (green) and [🔗](#) (red).

In addition to the wavelength calibration, we adopted the neutral hydrogen and helium lines to measure the instrumental broadening. As the thermal and nonthermal broadening of these calibration lines is negligible, the widths of calibration lines provide a direct measurement of the instrument widths. We noticed the interpolation to correct the line curvature might affect the fitted line widths because the calibration lines are very narrow and usually only sampled by 4-5 pixels in the x -direction.

To address this concern, we compared the curvature-corrected or uncorrected widths as a function of CCD y -pixel in Figure 2.9. We found that the two line widths agree with each other where the curvature is negligible ($y \approx 400$). However, at locations where lines are curved, the uncorrected widths fluctuate from 1.4 to 1.9 pixels (green) and 1.5 to 2.1 pixels (red), which might be attributed to the insufficient sampling of the line profile. Notably, the curvature correction failed to remove the fluctuation either, particularly for the red detector, where the curvature-corrected widths vary from 1.6 pixels to 2.5 pixels.

Finally, we selected the region where the uncorrected widths do not vary significantly to measure the instrumental widths. Specifically, we measured the instrumental widths at $y \sim 380$ for the green detector and $y \sim 350$ for the red detector. The instrumental widths $\Delta\lambda_{\text{inst,green}} = 1.86 \text{ px}$ and $\Delta\lambda_{\text{inst,red}} = 2.12 \text{ px}$ are used in this study, with an uncertainty of

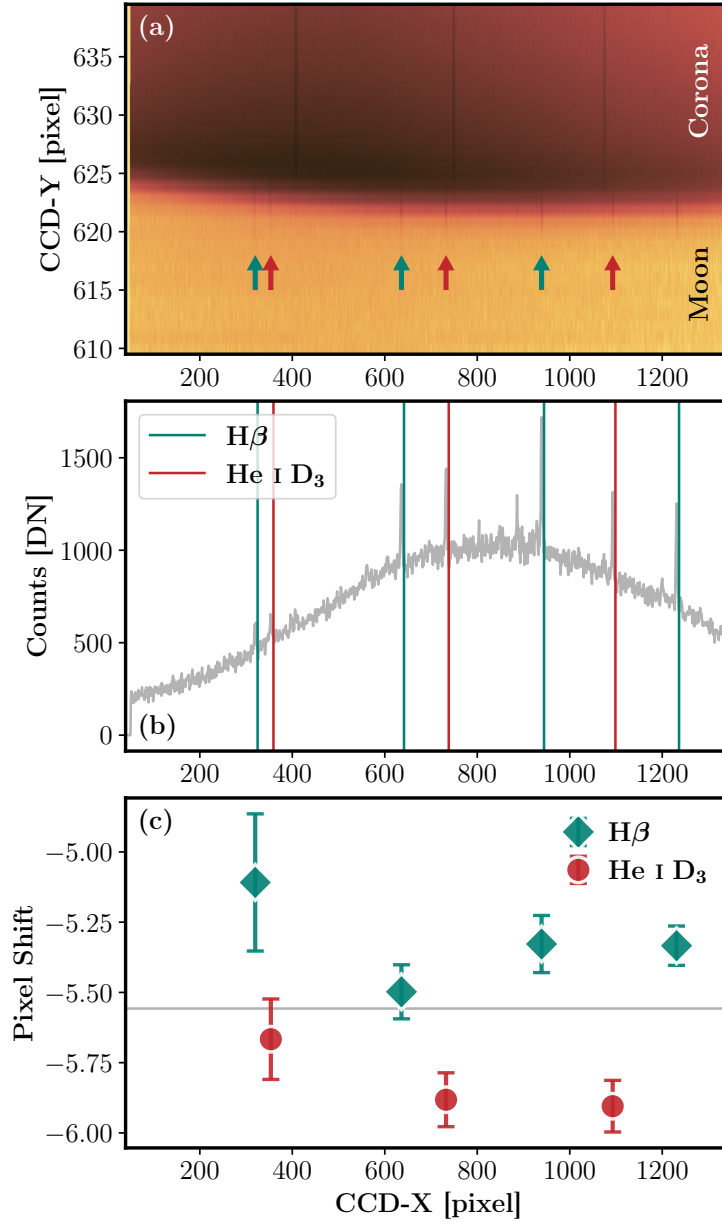


Figure 2.8: Absolute wavelength calibration of the green detector. (a) Chromospheric $H\beta$ (green arrow) and He I (red arrow) emissions between the lunar disk and corona. (b) The average chromospheric spectrum (grey curve) between the two red ticks in panel (a). The vertical green and red lines indicate the line centroids of laboratory $H\beta$ and He I. (c) The shift between the chromospheric lines and the laboratory lines at different orders. The horizontal grey line indicates the average pixel shift for the absolute wavelength calibration. Link to the [Jupyter notebook](#) creating this figure: [🔗](#).

approximately 20 – 30%. We estimated the uncertainties of instrumental widths as $\sigma_{\text{inst}} = 0.4$ px (green) and $\sigma_{\text{inst}} = 0.5$ px (red), based on the spread of values depicted in Figure 2.9.

The instrumental widths are removed by

$$\Delta\lambda_{\text{true}} = \sqrt{\Delta\lambda_{\text{fit}}^2 - \Delta\lambda_{\text{inst}}^2} \quad (2.3)$$

where $\Delta\lambda_{\text{true}}$ is the deduced true line width. We also propagated the uncertainty by

$$\sigma_{\text{true}} = \left(\frac{\lambda_{\text{fit}}^2}{\lambda_{\text{true}}^2} \sigma_{\text{fit}}^2 + \frac{\lambda_{\text{inst}}^2}{\lambda_{\text{true}}^2} \sigma_{\text{inst}}^2 \right)^{1/2} \quad (2.4)$$

where σ_{true} is the uncertainty of $\Delta\lambda_{\text{true}}$, σ_{fit} denotes the fitting uncertainty.

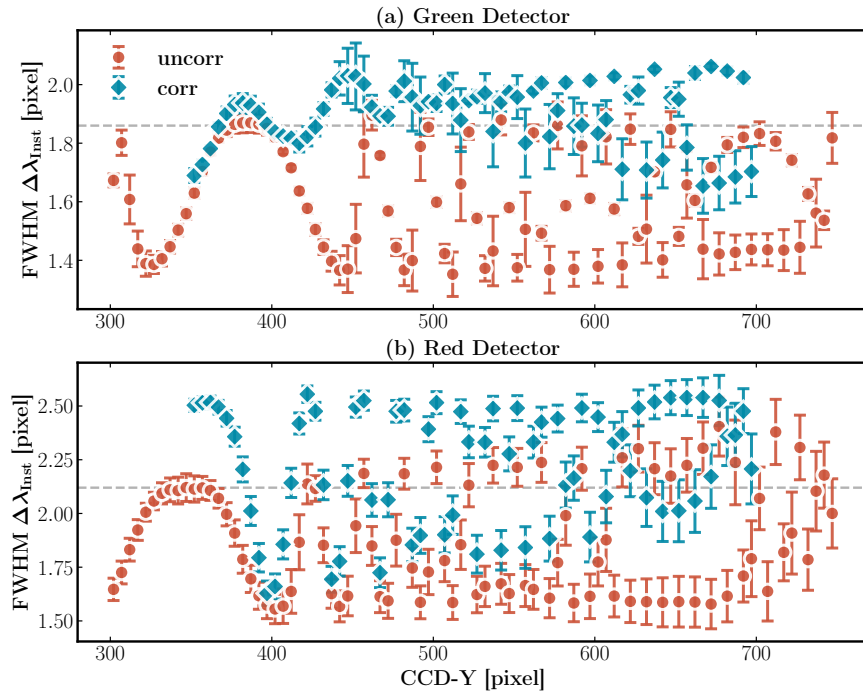


Figure 2.9: Line widths of the narrow neutral hydrogen and helium lines as a function of CCD y -pixel position in the green (a) and red (b) detectors. The blue diamonds represent the curvature-corrected widths, and the red dots are for the uncorrected widths. The dashed horizontal lines indicate the instrumental widths used in this study. Link to the `Jupyter` notebook creating this figure: [🔗](#).

Regrettably, the 3PAMIS FITS headers do not include any pointing information. Therefore, we had to rely on the white light images taken by the context camera to determine the pointing. Although the context camera did not record the time of observation, this information was available in 3PAMIS FITS headers. Hence, we compared the 3PAMIS images taken at the onset of totality with the context images to determine the reference time.

To begin, we determined the slit position relative to the solar disk. As the pointing of the slit was fixed, our task involved measuring the motion of the Sun in the context

images. To accomplish this, we adopted the circle Hough Transform method (Duda & Hart, 1972) available in OpenCV to detect the lunar limb as a circular feature in the images (see Figure 2.10a). Subsequently, we performed linear fitting on the x and y -coordinates of the lunar disk when the Sun crossed the slit (Figure 2.10b and c) to measure the velocities of the Sun $v_{\odot,x}$ and $v_{\odot,y}$. To convert these velocities in pixels into arcsecs, we compared the radius of the lunar disk (approximately 71.4 pixels, see Figure 2.10d), with the lunar radius of $976''$ reported in Boe et al. (2020).

We took advantage of the semi-transparent slit mirror to measure the spatial scale Δy of the detectors. Figure 2.10e displays a CCD image captured when the slit was pointed to the off-limb. Two faint horizontal lines can be identified on the image, which are caused by the dispersion of the limb image leaking from the semi-transparent slit mirror. We used the positions of these lines to derive the spatial scale Δy of two detectors and the position of the disk center y_c on the detector. The spatial scales Δy of the two detectors are measured to be $8''.26 \text{ px}^{-1}$ (green) and $8''.37 \text{ px}^{-1}$ (red).

The final crucial parameter is the angle α between the slit and the solar north–south direction. The slit was slightly tilted from solar northwest to southeast as depicted in Figure 2.10a. Initially, we compared the locations of streamers in the white light context images with the reference eclipse images from Boe et al. (2020). However, because the inner corona was saturated in the context images, this approach only yielded an angle of approximately 30° . Therefore, we compared the fitted Fe XIV intensity with Fe XIV narrowband images from Boe et al. (2020) to obtain a better estimation of the angle $\alpha = 27^\circ.5$.

Finally, the transformation from detector pixel at y -pixel y_i taken at time t_i to the helio-project coordinates (θ_x, θ_y) in arcsec is given by

$$\begin{bmatrix} \theta_x \\ \theta_y \end{bmatrix} = \begin{bmatrix} \cos \alpha & \sin \alpha \\ -\sin \alpha & \cos \alpha \end{bmatrix} \begin{bmatrix} (t_i - t_0)v_{\odot,x} + \theta_{x,0} \\ (y_i - y_c)\Delta y + (t_i - t_0)v_{\odot,y} \end{bmatrix} \quad (2.5)$$

where $\alpha = 27^\circ.5$ is the slit tilting angle. $v_{\odot,x}$ and $v_{\odot,y}$ are the velocities of Sun in arcsec captured by the context camera. $t_0 = 17:46:38$ corresponds to the reference time when the slit first pointed to off-limb. $\theta_{x,0}$ denotes the distance between the slit and disk center at t_0 in arcsec. y_c represents the disk center position on the detector at t_0 .

It is important to acknowledge that the method used to determine the instrumental pointing has certain limitations. First, the circle Hough Transform method used to detect the lunar limb has a precision of 1/2 pixels, which translates to about $6''.7$. Second, the time of observation recorded in the 3PAMIS FITS header has a limited precision of 1 sec. Given that the Sun moved nearly perpendicular to the slit at a speed of about $15'' \text{ s}^{-1}$, an inaccurate time of observation may result in an uncertainty of $\sim 10''$ perpendicular to the

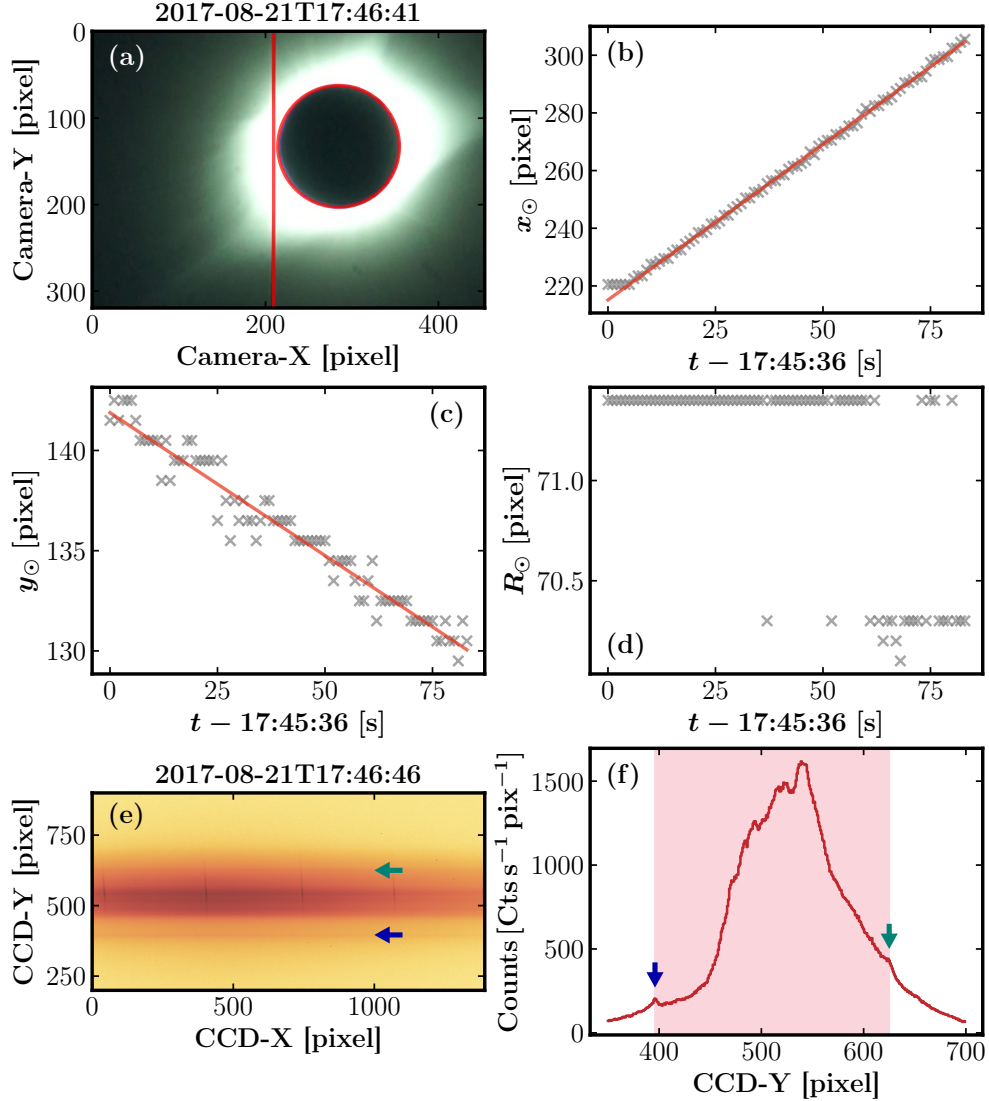


Figure 2.10: Determining the spectrograph pointing: (a) Fitting the lunar limb on context images. The red cycle highlights the lunar limb, and the red vertical line represents the position of the slit. (b) and (c) Linear fitting of the motion of the disk center on context images. (d) Variation of the fitted disk radius. (e) An off-limb CCD image. The blue and green arrows indicate limb emission leaking from the slit mirror. (f) CCD counts averaged along the x -axis, with the arrows being the same as Panel (e). The shaded pink area between the two arrows is used to calculate the spatial sampling of the detector. Link to the [Jupyter notebook](#) creating this figure: [🔗](#).

slit. Third, the slit tilt angle α determined by comparing Fe XIV intensity with narrowband images cannot achieve better results than the spatial scale of the detector, which is $\sim 8''$. This limitation could be more significant towards the two ends of the slit due to the focus on comparing the features in the active region. Additionally, the rotation of the slit mixes the uncertainty along and perpendicular to the slit. Overall, we estimated that the pointing

used in this study might have an uncertainty up to 20–30''.

No radiometric calibration was performed due to the lack of laboratory light sources. However, we still estimated the uncertainty in each pixel, assuming the photon shot noise follows the Poisson statistics:

$$\sigma_D = \sqrt{D_0 + \sigma_0^2} \quad (2.6)$$

where D_0 is the total counts in data number (DN) after the dark frame subtraction, and σ_0 is the combination of CCD readout noise and dark current noise estimated from the standard deviation of the master dark frames. We note that σ_D only represents the relative magnitude of the uncertainty in each pixel since the absolute magnitude of the photon shot noise is the square root of the photon counts or photon electron counts. The non-linear least square routine to fit the Gaussian profiles will automatically rescale these uncertainties to reach a unity χ^2 .

2.1.5 CoMP

The COronal Multi-channel Polarimeter (CoMP) is a tunable coronagraph located at the Mauna Loa Solar Observatory (MLSO). CoMP can perform spectropolarimetric observations of Fe XIII 1074.7 and 1079.8 nm lines in the near-infrared between 1.05–1.35 R_\odot . The Stokes parameters I , Q , U , and V are sampled at 3 or 5 wavelength positions across the Fe XIII profiles using Lyot filters. The three-point Stokes I profiles are inverted analytically to obtain the line intensity, Doppler shifts, and widths (Tian et al., 2013).

2.2 Spectroscopic Diagnostics

2.2.1 Formation of Optically thin emission

Due to the decrease in density, spectral lines originating from the transition region and solar corona are typically considered optically thin, i.e., the absorption is negligible or the optical depth $\tau \ll 1$. The assumption is valid in most regimes, although exceptions can be found in some strong lines, for example, Fe XII 195 Å line in the QS (Del Zanna et al., 2019) and Si IV doublets during flares (Kerr et al., 2019).

In the optically thin regime, the observed total intensity I_{ij} of a spontaneous transition from the upper level j to lower level i is the integration of the line emissivity ϵ_{ij} along the LOS (Del Zanna & Mason, 2018):

$$I_{ij} = \frac{h\nu_{ij}}{4\pi} \int \epsilon_{ij} ds \quad (2.7)$$

where $h\nu_{ij} = E_j - E_i$ is the photon energy corresponding to the energy difference between the levels j and i . 4π is the solid angle of a unit sphere, assuming isotropic spontaneous emission and ds is the differential length along LOS.

The local emissivity ϵ_{ij} is determined by the number density of ions X^{+q} at energy level j , $N_j(X^{+q})$, and the frequency of spontaneous emission, which is characterized by the Einstein coefficient A_{ji} :

$$\epsilon_{ij} = N_j(X^{+q})A_{ji} \quad (2.8)$$

In the low-density corona, collisional excitation occurs at a much shorter timescale compared to ionization and recombination processes. Therefore, it is advantageous to separate the level population $\frac{N_j(X^{+q})}{N(X^{+q})}$ and the ionization ratio $\frac{N(X^{+q})}{N(X)}$ ⁴:

$$N_j(X^{+q}) = \frac{N_j(X^{+q})}{N(X^{+q})} \frac{N(X^{+q})}{N(X)} \frac{N(X)}{N_H} \frac{N_H}{N_e} N_e \quad (2.9)$$

Here, the remaining terms are elemental abundance $N(X)/N_H$, proton-to-electron ratio $N_H/N_e \approx 0.83$ in the fully ionized corona, and the electron density N_e . The local thermodynamic properties, e.g., electron density and temperature, play essential roles in determining the level population and ionization ratios, thus affecting the emitted intensity. In essence, the observed intensity serves as a valuable tool for inferring the electron density, temperature, and element abundances of the emitting plasma. However, a thorough understanding of the processes populating the atomic levels is essential before utilizing the line intensity for diagnostic purposes.

2.2.1.1 Excitation Mechanisms

In the solar corona, populations of ions enter or leave an excited level j through the following processes:

- **Electron collisional excitation or de-excitation** from the level j to a lower level i or higher level k . The respective rates are denoted by C_{ij}^e and C_{jk}^e . Assuming a Maxwellian electron velocity distribution, the excitation rate C_{ij}^e can be written as follows (Del Zanna & Mason, 2018)

$$C_{ij}^e = 8.63 \times 10^{-6} \frac{\Upsilon_{ij}(T_e)}{g_i T_e^{1/2}} \exp\left(-\frac{\Delta E_{ij}}{k_B T_e}\right) \text{ cm}^3 \text{ s}^{-1} \quad (2.10)$$

where ΔE_{ij} is the energy difference between levels i and j , and k_B is the Boltzmann

⁴<https://www.chiantidatabase.org/cug.pdf>

constant. Υ_{ij} is the thermally-averaged collision strength

$$\Upsilon_{ij} = \int_0^\infty \Omega_{ij} \exp\left(-\frac{E'}{k_B T_e}\right) d\left(\frac{E'}{k_B T_e}\right) \quad (2.11)$$

where Ω_{ij} is the dimensionless collisional strength and $E' = E - E_{ij}$ is the remaining electron energy after scattering.

- **Proton collisional excitation or de-excitation** from the level j to a lower level i or higher level k , denoted by C_{ij}^p and C_{jk}^p , respectively. They are only important in transitions within fine structure levels inside ground configuration multiplets.
- **Spontaneous emission** from the level j to a lower energy level i by emitting a photon. The rates are the famous Einstein coefficients A_{ji} .
- **Cascades** from any higher energy level k spontaneously radiating the energy ΔE_{kj} and decaying into the lower level j . and A_{ji} , respectively.
- **Photoexcitation** from level j into a higher energy level k or from a lower level i into the level j by the absorption of a photon. The corresponding Einstein coefficients are B_{jk} or B_{ij} , respectively.
- **Stimulated emission** from the level j into a lower level i or from a higher level k to level j by emitting a photon stimulated by the interaction with another photon at the same frequency. The rates are Einstein coefficients B_{ji} or B_{kj} . The contribution of stimulated emission in the corona is insignificant, especially in UV.

It is noteworthy that the relationships between Einstein coefficients can be derived under the condition of the detailed balance:

$$B_{ij} = \frac{g_j}{g_i} B_{ji} \quad (2.12)$$

$$B_{ji} = \frac{c^2}{2h\nu_{ij}^3} A_{ji} \quad (2.13)$$

where g_i and g_j are degrees of the degeneracy of the upper and lower energy levels, c is the speed of light, and h is the Planck constant.

Then, the rate of change in level population N_j can be calculated by summing populations entering level j and subtracting those leaving it (Del Zanna & Mason, 2018)

$$\frac{dN_j}{dt} = \sum_{i < j} N_i \left(C_{ij}^e N_e + C_{ij}^p N_p + B_{ij} J_{\nu_{ij}} \right)$$

$$\begin{aligned}
& + \sum_{k>j} N_k \left(C_{kj}^e N_e + C_{kj}^p N_p + B_{kj} J_{\nu_{jk}} + A_{kj} \right) \\
& - N_j \left[\sum_{i<j} \left(C_{ji}^e N_e + C_{ji}^p N_p + B_{ji} J_{\nu_{ij}} + A_{ji} \right) + \sum_{k>j} \left(C_{jk}^e N_e + C_{jk}^p N_p + B_{jk} J_{\nu_{jk}} \right) \right]
\end{aligned} \tag{2.14}$$

where $J_{\nu_{ij}}$ is the mean incoming intensity from the 4π solid angle. Collisional processes, spontaneous emission, photoexcitation, and stimulated emission are highlighted in red, blue, yellow, and green, respectively. The first row pertains to the excitation from lower levels, the second row describes the cascade from higher levels, and the last row measures the population leaving level j .

In the solar corona, the excitation and de-excitation processes typically reach a steady state much faster than the typical exposure times of the observation, except in some extreme regimes, such as flares. Therefore, under the assumption of statistical equilibrium $dN_j/dt = 0$, the level population can be computed by inverting a substantial matrix representing the systems of Equations 2.14. This constitutes the fundamental function of the CHIANTI database, a key tool widely used in this dissertation (Dere et al., 1997a; Del Zanna et al., 2021; Dere et al., 2023).

To gain insights into the relationship between line intensity and electron density, let us consider an over-simplified two-level atom, although the realistic atomic structures of heavy ions can be exceedingly complex, with hundreds or even thousands of energy levels. If the transition between levels 1 and 2 is allowed, and the density is sufficiently high for collisions to dominate the population entering level 2:

$$C_{12}^e N_e N_1 = (C_{21}^e N_e + A_{21}) N_2 \tag{2.15}$$

which can be further expressed as

$$\frac{N_2}{N_1 + N_2} = \frac{C_{12} N_e}{(C_{12} + C_{21}) N_e + A_{21}} \tag{2.16}$$

In most cases, especially for dipole transitions to ground states (so-called resonant lines), $A_{21} \gg (C_{12} + C_{21}) N_e$ (coronal-model approximation). This leads to two important conclusions:

1. $N_2/(N_1 + N_2) \ll 1$, which indicates the population of ions in excited levels is much lower than that in the ground level.
2. $N_2/(N_1 + N_2) \sim N_e$, which implies $N_j(X^{+q})/N(X^{+q}) \sim N_e$, and consequently, the

total intensity I_{ij} is proportional to N_e^2 (see Equations 2.7 and 2.9).

If the transition from level 2 to 1 is not allowed, for instance, only occurs through magnetic dipole or electric quadrupole transitions, A_{21} can become comparable with $(C_{12} + C_{21})N_e$. Such levels, known as metastable levels, possess a level population comparable to the ground state (in a pseudo-Boltzmann equilibrium population ratio with the ground level). Furthermore, it implies that the behavior of $N_2/(N_1 + N_2)$ will have a more intricate dependence on N_e , which is one of the basic density diagnostics detailed in Section 2.2.2.

Additionally, certain heavy ions have split ground states due to fine structures (e.g., Fe X and Fe XIV). The transitions between the two split ground states are strictly forbidden due to the absence of a parity change. Because of the small splitting between the two levels, the collisional excitation becomes significantly less effective in exciting and de-exciting those levels. Consequently, when the upper level 2 is primarily populated through photoexcitation when the density is low enough, we have

$$B_{12}N_1J_{\nu_{12}} = N_2A_{21} \quad (2.17)$$

in other words

$$\frac{N_2}{N_1 + N_2} = \left(\frac{B_{12}J_{\nu_{12}}}{A_{21}} + 1 \right)^{-1} = \left(\frac{c^2}{2h\nu_{12}^3} \frac{g_2}{g_1} J_{\nu_{12}} + 1 \right)^{-1} \quad (2.18)$$

Importantly, this relationship is independent of the local density. Therefore, when the upper level 2 is fully populated by photoexcitation, the line intensity I_{ij} reveals a linear proportionality with respect to N_e . This implies that the intensity of a forbidden transition decreases much more gradually with height compared to that of an allowed transition.

In practice, the observed intensity might contain both collisionally excited and radiatively excited components, which can be treated separately (Landi et al., 2016)

$$I_{\text{obs}} = I_{\text{coll}} + I_{\text{rad}} \quad (2.19)$$

note that $I_{\text{coll}} \propto N_e^2$ while $I_{\text{rad}} \propto N_e$. This approach is frequently employed to describe the intensity variation of the forbidden lines in visible, allowing for the study of emission in the higher corona (e.g., Habbal et al., 2013; Boe et al., 2018). Besides, in the case of the strong resonance doublets of lithium-like ions (e.g., Mg X and O VI), these lines can be photoexcited by their own bright emission on the disk. Therefore, the transition from collisional excitation to radiative excitation provides important information for the diagnostics of density (e.g., Antonucci et al., 2004) or the outflow velocity (e.g., Li et al., 1998).

2.2.2 Electron Density Diagnostics

As outlined in Section 2.2.1, the intensity of a transition to the ground state from a metastable level has a different dependence on the electron density compared to allowed transitions. Therefore, the ratios between a forbidden or intercombination line originating from a metastable level and an allowed transition populated from the ground state of the same ion could be used to infer the density in the solar atmosphere.

Applying the two-level model (Equation 2.16), it becomes evident that in the low-density regime, when $(C_{12} + C_{21})N_e \ll A_{21}$, the metastable level is primarily de-excited by radiative decay. Consequently, the intensity of the transition from the metastable level $I_{\text{meta}} \propto N_e^2$. Conversely, in the high-density regime where collision dominates, the level population approaches the Boltzmann distribution in equilibrium. In this regime, I_{meta} becomes linearly proportional to N_e .

Hence, the ratio between an allowed transition $I_{\text{allow}} \propto N_e^2$ and a transition from the metastable level becomes sensitive to the electron density when the collisional de-excitation is comparable to the radiative decay of the metastable level. Additionally, to minimize the temperature dependence of line ratios, it is preferable for these two lines to originate from levels with similar excitation energies (see temperature dependence in Section 2.2.3).

Furthermore, if a level can be collisionally populated from a metastable level, often resulting from the fine structure splitting of the ground state, then an allowed transition from this level can also be employed in electron density diagnostics. In practice, these lines are more commonly used in electron density diagnostics, for instance, in Hinode/EIS observations.

Figure 2.11 shows two examples of line ratios sensitive to the electron density N_e . Specifically, Mg IX 694 and 706 Å both arise from transitions within the first excited configuration $2s2p$ to the ground configuration $2s^2$. However, Mg IX 694 Å is highly forbidden ($^3P_2 - ^1S_0$), whereas Mg IX 706 Å is an intercombination line ($^3P_1 - ^1S_0$) that has a much greater Einstein coefficient. Therefore, the Mg IX 706/694 Å ratio demonstrates a high sensitivity to the electron density variation.

The ratio involving the self-blended Fe XII 186.854 Å and 186.887 Å lines relative to the Fe XII 195.119 Å line offers one of the most commonly used density diagnostics in the Hinode/EIS observations (see Section 2.1.1). Here, the 186.854 Å and 186.887 Å primarily undergo collisional excitations from two metastable levels $3s^23p^3 \ ^2D_{3/2}$ and $3s^23p^3 \ ^2D_{5/2}$ within the ground configuration. On the other hand, the upper level of the prominent Fe XII 195 Å line is dominated by the collisional excitation from the ground state $3s^23p^3 \ ^4S_{3/2}$. Consequently, the ratio of Fe XII 186/195 Å depends on the electron density as well.

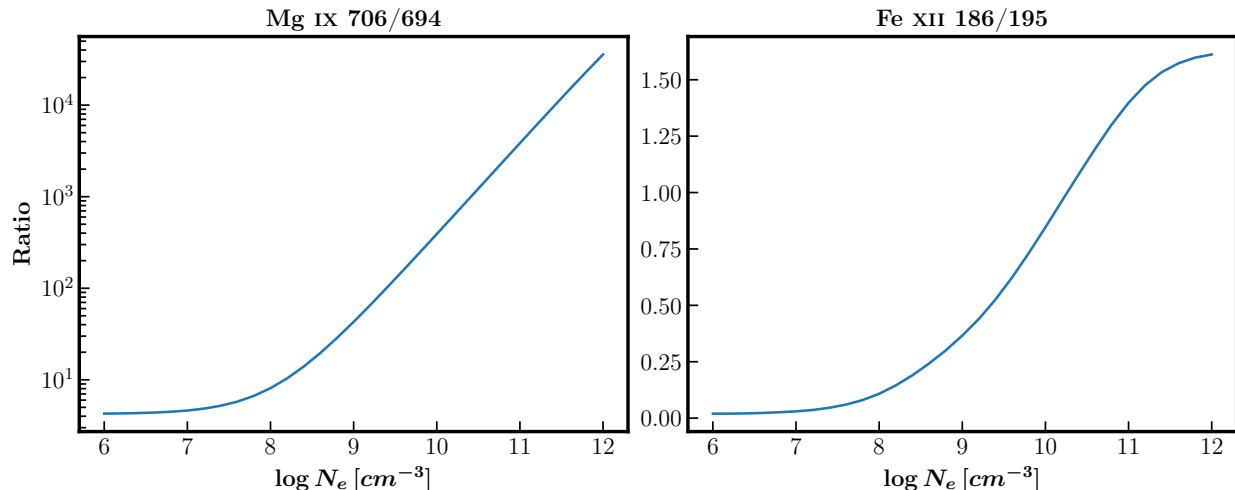


Figure 2.11: Intensity ratio of Mg IX 706/694 Å and Fe XII 186/195 Å at different electron density N_e .

2.2.3 Electron Temperature Diagnostics

The electron temperature diagnostics exploit the temperature dependence of the collisional excitation rate (Equation 2.10). If the upper levels 2 and 3 of two spectral lines are collisionally populated from the same lower level 1, typically the ground state, the intensity ratio of the two lines becomes proportional to the product of the collisional rates from the ground state and the Einstein coefficients, i.e.,

$$\frac{I_3}{I_2} \propto \frac{C_{13}A_{31}}{C_{12}A_{21}} \approx \frac{\Upsilon_{13}(T_e)}{\Upsilon_{12}(T_e)} \exp\left(-\frac{E_3 - E_2}{k_B T_e}\right) \quad (2.20)$$

Therefore, when the energy difference is sufficiently large, such that $|E_3 - E_2| \gg 1$, the intensity ratio becomes highly sensitive to variations in electron temperature. An extreme example is the ratio between an EUV line and a visible forbidden line between ground configurations, for example, Fe X 184/6374 Å ratio in Figure 2.12. However, simultaneous observation of these two lines with different instruments can be challenging due to their substantial wavelength differences and needs for accurate radiometric calibrations. Ratios between two EUV resonance lines can also serve as useful electron temperature diagnostics. For example, the Fe XI (188.216+188.299)/257.554 Å ratio is frequently used in Hinode/EIS observations because of the notable energy difference between the upper level of the 188 doublets ($3s^23p^33d \ ^3P_{1,2}$) and the upper level of 257 Å ($3s^23p^33d \ ^5D_3$). Nevertheless, results of T_e diagnostics using the Fe XI 188/257 Å ratio can also be influenced by the radiometric calibration between the two detectors (see Section 2.1.1).

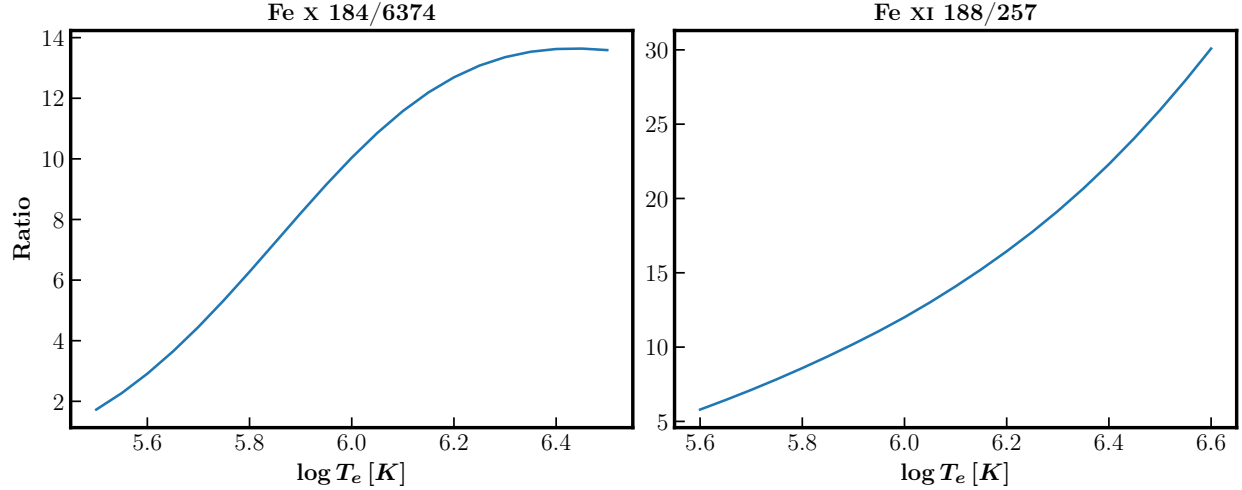


Figure 2.12: Intensity ratio of Fe x 184/6374 Å and Fe XI 188/257 Å at different electron density N_e .

2.2.4 Line Widths, Ion Temperature, and Nonthermal Motions

The broadening of spectral lines in the solar corona can be influenced by various mechanisms related to the local plasma conditions. While the atomic level energy is sharp due to the negligible natural and pressure broadening, the coronal lines are primarily broadened by substantial microscopic Doppler shifts due to the high temperature and other unresolved motions.

The observed coronal line profiles are often interpreted and fitted by a Gaussian profile plus a constant continuum background intensity I_{bg} :

$$I_{\text{obs}}(\lambda) = \sqrt{\frac{4 \ln 2}{\pi}} \frac{I_{\text{tot}}}{\Delta\lambda} \exp \left[-\frac{(\lambda - \lambda_0)^2}{\Delta\lambda^2/4 \ln 2} \right] + I_{\text{bg}} \quad (2.21)$$

where λ is the wavelength, I_{tot} represents the total or integrated intensity, $\Delta\lambda$ stands for the full width at half maximum (FWHM), and λ_0 is the line center wavelength. Notably, there are some other representations of line widths in the literature, including the standard deviation σ_λ , half width at half maximum (HWHM), and $1/e$ or Doppler widths $\Delta\lambda_{1/e}$. Their relations to FWHM can be summarized as

$$\sigma_\lambda = \frac{\Delta\lambda}{2\sqrt{2 \ln 2}} \quad (2.22)$$

$$\text{HWHM} = \frac{\Delta\lambda}{2} \quad (2.23)$$

$$\Delta\lambda_{1/e} = \frac{\Delta\lambda}{2\sqrt{\ln 2}} \quad (2.24)$$

Furthermore, the observed FWHM $\Delta\lambda$ is often assumed to consist of a Gaussian instrumental width $\Delta\lambda_{\text{inst}}$, a thermal width arising from the ion temperature T_i , and a nonthermal component ξ through a root sum square:

$$\Delta\lambda_{\text{obs}} = \left[\Delta\lambda_{\text{inst}}^2 + 4 \ln 2 \left(\frac{\lambda_0}{c} \right)^2 \left(\frac{2k_B T_i}{m_i} + \xi^2 \right) \right]^{1/2} \quad (2.25)$$

where c is the speed of light, k_B represents the Boltzmann constant, m_i is the ion mass, and ξ denotes the nonthermal velocity. After removing the instrumental widths $\Delta\lambda_{\text{inst}}$, the rest true width $\Delta\lambda_{\text{true}} = (\Delta\lambda_{\text{obs}}^2 - \Delta\lambda_{\text{inst}}^2)^{1/2}$ can be represented by so-called effective velocity v_{eff} or effective temperature T_{eff} to drop the dependence on λ_0 :

$$v_{\text{eff}}^2 = \frac{2k_B T_{\text{eff}}}{m_i} \equiv \frac{2k_B T_i}{m_i} + \xi^2 = \frac{\Delta\lambda_{\text{true}}^2}{4 \ln 2} \quad (2.26)$$

Notably, the v_{eff} is often referred to as, and equivalent to the $1/e$ velocity $v_{1/e} = \Delta\lambda_{1/e}/\lambda_0$ used in other publications (e.g., [Wilhelm et al., 2005](#)).

2.3 Simulations

2.3.1 AWSoM

The Alfvén Wave Solar atmosphere Model (AWSoM; [van der Holst et al., 2014, 2022](#)) serves as the solar corona (SC) and inner heliosphere (IH) components of the open-source Space Weather Modeling Framework (SWMF; [Tóth et al., 2012](#); [Gombosi et al., 2021](#)). AWSoM solves the three-temperature MHD equations (isotropic electron temperature T_e and anisotropic proton temperature $T_{i,\text{perp}}$ and $T_{i,\parallel}$) alongside equations characterizing low-frequency Alfvén wave turbulence ([van der Holst et al., 2014](#)):

$$\frac{\partial \rho}{\partial t} + \nabla \cdot (\rho \mathbf{u}) = 0 \quad (2.27)$$

$$\begin{aligned} \frac{\partial(\rho \mathbf{u})}{\partial t} + \nabla \cdot \left[\rho \mathbf{u} \mathbf{u} + \left(P_{i,\parallel} - P_{i,\perp} \hat{\mathbf{b}} \hat{\mathbf{b}} \right) - \frac{\mathbf{B} \mathbf{B}}{\mu_0} \right] + \nabla \cdot \left(P_{i,\perp} + P_e + \frac{B^2}{2\mu_0} + P_A \right) \\ = -\rho \frac{GM_\odot}{r^3} \mathbf{r} \end{aligned} \quad (2.28)$$

$$\frac{\partial \mathbf{B}}{\partial t} - \nabla \times (\mathbf{u} \times \mathbf{B}) = 0 \quad (2.29)$$

$$\frac{\partial}{\partial t} \left(\frac{P_i}{\gamma - 1} + \frac{\rho u^2}{2} + \frac{B^2}{2\mu_0} \right) + \nabla \cdot \left[\left(\frac{\rho u^2}{2} + \frac{\gamma P_i}{\gamma - 1} + \frac{B^2}{\mu_0} \right) \mathbf{u} \mathbf{P}_i \cdot \mathbf{u} - \frac{\mathbf{B}(\mathbf{u} \cdot \mathbf{B})}{\mu_0} \right] =$$

$$-\mathbf{u} \cdot \nabla (P_e + P_A) + \frac{N_i k_B}{\tau_{ei}} (T_e - T_i) + Q_i - \rho \frac{GM_\odot}{r^3} \mathbf{r} \cdot \mathbf{u} \quad (2.30)$$

$$\begin{aligned} \frac{\partial P_{i,\parallel}}{\partial t} + \nabla \cdot (P_{i,\parallel} \mathbf{u}) + 2P_{i,\parallel} \mathbf{b} \cdot (\nabla \mathbf{u}) \cdot \mathbf{b} &= \frac{\delta P_{i,\parallel}}{\delta t} \\ &+ (\gamma - 1) \frac{N_i k_B}{\tau_{ei}} (T_e - T_{i,\parallel}) + (\gamma - 1) Q_{i,\parallel} \end{aligned} \quad (2.31)$$

$$\frac{\partial}{\partial t} \left(\frac{P_e}{\gamma - 1} \right) + \nabla \cdot \left(\frac{P_e}{\gamma - 1} \mathbf{u} \right) + P_e \nabla \cdot \mathbf{u} = -\nabla \cdot \mathbf{q}_e + \frac{N_i k_B}{\tau_{ei}} (T_i - T_e) - Q_{\text{rad}} + Q_e \quad (2.32)$$

$$\frac{\partial w_\pm}{\partial t} + \nabla \cdot [(\mathbf{u} \pm \mathbf{V}_A) w_\pm] + \frac{w_\pm}{2} (\nabla \cdot \mathbf{u}) = \mp \mathcal{R} \sqrt{w_- w_+} - \Gamma_\pm w_\pm \quad (2.33)$$

The first three equations are conversation, momentum, and induction equations. Here, ρ denotes plasma density (assuming quasi-neutrality), \mathbf{u} refers to the bulk velocity, \mathbf{B} is the background magnetic field, $\hat{\mathbf{b}} = \mathbf{B}/B$. $P_{i,\parallel}$ and $P_{i,\perp}$ are parallel and perpendicular proton pressure, which solves the average proton pressure as $P_i = (2P_{i,\perp} + P_{i,\parallel})/3$. $\mathbf{P}_i = P_i \mathbf{I} + (P_{i,\parallel} - P_{i,\perp}) \hat{\mathbf{b}} \hat{\mathbf{b}}$ is the proton pressure tensor. P_e represents the electron pressure. $P_A = (w^+ + w^-)/2$ is the additional pressure due to Alfvén waves to accelerate the solar wind plasma.

Equations (2.30), (2.31), (2.32) are energy equations for the average proton pressure, parallel proton pressure, and electron pressure, respectively. Here, $\gamma = 5/3$ and τ_{ei} is the timescale of heat exchange through Coulomb collisions. Q_{rad} represents the EUV radiation cooling. Q_i , $Q_{i,\parallel}$, Q_e are the turbulence heating terms of protons and electrons. $\delta P_{i,\parallel}/\delta t$ is a relaxation term of proton pressure anisotropy by various instability constraints.

Equation (2.33) is the key equation describing the manner in which Alfvén wave energy densities w^+ and w^- (with "+" signifying the wave propagation parallel to \mathbf{B} whereas "-" indicates antiparallel propagation) propagate and dissipate in the solar corona and heliosphere. \mathbf{V}_A symbolizes the local Alfvén speed. \mathcal{R} represents the signed reflection rate of Alfvén wave due to wave speed gradient and vorticity along field lines. Γ_\pm is a phenomenological dissipation rate caused by counter-propagating Alfvén wave turbulence.

The coronal heating and solar wave acceleration in the model are realized by the dissipation of Alfvén wave turbulence, incorporated with the partial reflection of Alfvén waves along the field lines. Energy partition to electron and proton heating is constrained by linear wave damping and nonlinear stochastic heating. This approach has been further improved by the observations from NASA's Parker Solar Probe (PSP; Fox et al., 2016) spacecraft (van der Holst et al., 2022).

To compare with remote-sensing observations of the lower solar corona, we focus on the SC component, with a spherical grid from 1 to $24 R_\odot$ and spans the upper chromosphere to the solar corona. Grid refinements are employed near the solar surface, especially radially, to

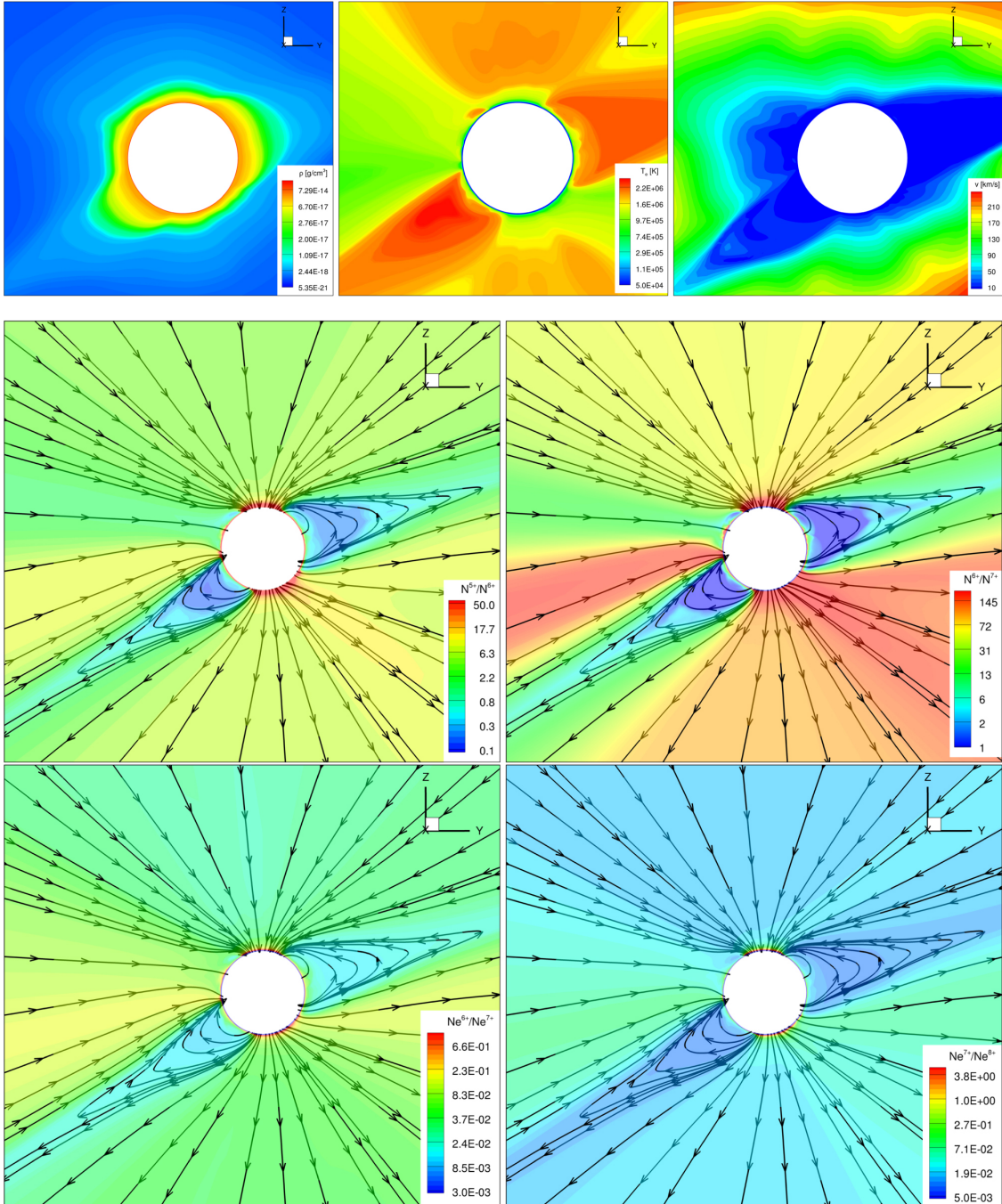


Figure 2.13: Meridional cuts of steady-state AWSoM simulation of the corona density, electron temperature, solar wind velocity (top three panels), and NEI heavy ion charge state ratios (middle and bottom rows). Figure taken from Szente et al. (2022).

resolve the large density and temperature gradients in the TR. Furthermore, AWSoM adopts an artificially broadened transition region, similar to Lionello et al. (2009) and Sokolov et al. (2013).

AWSoM utilizes the block-adaptive tree library (Tóth et al., 2012) based on the Block Adaptive Tree Solarwind Roe Upwind Scheme (BATS-R-US Powell et al., 1999) to decompose the simulation domain. This decomposition features the adaptive mesh refinement along three directions: radial, longitude, and latitude. Additional layers of Adaptive Mesh Refinement (AMR) are often applied to specific regions, such as the lower corona (van der Holst et al., 2022, e.g., below $1.7 R_{\odot}$), heliospheric current sheet (HCS), and ARs (e.g., Shi et al., 2022) to increase the spatial resolution. Additionally, the IH component can extend the simulation domain into the heliosphere to assess the performance of the model by comparing in-situ solar wind measurements.

The inner boundary of AWSoM is situated at 50,000 K, at the upper chromosphere and lower transition region. The magnetic field at the inner boundary is extrapolated from a photospheric synoptic radial magnetogram covering a Carrington Rotation. AWSoM typically utilizes a Global Oscillation Network Group magnetogram (GONG; Harvey et al., 1996) processed with Air Force Data Assimilative Photospheric flux Transport (ADAPT; Henney et al., 2012). The default density and temperature at the inner boundary are $2 \times 10^{17} \text{ m}^{-3}$ and 50 kK.

Two other important input parameters are the Poynting flux S_A of the Alfvén waves propagating outwards at the bottom boundary and the transverse correlation length L_{\perp} of Alfvén wave perpendicular to the magnetic field. The optimal Poynting flux to field strength ratio S_A/B usually ranges from $0.2\text{--}1.2 \times 10^6 \text{ W m}^{-2} \text{ T}^{-1}$. This fluctuation correlates with the variation of the open-field area throughout the solar cycle (Huang et al., 2023a).

The correlation length L_{\perp} determines the Alfvén wave turbulence dissipation rate Γ_{\pm} by

$$\Gamma_{\pm} = \frac{2}{L_{\perp}} \sqrt{\frac{w_{\mp}}{\rho}} \quad (2.34)$$

AWSoM assumes the correlation length L_{\perp} is proportional to the mean spacing of the magnetic flux tubes (Spruit, 1981; Hollweg, 1986). This relationship implies a simple scaling law with the field strength as $L_{\perp} \propto B^{-1/2}$. The product of L_{\perp} and $B^{1/2}$ is a free input parameter of the model. By default, $L_{\perp} B^{1/2}$ is set to $1.5 \times 10^5 \text{ m T}^{1/2}$.

The inclusion of the non-equilibrium ionization (NEI) calculations in AWSoM by Szente et al. (2022) represents a significant advancement in its capability in modeling the solar corona and solar wind. The NEI calculations allow AWSoM to trace the heavy ion charge state evolution from the lower corona to the solar wind at 1 au and connect the remote-sensing observations with in-situ measurements. Furthermore, the NEI calculations are pivotal to simulations of dynamic phenomena like CMEs, and improve the spectrum synthesis (Szente et al., 2023, also see Section 2.3.3). Figure 2.13 shows an example of the AWSoM simulation

results of the corona’s thermodynamic properties and non-equilibrium heavy ion charge states.

2.3.2 AWSoM-R

Alfvén Wave Solar atmosphere Model - realtime (AWSoM-R, [Sokolov et al., 2021](#)) is a specialized version of AWSoM tailored for real-time space weather prediction. By altering the numerical treatments of the TR and low solar corona and using two temperature MHD equations, AWSoM-R reduces the computational resources required to capture the distinct temperature and density gradients in the lower solar atmosphere.

Instead of using the artificial grid stretching in the transition region ([Lionello et al., 2001](#)), AWSoM-R introduces the threaded-field-line Model (TFLM). TFLM assumes the potential fields in the lower corona and solves 1D MHD and wave equations along 1D field lines between 1 and $1.05 R_{\odot}$. In AWSoM-R, TFLM bridges the chromosphere at $1 R_{\odot}$ to the 3D global coronal model (AWSoM) at $1.05 R_{\odot}$. Incorporating TFLM, AWSoM-R sacrifices the fine grids to resolve the transition region and lower corona but realizes faster-than-realtime simulations of the solar corona on hundreds of CPU cores. A notable advantage of AWSoM-R, especially for comparing the model results to remote-sensing observations, is its ability to synthesize low-corona observations without the artificial transition-region stretching.

2.3.3 Spectrum Synthesis

AWSoM and AWSoM-R can predict remote-sensing observations of the solar corona with the SPECTRUM module ([Szente et al., 2019, 2023](#)). Initially introduced as a post-processing module in [Szente et al. \(2019\)](#), SPECTRUM is now fully integrated into BATS-R-US ([Szente et al., 2023](#)). This allows spectrum synthesis on the original block adaptive grid, similar to [Downs et al. \(2010\)](#), instead of an interpolated Cartesian grid. In practice, SPECTRUM forward models the emissivity profiles at each voxel and then integrates along a user-defined LOS. For the detailed implementation of synthetic spectral calculations, please refer to [Szente et al. \(2019, 2023\)](#).

SPECTRUM takes care of two different Doppler-broadening mechanisms:

1) **Macroscopic Doppler broadening** due to the LOS integration of the line profile with different centroids. The centroid of the emissivity profile at each voxel is Doppler shifted by the local bulk plasma motion along the LOS u_{LOS}

$$\lambda_{\text{shifted}} = \left(1 - \frac{u_{\text{LOS}}}{c}\right) \lambda_0, \quad (2.35)$$

where c is the speed of light.

2) **Microscopic Doppler broadening** in individual voxels caused by the thermal motion and Alfvénic turbulence,

$$\Delta\lambda = \left[4 \ln 2 \left(\frac{\lambda_0}{c} \right)^2 \left(\frac{2k_B T_{\text{LOS}}}{m_p A_i} + \xi^2 \right) \right]^{1/2} \quad (2.36)$$

where m_p is the proton mass, and A_i is the mass number of the ion. Because AWSOM does not yet predict ion temperatures, we assumed the LOS ion temperature to be given by the LOS proton temperature $T_{\text{LOS}} = T_{\text{perp}} \sin^2 \alpha + T_{\text{par}} \cos^2 \alpha$, where T_{perp} and T_{par} are proton temperatures perpendicular and parallel to the magnetic field, and α is the angle between the direction of the local magnetic field and the LOS.

The nonthermal component is

$$\xi^2 = \frac{1}{2} \langle \delta u^2 \rangle \sin^2 \alpha = \frac{1}{2} \frac{\omega^+ + \omega^-}{\rho} \sin^2 \alpha = \frac{1}{8} (z_+^2 + z_-^2) \sin^2 \alpha. \quad (2.37)$$

Here z_{\pm} are the Elsässer variables for forward- and backward-propagating waves, and the respective energy densities are ω_{\pm} .

Notably, the nonthermal velocity in this dissertation is defined in a slightly different but mathematically equivalent way compared to the definitions in [Szente et al. \(2019\)](#). [Szente et al. \(2019\)](#) adopted the standard deviation to describe the line broadening, and the non-thermal velocity is defined as $v_{\text{nth}}^2 = \frac{1}{4} \langle \delta u^2 \rangle \sin^2 \alpha = \frac{1}{2} \xi^2$.

A comparison between the SPECTRUM synthetic spectra and Hinode/EIS observation of an AR made by [Shi et al. \(2022\)](#) is shown in Figure 2.14. This highlights the unique capability of SPECTRUM to understand the corona heating and access the model performance.

Furthermore, SPECTRUM can forward model the spectral line intensity using the non-equilibrium charge state calculation results from AWSOM ([Szente et al., 2022](#)). When no non-equilibrium charge state information is provided, SPECTRUM assumes ionization equilibrium and refers to a CHIANTI look-up table to calculate the line emissivity (Equations 2.8 and 2.9). SPECTRUM can also model the profiles of coronal forbidden lines in visible and near-infrared, with the photoexcitation effect considered ([Szente & Landi, in prep](#)).

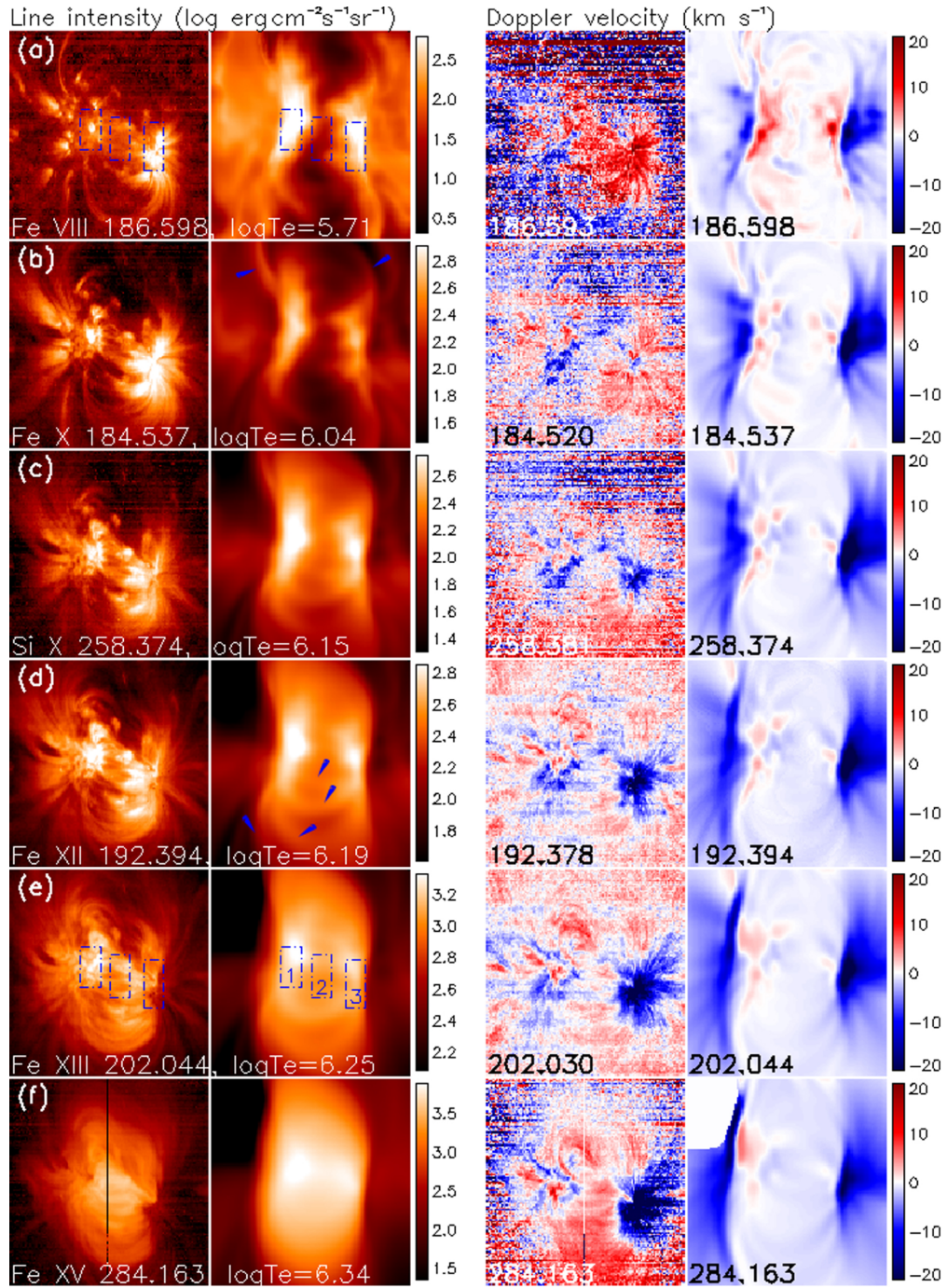


Figure 2.14: Comparison between AWSoM synthetic line intensity and Doppler shift of an AR with Hinode/EIS observations from Shi et al. (2022).

CHAPTER 3

Line Width Variation in the CHs

3.1 Preface

The materials present in this chapter have been published in the *Astrophysical Journal*, 913, 74 (Zhu et al., 2021). The paper is co-authored by Judit Szente and Enrico Landi.

3.2 Introduction

The nonthermal broadening of spectral lines is often used to detect signatures of Alfvén waves propagating in the corona (see introductions in Section 1.3). Despite extensive studies dedicated to the behavior of line width as a function of radial distance, the interpretation of observations is still challenging. First, due to the low signal-to-noise ratio (SNR) in the off-limb spectroscopic observations, previous studies usually relied on a large spatial binning along the slit (e.g., Hahn et al., 2012, 32 pixels), or they were restricted to a limited field of view (FOV; e.g., Banerjee et al., 1998, around $1.25 R_{\odot}$). In addition, concerns about the fidelity of line profiles measured at greater heights were raised due to instrumental scattered light in SOHO/SUMER and Hinode/EIS observations. Furthermore, Szente et al. (2019) modeled the EIS line profiles in the region studied by Hahn et al. (2012) using AWSoM and an improved spectral synthesis code, unveiling the absence of any decrease in line widths between 1.0 – $1.4 R_{\odot}$.

To address these unresolved issues, this chapter presents the measurements of the Fe XII 192.4 \AA , 193.5 \AA , and 195.1 \AA and Fe XIII 202.0 \AA line widths as a function of radial distance within a southern coronal hole (CH) observed by EIS with a 33,600 s long total exposure time. The extended exposure time affords a smaller spatial binning to measure the line profiles up to $\sim 1.5 R_{\odot}$. Our analysis also assesses the influence of various stray light levels on the line fitting procedure. Furthermore, we also compare the results with line profiles modeled by an upgraded version of the AWSoM and SPECTRUM module (van der Holst

et al., 2022). The rest of this chapter are structured as follows: Section 3.3 outlines the methods we used in data reduction and analysis. We present the comparative analysis of the observations and simulations in Section 3.4. Section 3.5 discusses the discoveries and their implications.

3.3 Methodology

3.3.1 Data Reduction

We investigated the observations of a southern CH made by Hinode/EIS during CR 2107 on March 5, 6, and 11, 2011. The main strength of this dataset is the extremely long total exposure time — over 30,000s per day. The center of the $2'' \times 512''$ slit was pointed at $(0'', -1242'')$ during the off-limb observations, covering a region from $\sim 1.00 R_{\odot}$ to $1.54 R_{\odot}$. A few on-disk images are taken when the slit center was pointed at $(0'', -842'')$ to estimate the stray-light levels in off-limb exposures (see Figure 3.1). Finally, we obtained 143 frames of the off-limb spectrum and 9 frames of the on-disk spectrum, each with an exposure time of 600s. The position of the EIS slit during on-disk exposures is shown in Figure 3.1.

Part of the dataset was not converted into FITS files by the EIS pipeline for technical reasons. A parallel suite of IDL programs that converted individual data packets telemetered down from the satellite into science-ready IDL save data files was developed by the authors. We compared the results of this suite of codes with `eis_prep` on the datasets for which both the fits files and the data packets were available, showing good consistency. Standard EIS data calibration described in Section 2.1.1 has been applied in data reduction. The radiometric calibration is performed in two steps: first, we perform the original laboratory calibration, followed by the HPW correction Warren et al. (2014). Because we are interested in the line widths and the only use we make of line intensities is to determine the intensity ratios of lines close in wavelength, the choice of intensity calibration correction plays a minor role in the present work. We experimented with many different spatial binnings (see Section 3.5.3 and Figure 3.10) and found that by increasing the pixels in each bin, the result did not change, but the noise decreased up to a binning over 16 pixels. Beyond the 16-pixel spatial binning, there was no particular gain in noise, but only loss in resolution. Therefore we binned the data along the slit direction by every 16 pixels to further increase the S/N.

Additionally, we removed the instrumental broadening along the $2''$ slit calculated by the IDL routine `eis_slit_width.pro` (Young, 2011b) after the fitting detailed in Section 3.3.3.

3.3.2 Stray-light Correction

Solar EUV emission from the quiet Sun and active regions can be scattered into the EIS FOV, contaminating the observed line profiles when EIS points above the limb. Ugarte-Urra (2010a) measured a 2% stray-light level using observations during an eclipse, and this value is widely used in studies of coronal line broadening (e.g., Hahn et al., 2012; Hahn & Savin, 2013c). However, a recent study of an orbital eclipse suggested that the amount of stray light in EIS FOV could be higher than 2% above the distance of $1.3 R_{\odot}$ (Hara, 2019). In addition, Wendeln & Landi (2018) estimated that about a fraction of 10% radiation from surrounding active and quiet-Sun regions contaminated an equatorial CH observed on the disk. They suggested that the 2% stray light value might either be underestimated or dependent on the specific configuration of the observation being analyzed so that the 2% value proposed by Ugarte-Urra (2010a) may not apply to all observations.

Unfortunately, it is difficult to determine the contribution of stray light directly from EIS observations. To estimate the stray-light level, the on-disk portion of the slit in the cross-limb observations was averaged along the slit direction and multiplied by a fraction of 2%, 4%, and 10%. We took these three fractions as possible estimates of the stray light level to estimate the uncertainties introduced by removing the stray light.

The 2% stray-light intensity inferred from on-disk exposures on March 5, 6, and 11 are shown in Figure 3.2 together with the averaged off-limb intensity at $\sim 1.4 R_{\odot}$ on the same date to show the relative strength of the stray light and the measured emission at the slit location where the latter is weakest. The estimated stray light on March 11 contributes much less to the total line intensity than that on the other two days. This is because the slit was pointing to the brighter quiet-Sun plasma during the on-disk exposures on March 5 and 6 (see Figure 3.1), rather than the CH on March 11. The stray light was evaluated by fitting a single-Gaussian profile to the on-disk intensity; the fitted profile was rescaled by the stray-light fractions and used to fit the off-limb spectrum, as described in Section 3.3.3. We note that there is a small wavelength shift (~ 0.01 – 0.02 \AA) between the line centroids of the on-disk and off-limb spectrum in Figure 3.2. We compared the line profiles from the overlapped region (~ 1.01 – $1.12 R_{\odot}$) covered by on-disk and off-limb exposures and found that the line profiles match perfectly after slit-tilt correction. Therefore, we suggest that this is not a systematic shift in the wavelength calibration or slit-tilt correction and use the same line centroid wavelength of the stray-light profiles in the fitting discussed in Section 3.3.3. We will further discuss this wavelength shift in Section 3.5.

To avoid the negative DNs when subtracting the estimated stray-light profiles from the off-limb profiles at high altitudes, we discarded the March 5 and 6 data in the rest of the study, leaving 56 off-limb and three on-disk exposures. The total exposure time of the

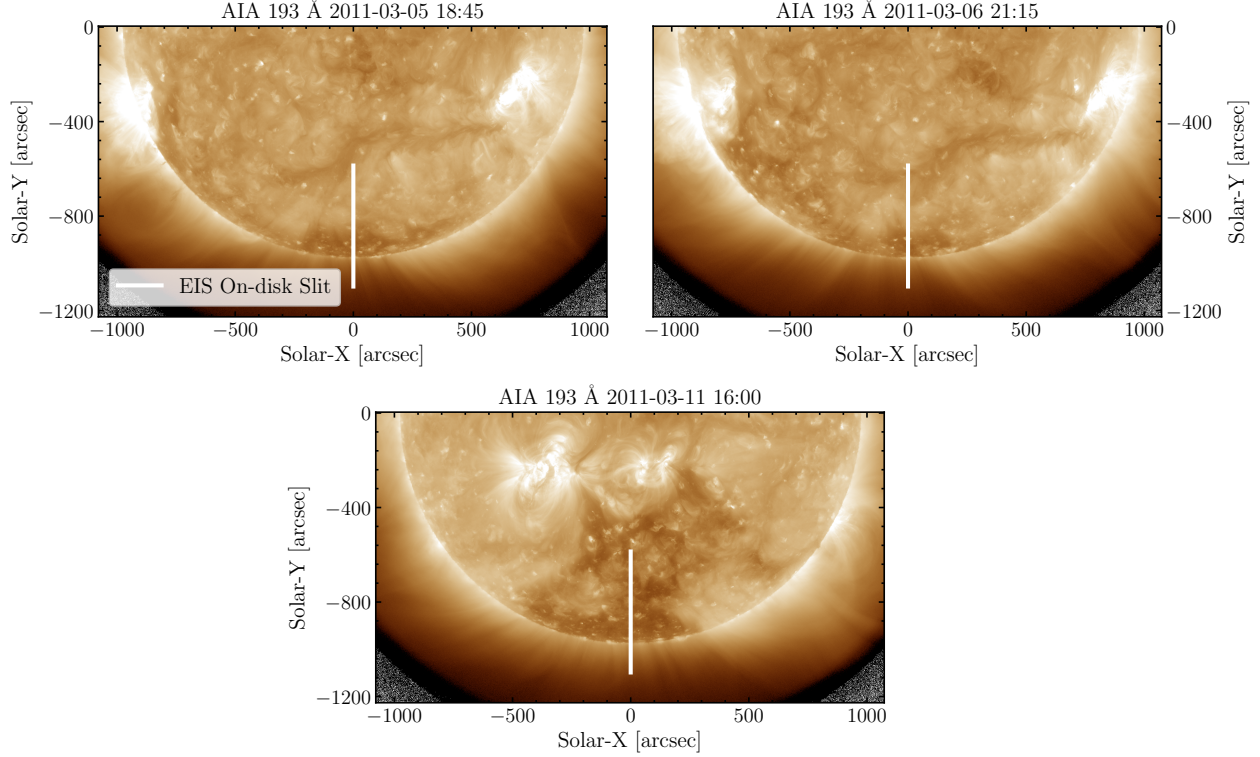


Figure 3.1: The positions of the EIS Slit over SDO/AIA 193 Å observations during on-disk exposures on 2011 March 5, 6, and 11. On March 5 and 6, most of the slit was covered by the quiet-Sun plasma. On March 11, the slit was directed at the CH, which explains why the stray-light intensity estimated on March 11 is much lower.

off-limb observations is 33,600 s.

3.3.3 Fitting

We fitted observed spectral lines to the summation of two Gaussian profiles with the emcee Markov chain Monte Carlo (MCMC) algorithm (Foreman-Mackey et al., 2013). One component is the "real" off-limb spectrum, and the other is the fixed stray-light profile. The off-limb profile can be determined with four parameters: the integrated intensity I_0 , the centroid wavelength λ_0 , the full width at half maximum (FWHM) $\Delta\lambda$, and the background intensity I_{bg} .

$$\ln P(I_{\text{obs}}|\lambda, \sigma_I, I_0, \lambda_0, \Delta\lambda, I_{\text{bg}}) = -\frac{1}{2} \sum_i \left\{ \left[\frac{I_{\text{obs},i} - g(\lambda_i)}{\sigma_i} \right]^2 + \ln(2\pi\sigma_i^2) \right\} \quad (3.1)$$

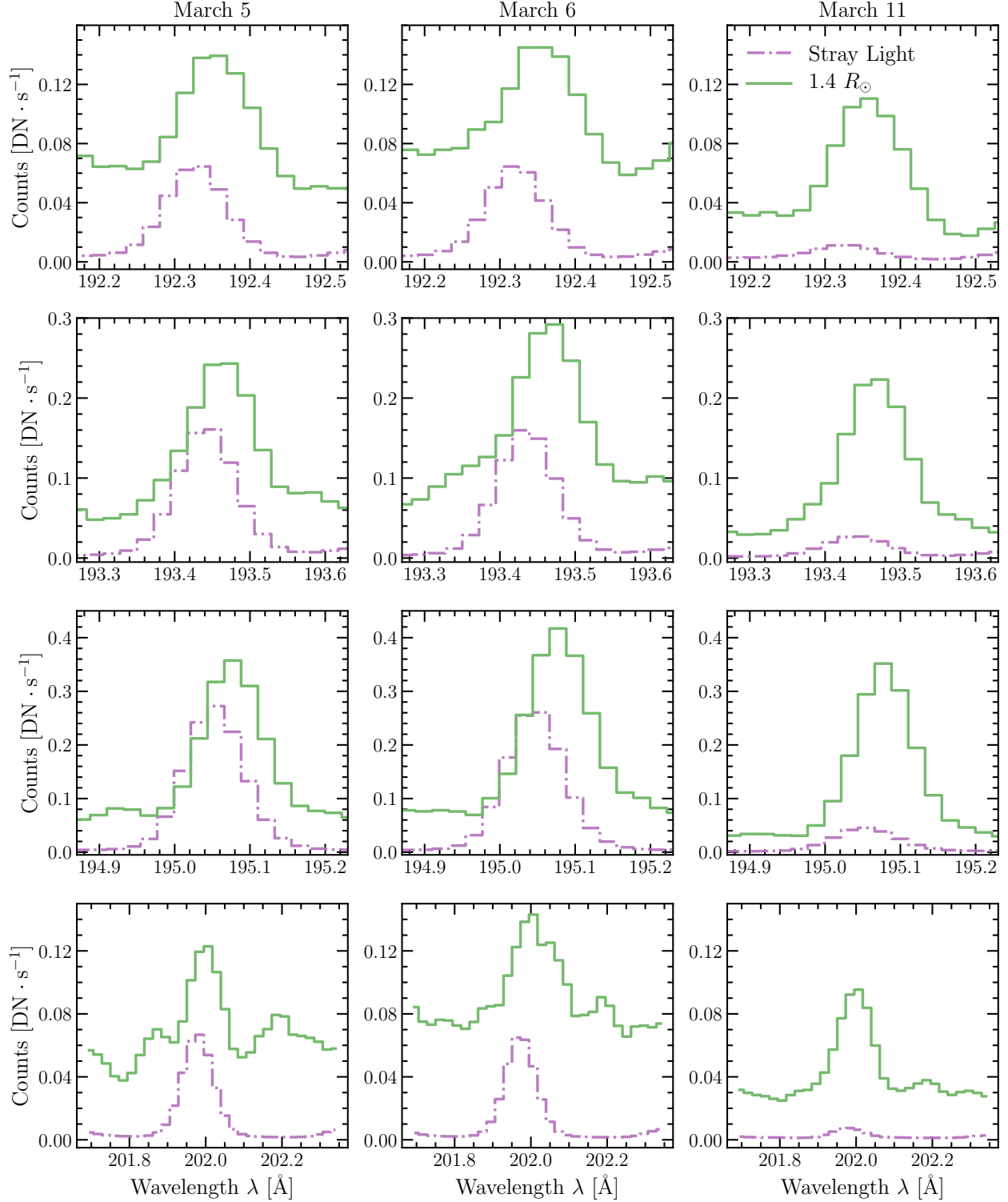


Figure 3.2: 2% stray-light intensity (dot-dashed) of Fe XII and Fe XIII lines vs. off-limb spectrum (solid) at $1.4 R_{\odot}$ on March 5 (left), 6 (middle), and 11 (right). The inferred stray-light contribution on March 11 is much lower than that on March 5 and 6.

where $g(\lambda_i)$ is the double-Gaussian profile determined by the parameters describing the true emission: $I_0, \lambda_0, \Delta\lambda, I_{\text{bg}}$ and the stray-light profile. The σ_i^2 is determined by the Poisson statistical noise and the CCD readout noise. We used a constant prior in the fitting. The uncertainty of each parameter is defined by 90% credible levels.

3.3.4 AWSoM Simulations and Line Synthesis

We ran AWSoM for CR 2107 and forward modeled the Fe XII and Fe XIII profiles in the southern polar CH with the SPECTRUM module. A comprehensive review of AWSoM and SPECTRUM can be found in Section 2.3.1. To obtain plasma parameters for the times of the observation, we used a Global Oscillation Network Group magnetogram (GONG, Harvey et al., 1996) of CR 2107 processed with Air Force Data Assimilative Photospheric flux Transport (Henney et al., 2012) into magnetograms as the radial magnetic field at the inner boundary, while the solar wind initial condition was the Parker solution. Then, we obtained a steady-state solution after 100,000 steps. We extracted the observed plasma parameters into Cartesian boxes covering the region of emission observed by Hinode/EIS to synthesize line profiles using the post-processing version of the SPECTRUM module (Szente et al., 2019).

3.4 Results

We first show three examples of fitting a Fe XII 195 Å line observed at $\sim 1.03, 1.26,$ and $1.49 R_\odot$ assuming a 2% stray-light level in Figure 3.3. The observational uncertainties are too small to be shown in the figure due to the 33,600 s total exposure time and the spatial binning. The inferred integrated intensity I_0 , the line centroid position λ_0 , the FWHM $\Delta\lambda$, and the background intensity I_{bg} are listed in each panel. At $1.03 R_\odot$, the stray-light profile is negligible. At $1.26 R_\odot$, the stray light only contributes a tiny portion of the intensity at the line core and does not significantly affect the line width. At $1.49 R_\odot$, the 2% stray-light intensity is still too low to dominate the off-limb profile. Therefore, we can still fit the off-limb spectrum with two Gaussian components with good precision.

The 2D posterior probability distribution of the four parameters, integrated intensity I_0 , line centroid wavelength λ_0 , FWHM $\Delta\lambda$, and background intensity I_{bg} of the Figure 3.3(b) are shown in Figure 3.4. The fitted FWHM $\Delta\lambda$ shows some correlations between other parameters. The FWHM $\Delta\lambda$ is positively correlated with the total intensity I_0 because the maximum of the Gaussian profile is well determined. Therefore, a greater FWHM $\Delta\lambda$ leads to a higher total intensity I_0 . The correlations between the FWHM $\Delta\lambda$ and the line centroid

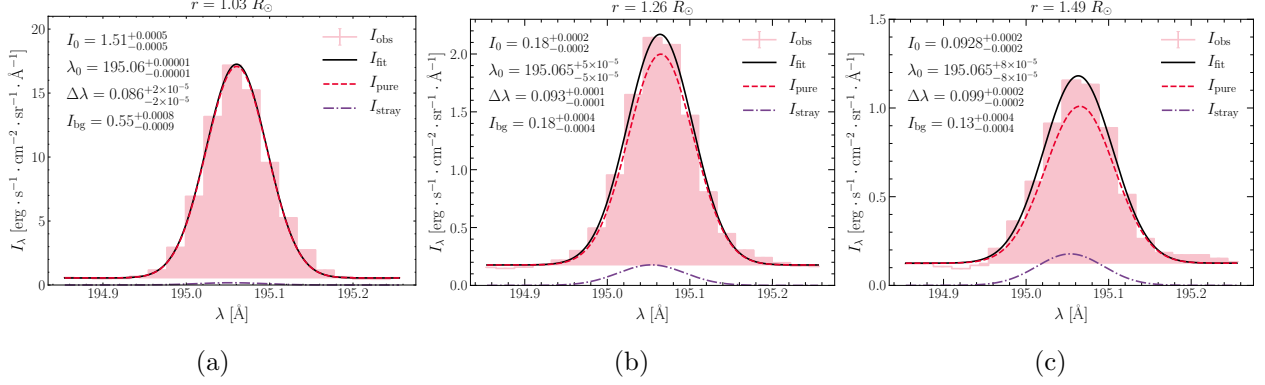


Figure 3.3: Examples of fitting an observed Fe XII 195.1 Å line profile at $\sim 1.03, 1.26,$ and $1.49 R_{\odot}$ assuming a stray-light level of 2%. The pink histogram represents the observed line profiles. The dashed red profiles are the fitted off-limb true emission. The dot-dashed purple lines are the 2% stray-light profile. The solid black lines are the sum of the fitted off-limb spectrum and the stray-light profile. The fitting parameters and their 90% credible levels are listed as well (integrated intensity I_0 , line centroid wavelength λ_0 , FWHM $\Delta\lambda$, and background intensity I_{bg}).

wavelength λ_0 imply the underlying asymmetry in the observed line profile. The FWHM negatively correlates with the background intensity I_{bg} . This is because the far wings can be fit either with a greater line width $\Delta\lambda$ or with a higher background intensity I_{bg} . A higher background level masks the wings and narrows the widths down.

In Figure 3.5, we show the measured FWHMs (instrumental widths subtracted) of the Fe XII 192.4, 193.5, and 195.1 Å and Fe XIII line 202.0 Å lines as a function of height using different stray-light levels with a 16-pixel spatial binning. The FWHMs estimated from the SPECTRUM synthetic spectrum are also shown as a comparison. The undamped line widths at different heliocentric distances assuming $\Delta\lambda \propto n_e^{-1/4}$ are normalized to each measured FWHM curve at around $1.05 R_{\odot}$ for reference, except for the broader Fe XII 195 Å line (see the discussion in Section 3.5.6). We estimated the electron density n_e from two independent line pairs using the CHIANTI database version 9 (Dere et al., 1997a, 2019): (1) the intensity ratio of Fe XII 195.1 and blended 186.9 Å lines, and (2) the intensity ratio of Fe VIII 185.2 and 186.5 Å lines. The inferred electron density below approximately $1.1 R_{\odot}$ was fit by an exponential function and extrapolated to higher altitudes where the rapidly decreasing Fe XII 186.9 Å and Fe VIII line intensities prevented a reliable measurement of the electron density. The density (pressure) scale heights are 75^{+50}_{-20} Mm (Fe XII) and 110^{+100}_{-35} Mm (Fe VIII), which correspond to scale-height temperatures $T \sim 1.6^{+1.0}_{-0.5}$ MK (Fe XII) and $T \sim 2^{+2}_{-0.5}$ MK (Fe VIII) in the hydrostatic case, respectively. The differences in the scale height inferred from the Fe VIII and Fe XII line ratios might be due to the different structures from which the photons are emitted.

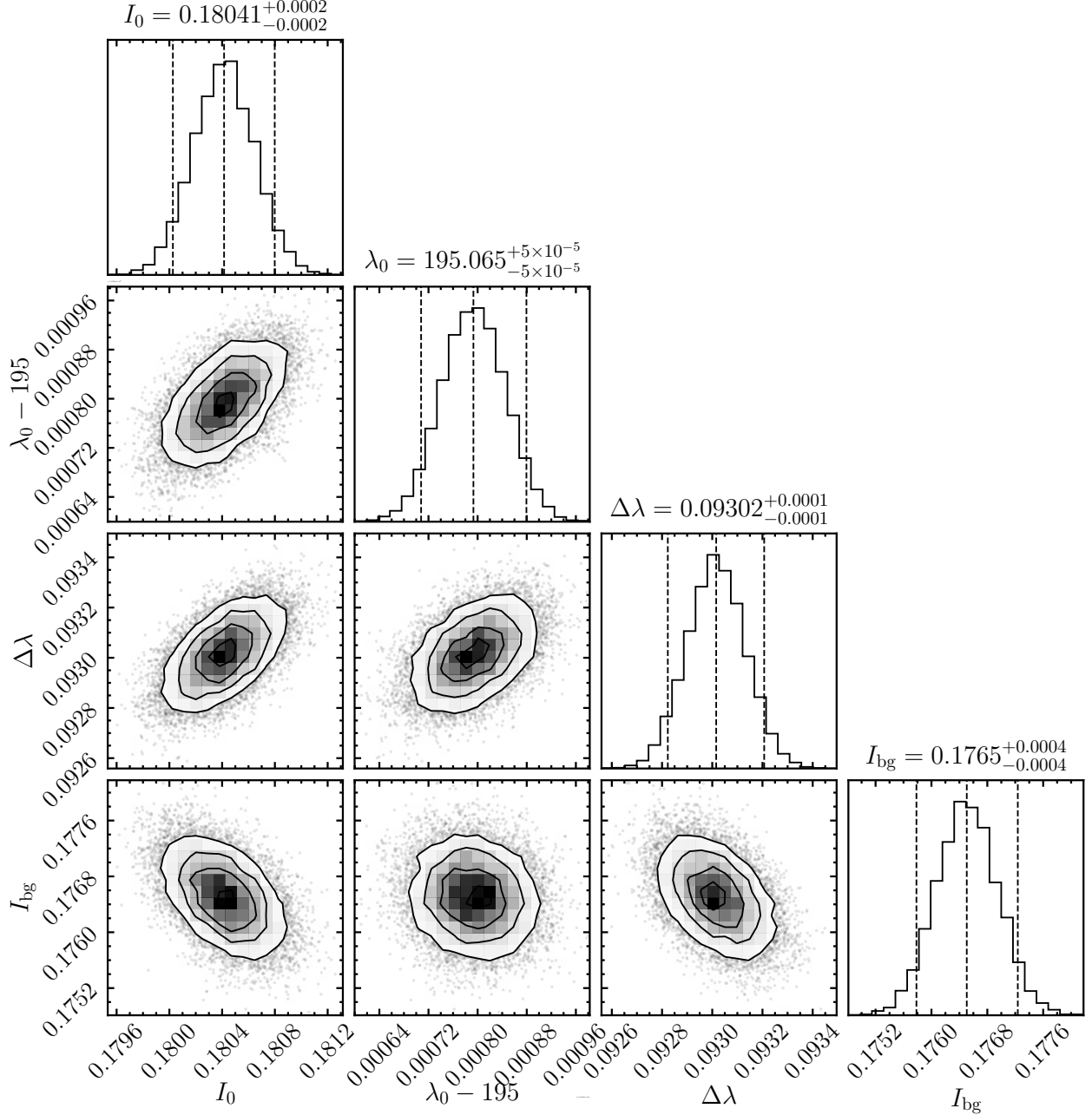


Figure 3.4: A corner plot of the marginalized distribution of the posterior probability sampled by MCMC algorithms from the Fe XII 195 Å line profile in Figure 3.3 (b), corresponding to $1.26 R_{\odot}$: I_0 integrated intensity, λ_0 line centroid wavelength, $\Delta\lambda$ FWHM, and I_{bg} background intensity. The diagonal panels show the 1D distribution of the parameters. The vertical lines in each panel stand for the 5%, 50%, and 95% cumulative probability (i.e., 90% credible levels). The 2D posterior probability distribution between each of the two parameters is shown in the off-diagonal panels. This figure is generated using the python package `corner.py` (Foreman-Mackey, 2016).

Figure 5 shows several different things. First of all, there is no significant evidence showing that line widths start to decrease between $1.2 R_{\odot}$ to $1.5 R_{\odot}$ in all the four strong Fe XII

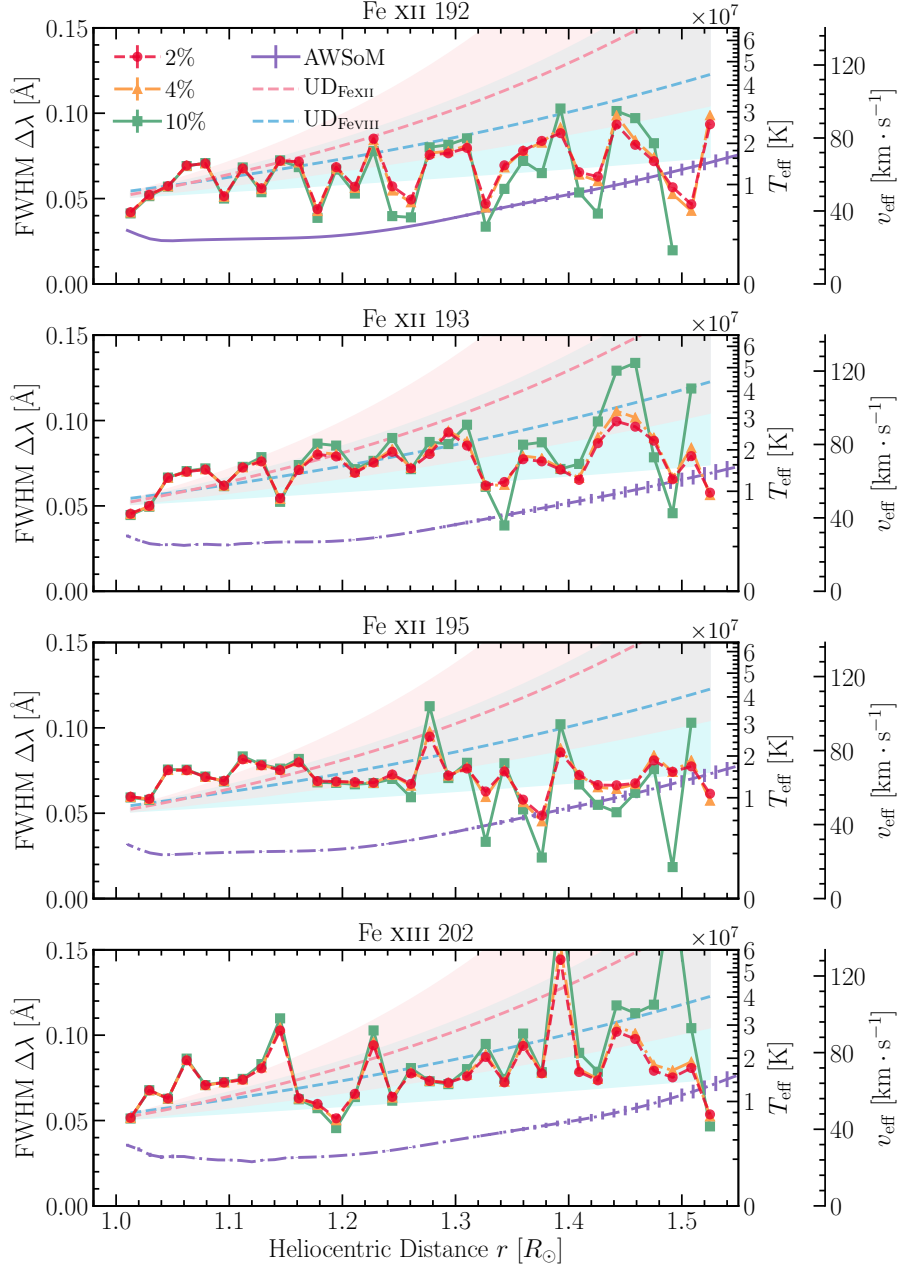


Figure 3.5: The measured FWHMs and the effective temperature or the effective velocity of the Fe XII 192.4, 193.5, and 195.1 \AA and Fe XIII 202.0 \AA lines as a function of heliocentric distance using different stray-light levels. The data were spatially binned in every 16 pixels along the y-axis. The red, yellow, and green lines illustrate the FWHMs fitted using 2%, 4%, and 10% stray-light levels, respectively. The purple lines represent the line widths inferred from the SPECTRUM synthetic spectrum. The line widths caused by undamped (UD) waves are shown in blue and pink curves. The shaded blue and pink area indicates the uncertainty in estimating the undamped widths.

and Fe XIII lines. The line widths of Fe XII 192.4 and 193.5 \AA lines first increase from approximately 0.04 \AA to $\sim 0.06 \text{\AA}$ between ~ 1.0 – $1.05 R_{\odot}$. Then the 192.4 and 193.5 \AA line

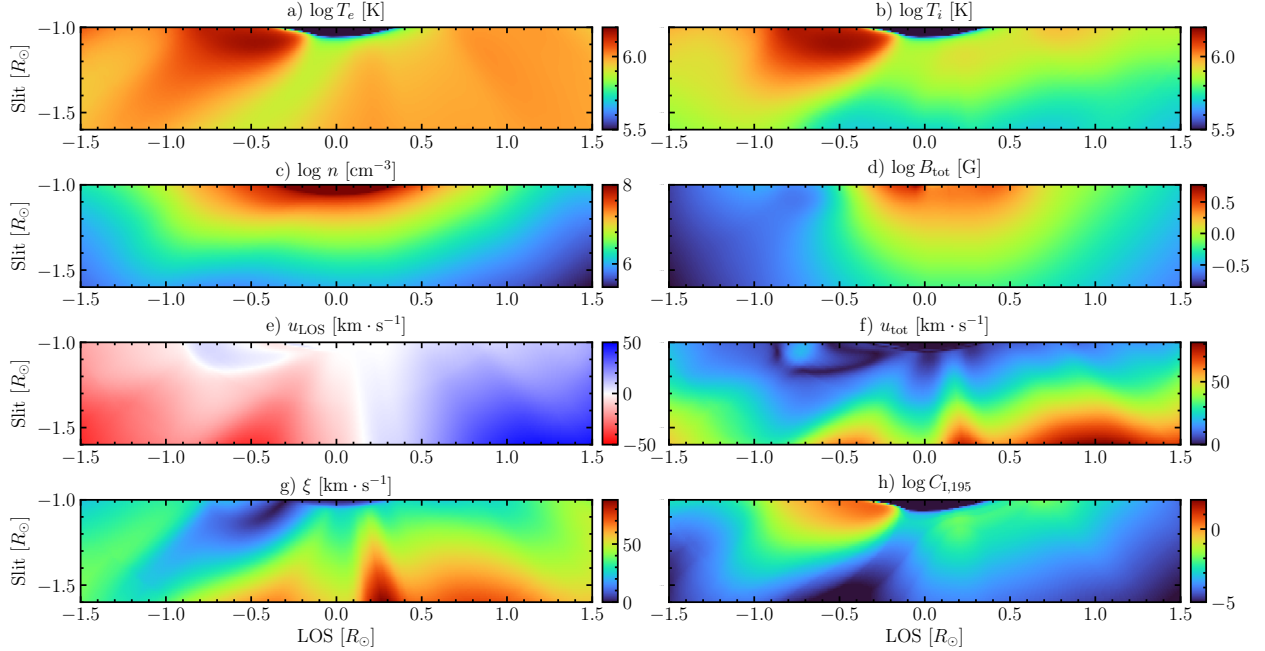


Figure 3.6: Physical quantities in AWSoM outputs in the meridional cuts of the solar corona taken in the plane corresponding to the LOS, perpendicular to the ecliptic: (a) electron temperature T_e ; (b) ion temperature T_i ; (c) particle number density n ; (d) total magnetic field strength B_{tot} ; (e) LOS velocity u_{LOS} ; (f) total velocity u_{tot} ; (g) local LOS nonthermal velocity ξ ; and (h) contribution function of the Fe XII 195 Å line $C_{\text{I},195}$.

widths start to fluctuate between 0.05 and 0.10 Å up to $1.5 R_{\odot}$. The Fe XII 195.1 Å line widths are slightly larger than Fe XII 192.4 and 193.5 Å line below $1.2 R_{\odot}$ by $\sim 0.005\text{--}0.01$ Å. The Fe XII 195.1 Å line widths also continue to rise and fall between $\sim 0.05\text{--}0.1$ Å and we cannot find any systematic decrease in line widths above $1.2 R_{\odot}$. The Fe XIII 202.0 Å line widths vary with height in a similar manner to the Fe XII line widths. At some heights (e.g., $\sim 1.15 R_{\odot}$, $1.4 R_{\odot}$), the Fe XIII 202.0 Å line is extremely broadened, showing widths larger than 0.1 Å. The fluctuations in the FWHMs of the four spectral lines have a spatial period of $\sim 0.05\text{--}0.1 R_{\odot}$ and an amplitude of $\sim 0.01\text{--}0.02$ Å ($\sim 10\text{--}20$ km s $^{-1}$ in effective velocity). Assuming no nonthermal broadenings, the line width measured in the off-limb spectrum corresponds to an effective temperature of more than 10 MK.

Second, different stray-light levels do not affect the fitting results below $1.3 R_{\odot}$ because the stray-light contributions to the total intensity are negligible. The line widths inferred from the 2% and 4% stray-light level are almost identical at all heights. Above $1.3 R_{\odot}$, the line widths measured assuming 10% stray-light level are significantly different from those from the 2% or 4% stray-light level by 0.01–0.05 Å. When there is no significant wavelength shift between the stray light and the observed profile, a higher stray-light level results in a larger

fitted width because the stray-light intensity becomes comparable to or even dominates the total off-limb intensity and maximizes at the line core, so that the core intensity is decreased more than the wing intensity, broadening the line. However, the measured widths in 10% of the stray-light level can sometimes be smaller than the 2% level. This is because the wavelength shift between the stray-light and off-limb profile causes the stray-light removal to affect the portion of the observed line profile to the blue wing more than the one at the red wing, causing an artificial narrowing of the line.

Third, the line widths of the Fe XII and XIII lines measured by EIS are much larger than the synthetic line widths, but are smaller than the normalized undamped widths. The line widths of the AWSoM simulations are $\sim 0.03 \text{ \AA}$ below $1.2 R_{\odot}$, which is $\sim 0.03\text{--}0.04 \text{ \AA}$ smaller than the EIS observations. At larger heights, the AWSoM widths begin to increase monotonically with height, from $\sim 0.02 \text{ \AA}$ to $\sim 0.07 \text{ \AA}$ at $1.6 R_{\odot}$. Neither fluctuation nor decrease in line widths is found in the AWSoM results. The undamped widths inferred from Fe XII line ratios grow more rapidly than the Fe VIII curves because the measured density scale height is smaller. The undamped line widths, especially the Fe VIII curves, are close to the upper limit of the fluctuating EIS widths below $1.4 R_{\odot}$ after which they become larger. The AWSoM widths increase at a slightly lower rate than the undamped waves, which implies that the AWSoM may account for some wave dissipation, but less than the observations indicate.

Figure 3.6 shows the physical quantities of AWSoM simulations in the meridional cuts of the solar corona taken in the plane corresponding to the LOS of the entire EIS slit, perpendicular to the ecliptic. The electron temperature T_e and proton temperature T_i in Figure 3.6 (a) and (b) have similar distributions. A possible streamer is revealed in the temperature plots with an almost identical electron temperature and ion temperature $\log T \sim 6.1$. The ion temperature T_i in the polar CH ($\log T_i \sim 5.9$) is slightly lower than the electron temperature T_e ($\log T_e \sim 6.0$). The particle density in the CH drops from $\log n \sim 8$ to $\log n \sim 6$ from the limb to $1.5 R_{\odot}$. The total magnetic field strength in the polar region is $\sim 1\text{--}3 \text{ G}$. The LOS velocity u_{LOS} shown in Figure 3.6 (e) increases from $\sim 10 \text{ km s}^{-1}$ at the limb to $\sim 50 \text{ km s}^{-1}$ at $1.6 R_{\odot}$. The bulk flow in the streamer at the far side of the Sun is moving toward the observer, unlike the other solar wind flows at the far side. The total velocity u_{tot} also increases from $\sim 20 \text{ km s}^{-1}$ to $\sim 90 \text{ km s}^{-1}$ from the limb to $1.6 R_{\odot}$. Moreover, neither LOS nor total speed in the CH are symmetrically distributed but rather show structures in which the wind acceleration is stronger than in the rest of the CH.

In Figure 3.6 (g), we show the distribution of local nonthermal velocity ξ caused by Alfvén waves. The distribution of the nonthermal velocity ξ reveals similar fine structures along the LOS, including a plume in the CH where the nonthermal velocity is much smaller.

In the streamer, the local nonthermal velocity is only $\sim 10 \text{ km s}^{-1}$ because the local Alfvén wave energy density is low. In the polar CH, the nonthermal velocity ξ is much higher, it increases from $\sim 50 \text{ km s}^{-1}$ to $\sim 100 \text{ km s}^{-1}$, due to the dramatic decrease in particle density with height.

The contribution function of the Fe XII 195.1 Å line is shown in Figure 3.6 h). Compared with the emission from the CH, the streamer makes a large contribution to the Fe XII radiation below $1.2 R_{\odot}$ in the AWSoM simulation because of the higher electron density and an electron temperature that is closer to the maximum abundance temperature of Fe XII.

3.5 Discussion

We compared the Fe XII 192.4, 193.5, and 195.1 Å and Fe XIII 202.0 Å line widths in the southern CH observed by Hinode/EIS with the AWSoM simulations. There is no trend for the measured line widths to decrease above $1.2 R_{\odot}$, which is found in some previous research (e.g., [Bemporad & Abbo, 2012](#); [Hahn et al., 2012](#)) with a large uncertainty on measured line widths. The measured line widths are within the uncertainty of the undamped profiles, which means that the waves might or might not be damped below $1.5 R_{\odot}$. In addition, there is a greater discrepancy between the EIS observations and AWSoM simulations.

Here we discuss a few factors that may cause discrepancies between our observations and the AWSoM simulations or previous measurements.

3.5.1 Streamer Contamination

The presence of a streamer at the far side of the Sun is demonstrated in the meridional cut of the AWSoM simulations in Figure 3.6. To understand how the streamer affects the formation of the monotonically increasing line widths in simulations, we plot the contours of the Fe XII 195.1 Å contribution function normalized to its maximum $C_{I,195}/C_{I,195,\text{max}}$ over the local FWHMs $\Delta\lambda$ along the LOS in the upper left panel of the Figure 3.7. The relative contribution of the Fe XII 195.1 emission from the polar CH or the streamer is shown in the upper right panel. First, the local FWHMs are dominated by nonthermal velocity and increase from $\sim 0.06 \text{ Å}$ to $\sim 0.1 \text{ Å}$ in the CH. Second, photons from the streamer dominate the synthetic profiles with narrower line widths, even up to $1.4 R_{\odot}$.

The middle and lower panel of Figure 3.7 show the LOS distribution of the relative contribution of the Fe XII 195.1 emission per voxel along the LOS (i.e., the local contribution function normalized to the total Fe XII 195.1 Å emergent intensity) and the local FWHM at a heliocentric distance of $1.2 R_{\odot}$ and $1.5 R_{\odot}$. The fitted line widths from the synthetic

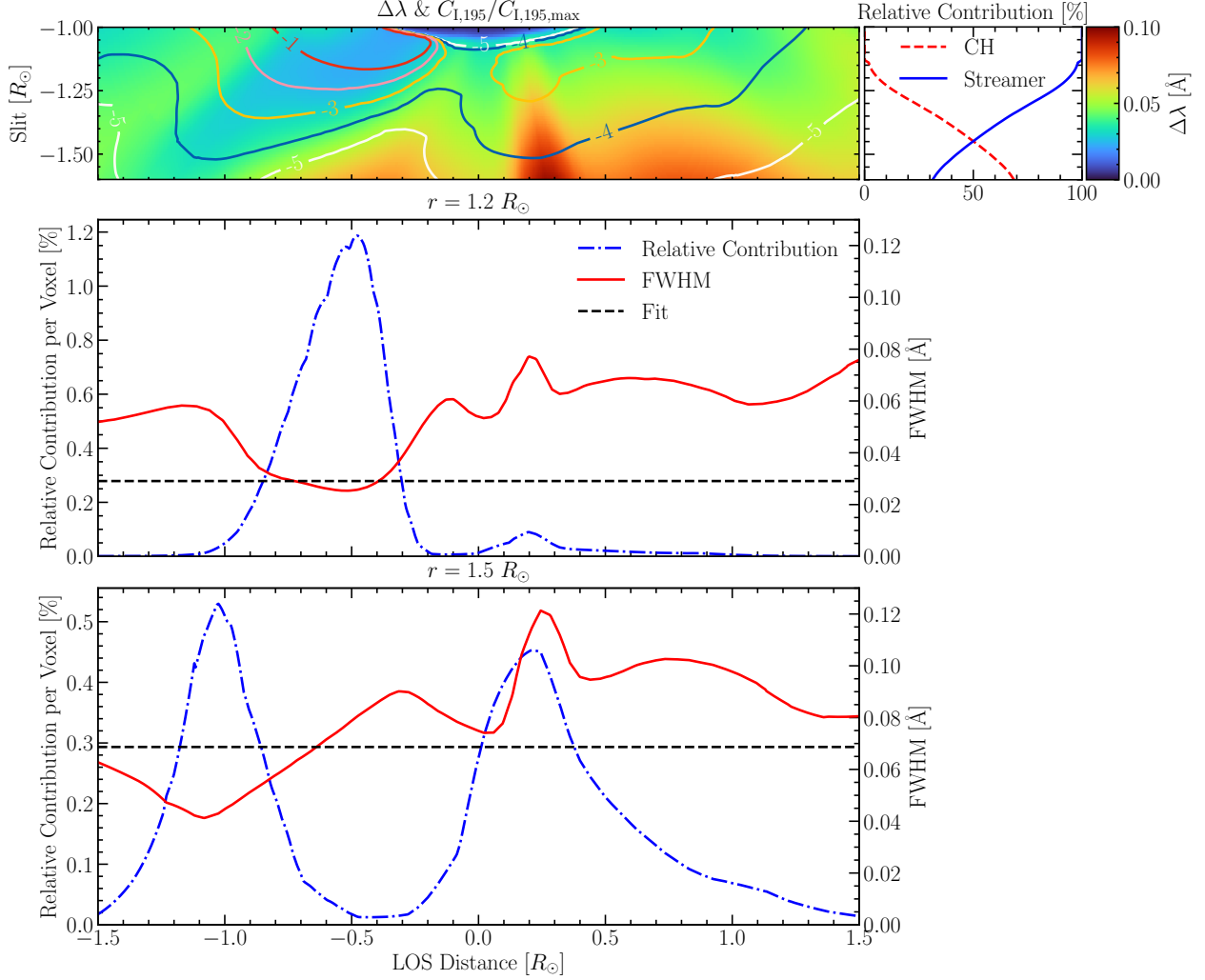


Figure 3.7: (Upper left) Local total FWHM $\Delta\lambda$ distribution in the meridional cut of the AWSoM results. The contours show the levels of the Fe XII 195.1 Å contribution function normalized to its maximum $C_{1,195}/C_{1,195,\max}$. The contour labels are in the logarithmic scale, i.e., -1 means 10^{-1} of the maximum value. (Upper right) Relative contribution of Fe XII 195.1 emission originated from the CH or the streamer at different heights in AWSoM simulations. (Middle) Relative contribution of Fe XII 195.1 emission per voxel along the LOS (dot-dashed blue) and local FWHM distribution along the LOS (solid red) at a heliocentric distance of $1.2 R_{\odot}$. The dashed horizontal line indicates the fitted emergent Fe XII line width at $1.2 R_{\odot}$. (Bottom) The same as the middle panel, but at a heliocentric distance of $1.5 R_{\odot}$.

profiles are also provided as references. The line profiles in the AWSoM simulation are much narrower in the lower corona, e.g., at $1.2 R_{\odot}$, because the SPECTRUM LOS integration causes the streamer emission to provide the bulk of the observed photons. The AWSoM line widths begin to increase with height because the streamer contributes fewer photons in higher altitudes, e.g., $1.5 R_{\odot}$ and the CH FWHMs start to increase with height. So the fitted

line width at $1.5 R_{\odot}$ is $\sim 0.07 \text{ \AA}$, which is much larger than that of $\sim 0.03 \text{ \AA}$ at $1.2 R_{\odot}$.

The AWSoM simulation shows how the streamer photons will likely contaminate the spectrum and result in much narrower line profiles. The simulation also shows how complex the variation of local nonthermal velocity along the LOS is even within CHs, which means that a simple Gaussian fitting may not explain the observed profiles. In addition, AWSoM has a limited spatial resolution and uses a synoptic magnetogram to calculate the inner boundary, which cannot resolve the small-scale effects or structures of the sizes of the FWHM fluctuations. Therefore we cannot use AWSoM to investigate the nature of the FWHM periodic spatial fluctuations in the line widths shown in Figure 3.5.

Based on the AWSoM simulations, we suggest that the Fe XII and Fe XIII emission in the observation is also significantly contaminated by the streamer emission. In addition, the streamer was also observed by SECCHI EUVI (Howard et al., 2008) 195 \AA imaging on board the STEREO-B spacecraft (Kaiser et al., 2008), as both the STEREO spacecraft were in quadrature with Earth and Sun (see Figure 3.8). The fluctuations in the line widths may come from the streamer (also see Singh et al., 2003, Figure 4).

Synthetic line widths are much narrower than the observed ones either because AWSoM underestimates the nonthermal broadening in the streamer or because the observed Fe XII line profiles are less contaminated by the streamer emission than predicted. The possible differences between the variation of FWHM versus height in this study and previous studies (e.g., Bemporad & Abbo, 2012; Hahn et al., 2012) may be due to (1) contamination from the streamer, (2) different wave damping levels in other CHs, and (3) wave-damping levels affected by different phases of the solar cycle.

3.5.2 Ion Temperature in AWSoM

The SPECTRUM module uses the LOS component of the anisotropic proton temperature to evaluate the thermal broadening of the spectral lines in place of the temperature of each ion because the current version of AWSoM does not calculate the temperature of each ion. However, a previous study (e.g., Moran, 2003) suggested that there is no uniform ion temperature in the off-limb corona. The ion temperature could also deviate greatly from the local proton and electron temperatures due to some other heating mechanisms such as ion-cyclotron resonance (e.g., Tu et al., 1998). Landi & Cranmer (2009) measured the Fe XII temperature in the CH between 1.03 and $1.17 R_{\odot}$ and obtained a result of $\log T_i \sim 6.7\text{--}6.95$, which corresponds to a thermal FWHM of $\sim 0.05 \text{ \AA}$. The Fe XII ion temperature in the quiet solar corona is about $\log T = 6.2\text{--}6.6$ (Landi, 2007), which is also higher than the proton temperature used in AWSoM/SPECTRUM simulations.

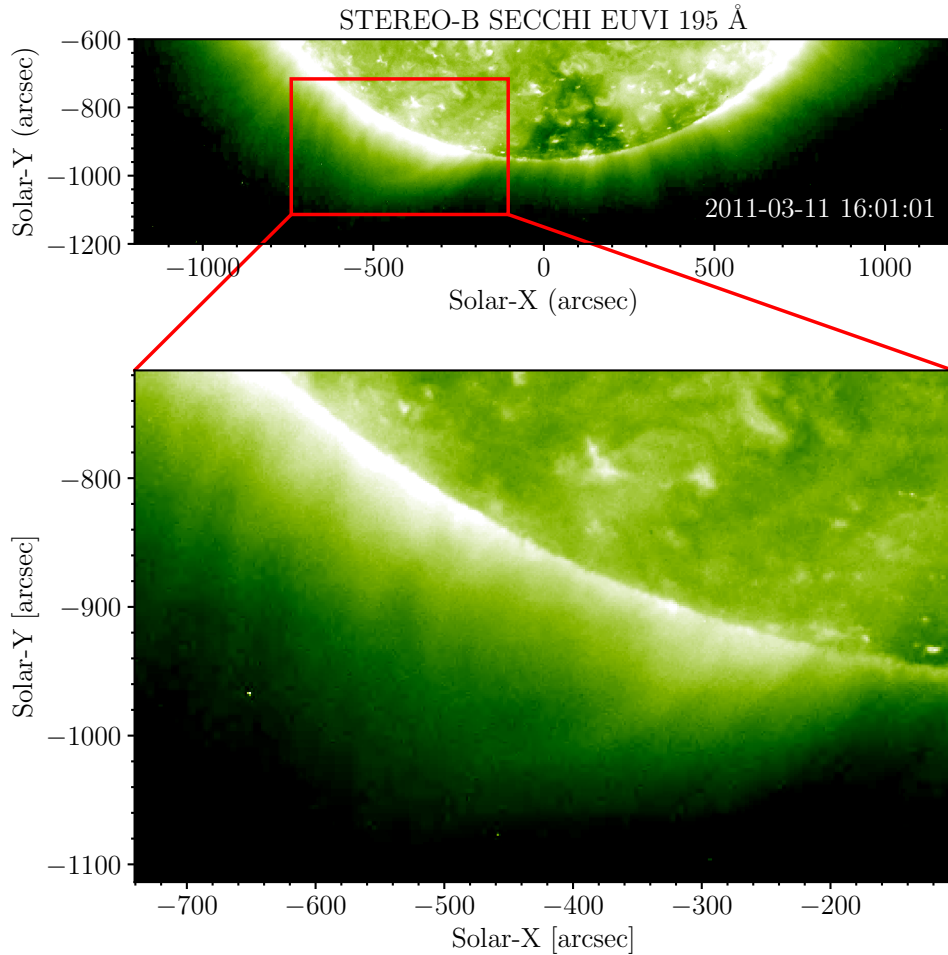


Figure 3.8: SECCHI EUVI 195 Å imaging of the streamer on 2011 March 11, when the STEREO-B spacecraft was in the quadrature with Earth and Sun. The red rectangle in the upper panel outlines the FOV of the lower panel. Note that the intensity in the lower panel has been rescaled.

To investigate the influence of a higher ion temperature on the line broadening, we manually changed the temperatures in the meridional cut, as shown in Figure 3.9 a). We first determined the streamer region using the contribution function of the Fe XII 195 Å line and then arbitrarily assigned a temperature of $\log T = 6.4$ to this region. The ion temperature in the remaining grid is set to be $\log T = 6.8$. Then we resynthesize the Fe XII 195 Å line profiles using the new thermal broadening. We compare the line widths measured from the modified line profiles with those from the current ASoM simulation and EIS observations in Figure 3.9 (b). Because most of the emission in the lower corona comes from the streamer, the line widths only increase by ~ 0.01 Å below $1.35 R_{\odot}$, which is still insufficient to explain the line broadening at lower altitudes. Above $1.4 R_{\odot}$, the increased ion temperatures ($\log T \sim 6.8$) broaden the line profiles by ~ 0.02 Å, which causes the synthetic widths to

become much closer to the EIS observations. We must stress that these results come from a crude and arbitrary approximation of the real ion temperatures. Nevertheless, they point toward an important parameter that could be responsible for the disagreement between the measured and observed FWHM values. Still, while the much higher ion temperature may account for the widths at heights where the streamer is absent, it cannot reproduce the widths where the streamer dominates the emission.

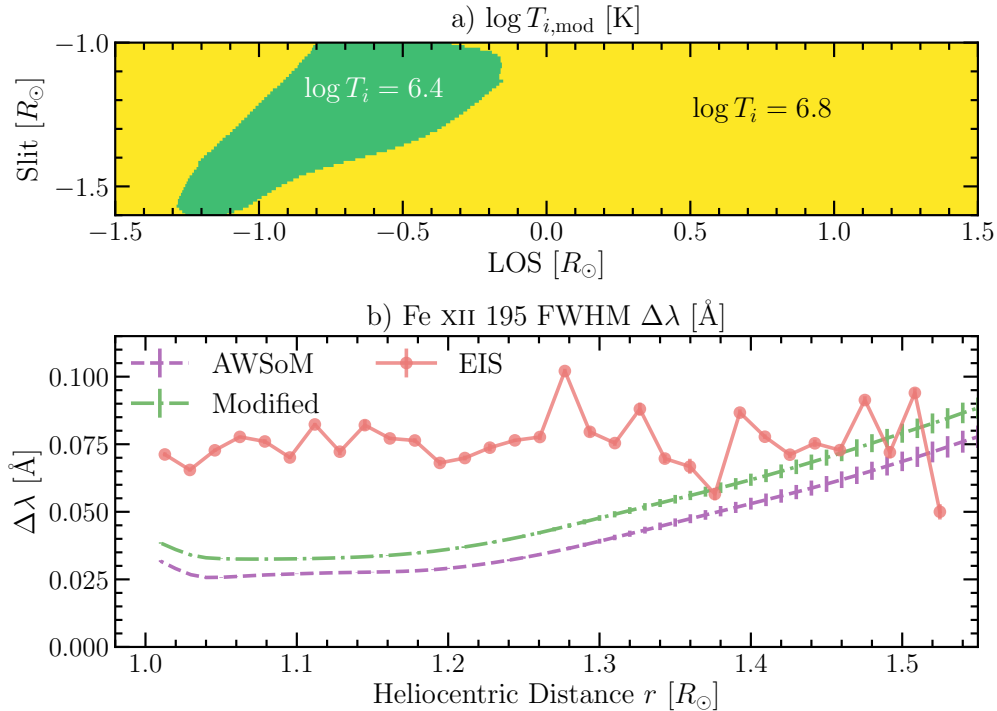


Figure 3.9: (a) Modified Fe XII ion temperature distribution in the meridional cut of the solar corona taken in the plane corresponding to the LOS, where the green region stands for the streamer and the yellow region is treated as the CH. (b) Fe XII 195 Å line widths synthesized from the modified Fe XII ion temperature compared with the current AWPSoM simulation and EIS observations.

3.5.3 Spatial Binning and FOV

Previous studies have used large spatial binning, usually more than 30 pixels, to increase the S/N and obtain Gaussian profiles to fit. Because our observations have an extremely long exposure time of 33,600 s, we fitted the line profiles with different spatial binnings every 2, 4, 8, 16, and 32 pixels. The results are shown in Figure 3.10. Smaller spatial binnings like 2 or 4 pixels provide a larger uncertainty as well as more fluctuating FWHMs. An 8- or 16-pixel binning removes the smallest-scale fluctuations due to a strong noise reduction, but it maintains variations at the 0.05–0.1 R_{\odot} level, making them significant. However, the 32-pixel

binning is so large that it smooths these fluctuating fine structures without improving the uncertainty. Therefore we suggest that the fluctuations may not be found in previous studies due to the large spatial binning, even if the emission is contaminated by other structures.

3.5.4 Stray-light Level

The measured line centroid wavelengths from EIS observations and AWSoM simulations are shown in Figure 3.11. By choosing different stray-light levels, we show that a larger stray-light component may result in a larger FWHM. Most of the previous studies used the 2% stray-light level obtained from Ugarte-Urra (2010a). However, the wavelength offset between the stray light might be due to the real Doppler shifts in the solar wind flows. In this case, it is possible that the stray light does not dominate the off-limb spectrum at $1.5 R_{\odot}$, because otherwise, the off-limb profiles should have the same line centroid wavelength as the stray light. The line centroids in AWSoM simulations are first blueshifted because of the bulk motion in the streamer toward the observer. The AWSoM line centroid wavelength increases by $\sim 0.01 \text{ \AA}$ at higher altitudes because the photons are increasingly emitted by the redshifted and blueshifted flows from the solar wind, and less from the blue-shifted streamer. Because shifts of the AWSoM line centroid show a similar trend as EIS observations, we suggest that the stray light does not significantly affect the line profiles, even at $1.5 R_{\odot}$. Moreover, the 10% stray light would make the redshift even larger and the line widths artificially narrower at large heights, so it is likely an overestimation. After all, the off-disk configuration of the EIS slit in our observation is much more similar to that of the eclipse configuration from Ugarte-Urra (2010a) than the full-disk configuration of Wendeln & Landi (2018). Therefore, estimating the stray-light fraction of 2%-4% may be sufficient in this study.

3.5.5 Photoexcitation

The Fe XII 192.4, 193.5, and 195.1 \AA line ratios may be sensitive to photoexcitation at large heights, where collisional excitation is less efficient and self-absorption of Fe XII emission coming from a lower altitude, brighter area could contribute to populating the parent 4P levels. In this case, their ratios should be dependent on height. We show the intensity ratios of each two of the three lines in Figure 3.12 as a function of height using two different radiometric calibration methods: those of Del Zanna (2013) and of Warren et al. (2014). The reference values given by CHIANTI are also plotted. The line ratios do not vary significantly below $1.2 R_{\odot}$. The ratio of the Fe XII 192.4 and 195.1 \AA lines and the ratio of the Fe XII 193.5 and 195.1 \AA lines increase with height, while the Fe XII 192.4 and 193.5 \AA line ratios do not show significant variations. Hahn et al. (2012) calculated the line ratios, but found no

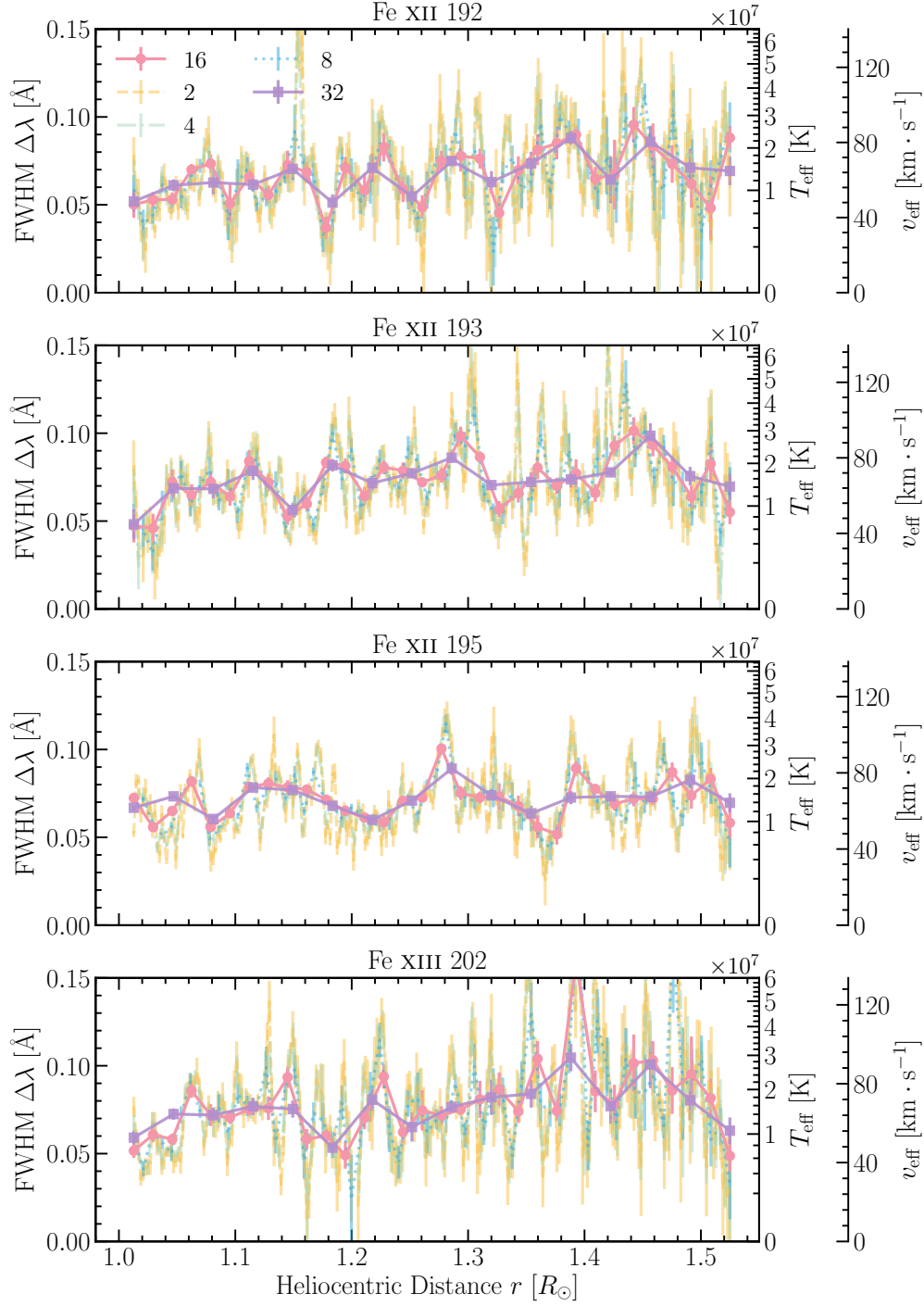


Figure 3.10: FWHMs of Fe XII 192.4, 193.5, and 195.1 Å and Fe XIII 202.0 Å measured by different spatial binnings: every 2, 4, 8, 16, and 32 pixels along the slit using a 2% stray-light level. In order to save the computation time, the line profiles used in this figure are fit using a maximum likelihood optimization method. The error bars in this figure are from the diagonal components of the covariance metrics.

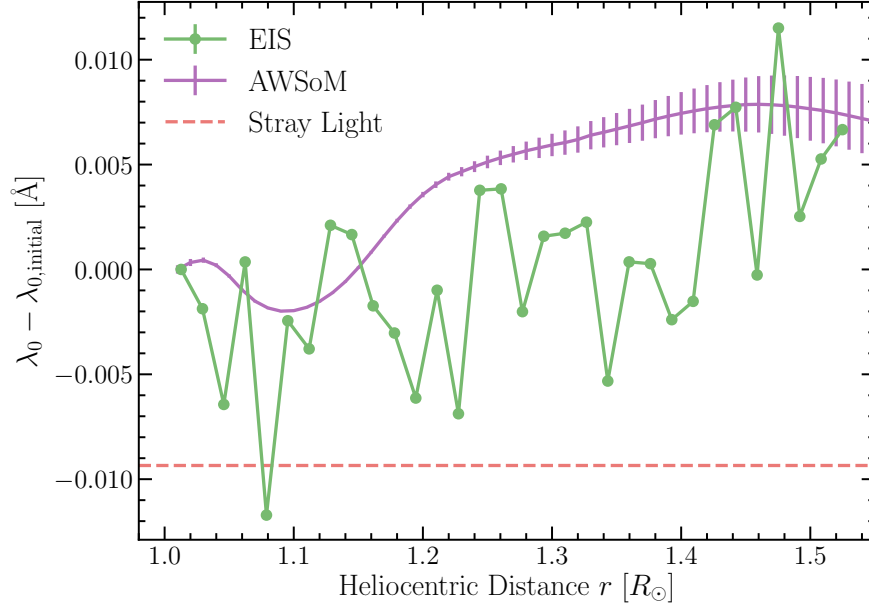


Figure 3.11: The variation in the Fe XII 195 Å line centroid wavelengths λ_0 as a function of height measured from EIS observations and AWSoM simulations. We show the differences between the line centroid wavelengths λ_0 and the line centroid wavelength $\lambda_{0,\text{initial}}$ of the pixel closest to the limb. The horizontal line indicates the line centroid wavelength of the fitted stray-light profile.

notable changes at different heights. Because these ratios are independent of temperature and density, different structures along the LOS should not alter the ratios. Moreover, if photoexcitation were active, the brightest line (i.e., Fe XII 195 Å) should become brighter with the height relative to the others, so that the ratios should decrease rather than increase. The systematic increase in the Fe XII 192/195 and 193/195 line ratios may not result from photoexcitation, but may be caused by other instrumental and physical effects.

3.5.6 Instrumental Effect

Ideally, the Fe XII triplets should have identical line widths at any given height. However, in EIS observations, the Fe XII 195.12 Å line is always broader than the other two. The differences in the Fe XII triplet line widths along the slit measured in this study are shown in Figure 3.13. We note that below $1.2 R_\odot$ (corresponding to CCD pixel $\sim 300\text{-}500$), the Fe XII 195.1 Å line is broader than the other two lines.

Hara (2019) suggested that another weaker Fe XII line at 195.18 Å may blend with the Fe XII 195.12 Å line and broaden the profile. The Fe XII 195.18 Å line was found in laboratory spectra (Arthanayaka et al., 2020), although some previous experiments did not resolve the line (e.g., Träbert et al., 2014). We used CHIANTI to calculate the intensity ratio of these

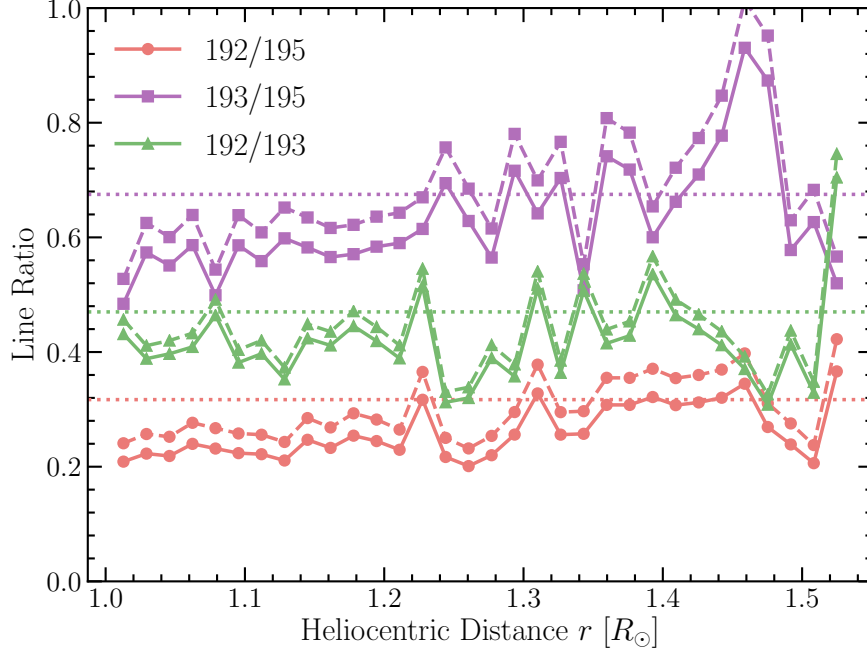


Figure 3.12: Fe XII 192.4, 193.5 and 195.1 Å line intensity ratios at different height using different radiometric calibration method: Warren et al. (2014) (solid) and Del Zanna (2013) (dashed). The dotted horizontal lines indicate the reference values given by the CHIANTI database.

two lines and found that the intensity of the suggested blended line is about 2% of the Fe XII 195.12 Å intensity in the streamer condition ($\log n_e \sim 8.5$, measured from the Fe XII 195.12 to 186.86 ratio). Young et al. (2009) measured the ratio of the two blended lines by double-Gaussian fitting and showed that the Fe XII 195.18 to 195.12 ratio is about 5% when $\log n_e < 9$. We also attempted to fit the Fe XII 195.12 Å line double-Gaussian profiles, but we found the fitted Fe XII 195.12 Å width only narrows by 0.007 Å, which is insufficient to explain the maximum discrepancy by ~ 0.02 Å between the widths of Fe XII 195.12 and 192.39. Furthermore, the fitted Fe XII 195.18 intensity is more than 10% of the Fe XII 195.12 intensity, which disagrees with the density measurements. The inconsistency may be caused by the LOS integration because Young et al. (2009) used on-disk observations of an active region, or some other factors.

In a recent study of EIS line widths in the quiet solar corona, Del Zanna et al. (2019) suggested that the anomalous widths of the strongest Fe XII 193.5 Å and 195.1 Å line are due to instrumental reasons. They questioned whether firm conclusions could be obtained because of the uncertainties on the instrumental broadening described in Young (2011b). Our results show similar patterns in the difference of the FWHMs of Fe XII measured by Del Zanna et al. (2019, see Figure 2) in 2006, but with larger standard deviations. Therefore we cannot exclude the existence of instrumental broadening that depends not only on the

position along the slit, but also on wavelength.

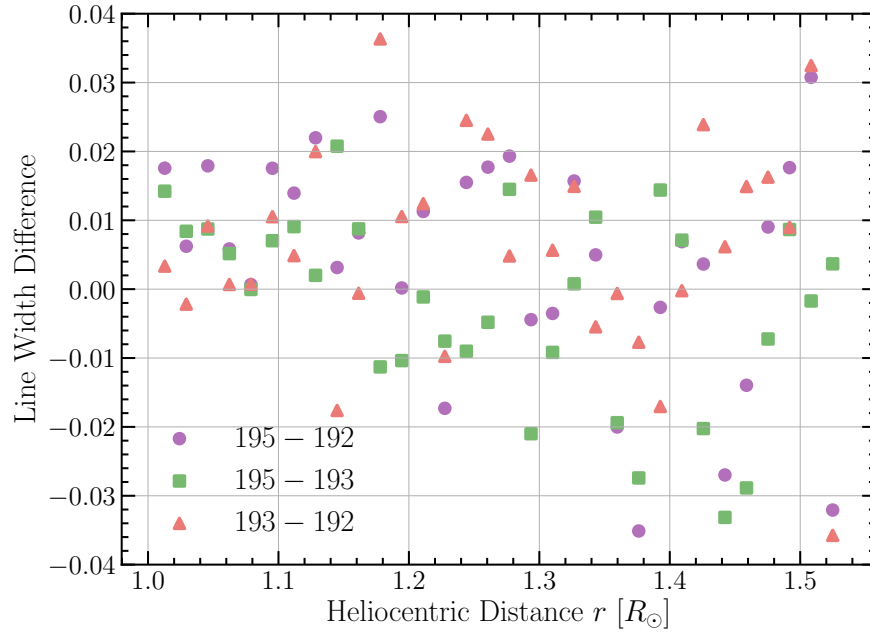


Figure 3.13: The difference between the FWHM of the Fe XII 192.4, 193.5, and 195.1 Å lines at different heights.

CHAPTER 4

Ion Temperature in Coronal Holes

4.1 Preface

The materials present in this chapter have been published in the *Astrophysical Journal*, 948, 90 (Zhu et al., 2023). The paper is co-authored by Judit Szente and Enrico Landi.

4.2 Introduction

The thermal widths of spectral lines reflect the temperature of heavy ions in the solar corona, which is a pivotal prediction for several coronal heating models such as the ion-cyclotron resonance (also see Sections 1.2.4.3 and 1.3). Nevertheless, the presence of nonthermal broadening poses challenges to separate the thermal widths in practice. Besides, the line-of-sight (LOS) integration of the optically thin emission from the solar wind can also affect the observed line widths above the coronal hole (e.g., Akinari, 2007; Gilly & Cranmer, 2020).

This chapter details the investigation of the dependence of T_i on Z/A in the polar coronal hole, which is predicted to be highly associated by ion-cyclotron heating models. To have better Z/A coverage and a comparison between different instruments, we used a coordinated observation by SOHO/SUMER and Hinode/EIS. Because these two instruments cover different wavelengths and observe ions with different Z/A . We used the method proposed by Tu et al. (1998) to separate the thermal and nonthermal widths, which only assumes all ions have the same nonthermal velocity. Furthermore, we performed the global magnetohydrodynamic (MHD) simulation to validate the method and study the LOS integration effect. We describe the data reduction and analysis and MHD simulation in Section 4.3. Section 4.4 shows the measured ion temperatures T_i versus Z/A and compares the observed and synthetic profiles. We discuss the factors affecting our diagnostics in Section 4.5.

4.3 Methodology

4.3.1 Observation and Data Reduction

On 2007 November 16, SOHO/SUMER and Hinode/EIS made a coordinated observation of the off-limb coronal hole boundary region at the north pole (see Figure 4.1). SUMER observed this region from 09:01 UT to 10:03 UT. The center of the $4'' \times 300''$ SUMER slit 1 was pointed to $(230'', 1120'')$, which covers the off-limb plasma from around 1.01 to $1.32 R_{\odot}$. SUMER detector B recorded the solar UV spectrum in four 45 \AA wide spectrum windows. The four windows covered first-order wavelengths of 672–717 \AA , 746–791 \AA , 1015–1060 \AA , and 1210–1255 \AA . SUMER made three consecutive 300 s exposures in each window.

EIS observed this coronal hole from 07:26 UT to 08:01 UT in EUV from 170 to 210 \AA (short wavelength, SW) and 245 to 290 \AA (long wavelength, LW). The center of the EIS $2'' \times 512''$ slit was pointed to $850''$ in Solar-Y. In the x direction, EIS performed a seven-step raster scan from $232''.5$ to $246''.5$. The off-limb portion of the EIS slit covered the coronal hole plasma from about 1.00 to $1.15 R_{\odot}$ (depending on the wavelength due to the tilt of the EIS grating and spatial offset between two EIS CCDs). EIS and SUMER have a spatial resolution of $1''$ along the slit. We note that [Hahn et al. \(2010\)](#) used the same EIS data set to study the ion temperature in the polar coronal hole, but we processed the EIS data with the latest EIS calibrations that were not available back then.

We corrected and calibrated the SUMER and EIS data following the standard procedures described in the SUMER Data Cookbook ([Schühle, 2014](#)) and the EIS software notes (see Sections 2.1.1 and 2.1.2).

We coaligned the SUMER and EIS observations using the EUV images taken by SOHO/EIT in two steps: (1) We coaligned EIT and EIS by comparing the on-disk features in the EIT 195 \AA image and the EIS SW spectrum filtered by the effective area of the EIT 195 \AA quadrant. (2) We empirically coaligned SUMER and EIS by comparing the slope of the O VI 184.1 \AA (EIS) and 1031.9 \AA (SUMER) intensities along the slit. No coalignment in the east–west direction was performed between the EIS and SUMER data. The uncertainty of the coalignment between EIT and EIS is less than $5''$ (EIT pixel size) since the features on the disk are well matched. However, since the off-limb SUMER images do not contain any features (e.g., limb brightening), the coaligned EIS and SUMER images might have a residual offset up to $10''$ to $15''$ in the north–south direction.

Finally, to maximize the number of observed ions, we averaged intensities of the 30 pixels (blue line in Figure 4.1) between 1.01 and 1.04 solar radii for further analysis. Since this region is very close to the limb where the stray light does not significantly affect the fitting of the line width (see Appendix A), no stray-light correction is implemented to the EIS or

SUMER data.

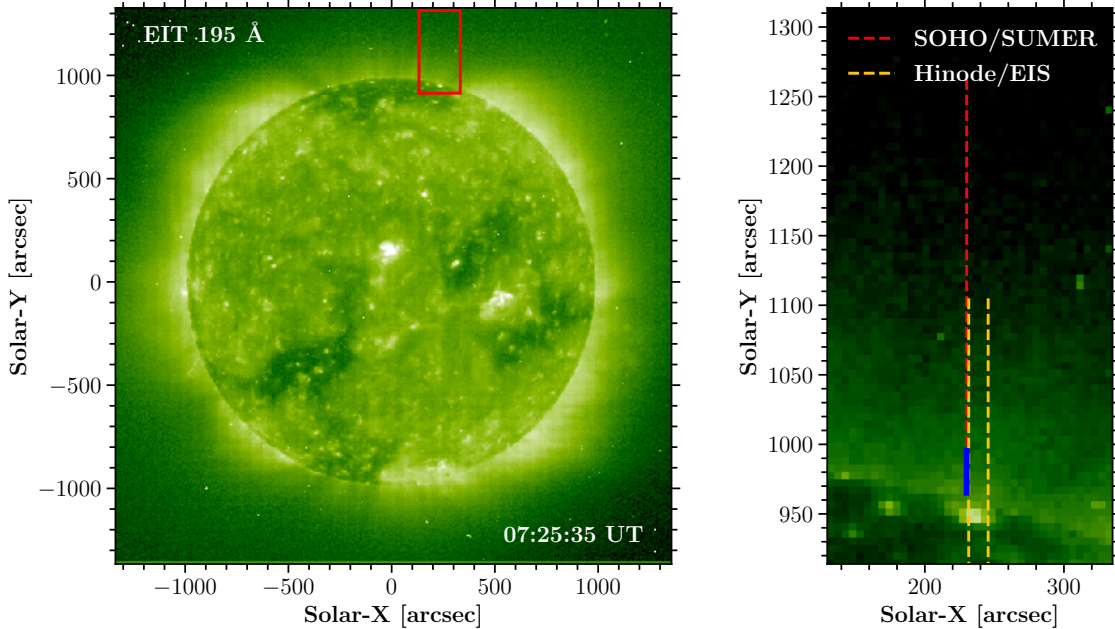


Figure 4.1: Positions of SUMER and EIS slits on the EIT 195 context image. **Left:** EIT 195 image of the full solar disk on 2007 November 16 at 07:25:35 UT. The red rectangle displays the FOV of the right panel. **Right:** slit pointing at the coronal hole boundary. The red dashed line shows the location of the 300'' slit of SUMER. The yellow dashed lines show the first and the last pointing location of the EIS slit during the seven-step raster. The solid blue line shows the region of the data analyzed in this paper. Link to the [Jupyter notebook](#) creating this figure: [🔗](#).

4.3.2 Data Fitting

We performed the single/multi-Gaussian fitting to the unblended/blended spectral lines, using a constant background I_{bg} . Each Gaussian profile is described by the total intensity $I_{\text{tot},i}$, the wavelength of the line centroid $\lambda_{0,i}$, and the FWHM $\Delta\lambda_i$, i.e., the fitting model I_{model} can be written as

$$I_{\text{model}}(\lambda) = \sqrt{\frac{4 \ln 2}{\pi}} \sum_{i=1}^m \frac{I_{\text{tot},i}}{\Delta\lambda_i} \exp \left[-\frac{(\lambda - \lambda_{0,i})^2}{\Delta\lambda_i^2/4 \ln 2} \right] + I_{\text{bg}} \quad (4.1)$$

where m is the total number of spectral lines to be fitted. We used χ^2 minimization to fit the complicated blended spectral lines.

To better estimate the fitting uncertainty in the single-Gaussian fitting, we adopted the Monte Carlo analysis (Hahn et al., 2012) in the following steps: (1) We fit the unblended spectral line by simple χ^2 minimization using the original uncertainty. (2) We reassigned the

uncertainty of the intensity σ_I to be the larger of the fitting residual or the original uncertainty. (3) We added noise to the observed intensities generated from a normal distribution $\mathcal{N}(\mu = 0, \sigma^2 = \sigma_I^2)$ and then fit the spectrum with additional noise. (4) We repeated step (3) 10,000 times and calculated the standard deviations of the fitting results as the fitting uncertainty.

We corrected the EIS line width according to the formula

$$\Delta\lambda_{\text{true}} = (\Delta\lambda_{\text{fit}}^2 - \Delta\lambda_{\text{inst}}^2)^{1/2} \quad (4.2)$$

where $\Delta\lambda_{\text{fit}}$ is the fitted FWHM and $\Delta\lambda_{\text{inst}}$ is the EIS instrumental widths given by [Young \(2011b\)](#). The instrumental width $\Delta\lambda_{\text{inst}}$ of SUMER is removed directly by the IDL routine `con_width_funct_4` using deconvolution lookup tables based on measurements of [Chae et al. \(1998\)](#).

4.3.3 Ion Temperature Estimation

The information about ion temperatures in the solar corona is embedded in spectral line widths $\Delta\lambda_{\text{true}}$:

$$\Delta\lambda_{\text{true}} = \left[4 \ln 2 \left(\frac{\lambda_0}{c} \right)^2 \left(\frac{2k_B T_i}{m_i} + \xi^2 \right) \right]^{1/2} \quad (4.3)$$

where c is the speed of light, k_B is the Boltzmann constant, T_i stands for the LOS ion temperature, m_i is the mass of the ion, and ξ is the nonthermal velocity. In observations, ξ might be contributed by the propagation of Alfvén waves and other unresolved bulk motion along the LOS. As λ_0 is well determined, we can obtain the effective LOS velocity v_{eff} from the width of each fitted spectral line:

$$v_{\text{eff}} = \left(\frac{2k_B T_i}{m_i} + \xi^2 \right)^{1/2} \quad (4.4)$$

The effective velocities v_{eff} of the lines originating from the same ion should be identical unless the lines of the same ion have very different excitation energies, which might cause the lines to form at different positions along the LOS. Therefore, to use multiple fitted lines from the same ion, we calculated the weighted average \bar{v}_{eff} of the effective velocity v_{eff} from k spectral lines that have high signal-to-noise ratio (S/N) and small fitting uncertainties:

$$\bar{v}_{\text{eff}} = \frac{\sum_{i=1}^k w_i v_{\text{eff},i}}{\sum_{i=1}^k w_i} \quad (4.5)$$

where the weight is inversely proportional to the square of its uncertainty $w_i = 1/\sigma_{v,i}^2$. The uncertainty of the weighted average $\sigma_{\bar{v}}$ is given by [Bevington & Robinson \(2003\)](#)

$$\sigma_{\bar{v}} = \sqrt{\frac{1}{k-1} \left(\frac{\sum_{i=1}^k w_i v_{\text{eff},i}^2}{\sum_{i=1}^k w_i} - \bar{v}_{\text{eff}}^2 \right)} \quad (4.6)$$

In this way, multiple spectral lines provide a single v_{eff} measurement for each ion, which avoids confusion.

We estimated the limits of ion temperatures T_i from the averaged effective velocities \bar{v}_{eff} using the method proposed by [Tu et al. \(1998\)](#). This method assumes that the nonthermal velocity ξ is the same for all ions. To estimate the upper limit, we assumed that the line profiles are dominated by thermal broadening, i.e., $\xi = 0$, therefore,

$$T_{i,\text{max}} = \frac{m_i}{2k_B} \bar{v}_{\text{eff}}^2 \quad (4.7)$$

To obtain the lower limit $T_{i,\text{min}}$, we first set the upper limit of the nonthermal velocity ξ_{max} to be the smallest effective velocity \bar{v}_{eff} among all lines. Then, we removed ξ_{max} from all \bar{v}_{eff} to calculate $T_{i,\text{min}}$

$$T_{i,\text{min}} = \frac{m_i}{2k_B} (\bar{v}_{\text{eff}}^2 - \xi_{\text{max}}^2) \quad (4.8)$$

We note that the interval $[T_{i,\text{min}}, T_{i,\text{max}}]$ should not be interpreted as an uncertainty but as a range of equally likely values. We propagated the uncertainty in the average effective velocity \bar{v}_{eff} to the uncertainty of each $T_{i,\text{max}}$ and $T_{i,\text{min}}$.

Given the uncertainties in the instrumental width, we carried out the T_i diagnostics for SUMER and EIS lines separately, so that the ions observed by the two instruments had an EIS measurement and a SUMER measurement.

4.3.4 Electron Density and Temperature Diagnostics

We measured the electron density n_e and temperature T_e at the coronal hole boundary using the intensity ratios of the two lines originating from the same ion. The measured T_e would be compared with T_i to study the preferential heating of heavy ions. We listed the lines used for n_e and T_e diagnostics in Tables 4.1 and 4.2. We assumed that the plasma along the LOS is nearly homogeneous in density and isothermal and used the latest CHIANTI 10 atomic database ([Dere et al., 1997a](#); [Del Zanna et al., 2021](#)).

Besides the fitting uncertainty, the radiometric calibration might also affect the precision of electron density and temperature diagnostics. The SUMER radiometric calibration has

an absolute uncertainty of 36% in detector B (Pauluhn et al., 2001) after the SOHO recovery in 1998. Although the ratios of two lines might have a smaller uncertainty, we conservatively use those values. EIS has two competing in-flight radiometric corrections to the laboratory calibration proposed by Del Zanna (2013) (GDZ) and Warren et al. (2014) (HPW). The two methods show different detector responses in the SW and LW detectors. We show the variation of two correction factors versus wavelength and the wavelengths of the spectral lines used for diagnostics in Figure 4.2. The two correction curves are similar, but the GDZ curve has more small bumps. For example, the increase in the GDZ correction factor around 188 Å makes the Fe VIII 185.213/186.598 Å ratio 10% smaller than the HPW ratio. The difference in the absolute LW detector calibration affects most EIS ratios used to measure the electron temperature.

We applied the two corrections to EIS line intensities to investigate their differences. The exception is the Fe IX 188/189 Å ratio because the two lines are very close on the detector. Another exception is the Mg IX 706 Å line observed by SUMER, located at the boundary of the coated and bare part of the detector. Although the KBr and bare responsivities at ~ 700 Å are very similar, we still measured the electron density and temperature assuming that the entire Mg IX 706 Å line is recorded in the KBr or bare parts.

Ion	$\log T_{\max}$ (K)	Wavelength (Å)	Instrument
Fe VIII	5.75	185.213/186.598	EIS
Mg VII	5.80	276.154/280.742	EIS
Fe IX	5.85	188.493/189.935	EIS
Mg IX	5.95	694.006/706.060	SUMER
Si X	6.00	258.374/261.056	EIS
Fe XI	6.00	182.167/(188.216+188.299)	EIS
Fe XII	6.05	(186.854+186.887)/195.119	EIS

Table 4.1: Spectral lines ratios used for electron density diagnostics. T_{\max} is the temperature of the maximum line formation calculated by CHIANTI using the DEM derived from the average coronal hole spectra in Vernazza & Reeves (1978).

4.3.5 AWSoM-R Simulation

We used the MHD simulation to study the LOS integration effect, including the line formation regions and macroscopic Doppler broadening due to the bulk motions. We simulated the global solar corona and synthesized line profiles at the coronal hole boundary with the AWSoM-R model and the postprocessing tool SPECTRUM. AWSoM-R avoids the artificial stretching of the transition region (Lionello et al., 2001) in AWSoM using the TFLM, which

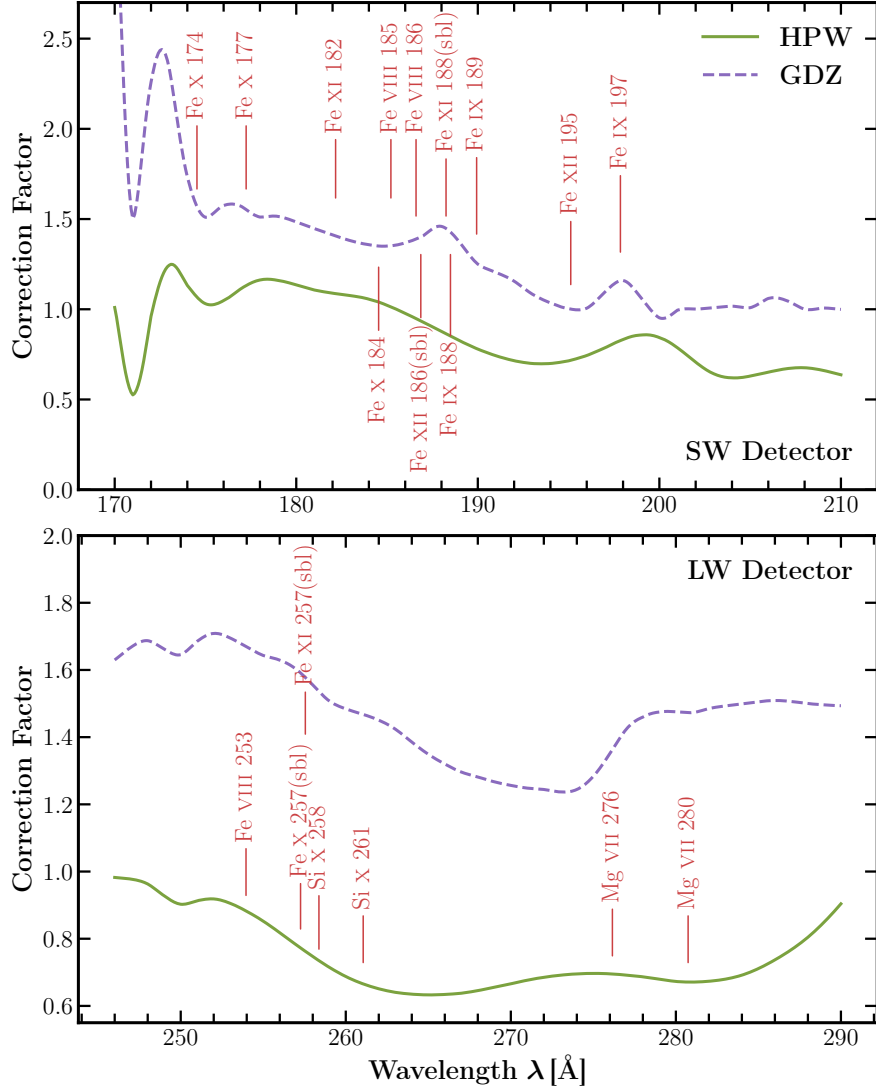


Figure 4.2: Two in-flight radiometric corrections in the SW (**top**) and LW (**bottom**) detectors of EIS. Locations of the spectral lines used for electron temperature and density diagnostics are also displayed. Link to the [Jupyter](#) notebook creating this figure: [🔗](#).

provides a better comparison with observations close to the limb. For more details about AWSoM-R, we refer the readers to Section 2.3.2 and [Sokolov et al. \(2021\)](#).

Ion	$\log T_{\max}$ (K)	Wavelength (\AA)	Instrument
Fe VIII	5.75	185.213/253.956	EIS
Fe IX	5.85	191.206/197.854	EIS
Fe X	5.95	174.531/(257.259+257.261)	EIS
Fe X	5.95	177.240/(257.259+257.261)	EIS
Fe X	5.95	184.537/(257.259+257.261)	EIS
Mg IX	5.95	706.060/749.552	SUMER
Fe XI	6.00	(188.216+188.299)/(257.547+257.554)	EIS

Table 4.2: Spectral lines ratios used for electron temperature diagnostics. T_{\max} is the temperature of the maximum line formation calculated by CHIANTI using the DEM derived from the average coronal hole spectra in [Vernazza & Reeves \(1978\)](#).

4.4 Results

4.4.1 Observations

4.4.1.1 Line Fitting and Average Effective Velocity

We fitted all available SUMER and EIS spectral lines. Figure 4.3(a) displays the single-Gaussian fitting of the Na IX 681 \AA line observed by SUMER. The line wings resolved by SUMER are well fitted by the Gaussian function. On the other hand, the peak intensity of the observed line core is larger than the best-fit line profile. A multi-Gaussian fitting example of several spectral lines around 192 \AA observed by EIS is shown in Figure 4.3(b). Although the Fe XII 192.394 \AA line is blended with some unidentified lines in the blue wing, we can still get a proper fitting of line widths. The reduced χ^2 function in both examples is less than 1, which might indicate that the Poisson statistics or propagation of errors overestimates the uncertainty. The other EIS and SUMER line widths used for ion temperature diagnostics are listed in Table B.1.

Then, we calculated the average effective velocity for ions with multiple spectral lines observed by the same instrument. We separately treated spectral lines originating from the same ion but observed by different instruments for comparison (e.g., the O VI 184 \AA line observed by EIS and the O VI 1032, 1037 \AA lines observed by SUMER). As an example, Figure 4.4 shows the effective velocity of the Fe XII 192.394, 193.509, and 195.119 \AA triplet lines and the average effective velocity \bar{v}_{eff} . The Fe XII 192 \AA line width shows greater uncertainty because of the low intensity and blending. The Fe XII 195 \AA line is slightly broader than the 192 and 193 \AA lines by $\sim 5 \text{ km s}^{-1}$, which could be related to the instrumental effect ([Del Zanna et al., 2019](#)) and the blended Fe XII 195.179 \AA line ([Young et al., 2009](#)). The average effective velocity of Fe XII is $41.1 \pm 2.2 \text{ km s}^{-1}$.

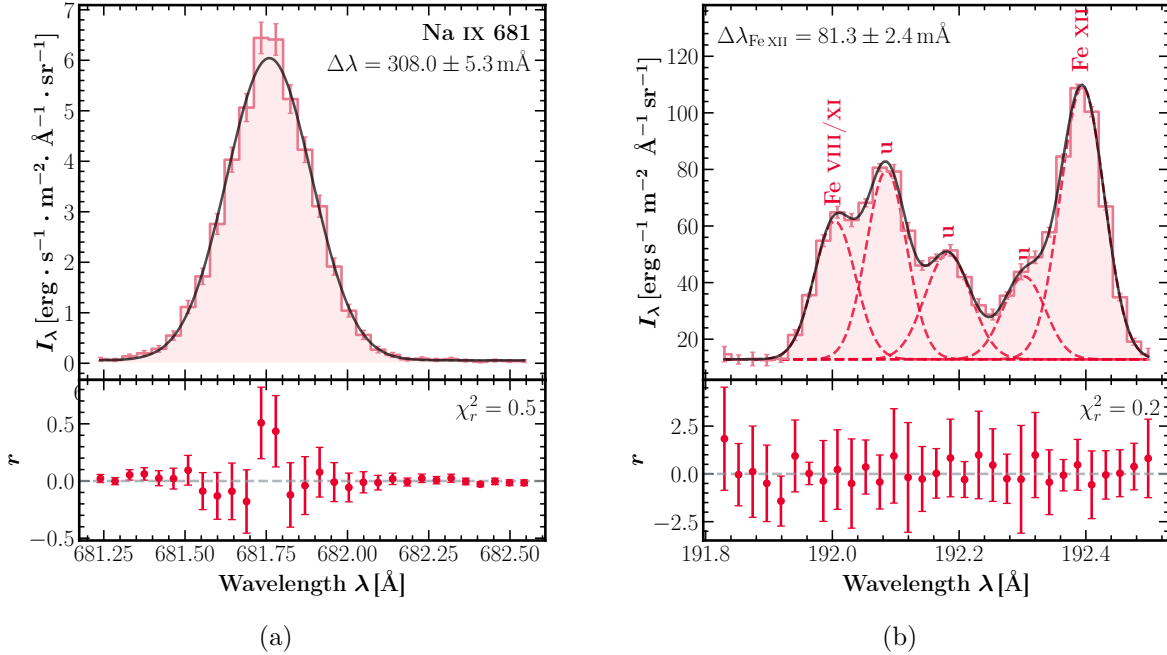


Figure 4.3: Examples of the single and multi-Gaussian fitting. (a) Single-Gaussian fitting of the Na IX 681 Å line observed by SUMER. (b) Multi-Gaussian fitting of the blended lines near 192 Å observed by EIS, including the blended Fe VIII and Fe XI 192.021 Å, Fe XII 192.394 Å, and three other unidentified (u) lines. The top panel shows the observed spectrum (step line) and the fitting line profile (solid black line). The lower panel displays the fitting residual. Links to the [Jupyter notebook](#) creating panels (a) [🔗](#) and (b) [🔗](#).

4.4.1.2 Electron Density and Temperature Diagnostics

Figure 4.5 summarizes the measured n_e and T_e , where the ions are ordered by their formation temperature. The measured electron densities range from $\log n_e \sim 7.7$ to $\log n_e \sim 9.0$, depending on the line pairs and calibration methods. The measured electron density increases with the maximum formation temperature of the ion. The electron densities measured from cooler ($\log T_{\max} < 5.9$) line pairs like Fe VIII 185/186 Å, Mg VII 276/280 Å, and Fe IX 188/189 Å are around $\log n_e \sim 8.0$. The hotter Mg IX 694/706 Å ($\log T_{\max} \sim 5.95$) ratio gives the electron density $\log n_e \sim 8.5$. We found the highest electron densities $\log n_e \sim 8.7$ – 9.0 in the hottest ($\log T_{\max} > 6.0$) Si X 258/261 Å, Fe XI 182/188 Å, and Fe XII 186/195 Å lines. The increase in n_e with T_{\max} implies that off-limb emissions might have two different source regions along the LOS: a cooler and less dense coronal hole and a hotter and denser region. However, it is difficult to identify the hotter region from both the observation and the simulation in Section 4.4.2.

We chose two electron densities $\log n_e = 8.0$ and $\log n_e = 8.5$ to calculate temperature-sensitive line ratios using CHIANTI. The inferred electron temperatures from different line

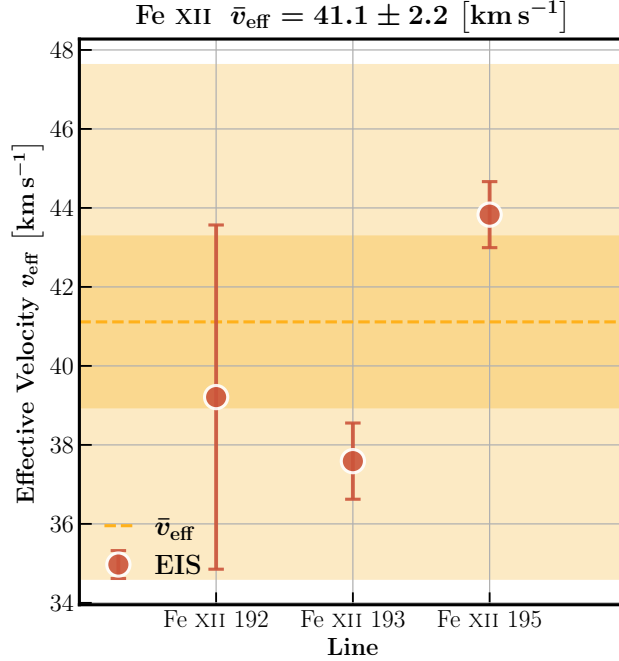


Figure 4.4: The measured effective velocity v_{eff} of the Fe XII 192, 193, and 195 Å lines and the average effective velocity \bar{v}_{eff} of Fe XII. The horizontal dashed line indicates the average effective velocity \bar{v}_{eff} . The darker/lighter shaded regions show the $1\sigma/3\sigma$ uncertainty level, respectively. Link to the `Jupyter` notebook creating this figure: [🔗](#).

ratios are shown in the right panel of Figure 4.5. Most electron temperatures range from $\log T_e \sim 5.9$ to $\log T_e \sim 6.2$. EIS electron temperatures show a wider distribution due to different radiometric calibrations. The T_e inferred from the HPW correction are higher than the T_e inferred from the GDZ correction by 0.1–0.3 dex (a factor of 1.3–2.0 on the linear scale). The T_e measured from hotter line pairs like Fe x 174/257 and Fe XI 188/257 are slightly greater than T_e inferred from cooler line ratios like Fe VIII. Although the Fe IX 191/197 Å ratio is less affected by the cross-calibration between two detectors, the line ratio is more sensitive to the electron density. We measured a higher T_e in the Fe x 184/257 Å ratio than the other two Fe x 174/257 Å and 177/257 Å ratios. As the magnetic field in the coronal hole is very weak, the blended Fe x 257 Å magnetic-induced transition (MIT) should not affect the Fe x line ratios. The T_e inferred from the Mg IX 706/749 Å ratio lies between most of the HPW and GDZ electron temperatures. We chose $\log T_e = 5.9$ to $\log T_e = 6.15$ as the electron temperature of the LOS plasma to cover most of the measurements.

4.4.1.3 Ion Temperature Diagnostics

Although the n_e measurements suggest the presence of two different structures along the LOS, we found it challenging to perform T_i diagnostics on each structure separately. First,

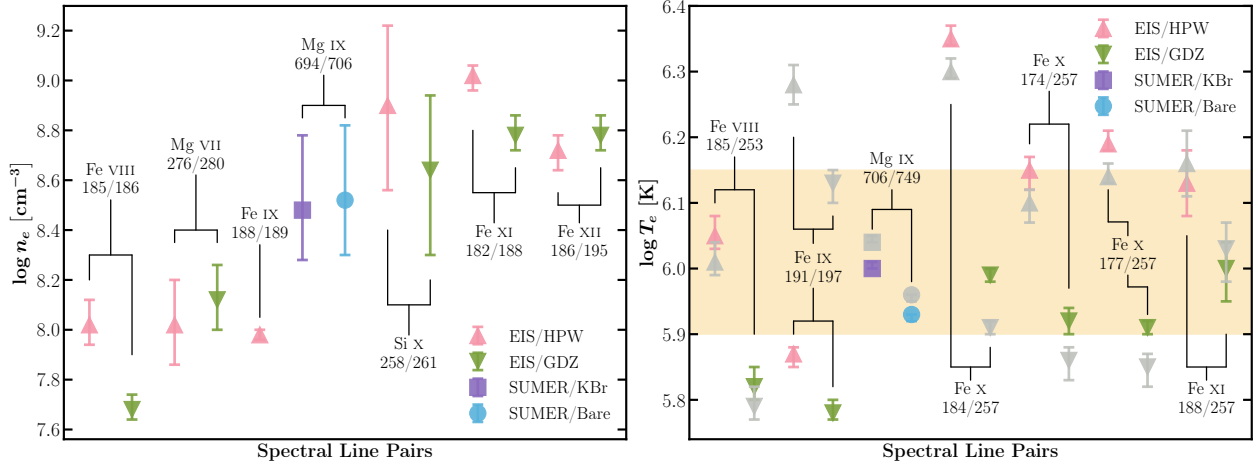


Figure 4.5: Left: electron density n_e diagnostics of the coronal hole boundary region shown in Figure 4.1. **Right:** electron temperature T_e diagnostics in the same region. The colored data points in the right panel represent T_e at $\log n_e = 8.0$, while the gray ones stand for the T_e inferred at $\log n_e = 8.5$. The yellow-shaded area displays the chosen range of the electron temperature. The line ratios are sorted from left to right by the maximum formation temperature T_{\max} (see Tables 4.1 and 4.2). Link to the [Jupyter notebook](#) creating this figure: [🔗](#).

the two regions might contribute emissivity to all observed spectral lines, although with different weights. Second, the number of ions is too limited to carry out T_i diagnostics in each region separately. Third, it would be more complicated to treat lines like Fe XII and Fe XIII, whose widths might be affected by the bulk motions along the LOS (see Section 4.4.2). Hence, we continued to use all spectral lines to measure T_i . Note that the measured T_i , like other measurements in the optically thin plasma, is an average along the LOS.

Figure 4.6 shows the minimum and maximum of the ion temperature $T_{i,\min}$ and $T_{i,\max}$ versus the ion Z/A , along with the T_e determined in Figure 4.5. The values of $T_{i,\min}$ and $T_{i,\max}$ are also listed in Table B.1. We measured the T_i of ions with Z/A ranging from 0.125 (Fe VIII) to 0.37 (Mg x). Since the coronal hole plasma is cooler than the plasma in the quiet-Sun or active regions, spectral lines from higher charge states are too weak to identify or fit. The narrowest lines are from Fe VIII (EIS) and Si x (SUMER), with similar effective velocities $\bar{v}_{\text{eff}} \sim 32 \text{ km s}^{-1}$. We used the \bar{v}_{eff} of Fe VIII as the maximum nonthermal velocity ξ_{\max} . Note that the Si x 624.694 Å line observed by SUMER is blended with the stronger Mg x 624.941 Å line, so the uncertainty of v_{eff} is quite large.

The measured T_i shows a U-shaped dependence on the charge-to-mass ratio Z/A similar to the T_i measured by Landi & Cranmer (2009) using a SUMER observation at the center of the coronal hole. Ions with $0.12 \leq Z/A \leq 0.19$, except for the two ions Fe VIII (EIS) and Fe IX with the smallest v_{eff} , show T_i much higher than the local T_e . The T_i decreases with Z/A between 0.19 and 0.25, then shows a plateau close to the local T_e ranging from $Z/A = 0.25$

to 0.33. Above $Z/A = 0.33$, the T_i becomes greater than the local T_e again. Mg x with the greatest $Z/A = 0.37$ reveals a lower T_i than the other ions with $Z/A > 0.33$ (Mg IX, Ne VIII and Na IX).

The observation did not suggest a clear dependence of T_i on formation temperatures T_{\max} . Although some cooler ions observed by EIS, like Mg VII and O VI, show lower T_i compared to the hotter ions like Fe XII, the T_i of ions with similar T_{\max} can be dramatically different, e.g., Fe VIII (SUMER) and Mg VII (EIS). We further investigate the influence of the ion formation temperature and bulk motions along the LOS in the AWSoM-R simulation (see Section 4.4.2).

Contrary to expectations, in most cases, the \bar{v}_{eff} and the T_i measured by SUMER are greater than \bar{v}_{eff} and T_i from the same ion measured by EIS. The only exception is Si x, which might be due to the fitting uncertainty caused by line blending. Both EIS and SUMER record strong emission lines from Fe VIII and O VI, providing the most reliable comparisons. The $v_{\text{eff}} = 50.2 \pm 7.5 \text{ km s}^{-1}$ of the SUMER Fe VIII is 30% to 50% higher than the EIS value of $\bar{v}_{\text{eff}} = 32.0 \pm 1.7 \text{ km s}^{-1}$, while the SUMER O VI $\bar{v}_{\text{eff}} = 50.3 \pm 0.6 \text{ km s}^{-1}$ is also about 25% larger than the EIS value of $v_{\text{eff}} = 40.6 \pm 2.3 \text{ km s}^{-1}$. We will discuss the uncertainty caused by instrumental broadening in Section 4.5.1.

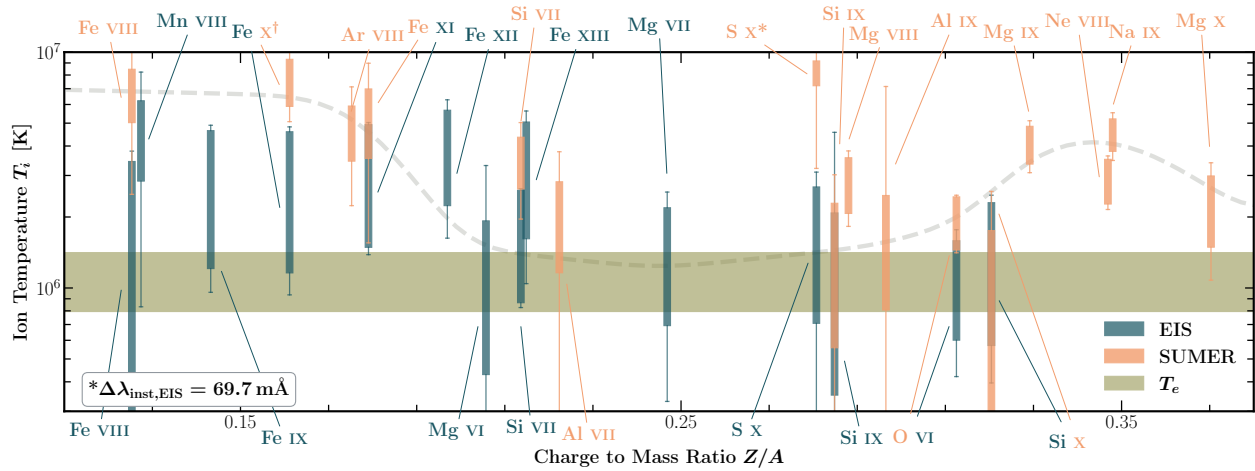


Figure 4.6: Estimated ion temperatures T_i vs. ion charge-to-mass ratio Z/A . For each ion, the boxes show possible ion temperature intervals between $T_{i,\min}$ and $T_{i,\max}$, while the whiskers indicate the uncertainty in $T_{i,\min}$ and $T_{i,\max}$. The ion temperatures inferred from lines observed by EIS and SUMER are shown in dark green and orange, respectively. The horizontal shaded area displays the electron temperature measurement shown in Figure 4.5. The dashed gray line is arbitrarily drawn to illustrate the U-shaped dependence. * The S x 776.373 Å line is poorly fitted. †The Fe x 1028 Å line is self-blended, but still kept for comparison. Link to the [Jupyter notebook](#) creating this figure: [🔗](#).

4.4.2 Simulations

Figure 4.7 shows the physical parameters in the AWSoM-R simulation. The coronal hole boundary region in the simulation does not show complicated structures along the LOS, except for a streamer at the far side. The T_e between 1.01 and $1.04 R_\odot$ is ~ 1 MK, and the electron density n_e is $\sim 10^8 \text{ cm}^{-3}$, matching the diagnostics results in Section 4.4.1.2. The LOS velocity varies from 0 to $\pm 20 \text{ km s}^{-1}$ where most spectral lines form in the studied region. The wave-induced nonthermal velocity ξ is about 20 km s^{-1} in the open field lines between 1.01 and $1.04 R_\odot$.

The maximum formation temperature T_{max} of the spectral line affects the line formation region along the LOS in Figure 4.7. For example, most Fe VIII 186 \AA emissions ($\log T_{\text{max}} \sim 5.75$) are contributed by the plasma from $-0.3 R_\odot$ to $0.3 R_\odot$ along the LOS. Most of the hotter Fe XII 192 \AA ($\log T_{\text{max}} \sim 6.05$) emission forms between $-0.5 R_\odot$ and $0.5 R_\odot$. The streamer at the far side does not contribute enough emissions to Fe XII to influence the density diagnostics. We did not find other hotter and denser regions along the LOS in the simulation.

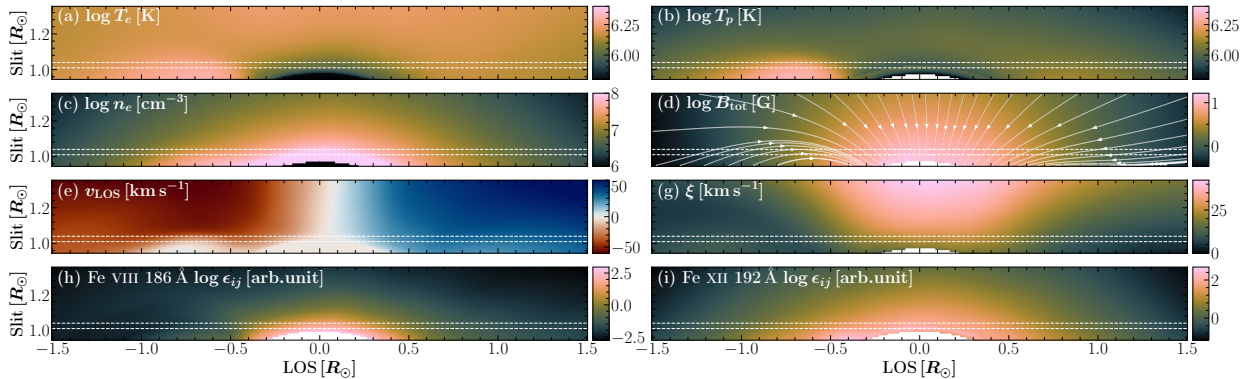


Figure 4.7: Physical parameters predicted by AWSoM-R along the LOS covering the entire SUMER slit. The dotted white lines show the region selected for analysis. **(a)** Electron temperature T_e , **(b)** proton temperature T_p , **(c)** electron density n_e , **(d)** total magnetic field B_{tot} and field lines, **(e)** LOS velocity v_{LOS} , **(g)** wave-induced nonthermal velocity ξ_w , **(h)** emissivity of the Fe VIII 186 \AA line, **(i)** and emissivity of the Fe XII 192 \AA line. Link to the [Jupyter notebook](#) creating this figure: [🔗](#).

To evaluate the influence of LOS bulk motions on line profiles, we synthesized Fe VIII 186 \AA and Fe XII 192 \AA profiles either with or without the Doppler effect in Figure 4.8. The macroscopic Doppler broadening only increases the Fe VIII width by about 2.5%. The LOS integration of bulk motions in Fe VIII becomes even more negligible when the profile is convolved with the instrumental width and degraded to EIS spectral resolution. The actual width of the hotter Fe XII 192 \AA line increases from 38.0 to 47.3 \AA due to the macroscopic

Doppler broadening. After the convolution with the instrumental widths, the bulk motion still increases the Fe XII line width from 81.3 to 85.2 Å, suggesting that the bulk motions might increase line widths noticeably in actual observations.

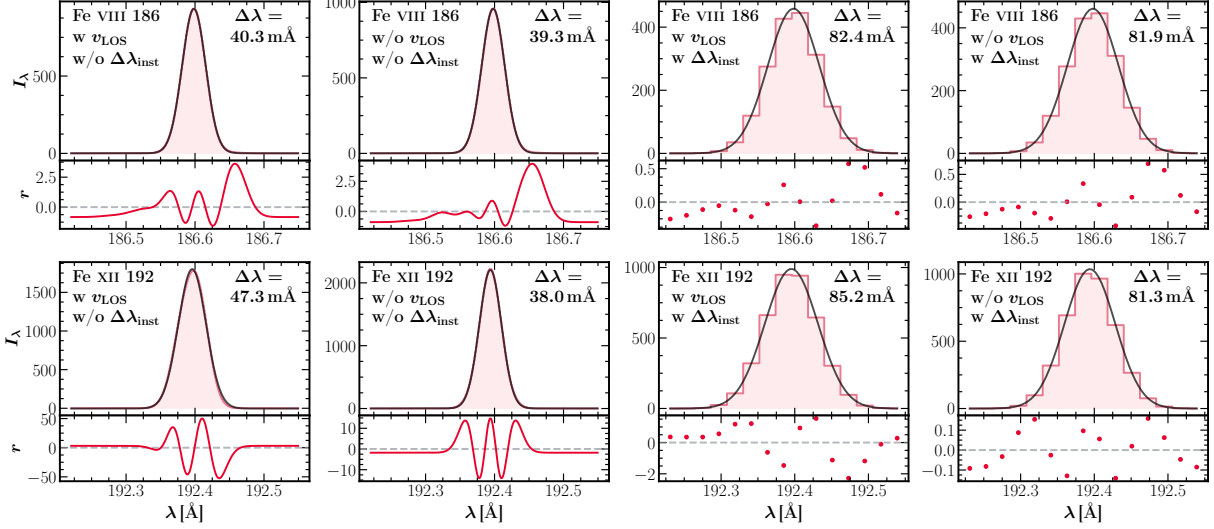


Figure 4.8: Fitting synthetic Fe VIII 186 Å and Fe XII 192 Å lines under different conditions. $w v_{\text{LOS}}$: synthetic profiles with the Doppler effect. $w/o v_{\text{LOS}}$: synthetic profiles without the Doppler effect. $w \Delta\lambda_{\text{inst}}$: synthetic profiles convolved with instrumental width $\Delta\lambda_{\text{inst}} = 70 \text{ mÅ}$ and rebinned to EIS spectral resolution. $w/o \Delta\lambda_{\text{inst}}$: synthetic profiles without instrumental effects. Link to the [Jupyter notebook](#) creating this figure: [🔗](#).

Figure 4.9 compares the observed line widths with the synthetic line widths. The SPEC-TRUM module uses the proton temperature T_p to approximate the T_i to calculate the thermal broadening. Therefore, the excessive widths in the observation might indicate the additional heating in heavy ions compared to the proton. Most of the spectral lines observed by SUMER show widths similar to or larger than the synthetic widths. On the other hand, most of the EIS lines are $\sim 5\text{--}10 \text{ km s}^{-1}$ narrower than the synthetic lines. The differences between the SUMER and synthetic line widths show a similar U-shaped dependence on Z/A , with SUMER lines being wider than synthetic ones by $\sim 5\text{--}20 \text{ km s}^{-1}$. For ions observed by both EIS and SUMER, AWSOM-R underestimates the SUMER line widths but overestimates the EIS line widths (e.g., Fe VIII, Fe XI, and O VI). This is because the v_{eff} measured by SUMER is usually greater than the v_{eff} of the same ion observed by EIS (see Section 4.4.1.3).

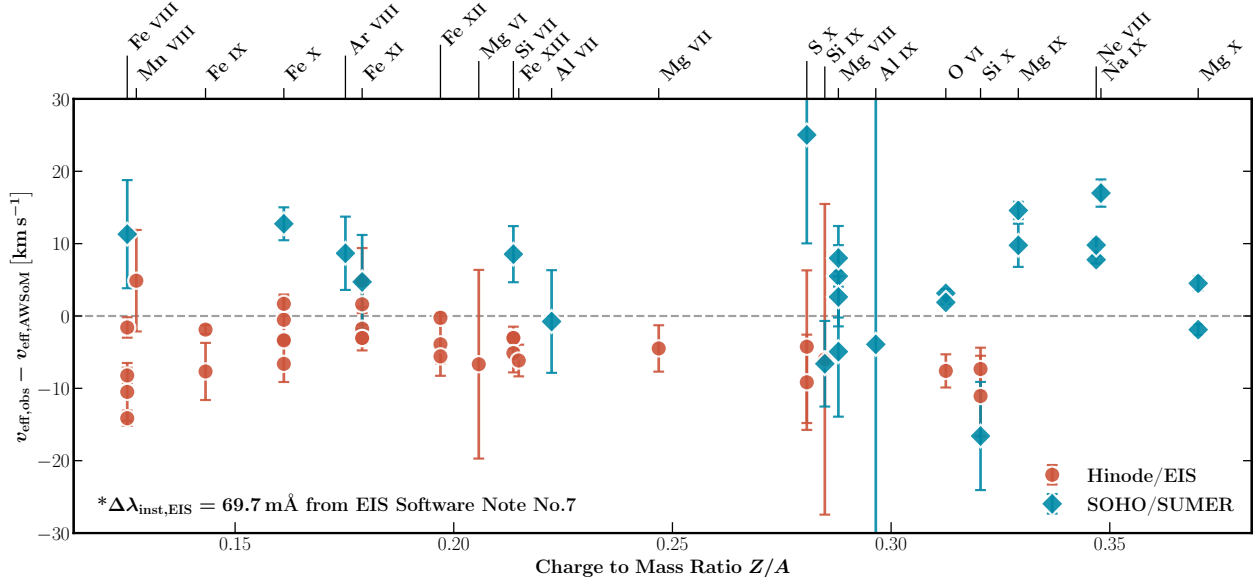


Figure 4.9: Differences between the observed effective velocity $v_{\text{eff,obs}}$ and the synthetic effective velocity $v_{\text{eff,AWSOM}}$ of each spectral line used in ion temperature diagnostics. Red dots with error bars: EIS lines. Blue diamonds with error bars: SUMER lines. Link to the [Jupyter notebook](#) creating this figure: [🔗](#).

4.5 Discussion

4.5.1 Uncertainty in Instrumental Broadening

Inconsistency in the v_{eff} and T_i of the same ion observed by SUMER and EIS might result from the instrumental widths used in this study. The instrumental widths of the EIS $2''$ slit are measured by searching for the smallest Fe XII 193.509 Å line widths in a series of off-limb quiet-Sun observations. Only a thermal width of $\Delta\lambda_{\text{th}} = 23.2 \text{ mÅ}$ was removed from the Fe XII width to obtain the instrumental width as a function of position along the slit, assuming $\log T_i = \log T_{\text{max}} = 6.2$ (Young, 2011b). This raises the concern that the EIS instrumental width might be overestimated; also, the instrumental widths might depend on the wavelength (see the discussion in Appendix 4.5.2). At the averaged 30 pixels, the EIS instrumental width for the $2''$ slit is 69.7 mÅ , with an uncertainty of $\sim 3 \text{ mÅ}$.

The SUMER instrumental widths were determined using the widths of narrow neutral lines in quiet-Sun observations (Chae et al., 1998) and P. Lemaire’s calculations of 1997 August 28. Chae et al. (1998) reported the instrumental width of SUMER detector B with $1''$ slit is about 3.0 pixels ($\approx 129 \text{ mÅ}$ in the first order) with a fluctuation of 0.5 pixels ($\approx 22 \text{ mÅ}$). Compared with the EIS instrumental width (69.7 mÅ), which dominates the observed profiles of $80\text{--}90 \text{ mÅ}$, the SUMER instrumental width of $\sim 129 \text{ mÅ}$ contributes

much less to the observed widths between 200 and 350 mÅ at the first order.

To investigate the influence of instrumental widths on the diagnostic results, we cross-calibrated the EIS instrumental widths $\Delta\lambda_{\text{eff,EIS}}$ with the SUMER observation by matching the width of O VI 184.117 Å (EIS) to the widths of O VI 1031.912 and 1037.613 Å (SUMER). We assumed that SUMER correctly measured the O VI width. That is because the SUMER in-flight instrumental widths are measured from the narrowest neutral lines, where the thermal and nonthermal broadening are negligible. We obtained a new EIS instrumental width $\Delta\lambda'_{\text{inst,EIS}} = 62.7 \text{ mÅ}$ for the 2'' slit at the averaged 30 pixels, which is about 9% smaller than the original instrumental width $\Delta\lambda_{\text{inst,EIS}} = 69.7 \text{ mÅ}$ and beyond the 3 mÅ uncertainty. The difference between the two EIS instrumental widths $(\Delta\lambda_{\text{inst,EIS}}^2 - \Delta\lambda'^2_{\text{inst,EIS}})^{1/2} = 30.4 \text{ mÅ}$ is equivalent to an effective velocity of 28.3 km s^{-1} , which might be caused by Fe XII nonthermal motions not properly removed in Young (2011b). Del Zanna et al. (2019) also reported the possible overestimation of EIS instrumental width.

We repeated ion temperature diagnostics with the new EIS instrumental width $\Delta\lambda'_{\text{eff,EIS}} = 62.7 \text{ mÅ}$ in Figure 4.10. The lowest v_{eff} is from the Si x 624.694 Å line observed by SUMER, which has a more considerable fitting uncertainty due to the blended Mg x 624.941 Å line. The EIS ion temperatures T_i at low Z/A increase significantly and overlap the T_i ranges of the same ion observed by SUMER (e.g., Fe VIII and Fe XI). The increase in the EIS T_i also makes the U-shaped dependence on Z/A more prominent. The T_i of the Fe XII and Fe XIII observed by EIS are much higher than the T_i of Mg VI, Si VII, and Al VII with similar Z/A between 0.20 and 0.23. This might be due to the macroscopic Doppler broadening of ions with higher T_{max} found in AWSOM-R simulations (see Sections 4.4.2 and 4.5.3).

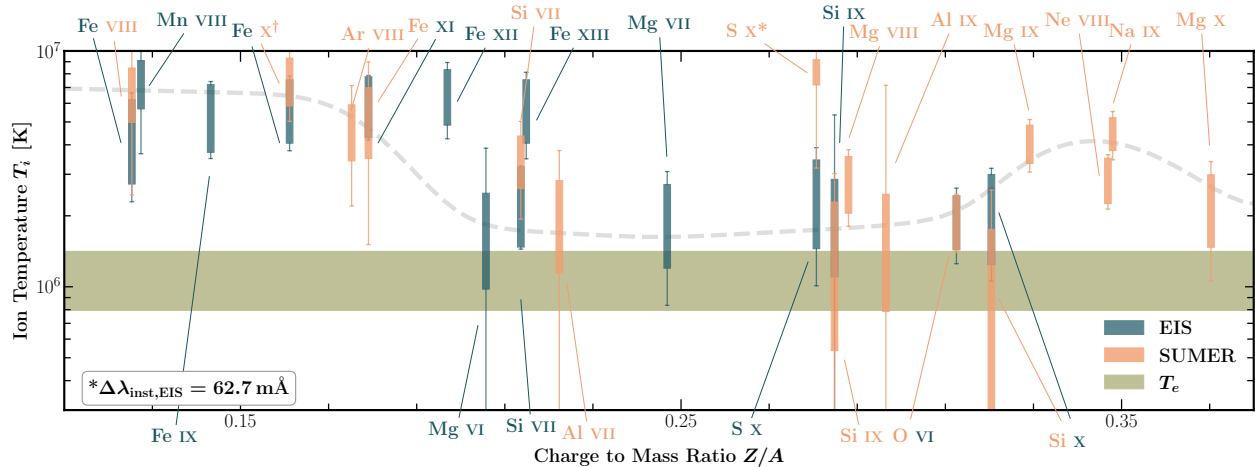


Figure 4.10: Same as Figure 4.6 but using the cross-calibrated EIS instrumental width $\Delta\lambda'_{\text{inst,EIS}} = 62.7 \text{ mÅ}$. The dashed gray line is arbitrarily drawn to illustrate the U-shaped dependence. Link to the [Jupyter notebook](#) creating this figure: [🔗](#).

Figure 4.11 compares the observed line widths and the synthetic line widths using the cross-calibrated instrumental width of EIS. The v_{eff} of the EIS lines increase by $\sim 5\text{--}10\text{ km s}^{-1}$. The EIS lines with $0.12 \leq Z/A \leq 0.19$ are about $0\text{--}15\text{ km s}^{-1}$ wider than the synthetic lines, which is consistent with the SUMER observation. The EIS lines with $0.2 \leq Z/A \leq 0.32$ show similar line widths compared to the synthetic ones (within $\pm 5\text{ km s}^{-1}$).

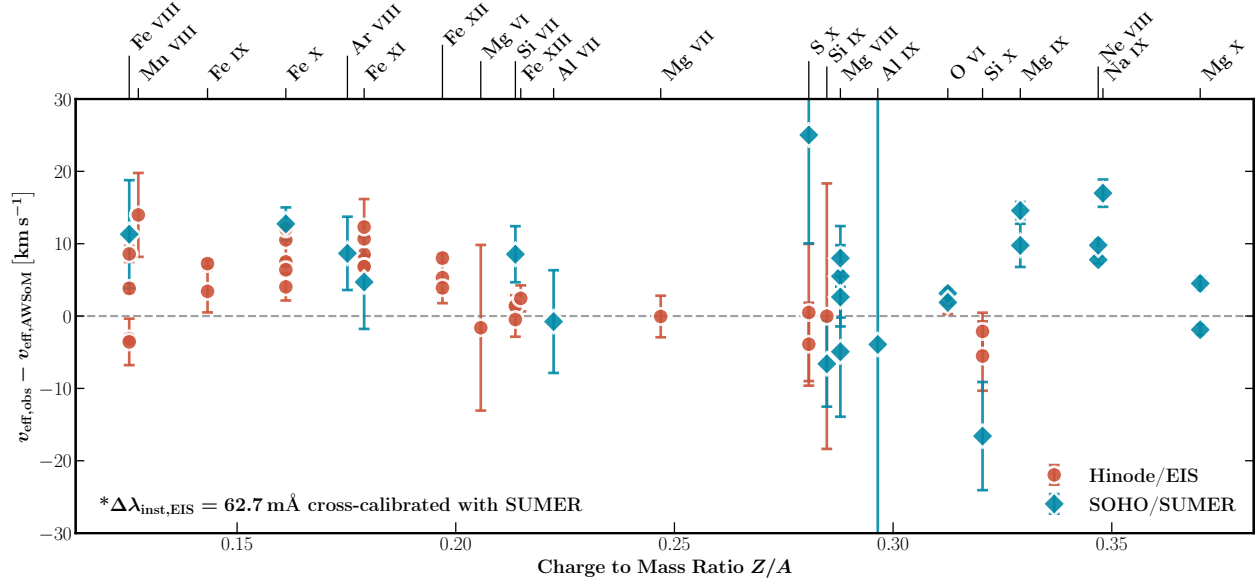


Figure 4.11: Same as Figure 4.9 but using EIS instrumental broadening $\Delta\lambda'_{\text{inst,EIS}} = 62.7\text{ mÅ}$ cross-calibrated with SUMER. Link to the [Jupyter notebook](#) creating this figure: [🔗](#).

4.5.2 Wavelength Dependence of the EIS instrumental Widths

The latest EIS instrumental width provided by the EIS software in SolarSoft is constant at different wavelengths. However, earlier studies of the EIS instrumental width suggested that the instrumental widths in the two detectors are slightly different (e.g., [Brown et al., 2008](#)). We used the following method to investigate whether the EIS instrumental width depends on the wavelength. The fitted FWHM $\Delta\lambda_{\text{fit}}$ is often interpreted as

$$\Delta\lambda_{\text{fit}}^2 = \Delta\lambda_{\text{inst}}^2 + 4 \ln 2 \frac{v_{\text{eff}}^2}{c^2} \lambda_0^2 \quad (4.9)$$

where $\Delta\lambda_{\text{inst}}$ is the instrumental FWHM. Assuming that the effective velocity $v_{\text{eff}}^2 = 2k_B T_i / m_i + \xi^2$ is a constant for all spectral lines from the same ion, we can treat $\Delta\lambda_{\text{fit}}$ as a function of λ_0 with two parameters $\Delta\lambda_{\text{inst}}$ and v_{eff} , i.e., $\Delta\lambda_{\text{fit}} = f(\lambda_0; \Delta\lambda_{\text{inst}}, v_{\text{eff}})$.

If $\Delta\lambda_{\text{inst}}$ does not depend on the wavelength, we could use $(\Delta\lambda_{\text{fit}}, \lambda_0)$ pairs from different spectral lines of the same ion to fit the optimized $\Delta\lambda_{\text{inst}}$ and v_{eff} .

We implemented this method on an EIS observation of the west off-limb quiet-Sun corona on 2007 April 13. The data set has been studied in Landi et al. (2010) to cross-calibrate the intensity between EIS and SUMER, and we chose it because of its high S/N. We averaged the data at the same 30 pixels on the CCD detector used in this study. Although there are barely isolated and strong lines of the same ion across the EIS detector, we found the Fe XI and Fe XII lines are the best candidates. Figure 4.12 shows the fitted FWHM $\Delta\lambda_{\text{fit}}$ and the line centroid wavelength λ_0 of the Fe XI and Fe XII lines. For Fe XI lines, we obtained an instrumental width $\Delta\lambda_{\text{inst}} = 71.9 \pm 1.2 \text{ m}\text{\AA}$, which is more consistent with the instrumental width $\Delta\lambda_{\text{inst}} = 69.7 \text{ m}\text{\AA}$ given by the EIS software. However, there are some outliers in the Fe XI lines, including Fe XI 181.130 \AA and 257.772 \AA . The Fe XII triplets at 192.394, 193.509, and 195.119 \AA have very similar line widths $\Delta\lambda_{\text{fit}} \sim 77 \text{ m}\text{\AA}$. However, the $\Delta\lambda_{\text{fit}}$ of the Fe XII 249.388, 259.973, and 291.010 \AA line does show a monotonic dependence on λ_0 . Therefore, we cannot obtain the instrumental width from the Fe XII widths. We suggest that the instrumental width of the EIS 2'' slit might depend on the wavelength.

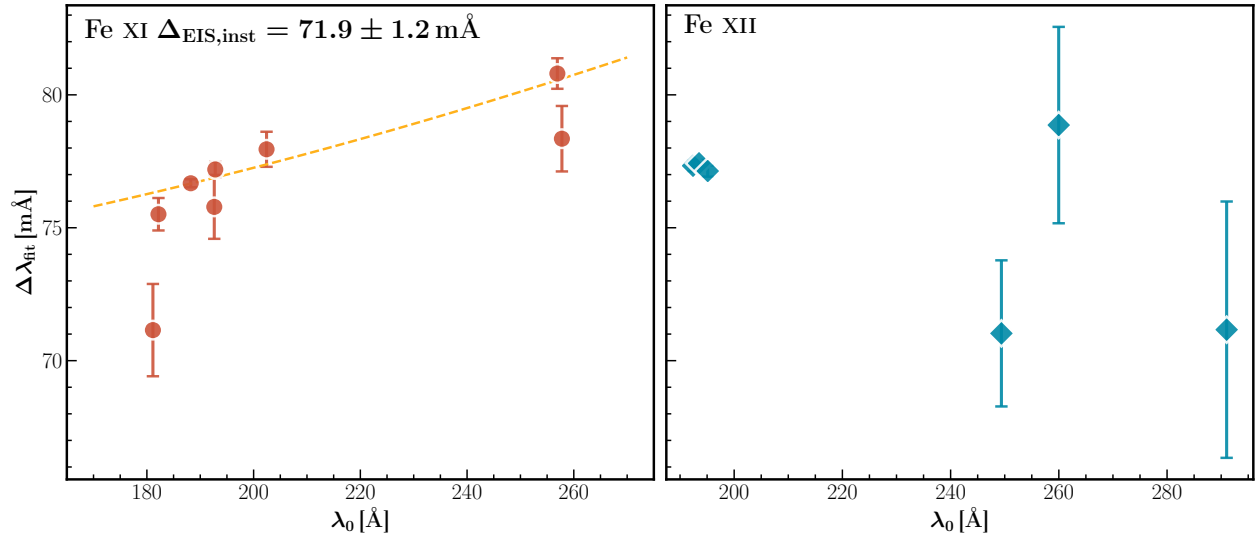


Figure 4.12: Fitted FWHM $\Delta\lambda_{\text{fit}}$ versus line centroid wavelength λ_0 of the Fe XI and Fe XII lines in off-limb quiet-Sun corona. The dashed line in the left panel shows the best fitting of $\Delta\lambda_{\text{fit}} = f(\lambda_0 | \Delta\lambda_{\text{inst}}, v_{\text{eff}})$. Link to the [Jupyter notebook](#) creating this figure [🔗](#).

4.5.3 Validation of the Technique

To validate the T_i diagnostics technique, we performed the same diagnostics on the AWSoM-R synthetic line widths. The SPECTRUM module uses the proton temperature T_p to cal-

culate the thermal widths of all spectral lines. Hence, the measured T_i should show no dependence on Z/A . Figure 4.13 shows the diagnostic results along with the weighted average of the electron temperature \bar{T}_e and the proton temperature \bar{T}_p along the LOS. We used the emissivity ϵ_{ij} of Fe VIII 186 Å and Fe XII 192 Å line as the weights:

$$\bar{T} = \frac{\int \epsilon_{ij}(x)T(x)dx}{\int \epsilon_{ij}(x)dx} \quad (4.10)$$

to determine the interval of the weighted average \bar{T}_e and \bar{T}_p .

As expected, the measured T_i intervals $[T_{i,\min}, T_{i,\max}]$ do not show U-shaped relations with Z/A and are consistent with both \bar{T}_e and \bar{T}_p , because there is no preferential heating in the simulation. The only exceptions are the Fe XII and Fe XIII due to the bulk motions along the LOS. Hence, we validated that the T_i diagnostic technique can be used to search for the preferential heating of heavy ions, especially for the cooler ions observed by SUMER and EIS (e.g., Fe VIII and Ne VIII).

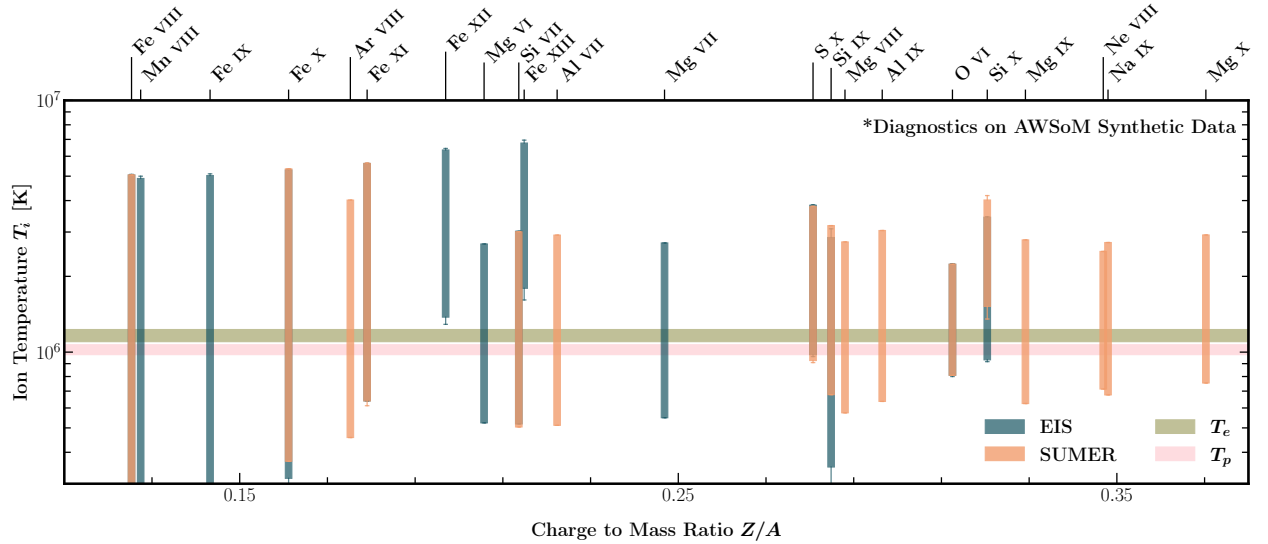


Figure 4.13: Same as Figure 4.6, but using line widths from AWSOM-R simulations. The colored horizontal area represents the range of average electron temperature T_e and proton temperature T_p along the LOS weighted by either Fe VIII 186 Å emissivity or Fe XII 192 Å emissivity. Link to the Jupyter notebook creating this figure: [🔗](#).

4.5.4 Non-Gaussian Profiles

The line-fitting and T_i diagnostics assume that the observed line profiles are close to Gaussian. However, we found that the brightest lines observed by SUMER ($I_{\text{tot}} > 1 \text{ erg s}^{-1} \text{ cm}^{-2} \text{ Å}^{-1} \text{ sr}^{-1}$) show non-Gaussian wings at the coronal hole boundary. These lines

include O VI, Ne VIII, Mg IX, and Mg X. The non-Gaussian wings in the plumes and interplume regions were reported in early SUMER observations (e.g., Hassler et al., 1997; Wilhelm, 1999). Wilhelm (1999) found non-Gaussian wings of the Ne VIII 780 Å line in the coronal hole; on the contrary, the Ne VIII profiles in closed magnetic field regions do not show broad non-Gaussian wings. They also suggested that the non-Gaussian wings are not instrumental effects because the brightest C III stray-light line does not show the non-Gaussian wings. Similarly, we did not find non-Gaussian wings in the brightest N IV 765 Å stray-light line in this data set either.

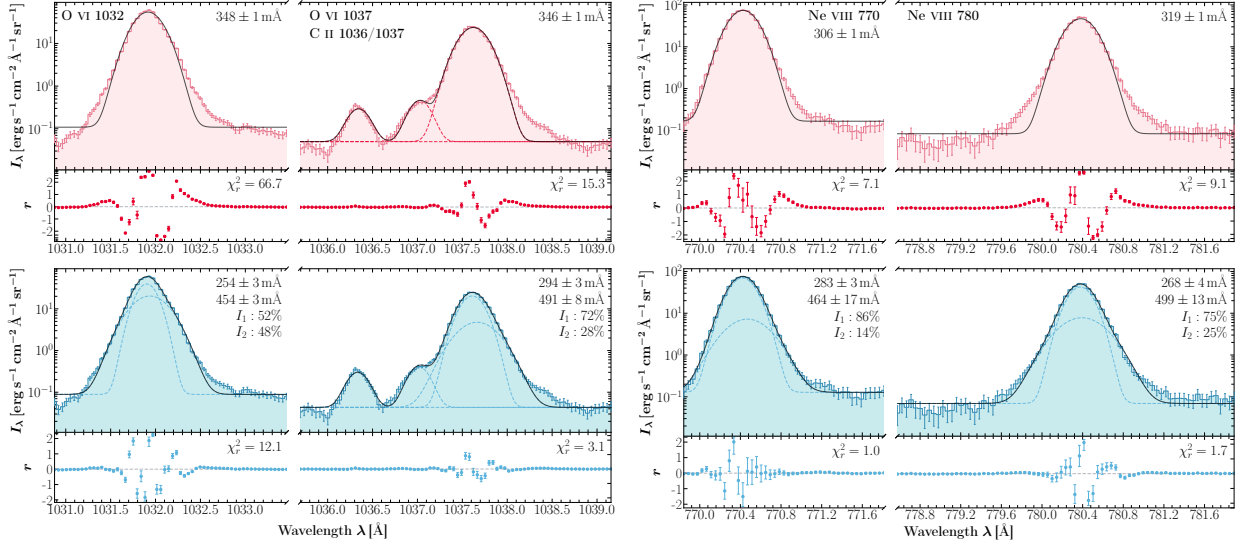
To examine the influence of the non-Gaussian wings on the single-Gaussian fitting, we first fitted the non-Gaussian profile by the Voigt function or a secondary Gaussian component. We found that the double-Gaussian function better reproduces the non-Gaussian wings, consistent with negligible pressure broadening in the coronal holes to produce Voigt profiles.

We compared the single-Gaussian and double-Gaussian fitting results of O VI 1032/1037 Å, Ne VIII 770/780 Å, and Mg X 609/624 Å in Figure 4.14. The secondary Gaussian component improves the fitting up to $\sim \pm 200 \text{ km s}^{-1}$, but still leaves some residuals in the red wings of the O VI and Ne VIII lines.

After removing instrumental broadening, the width of the narrower main component in the double-Gaussian fitting is 10%–40% less than the single-Gaussian width, equivalent to a reduction of 20%–60% in $T_{i,\text{max}}$. On the other hand, the broader secondary Gaussian component has a width about twice that of the primary component, corresponding to an effective temperature 2–3 times that of the single-Gaussian profile. Since none of these brightest lines is used to estimate the maximum nonthermal velocity ξ_{max} , most $T_{i,\text{min}}$ measurements will not be affected.

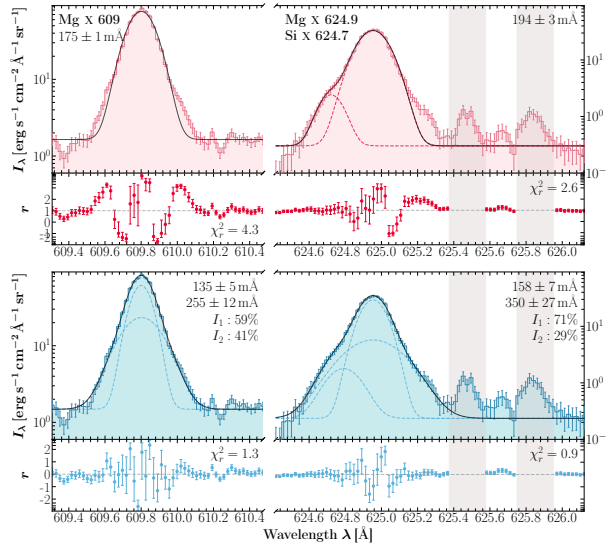
The intensity ratios between the two Gaussian components suggested that the flows along the LOS might not be the only cause of the non-Gaussian wings. If unresolved flows were present, the intensity ratio should be the same for both lines of the same ion. On the contrary, these ratios do not agree, let alone with the ratios from other ions. For example, in O VI 1032 Å and Mg X 609 Å, the secondary component contributes approximately half the intensity of the line profile, while the contribution of the secondary component in O VI 1037 Å and Mg X 624 Å is much less than 50%.

The inconsistency of the intensity ratios between the two Gaussian components raises the question of whether the double-Gaussian fitting is a good approximation to fit the high-energy tails. The κ distribution, first introduced empirically by Vasyliunas (1968) and Olbert (1968), is helpful in fitting the suprathermal tails of plasma particles (Lazar et al., 2016). Inspired by Jeffrey et al. (2018) who fitted EIS spectra in the coronal hole assuming a κ distribution, we also attempted fitting these brightest SUMER lines with the κ distribution



(a)

(b)



(c)

Figure 4.14: Single-Gaussian and double-Gaussian fitting to the (a) O VI 1032 and 1037 Å, (b) Ne VIII 770 and 780 Å, and (c) Mg X 609 and 624 Å lines, including the adjacent C II 1036 and 1037 Å and Si X 624 Å lines. The black solid curve shows the fitting result. The dashed curves show each Gaussian component. The single-Gaussian widths, the double-Gaussian widths, and relative intensities are also shown. The vertical gray areas in panel c indicate the masked pixels during the fitting. Note that we only fixed the line centroids in the double-Gaussian fitting of the Mg X 624 Å line. Link to the Jupyter notebook creating this figure: [🔗](#).

using the formula in Dudík & Dzifčáková (2021):

$$I_{\kappa}(\lambda) = I_0 \left[1 + \frac{(\lambda - \lambda_0)^2}{2(\kappa - 3/2)w_{\kappa}^2} \right]^{-\kappa} \quad (4.11)$$

where I_0 is the peak intensity and w_κ represents the characteristic width. The w_κ is related to the FWHM $\Delta\lambda_\kappa$ of κ distribution by (see [Dudík et al., 2017](#))

$$w_\kappa = \frac{1}{8} \frac{\Delta\lambda_\kappa^2}{(\kappa - 3/2)(2^{1/\kappa} - 1)} \quad (4.12)$$

Figure 4.15 shows the SUMER line profiles fitted with the κ distribution. The κ distribution well fitted the non-Gaussian wings. The six brightest resonant lines of O VI, Ne VIII, and Mg X show similar fitted $\kappa \sim 3$ –4, except for the Ne VIII 770 Å with $\kappa \sim 8$. The fainter Mg IX 706 Å and Na IX 681 Å show a larger $\kappa \sim 5$ and $\kappa \sim 8$, respectively. These κ values are slightly greater than the $\kappa \approx 1.9$ –2.5 obtained from EIS observations of the southern polar coronal hole reported by [Jeffrey et al. \(2018\)](#).

Since the SUMER software is designed to remove the instrumental broadening from Gaussian profiles rather than from κ profiles, we roughly estimated the influence of κ fitting on $T_{i,\max}$ using the line width before the instrumental broadening correction ([Dudík et al., 2017](#)):

$$\frac{T_{i,\max}^G}{T_{i,\max}^\kappa} \sim \frac{(\kappa - 3/2)(2^{1/\kappa} - 1)}{\ln 2} \frac{\Delta\lambda_G^2}{\Delta\lambda_\kappa^2} \quad (4.13)$$

where $T_{i,\max}^G$ is the maximum ion temperature estimated from the Gaussian FWHM $\Delta\lambda_G$, and $T_{i,\max}^\kappa$ is the maximum ion temperature estimated from the κ FWHM $\Delta\lambda_\kappa$. The $T_{i,\max}^G/T_{i,\max}^\kappa$ ratios of unblended O VI 1032 Å, Ne VIII 770 and 780 Å, and Mg X 609 Å are between 0.75 and 0.95, which means $T_{i,\max}$ might increase by 10%–20% if we take the high-energy tails into account.

We agree with [Jeffrey et al. \(2018\)](#) that nonequilibrium ion populations, non-Maxwellian turbulence, or both might cause the non-Gaussian wings in the coronal hole. We did not make further investigations into the formation mechanism of the high-energy tails, which is out of the scope of this paper.

4.5.5 Preferentially Heated Ions

Figure 4.16 compares our ion temperature T_i measurements at $\sim 1.03 R_\odot$ at the coronal hole boundary with two previous studies: [Landi & Cranmer \(2009, 1.06 \$R_\odot\$ \)](#) and [Dolla & Solomon \(2008, 1.05 \$R_\odot\$ \)](#), which used SUMER observations at the center of polar coronal holes to measure T_i . [Landi & Cranmer \(2009\)](#) also used the diagnostic method, while [Dolla & Solomon \(2008\)](#) separated the thermal and nonthermal widths by assuming the thermal width of Mg X 624 Å is constant at different altitudes and the variation of the nonthermal width is caused by undamped Alfvén waves.

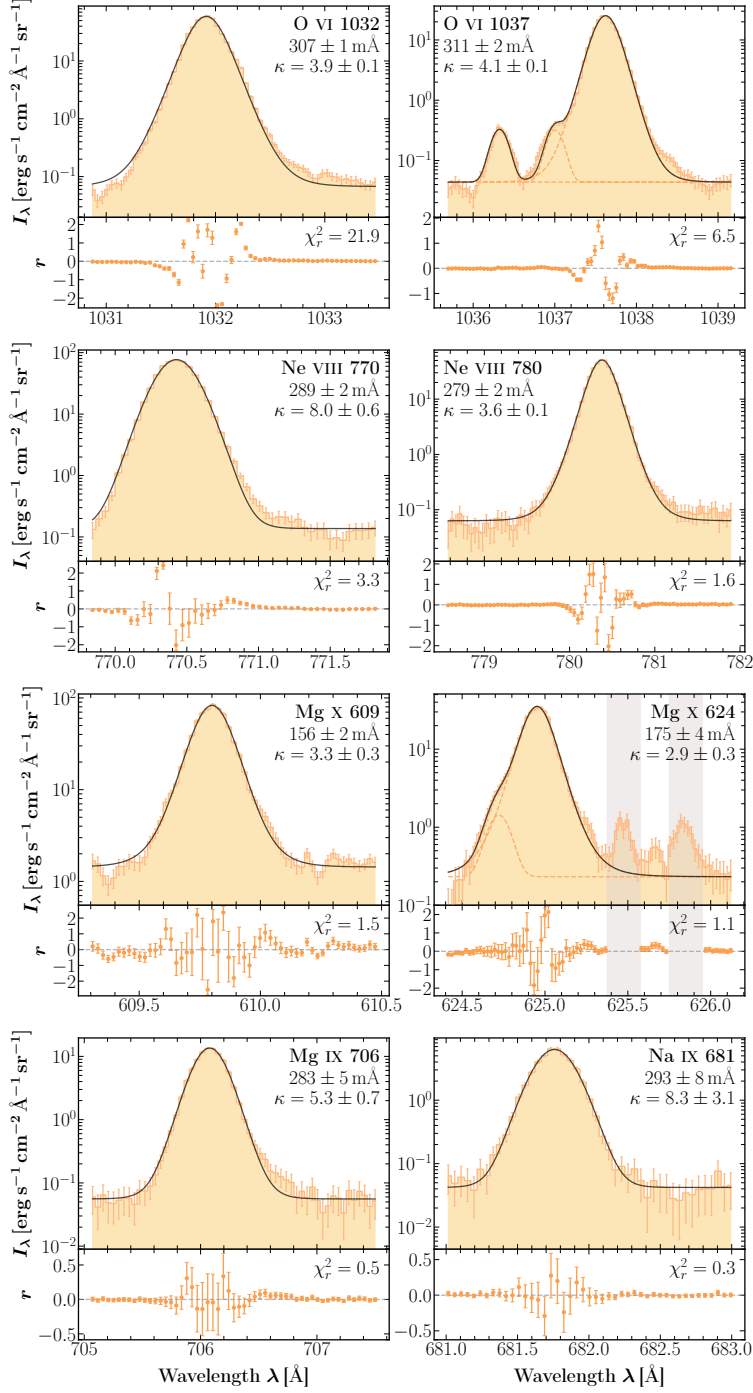


Figure 4.15: κ fitting of the brightest coronal lines observed by SUMER. The fitted κ and FWHM of the κ profile $\Delta\lambda_\kappa$ are shown as well. The weak blended or stray-light lines are still fitted with a Gaussian distribution. Link to the [Jupyter notebook](#) creating this figure: [🔗](#).

We confirmed the U-shape dependence of T_i on Z/A in the polar coronal hole and the preferential heating of the ions with $Z/A < 0.2$ or $Z/A > 0.33$. Furthermore, we extended

this result to $Z/A < 0.15$. The heating of the $Z/A > 0.33$ ions is inconsistent with the traditional cascade model of ion-cyclotron waves and implies additional resonant wave power at high frequencies (large Z/A , Landi & Cranmer, 2009). We note that the high- Z/A ions are only observed by SUMER, which makes the preferential heating at $Z/A \geq 0.33$ less robust than the heating at $Z/A \leq 0.19$ confirmed by both SUMER and EIS.

Although EIS observes most of the lower- Z/A lines used in this study, using the cross-calibrated EIS instrumental width, our results show remarkable consistency with the SUMER-based T_i values reported by Landi & Cranmer (2009). On the other hand, some of the T_i measured by Dolla & Solomon (2008) do not fall within the T_i interval found by this study, for example, Ar VIII, Fe x, Fe XII, and Na IX are found to be hotter in this study. We note that both Landi & Cranmer (2009) and this study used polar coronal hole observations during the solar minimum. In contrast, Dolla & Solomon (2008) analyzed the SUMER observations taken during the solar maximum, which might cause the differences in the measured T_i , as the ion charge state in the fast solar wind is found to vary from solar maximum to minimum (e.g., Lepri et al., 2013).

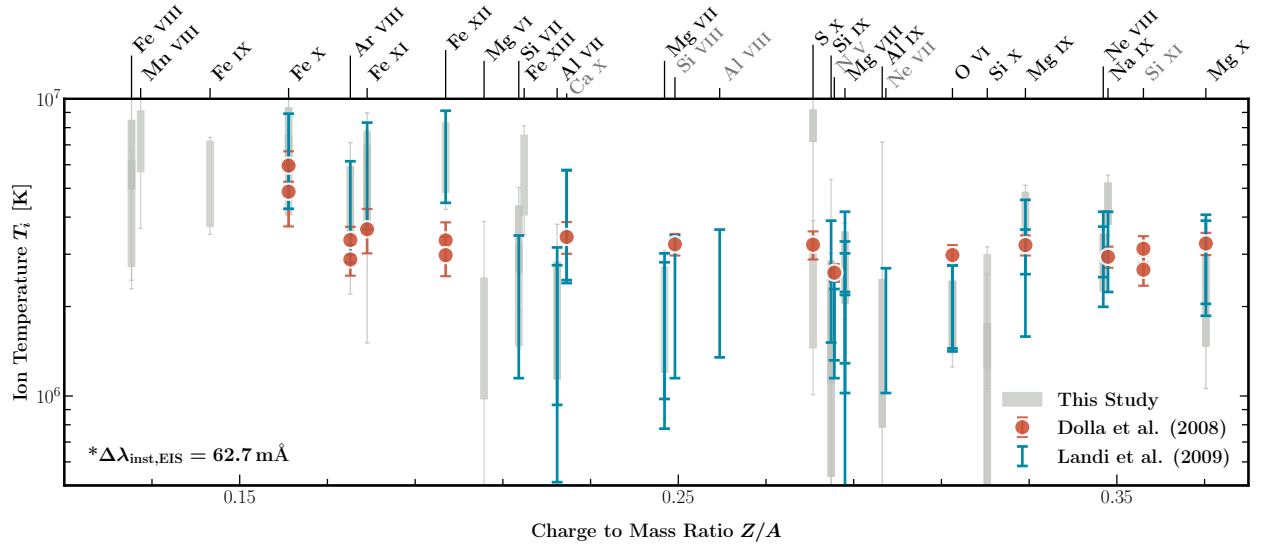


Figure 4.16: Comparison between the ion temperature T_i in the polar coronal hole measured by this study (gray box plot), Dolla & Solomon (2008, red error bars), and Landi & Cranmer (2009, blue error bars). Gray ion names represent ions that are not used in this study. Link to the Jupyter notebook creating this figure: [🔗](#)

Hahn et al. (2010) analyzed the same EIS data set and applied the same T_i diagnostics from 1.04 to 1.14 R_\odot . They found similar preferential heating of ions with $Z/A < 0.2$. However, the heating of $Z/A > 0.33$ ions (e.g., Mg IX and Ne VIII) was missing in their study because only SUMER can observe the spectral lines of these ions. The EIS T_i inter-

vals measured using the cross-calibrated instrumental width are slightly lower than the ion temperature $\log T_{i,\max} > 7.0$ reported by [Hahn et al. \(2010\)](#). This is because [Hahn et al. \(2010\)](#) measured T_i at higher altitudes ($\geq 1.04 R_\odot$) and used an old EIS instrumental width of 61 mÅ (SW detector) or 62 mÅ (LW detector).

CHAPTER 5

Line Widths Observed during the 2017 Total Solar Eclipse

5.1 Preface

The materials present in this chapter have been submitted to the *Astrophysical Journal*. The manuscript is co-authored by Shadia R. Habbal, Adalbert Ding, Bryan Yamashiro, Enrico Landi, Benjamin Boe, Sage Constantinou and Michael Nassir.

5.2 Introduction

Total solar eclipse (TSE) spectroscopic observations of the ‘green’ line in 1869 by Young and Harkness led to the discovery of a 1.8×10^6 K coronal electron temperature, when its correct identification as Fe XIV emission at 530.3 nm was made by [Grotrian \(1939\)](#) and [Edlén \(1943\)](#). Following this seminal discovery, TSE spectroscopic observations have been pursued in earnest. They led to the discovery of a rich coronal spectrum with different ionization states of elements, such as Ni, Ar, and Ca to name a few (see [Jefferies et al. 1979](#)). In addition to inferences of the electron temperature, and chemical composition, spectral lines offer fundamental diagnostic tools such as inferences of the ion effective temperature, which include contributions from ion temperatures and nonthermal motions along the line of sight. Doppler shifts, when present, yield mass motions, both steady and dynamic.

The list of identified emission lines in the early TSE spectroscopic observations did not always report the same emission lines. Furthermore, decades of spectroscopic observations also differed in the observed line widths and their variations across the corona, ([Kim, 2000](#); [Koutchmy et al., 2005](#); [Raju et al., 2011](#); [Prabhakar et al., 2019](#)). These differences can be readily accounted for by differences in underlying structures, covering a range of electron temperatures, as resolved more recently by complementary imaging observations of coronal

emission lines during totality.

Despite their paucity, TSE spectral and imaging data remain unique scientific assets for exploring the properties of the different manifestations of coronal heating and solar wind acceleration mechanisms responsible for these observables. The uniqueness of these observations stems from the properties of the emission from coronal forbidden lines, which is dominated by radiative excitation. This property enables the detection of the emission out to much larger distances than extreme ultraviolet imaging and spectroscopy, as the latter lines are dominated by collisional excitation, hence detectable only at shorter distances.

This chapter presents an analysis of spectroscopic observations of the Fe x 637.4 nm and Fe XIV 530.3 nm lines obtained during the 2017 August 21 TSE. They capitalize on the distinct advantage of the spatial extent of emission from coronal forbidden lines spanning at least $1 R_{\odot}$ above the limb, thus exploring a range of different coronal structures. The primary focus of the analysis is on the spectral line widths from which the effective ion temperature can be inferred, and on any Doppler shifts when present. The spectral observations are placed in the context of emission line imaging of Fe XI 789.2 nm and Fe XIV 530.3 nm acquired at the same time. The eclipse observations are complemented by spectroscopic observations of Hinode/EIS as well as in the Fe XIII 1074.7 nm near-infrared line with CoMP. The observations, including methodology and the specifics of the spectrometer, are given in Section 5.3. The ancillary space-based and ground-based observations are presented in Section 5.4. This is followed by a discussion including comparisons between the different instruments in Section 5.5.

5.3 3PAMIS Observations and Results

5.3.1 Operation and Data Acquisition

During the 2017 TSE, spectroscopic observations were made with a three-channel Partially Multiplexed Imaging Spectrometer (3PAMIS). The design and calibration of 3PAMIS is detailed in Section 2.1.3. During the eclipse, 3PAMIS data was acquired at Guernsey State Park, Wyoming, USA, at $42^{\circ}18'58.5''$ N, $104^{\circ}47'20.6''$ W, and an altitude of 1406 m. The totality began at 17:45:37 UT (second contact), when the Sun was $55^{\circ}4'$ above the horizon, and ended at 17:47:56 UT (third contact). At the start of the totality, the slit was initially placed across the disk center, tilted slightly from the solar northwest to southeast. Track motion was then disabled, and the Sun slowly drifted across the slit, allowing for the measurement of the coronal spectrum above the east limb. 3PAMIS made intermittent exposures when the slit scanned the east limb, leaving data gaps between each exposure due to the finite readout

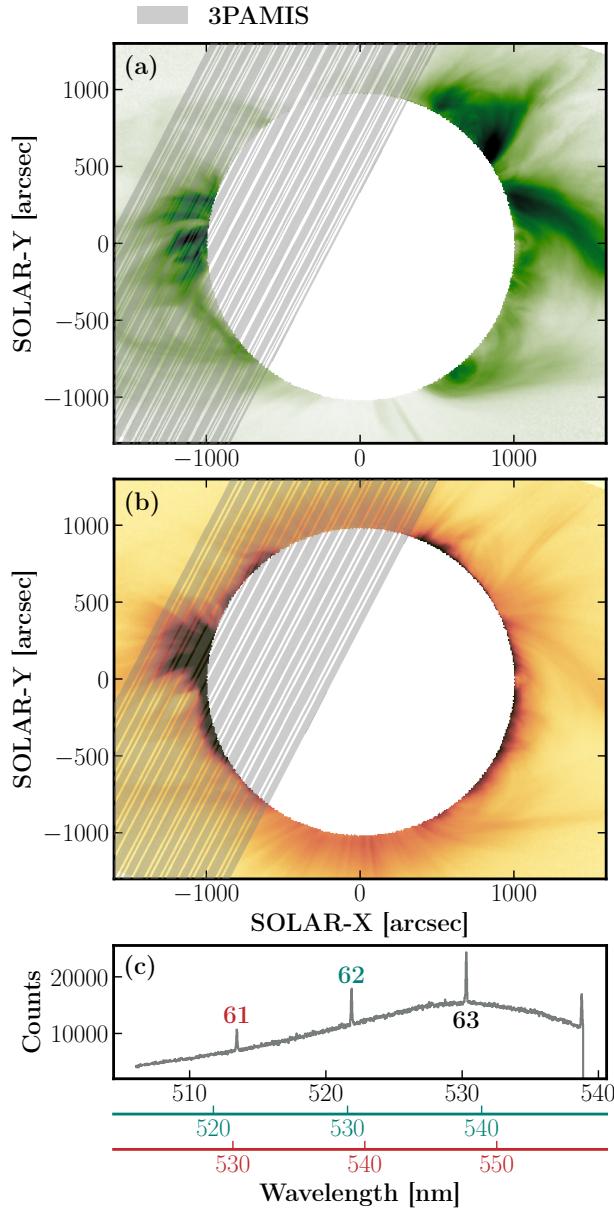


Figure 5.1: Overview of the 3PAMIS observation during the 2017 TSE and two Hinode/EIS observations made on 2017 August 21. (a) 3PAMIS/Green FOV (Gray) overplotted on the Fe XIV 530.3 nm line-to-continuum ratio image. (b) 3PAMIS/Red FOV (Gray) overplotted on the Fe XI 789.2 nm line-to-continuum ratio image. (c) An example streamer spectrum showing Fe XIV 530.3 nm line at the 61st, 62nd, and 63rd orders. Link to the Jupyter notebook creating this figure: [\[link\]](#).

and download time of the two CCD detectors (see Figure 5.1a and b). The typical exposure times of the green detector were 0.5 s, 1 s, and 3 s, while for the red detector, they were 1 s and 3 s.

We corrected and calibrated the 3PAMIS data through dark frame subtraction, curvature

correction, and flat-fielding. In addition, we performed the wavelength calibration and measured the instrumental broadening from the calibration frames taken in the laboratory. We determined the 3PAMIS pointing using the position of the slit on the context images and coaligned it with the narrow-bandpass images.

Figure 5.1c shows an example spectrum from the green detector, including the Fe XIV 530.3 nm line at 61st, 62nd, and 63rd orders and the stacked multi-order continuum. We first removed the ambient continuum by a linear fit and then performed a single-Gaussian fit to the strongest orders of Fe XIV 530.3 nm (63rd) and Fe X 637.4 nm (52nd) line. We did not co-add profiles in different orders because the camera was best focused on the strongest orders, and the wavelength scale varies with orders (see more discussion in Section C). Additionally, to maximize the S/N in fitting Doppler velocities and line widths, we averaged 5 pixels along the slit.

5.3.2 Data Analysis and Results

Figure 5.2 shows the line-to-continuum maps and line profiles of Fe XIV 530.3 nm and Fe X 637.4 nm observed in the off-limb regions. The profiles are obtained by averaging five pixels along the slit and removing the multi-order continuum. The intensity maps reveal several structures at the east limb, including the NOAA active region (AR) 12672 near the equator, a streamer in the northeast direction, and another streamer in the southeast. Global magnetohydrodynamic (MHD) simulations and white light observations confirmed that the emission from the northeast region is both contributed by a streamer cusp and polar plumes from a low-latitude coronal hole (CH) at the far side (Mikić et al., 2018). With 1-3 s exposures and spatial binning of approximately $40''$ along the slit, the Fe XIV 530.3 nm profiles can be fitted up to $1.5 R_{\odot}$ in the AR, while the Fe X 637.4 nm line can be observed up to $1.3 R_{\odot}$.

The Fe XIV emission appears most prominent above the AR, while other diffuse emission is observed in the southern streamer. Notably, the Fe XIV 530.3 nm profiles in the AR are narrower than the fainter Fe XIV profiles in streamers. Most Fe X emissions form close to the limb, below $1.1 R_{\odot}$, except for the northern boundary of the AR. The Fe X profiles in the northern CHs are remarkably broader than the Fe X profiles in the close-field regions.

The fitting results of Fe X and Fe XIV are shown in Figure 5.3. Panel d displays the relative line-to-continuum ratio of Fe XIV, demonstrating similarities to the line-to-continuum ratio measured using narrow-bandpass filters shown in Figure 5.3a, using the technique described by Boe et al. (2020).

Figure 5.3e shows the Doppler shifts in Fe XIV 530.3 nm line. The Doppler velocities

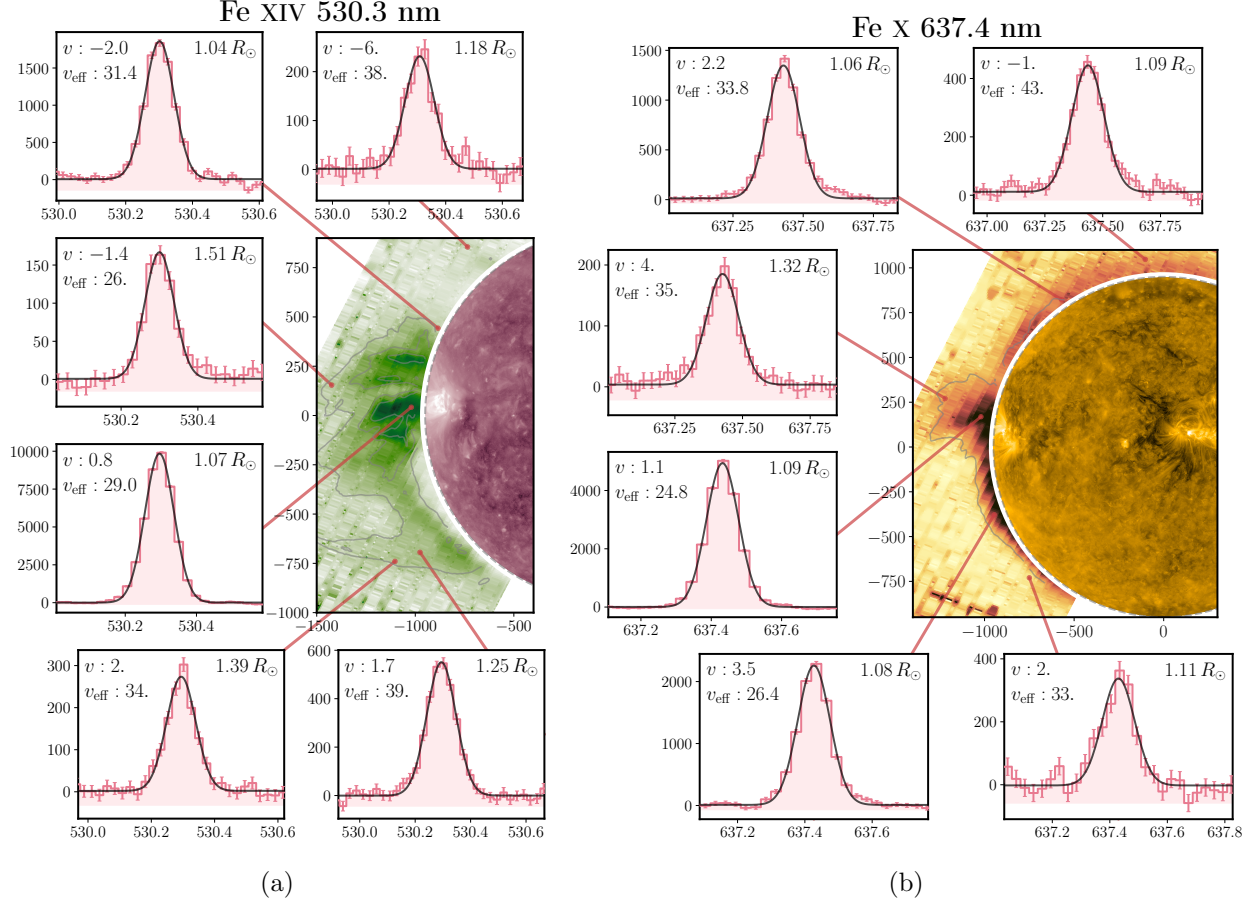


Figure 5.2: Overview of the Fe XIV 530.3 nm (left) and Fe X 637.4 nm (right) line intensities observed by 3PAMIS. The line-to-continuum ratios of the two lines are shown, along with the SDO/AIA images on the disk. To fill the data gaps, the intensity is interpolated using a 2-D Gaussian convolution kernel. The small zoom-in panels show Fe XIV 530.3 nm and Fe X 637.4 nm line profiles, which are binned over 5 pixels along the slit. Additionally, single-Gaussian fit results of these profiles are shown. v represents the Doppler velocity, and v_{eff} denotes the effective velocity, both of which are in units of km s^{-1} . Link to the [Jupyter](#) notebook creating this figure: [🔗](#).

in the AR range within $\pm 2 \text{ km s}^{-1}$. Larger Doppler shifts are evident in the southern and northern streamers. The northern streamer exhibits a redshift of up to $5\text{--}10 \text{ km s}^{-1}$, while the southern streamer reveals a blueshift of approximately 5 km s^{-1} .

As depicted in Figure 5.3f, the typical Fe XIV line widths in the off-limb AR range from 25 to 32 km s^{-1} . These line widths correspond to effective temperatures of $2.1\text{--}3.5 \text{ MK}$. In comparison, the Fe XIV line profiles in the northern and southern streamers are much broader. The effective velocities in these streamers are in the range of $v_{\text{eff}} = 35\text{--}40 \text{ km s}^{-1}$, equivalent to $T_{\text{eff}} = 4.2\text{--}5.4 \text{ MK}$.

Panels h to l of Figure 5.3 display the fitting results of the Fe X 637.4 nm line. For

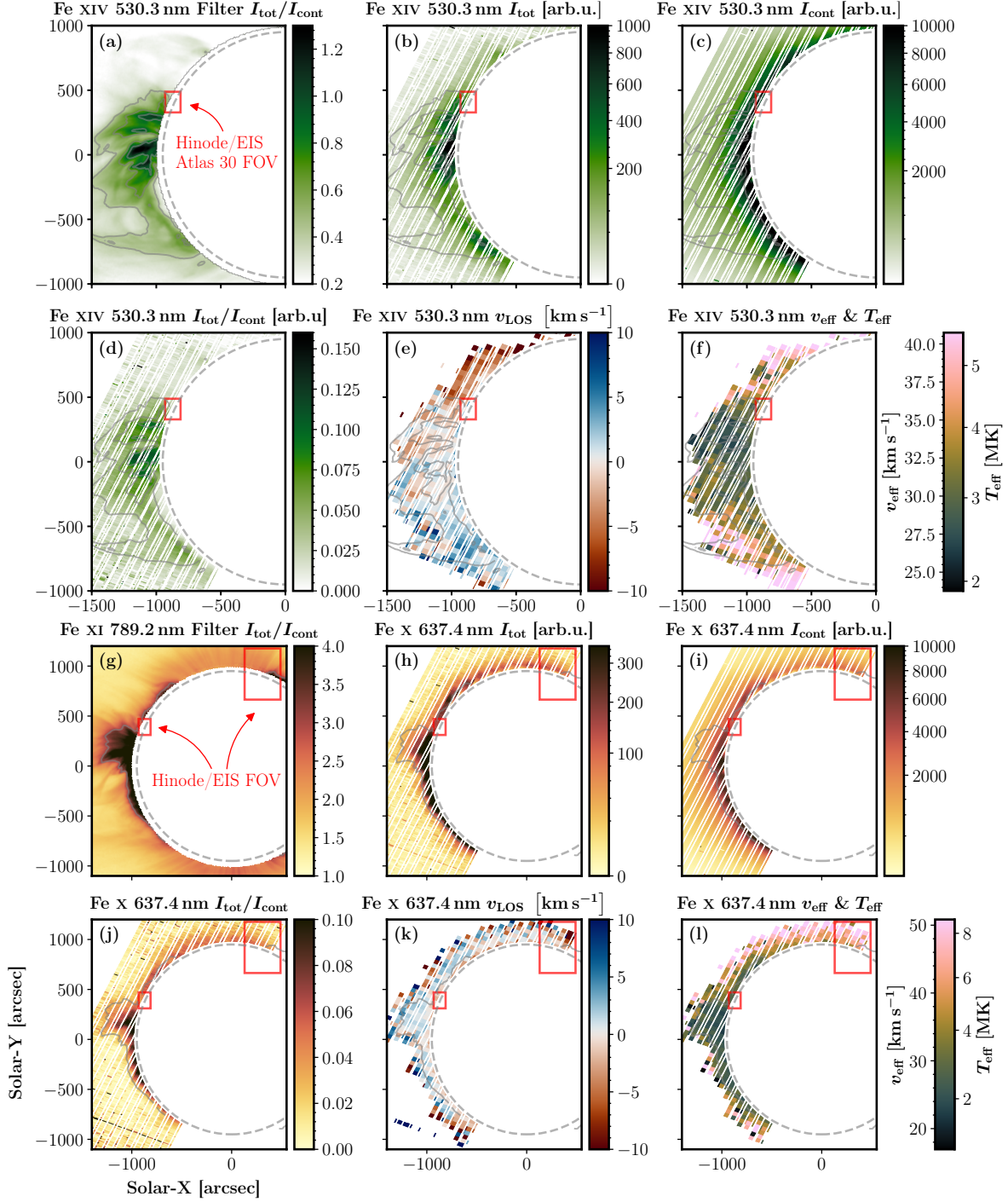


Figure 5.3: (a) Fe XIV 530.3 nm line-to-continuum ratio measured by a narrow-bandpass imager from Boe et al. (2020). (b) 3PAMIS Fe XIV 530.3 nm line intensity. (c) ambient continuum intensity. (d) line-to-continuum ratio. (e) Doppler velocity. (f) line width. (g) Fe XI 789.2 nm narrow-band image. (h-l) similar to panels (b-f) but for Fe X 637.4 nm. The red rectangles represent the FOVs of two complementary Hinode/EIS observations. Link to the Jupyter notebook: [🔗](#).

comparison, the Fe XI 789.2 nm intensity measured by a narrow bandpass imager is shown in panel a. Most Fe X line emission forms near the limb. The enhancement of Fe X emission in the AR appears to be located between the two other loop-like structures observed in Fe XIV, indicating the existence of cold (~ 1 MK) loop or plasma outflows in the vicinity of the hot (2 MK) AR.

The Doppler shifts of Fe X 637.4 nm, shown in Figure 5.3k, range between -5 and 5 km s^{-1} , which is within the uncertainty of the absolute wavelength calibration of 3PAMIS. In the AR and quiet Sun (QS) corona, Fe X shows an effective velocity v_{eff} of $20\text{--}25 \text{ km s}^{-1}$, corresponding to an effective temperature T_{eff} of approximately 2 MK. On the other hand, the Fe X line in the CH, similar to other observations (e.g., [Hahn et al., 2012](#)), shows extreme broadening with $v_{\text{eff}} > 40 \text{ km s}^{-1}$. The effective temperature T_{eff} of Fe X in the CH exceeds 6 MK, suggesting the presence of significant nonthermal velocities or additional heating of the Fe X ion.

Panels a–c of Figure 5.4 depict the variation of Fe XIV 530.3 nm line intensity and widths along four different cuts in various structures. Compared to Fe XIV in the AR, the Fe XIV lines in streamers are dimmer by at least a factor of 2. Fe XIV line intensities show a nearly exponential decrease in all four regions below a heliocentric distance of approximately $1.4 R_{\odot}$. Above this distance, the Fe XIV intensity decreases more slowly with height. This behavior might be attributed to the increase in photoexcitation to populate the upper energy level, the limitation of the instrument sensitivity, or the r -dependence in the hydrostatic and isothermal atmosphere ([Aschwanden, 2005](#)) as

$$p(r) = p_0 \exp \left[-\frac{r - R_{\odot}}{\lambda_p(T_e)} \cdot \frac{R_{\odot}}{r} \right] \quad (5.1)$$

where p_0 is the pressure at the surface, r denotes the heliocentric distance, and $\lambda_p(T_e)$ is the hydrostatic scale height. The intensity drop was fitted with the hydrostatic model along the cut in the southern streamer, noting that $I(r) \propto p(r)^2$ when collisional excitation dominates (also see Discussion in Section 5.5.1.1). We found a hydrostatic scale height λ_p of approximately 100 Mm in the streamer, corresponding to a temperature of around 2 MK.

Regarding the Fe XIV line widths, they appear to be nearly constant along the two cuts in the AR, showing an effective temperature T_{eff} of approximately 2.5 - 3 MK.

The variation of Fe X 637.4 nm line intensity and width along four different cuts are shown in Panels d–f of Figure 5.4. The Fe X line intensity decreases exponentially with height up to $1.3 R_{\odot}$ along these cuts. Similar to Fe XIV, the Fe X line width in the AR slightly increases from 20 to 25 km s^{-1} between $1.0\text{--}1.3 R_{\odot}$. The Fe X widths in the QS below $1.15 R_{\odot}$ also remains relatively constant at $v_{\text{eff}} \approx 25 \text{ km s}^{-1}$. Contrarily, the Fe X line widths in the CH

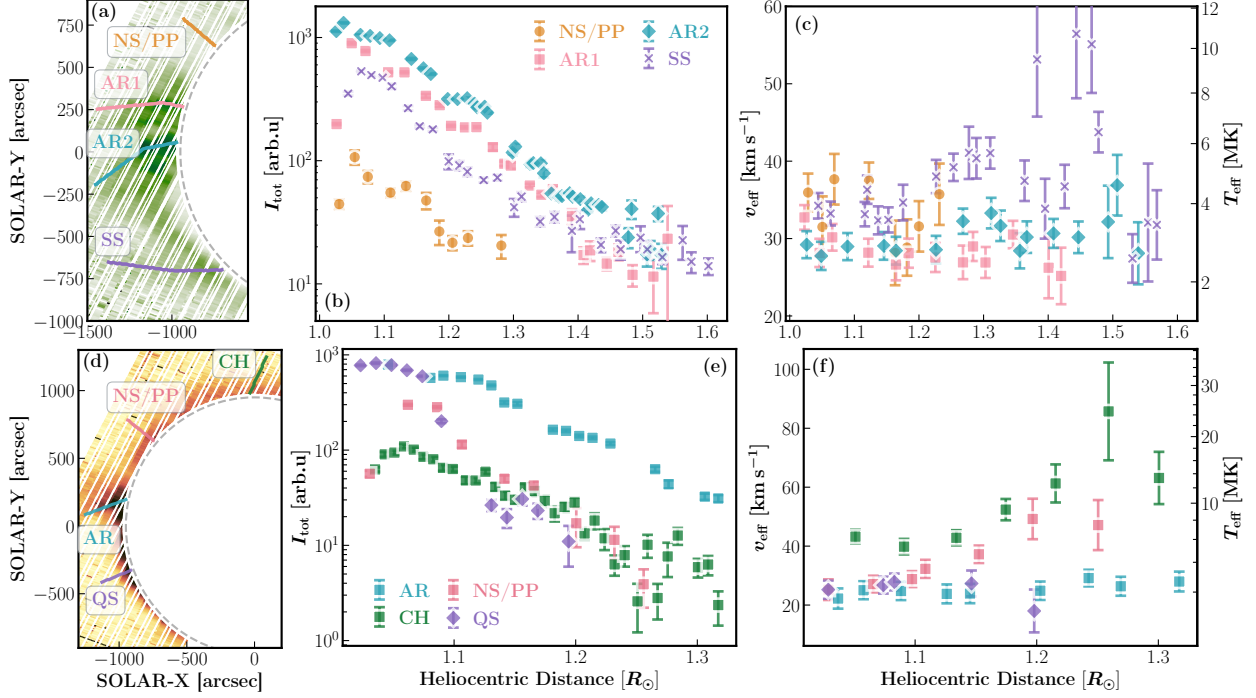


Figure 5.4: Fe XIV 530.3 nm line intensity I_{tot} (b) and line width (c) variation along four cuts: northern streamer and polar plumes (NS/PP), active region 1 (AR1), active region 2 (AR2), and southern streamer (SS). Fe X 637.4 nm line intensity I_{tot} (e) and line width (f) variation along four cuts: northern streamer and polar plumes (NS/PP), coronal hole (CH), active region (AR), and the quiet Sun (QS). Link to the `Jupyter` notebook creating this figure: [🔗](#)

show a drastic increase from 40 to 60 km s^{-1} between 1.1 and 1.2 R_{\odot} , reaching an effective temperature greater than 10 MK above 1.2 R_{\odot} . Notably, the Fe X line in the northeast region appears to be slightly broader than those in the AR below 1.1 R_{\odot} , but narrower than Fe XIV in the same region. However, its width increases from 25 to 50 km s^{-1} between 1.1–1.2 R_{\odot} , approaching the Fe X widths in the CH observed by 3PAMIS. This behavior might be attributed to the transition of the emission from the streamer cusp to polar plumes as height increases.

5.4 Comparison with Ancillary Space-based and Ground-based Data

5.4.1 Hinode/EIS

5.4.1.1 Overview and Data Reduction

Although Hinode/EIS did not acquire observations during totality, we compared the 3PAMIS observations with two EIS observations from August 21. One observation (`dhb_polar_scan`) was a raster scan of the north pole CH region, while the other (`Atlas_30`) was a QS observation with a limited FOV at the east limb. as shown in Figure 5.1.

The first CH observation was conducted from 11:08:18 to 14:44:03 UT using the 2'' slit. EIS made a 180-step raster scan with a step size of 2'', resulting in a FOV of 360'' \times 512''. The exposure time of each raster was 70 s. The center of the Fe XII 19.51 nm FOV was (308.4'', 920.9'') in the helioprojective Cartesian coordinate.

In the second observation, EIS made a 60-step raster scan of an off-limb QS region north of NOAA AR 12672 from 20:54:39 to UT 21:25:59 UT. Only 160'' along the 2'' slit were used with a step size of 2'', yielding a FOV of 120'' \times 160''. In each raster, EIS made a full CCD exposure with an exposure time of 30 s. The center pointing of EIS at Fe XII 19.51 nm was (-872.9'', 391.9'').

We downloaded the EIS level-1 HDF5 files hosted at the Naval Research Lab (NRL) website¹ and first processed them using the EIS Python Analysis Code (EISPAC)². We corrected the EIS pointing by comparing the Fe XII 19.51 nm intensity with the 19.3 nm broadband images taken by the Atmospheric Imaging Assembly (AIA; Lemen et al., 2012) on board the Solar Dynamics Observatory (SDO; Pesnell et al., 2012).

We found both EIS observations experienced data losses and hot pixels caused by the South Atlantic Anomaly (SAA), particularly in the QS observation. In addition, the off-limb signal-to-noise ratio (S/N) was too low to make a convincing fit of the spectral line widths. Therefore, additional data binning was required to increase the S/N. Since EISPAC does not support data binning along the slit, we developed our own codes to correct the slit tilt, average the data, and fit the spectral lines.

¹<https://eis.nrl.navy.mil/>

²<https://github.com/USNavalResearchLaboratory/eispac>

5.4.2 Data Analysis and Results

Figure 5.5 summarizes the EISPAC fitting results for several prominent spectral lines observed in the CH and AR data sets. The Fe XII 19.5 nm intensity map clearly outlines the boundary of the CH on the disk. Due to the data loss near the center of the FOV and the low S/N in the off-limb CH region, we averaged the EIS line profiles from three distinct regions between $1.03\text{--}1.08 R_{\odot}$, $1.08\text{--}1.13 R_{\odot}$, and $1.13\text{--}1.18 R_{\odot}$ on the left side of the EIS FOV. Additionally, we used the 2% on-disk intensity to estimate and remove the stray light in the off-limb CH (Ugarte-Urra, 2010b).

In the QS data set, data loss and the hot pixels caused by SAA were identified at the center of FOV. Similarly, we chose two regions, one spanning 1.035 to $1.06 R_{\odot}$ and the other between 1.06 and $1.1 R_{\odot}$, to average the EIS data. As the QS region is located close to the limb where the stray light intensity is negligible, and only a few rasters recorded the uncontaminated on-disk spectrum, we did not apply stray light correction to the QS data.

Figure 5.6 illustrates the relationship between T_{eff} and ion Z/A of different Fe charge states observed by EIS and 3PAMIS in the off-limb CH. To measure T_{eff} , we selected the strongest and unblended lines, including the Fe VIII 18.52 nm, Fe X 18.4 nm, Fe XI 18.82 nm, Fe XII 19.35 nm, and Fe XIII 20.20 nm lines. We only fitted the coolest Fe VIII 18.52 nm line between $1.03\text{--}1.08 R_{\odot}$ due to S/N limitations. Furthermore, the Fe X 637.4 nm line widths in the same regions are averaged for comparison.

The dependence of T_{eff} on ion Z/A , as observed by EIS, varies at different heights. Between $1.03\text{--}1.08 R_{\odot}$, Fe VIII, which has the lowest Z/A , shows the highest $T_{\text{eff}} \approx 6$ MK. The T_{eff} of the other ions gradually decreases from 4 MK to 3 MK as Z/A increases from 0.16 to 0.22. The decrease in T_{eff} for ions with $0.16 < Z/A < 0.22$ becomes more prominent at $1.08\text{--}1.13 R_{\odot}$, ranging from more than 6 MK to 2 MK. At $1.13\text{--}1.18 R_{\odot}$, T_{eff} first drops from about 7.5 MK to 3 MK at $Z/A \sim 0.18$, then gradually increases to 7 MK at $Z/A \sim 0.22$.

The Fe X 637.4 nm line width observed by 3PAMIS agrees with the Fe X 18.4 nm line width observed by EIS at $1.03\text{--}1.08$ and $1.13\text{--}1.18 R_{\odot}$. Nevertheless, between 1.08 and $1.13 R_{\odot}$, the Fe X 18.4 nm line appears to be much broader than the Fe X 637.4 nm line observed by 3PAMIS, which might be caused by the low S/N and hot pixels in EIS data set. Additionally, it should be noted that the averaging of line profiles in different rasters may include additional orbital drifts not removed by the EIS software (Kamio et al., 2019).

Figure 5.7 shows the T_{eff} measured by EIS in the QS region, along with a comparison with 3PAMIS results. Benefiting from the full CCD readout and higher S/N, more EIS lines from different ions are utilized, including the Fe IX 19.7 nm, Fe XIV 26.4 nm, Fe XV 28.4 nm, S X 26.4 nm, and Si X 25.8 nm lines. The EIS line widths in the two regions exhibit similarities, while T_{eff} at $1.06\text{--}1.1 R_{\odot}$ shows a broader distribution, likely due to the lower S/N.

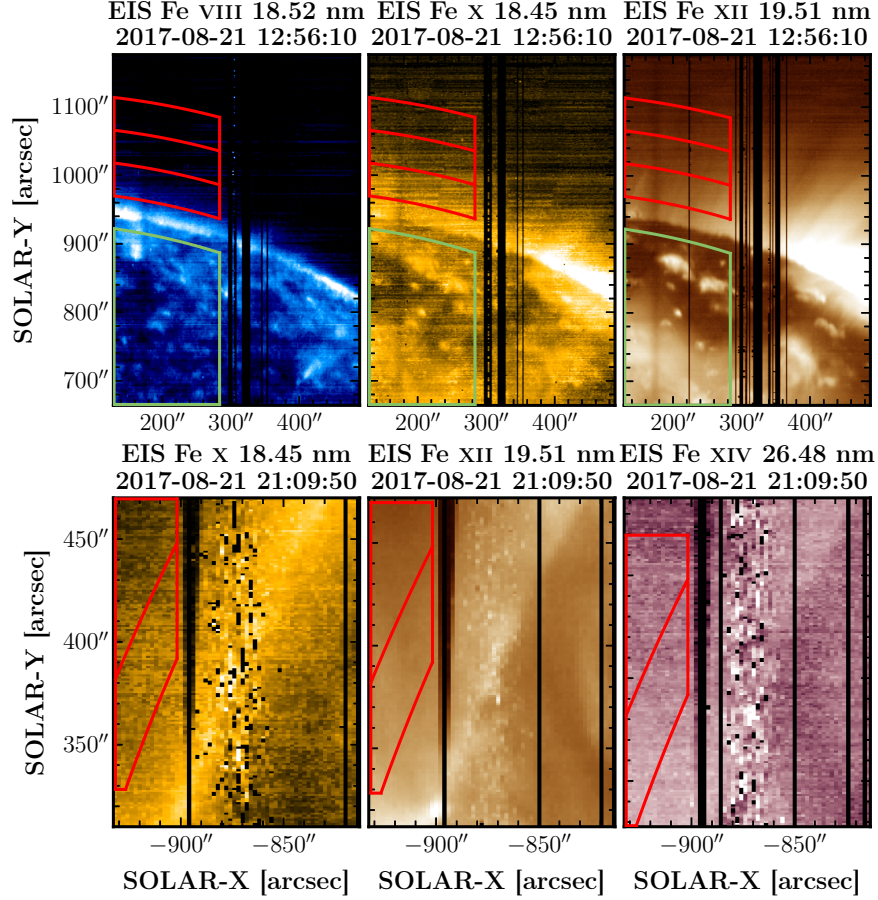


Figure 5.5: Overview of EIS line intensity fitted by EISPAC. Top: `dhb_polar_scan` observation of the CH. Bottom: `Atlas_30` observation of the east limb QS region. The red curves highlight the regions where line profiles are averaged. Profiles in the green boxes are averaged to estimate the off-limb stray light for the CH observation. Link to the `Jupyter` notebook creating this figure: [🔗](#).

Between 1.035 and $1.06 R_{\odot}$, T_{eff} for most ions observed by EIS range from 2–3 MK. Notably, the Fe VIII and Fe IX with the lowest Z/A display slightly higher temperatures compared to the other ions. However, T_{eff} does not show a distinct variation with respect to Z/A in the QS data set, which does not support the hypothesis of preferential heating of heavy ions in the QS region at 1.035 – $1.1 R_{\odot}$. Moreover, T_{eff} of Fe X and Fe XIV, independently measured by EIS in EUV and 3PAMIS in the visible, are consistent with each other.

EIS observations provide additional plasma diagnostics, including the electron density n_e and electron temperature T_e . Table 5.1 presents the measured n_e and T_e for the two QS regions, employing three different onboard radiometric corrections reported by Del Zanna (2013, GDZ), Warren et al. (2014, HPW), and the latest Del Zanna et al. (2023). The Fe XI and Fe XII diagnostics results using the latest radiometric corrections are quite different from the other two, which is probably due to the correction of the wavelength-dependent

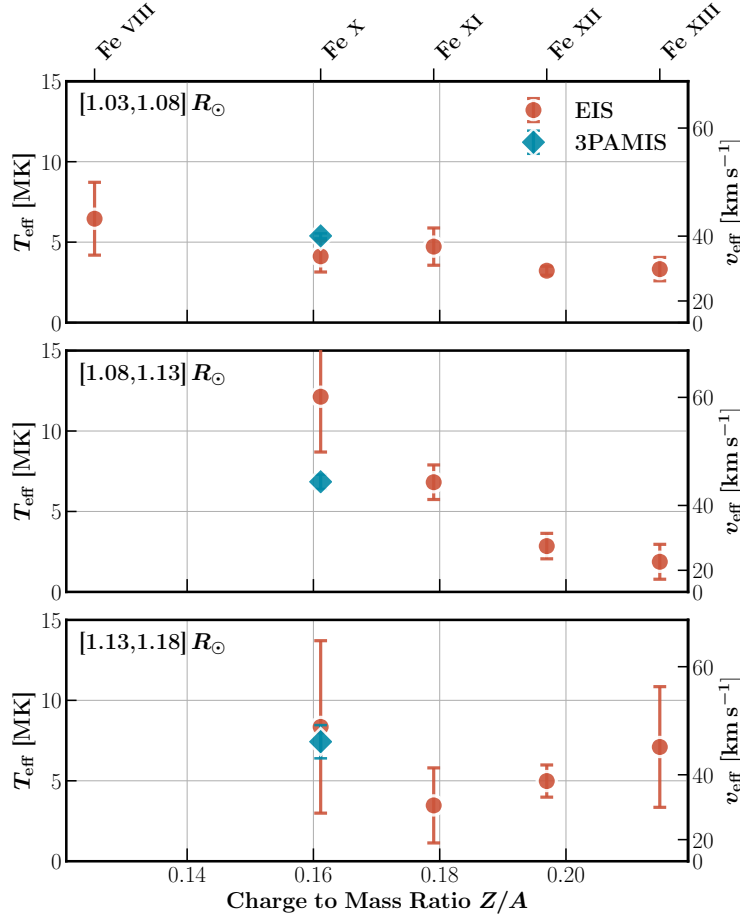


Figure 5.6: Effective temperature T_{eff} and effective velocity v_{eff} of different ions observed by 3PAMIS and EIS in the north pole coronal hole at three different heights: 1.03–1.08 R_{\odot} (top), 1.08–1.13 R_{\odot} (mid), and 1.13–1.18 R_{\odot} (bottom). Link to the Jupyter notebook creating this figure: [🔗](#).

degradation of the detectors after 2012. Notably, the new EIS radiometric calibration is still under review, so we focused on the results using the first two corrections.

Both regions show typical QS n_e and T_e (e.g., Laming et al., 1997; Kamio & Mariska, 2012; Feldman et al., 1999; Brooks et al., 2009). In Fe XII, n_e drops from $2.0 \times 10^8 \text{ cm}^{-3}$ to $1.5 \times 10^8 \text{ cm}^{-3}$, while T_e increases from 1.2 MK to 1.5 MK in Fe XI. The HPW and DDZ methods yield similar diagnostic results for Fe XII. However, the HPW method provides a higher T_e using Fe XI than the GDZ method. Additionally, n_e inferred from the Si x 25.8/26.1 ratio is much lower if the HPW method is used, amounting to about 50–60% of the GDZ values.

Consistent with numerous other observations (e.g., Hassler et al., 1990; Seely et al., 1997; Banerjee et al., 1998), we found that T_{eff} derived from the line widths are higher than T_e .

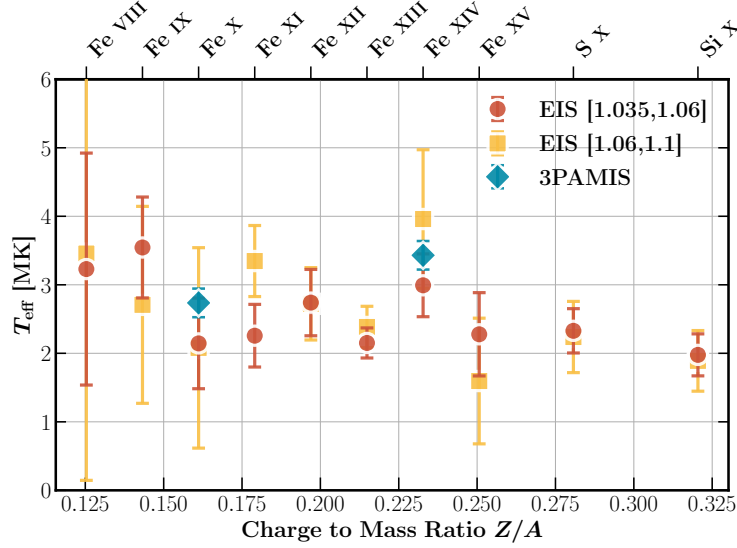


Figure 5.7: Effective temperature T_{eff} of different ions observed by 3PAMIS and EIS in the off-limb QS region. Link to the Jupyter notebook creating this figure: [🔗](#).

This implies the existence of unresolved nonthermal motions in both QS and CHs. Assuming $T_i \approx T_e$ in the QS region, we estimate a nonthermal velocity of approximately $15\text{--}25 \text{ km s}^{-1}$ for ions with $T_{\text{eff}}=2\text{--}3 \text{ MK}$. Additionally, the Z/A dependence of T_{eff} in the CH suggests preferential heating of heavy ions at the base of polar CHs.

n_e (10^8 cm^{-3})					
Ion	Line	Region	GDZ	HPW	New
Si X	25.8/26.1	1	$2.00^{+0.57}_{-0.55}$	$1.35^{+0.47}_{-0.44}$	$2.00^{+0.63}_{-0.49}$
Si X	25.8/26.1	2	$0.91^{+0.56}_{-0.49}$	< 1.36	$1.05^{+0.53}_{-0.50}$
Fe XII	18.6/19.3	1	$2.09^{+0.10}_{-0.09}$	$2.00^{+0.09}_{-0.09}$	$1.45^{+0.03}_{-0.07}$
Fe XII	18.6/19.3	2	$1.58^{+0.16}_{-0.10}$	$1.51^{+0.15}_{-0.10}$	$1.12^{+0.08}_{-0.10}$
T_e (10^6 K)					
Fe XI	18.8/25.7	1	$1.20^{+0.15}_{-0.13}$	$1.51^{+0.19}_{-0.16}$	$2.19^{+0.26}_{-0.28}$
Fe XI	18.8/25.7	2	$1.48^{+0.43}_{-0.38}$	$1.86^{+0.59}_{-0.54}$	> 1.95

Table 5.1: Electron density n_e and electron temperature T_e diagnostics of regions 1 (1.035–1.06 R_{\odot}) and 2 (1.06–1.1 R_{\odot}). Fe XII 18.68 nm and Fe XI 25.75 nm lines are self-blended. Entries in the GDZ, HPW, and New columns utilize the radiometric corrections reported by Del Zanna (2013), Warren et al. (2014), and the latest Del Zanna et al. (2023), respectively.

5.4.3 CoMP

CoMP is a tunable coronagraph located at the Manua Loa Solar Observatory (MLSO). CoMP can perform spectropolarimetric observations of Fe XIII 1074.7 and 1079.8 nm lines in the near-infrared between $1.05\text{--}1.35 R_{\odot}$. The Stokes parameters I , Q , U , and V are sampled at 3 or 5 wavelength positions across the Fe XIII profiles using Lyot filters. The three-point Stokes I profiles are inverted analytically to obtain the line intensity, Doppler shifts, and widths (Tian et al., 2013). During the 2017 August 21 TSE, CoMP carried out observations from 17:05 to 18:19 UT. We utilized the median Doppler velocity at the east limb as the zero point velocity. An instrumental width of 21 km s^{-1} was removed during the data reduction (Morton et al., 2015).

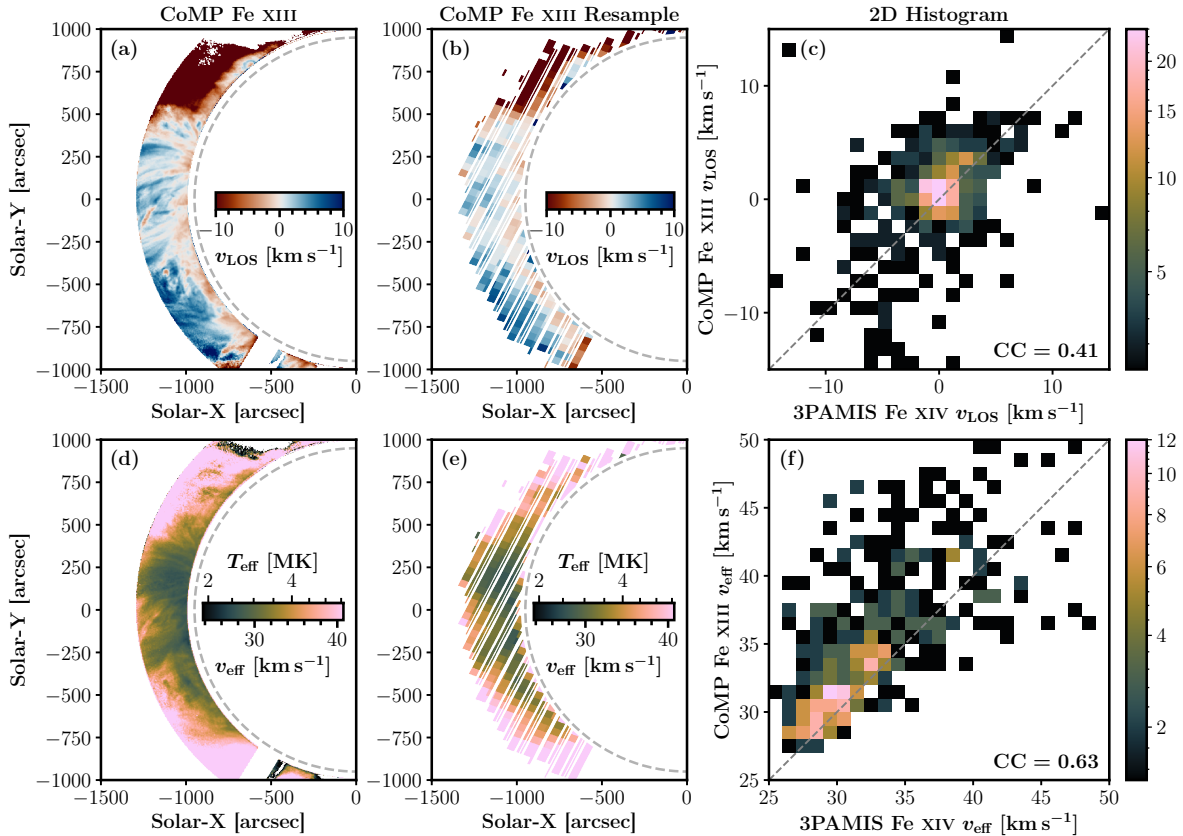


Figure 5.8: Comparison between the Doppler velocity v_{LOS} and line width observed in Fe XIII 1074.7 nm by CoMP and Fe XIV 530.3 nm 3PAMIS. (a) CoMP Doppler velocity. (b) CoMP Doppler velocity resampled to match the 3PAMIS pixels. (c) 2D histogram and Pearson correlation coefficient of the Doppler velocity measured by 3PAMIS and CoMP. (d) CoMP Fe XIII line widths. (e) CoMP widths resampled at 3PAMIS pixels. (f) 2D histogram and Pearson correlation coefficient of the widths measured by 3PAMIS and CoMP. Link to the Jupyter notebook creating this figure: [🔗](#).

We compared the inverted Doppler velocities and line widths from the CoMP average file with 3PAMIS observations in Figure 5.8. We focused on the comparison of the Fe XIV line widths and Doppler velocity, given its proximity in the formation temperature of Fe XIII observed by CoMP. To make a fair comparison, the CoMP values were resampled at the same pixel scales as 3PAMIS and compared with 3PAMIS values using 2D histograms.

In agreement with 3PAMIS observations, the northern streamer is dominated by a redshift of approximately 10 km s^{-1} . The equatorial AR, on the other hand, shows no significant Doppler shifts greater than 5 km s^{-1} , which slightly differs from the tiny redshifts in 3PAMIS observations. In the southern streamers, blueshifts ranging from 5 to 10 km s^{-1} were found in CoMP observations, slightly greater than 3PAMIS values. In addition, some minor redshifts of less than 2 km s^{-1} were observed at the bottom of the FOV. The 2D histogram reveals some correlation between the Doppler velocity measured by CoMP and 3PAMIS, with a Pearson correlation coefficient of 0.41. Moreover, no significant systematic Doppler shifts $> 2 \text{ km s}^{-1}$ were found between the 3PAMIS and CoMP observations. Most differences in Doppler shifts are within the uncertainty of 5 km s^{-1} in the 3PAMIS absolute wavelength calibration.

The line widths observed by CoMP and 3PAMIS also reveal a high level of agreement. The line widths obtained by CoMP are narrower in the equatorial regions, corresponding to $T_{\text{eff}} \approx 3 \text{ MK}$. In contrast, broader line profiles ($T_{\text{eff}} > 4 \text{ MK}$) were found in the northern and southern streamers. The 2D histogram confirmed a good correlation between v_{eff} observed by CoMP and 3PAMIS from 25 – 35 km s^{-1} , predominantly from the equatorial AR and the streamer structures in the vicinity. Notably, in the data bins with a count of more than 5, CoMP widths were found to be 1 – 3 km s^{-1} (approximately 5 – 10%) greater than the widths observed by 3PAMIS.

5.4.4 Comparison with Other Observations

Koutchmy et al. (2019, hereafter K19) performed a slit spectroscopic experiment during the 2017 TSE and recorded coronal deep spectra from 510 nm to 590 nm at six different positions. Fortunately, two positions (Positions 1 and 4) were at the east limb, overlapping with the FOV of 3PAMIS. Fe XIV line widths along these two positions, as digitized from Figures 8 and 9 of K19, are compared with 3PAMIS observations in Figure 5.9. Position 1 passes the AR and southern streamer, while Position 4 only covers the southern streamer.

Overall, the Fe XIV line widths v_{eff} observed by 3PAMIS were found to be approximately 40% greater compared to those reported by K19. However, 3PAMIS and K19 revealed similar trends in the variation of line widths. Along Position 1 (AR), 3PAMIS observed a relatively

constant $T_{\text{eff}} \approx 3$ MK, while K19 found a lower $T_{\text{eff}} \approx 1.6$ MK. In the southern streamer, both 3PAMIS and K19 exhibited an increase in Fe XIV line widths with height. In 3PAMIS observations, Fe XIV T_{eff} slightly increased from approximately 3 MK to 4 MK between 1.1–1.3 R_{\odot} . On the other hand, T_{eff} in K19 decreased from 3 to 1.5 MK between 1.0 and 1.15 R_{\odot} , followed by a gradual increase to 3.5 MK at 1.6 R_{\odot} . The differences between the 3PAMIS and K19 could be attributed to the uncertainty in instrumental widths and/or uncertainty in the coalignment between the two instruments.

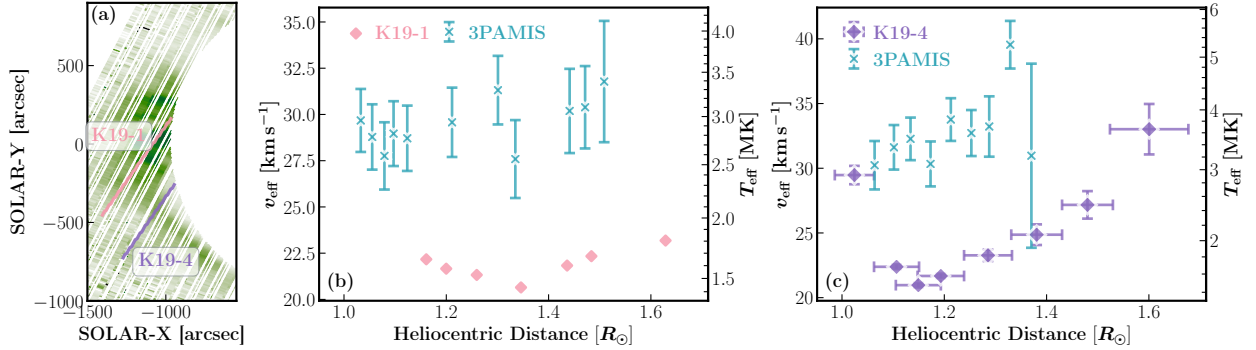


Figure 5.9: Comparison between the Fe XIV 530.3 nm line widths given as effective velocity v_{eff} in (b) and effective temperature T_{eff} (c) measured by Koutchmy et al. (2019) (red) and 3PAMIS along the slit position 1 (K19-1) and 4 (K19-4) shown in panel (a). Koutchmy et al. (2019) (blue, purple). Link to the Jupyter notebook creating this figure: [🔗](#).

5.5 Discussion

5.5.1 Line Widths and Their Variation with Height: Open and Closed Fields

The Fe X and Fe XIV line profiles observed by 3PAMIS during the 2017 TSE reveal substantial line width variations within and between different structures, especially between the open and closed field regions. In the open fields, line widths are observed to be broader and to increase with height below 1.3 R_{\odot} , while the line widths in closed fields appear to be narrower and nearly constant.

In Figure 5.10, we compared the observed line widths in different open- and closed-field regions during the TSE with the observed line widths reported by a great number of previous studies. These studies used UV or visible emission lines with similar formation temperatures to Fe X and Fe XIV. The lithium-like ions are also labeled because they usually have high-temperature tails in the equilibrium charge state population. Notably, the absolute

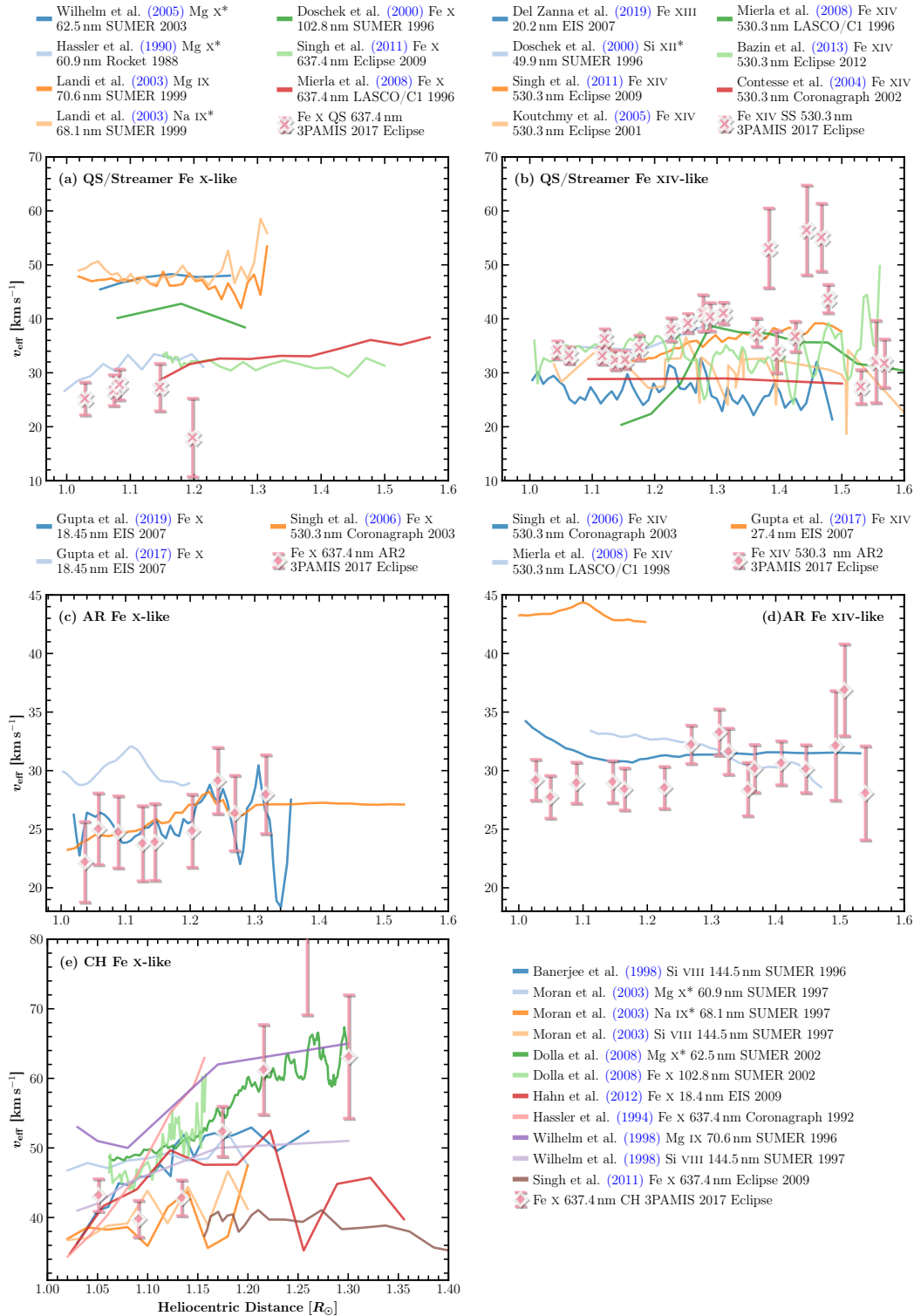


Figure 5.10: Comparison of the line widths variation different structures observed by 3PAMIS and other instruments, along with the spectral lines and years of observation. Lithium-like ions are labeled by *. Data is digitized from the listed publications. Link to the [Jupyter notebook](#) creating this figure: [🔗](#).

magnitudes of v_{eff} are not necessarily the same because of different ion masses and plasma conditions.

The line width variations observed by 3PAMIS are in general agreement with the previous studies using UV and visible observations, which reveal minor variations in the closed fields and an increase in the open fields. For instance, a similar increase-then-decrease Fe XIV widths in the streamer was also reported by Mierla et al. (2008).

To effectively address the differences in line widths across various structures or heights, we need to consider both changes in the local parameters, such as ion temperature and non-thermal velocity, and the potential influence of radiative processes on the line width. These processes may include the integration of emission with divergent Doppler shifts along the LOS, nonequilibrium ionization, photoexcitation, and resonant scattering (Gilly & Cranmer, 2020).

We chose not to delve into the nonequilibrium ionization in this paper for two primary reasons. First, it requires the comprehensive modeling of the coronal and solar wind plasma, which is beyond the scope of this work. Second, the nonequilibrium ionization does not directly affect the widths of local emissivity, while it potentially modifies the profiles through the LOS integration.

5.5.1.1 Photoexcitation and Resonant Scattering

As the height increases and density decreases, photoexcitation and resonant scattering become increasingly important. The visible forbidden lines are photoexcited by the white light continuum emission from the photosphere. Except for the Fe I 530.23 nm line at the blue wing of Fe XIV 530.3 nm, the continuum has no other features and does vary significantly across the profile. Therefore, for Case I scattering between two sharp levels, the Gaussian-like photon redistribution function will convolve with the nearly flat continuum, resulting in a Gaussian emissivity profile. The width of the Gaussian emissivity is still determined by v_{eff} , as explained in Appendix D. This is in contrast to the strong UV lines (e.g., Mg x, O VI, and Ly α), as they could be photoexcited by their profiles from the disk, affecting the width of the local emissivity profile.

Additionally, we estimated the contribution of photoexcitation to populate the upper energy level of Fe XIV in Figure 5.11, using the electron density inferred from Fe XIII 1074/1079 ratios observed by CoMP. The photoexcitation and three other collisional processes are considered, including electron and proton collisions and radiative decay from higher, collisionally-populated levels. Due to the limitation of the CoMP FOV and S/N, we extrapolated the n_e to $1.5 R_{\odot}$, assuming an exponential decrease. In the AR at $1.5 R_{\odot}$, where $\log n_e \approx 7.3$, photoexcitation only contributes a maximum of 40% of the population.

In the streamer, the photoexcitation dominates the level population where $\log n_e$ drops to 7.0 at $1.5 R_\odot$. Therefore, we suggest that the photoexcitation and resonant scattering may not play a significant role in broadening the spectral lines in the AR and streamers below $1.5 R_\odot$ as observed by 3PAMIS, in agreement with early studies by [Raju et al. \(1991\)](#).

5.5.1.2 LOS Integration

Emissions originating from multiple structures with various macroscopic Doppler velocities or line widths can integrate along the LOS in the optically thin plasma. This effect might be evident in the open-field structures where fast outflows in the lower corona are expected. Consequently, different Doppler shifts along the LOS may broaden profiles in the open-field structures (e.g., [Akinari, 2007](#); [Zhu et al., 2023](#)).

On the other hand, the relatively constant line width in closed-field structures suggests that the integration of multiple structures along the LOS might not play an important role in the broadening of closed-field profiles. This implication is also supported by the fact that the v_{eff} of approximately 25 km s^{-1} measured in a single AR loop ([Gupta et al., 2019](#)) is quite similar to the Fe x v_{eff} obtained by 3PAMIS. If the LOS integration is important, 3PAMIS, with its low spatial resolution, should have observed a larger excess width in the core of AR, where several coronal loops overlap along the LOS, which was not the case.

[Gilly & Cranmer \(2020\)](#) found the relatively constant line width in the lower corona might be an illusion caused by the LOS integration below the height where the density of the ion charge state reaches its maximum. According to their polar CH and streamer model, they suggested that the Fe x 18.45 nm line width appears constant below 20 Mm, and the width of Si XII, which has a similar formation temperature to Fe XIV, remains constant below 200 Mm. In contrast, during the eclipse, we observed constant line widths up to 200 Mm (Fe x) and 350 Mm (Fe XIV) in the AR. Furthermore, the off-limb AR region consists of the hottest and densest plasma near the POS, surrounded by cooler and more tenuous QS regions, which is opposite to the conditions in the polar CHs. Hence, we argue that the constant line widths cannot be solely explained by the plateauing effect proposed by [Gilly & Cranmer \(2020\)](#).

Finally, the open and close-field structures may overlap along the LOS, which makes it more challenging to interpret the behaviors of line widths (e.g., [Zhu et al., 2021](#)). This often occurs at the boundary of the open and closed-field regions, such as the variation of Fe x widths in the northern stream and polar plumes regions and Fe XIV widths in the southern streamer observed by 3PAMIS (see Figure 5.4f).

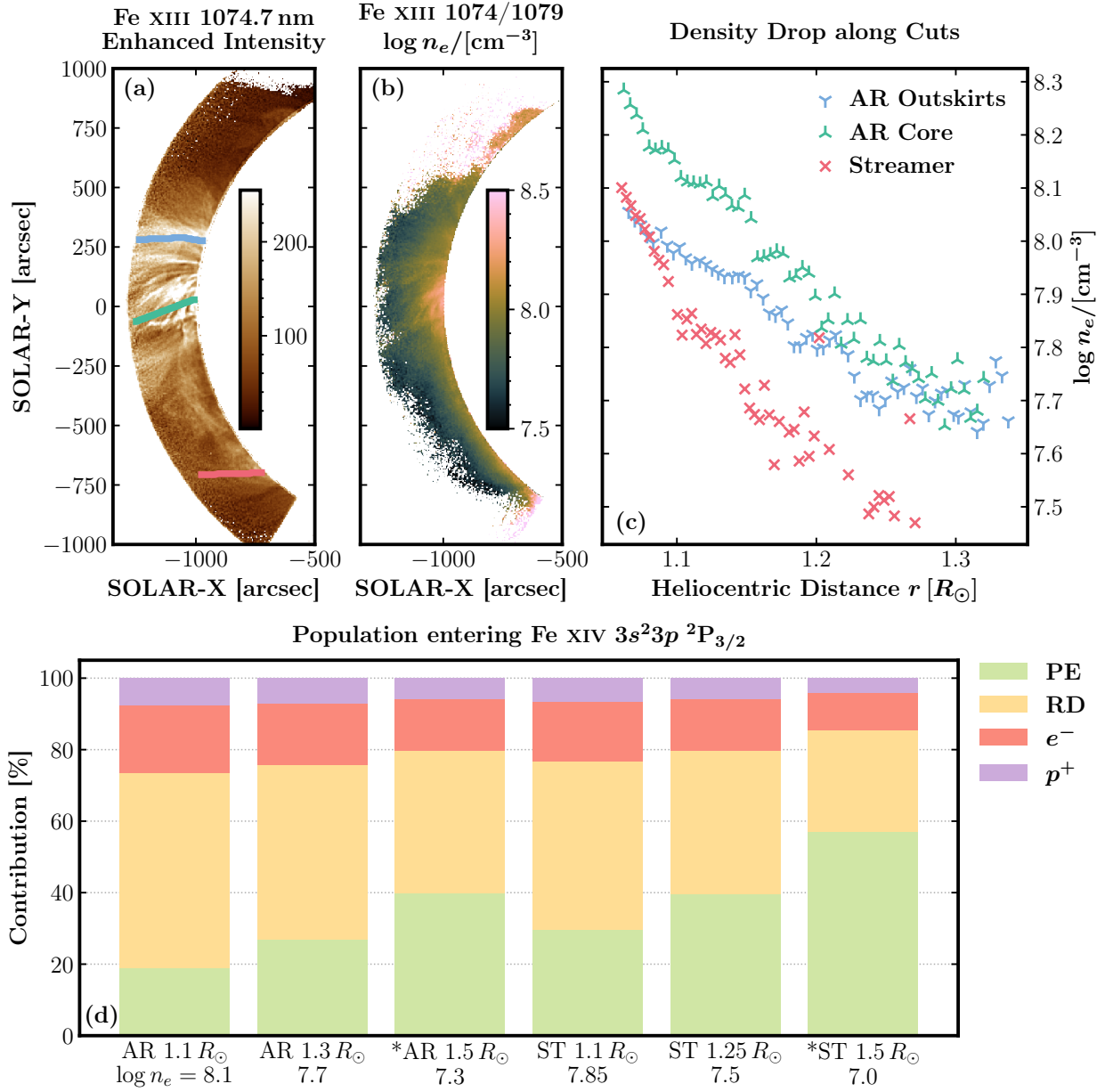


Figure 5.11: Electron density n_e measured by CoMP and the excitation of the upper energy level of Fe XIV. (a) Fe XIII 1074.7 nm intensity enhanced by a radial intensity filter. (b) Electron density n_e inferred by Fe XIII 1074/1079 ratio. (c) Decrease in n_e along the three cuts shown in Panel a. (d) Population entering the upper energy level of Fe XIV 530.3 nm by different processes at various densities and heights. PE: photoexcitation; RD: radiative decay through cascades from higher levels; e^- : collisions with electrons; p^+ : collisions with protons. $*n_e$ is extrapolated, assuming an exponential drop with height. Link to the Jupyter notebook creating this figure: [🔗](#).

5.5.1.3 Preferential Heating

Low Z/A ions like Fe x are found to be preferentially heated by ion cyclotron waves in CHs, creating excessive thermal broadening (e.g., Tu et al., 1998; Dolla & Solomon, 2008; Landi & Cranmer, 2009). In this study, the excessive heating to Z/A ions, such as Fe VIII, Fe x, and Fe XI, was also found in the EIS observation of the polar CH. Previous studies reported $T_{\text{eff}}=4\text{--}6$ MK for Fe x at the base of a polar CH during the solar minimum (Hahn et al., 2010; Zhu et al., 2023), which is consistent with 3PAMIS and EIS observations during the 2017 TSE.

In principle, the constant Fe XIV widths in QS and streamers could potentially be dominated by thermal broadening when nonthermal motions are negligible (Muro et al., 2023). However, this scenario suggests excessive heating of both Fe x and Fe XIV with charge-to-mass ratios (0.16 and 0.23, respectively) in the QS corona.

In contrast to Muro et al. (2023), EIS and 3PAMIS found no evidence of preferential heating in the QS plasma, in agreement with Landi (2007) who studied the QS plasma during solar minimum. In ARs, frequent collisions between ions and electrons can result in $T_i \approx T_e$ (Hara & Ichimoto, 1999). This is a common assumption supported by observations (e.g., Imada et al., 2009) and simulations (e.g., Shi et al., 2022).

Incorporated with the assumption of $T_i = T_e$, we used the measurements of T_e made by Boe et al. (2020) during the 2017 TSE to calculate the nonthermal widths of Fe x and Fe XIV in Figure 5.12. The electron temperatures are inferred by the intensity ratio between Fe XI 789.2 nm and Fe XIV 530.3 nm, which is sensitive to temperatures ranging from 1–2 MK. These two assumptions could introduce uncertainties because (1) T_i may deviate from T_e and (2) Fe XI and Fe XIV emissions may not originate from the same plasma structure along the LOS. The measured T_e in the close field regions ranges from 1.2 MK to 1.4 MK and does not show significant variations with height. Therefore, the distribution and variation of nonthermal widths in the off-limb corona look similar to that of total line widths. The nonthermal velocity ξ appears to be minimal and constant in the AR, with a value of approximately 15–20 km s⁻¹. Fe x ξ exceeds 40 km s⁻¹, suggesting the assumption $T_i \approx T_e$ might fail in these open field regions.

5.5.1.4 Wave or Turbulence-induced Nonthermal Motions

Nonthermal broadening in coronal emission lines has been widely attributed to the propagation of Alfvénic waves, including torsional Alfvén and kink modes, as well as turbulence (e.g., Seely et al., 1997). Essentially, the product of Alfvén wave energy flux and the flux tube cross-section is proportional to $n_e^{1/2}\xi^2$ (Hassler et al., 1990). Therefore, the wave prop-

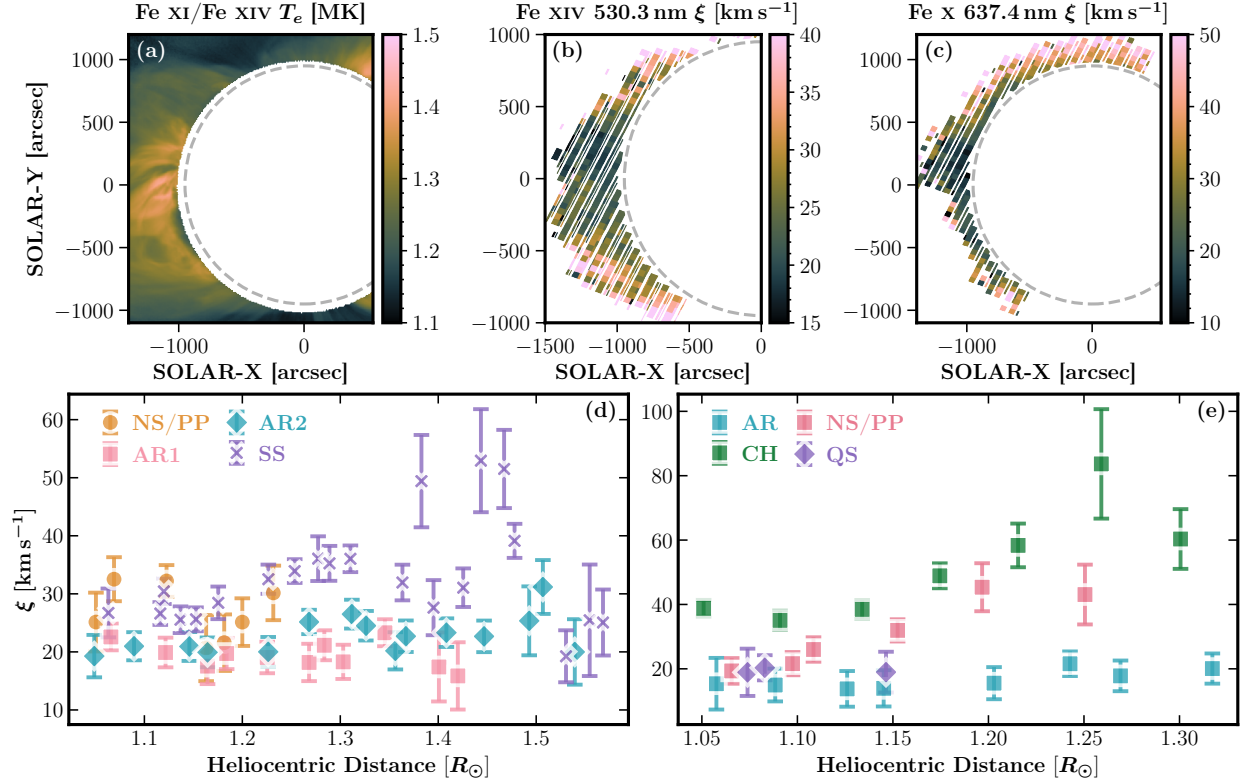


Figure 5.12: (a) Electron temperature T_e measured by Boe et al. (2020) using the Fe XI 789.2 nm and Fe XIV 530.3 nm ratio. (b) and (c) Nonthermal velocity ξ in Fe XIV 530.3 nm and Fe X 637.4 nm lines. (d) and (e) Nonthermal velocity along the cuts shown in Figure 5.4. Link to the Jupyter notebook creating this figure: [🔗](#).

agation theory, as $\xi \propto n_e^{-1/4}$ in the undamped regime, particularly favors the increase of line widths in the open fields (e.g., Dolla & Solomon, 2008; Banerjee et al., 2009).

The wave propagation may also result in narrower lines in closed fields. The wave energy flux leaked from the lower atmosphere should be relatively uniform across large scales, particularly in CHs and the QS, where the lower atmospheres are similar. Given $\xi \propto n_e^{-1/4}$, ξ has to be greater in open fields with lower density. Additionally, the nonlinear Alfvén turbulence generated by the counter-propagating waves may dissipate the wave energy more efficiently in closed field regions (van der Holst et al., 2014).

In the closed fields, relatively constant line widths, if caused by waves or turbulence, may imply wave or turbulence dissipation in the lower corona. For instance, the constant nonthermal width shown in Figure 5.12, if solely attributed by Alfvén waves, would imply a decrease in the wave energy flux due to the density decrease with height. If the density drops by an order of magnitude from 1.0–1.5 R_\odot in the AR, as shown in Figure 5.11, the wave energy will decrease by 60–70%. Considering typical values of $\xi \approx 15 \text{ km s}^{-1}$, $\log n_e \approx 9$, and $B \approx 20 \text{ G}$

at the base of AR, the resulting Alfvén wave energy flux is approximately $10^6 \text{ erg cm}^{-2} \text{ s}^{-1}$. This energy flux is insufficient to heat AR corona ($10^7 \text{ erg cm}^{-2} \text{ s}^{-1}$, [Withbroe & Noyes, 1977](#)).

On the other hand, even if the plasma is multithermal along the loop, the constant line width in the AR may still imply the existence of wave damping in ARs. To illustrate this, let's consider a simple case where $v_{\text{eff}} \approx 30 \text{ km s}^{-1}$ in Fe XIV is contributed by $T_i = 2 \text{ MK}$ and $\xi = 17 \text{ km s}^{-1}$ at the base of the AR. If the waves are undamped and density drops by an order of magnitude, the new $\xi' = 10^{1/4}\xi \approx 30 \text{ km s}^{-1}$ would dominate the line broadening if the v_{eff} remains nearly constant in ARs. Therefore, we should still consider the possibility of wave damping or other nonthermal motions not caused by wave propagation.

5.5.1.5 Other Nonthermal Motions

Despite the relatively constant line widths in closed-field structures could be evidence of wave damping in the closed fields (e.g., [Gupta et al., 2019](#)), an alternative explanation is that the nonthermal width ξ in closed fields does not primarily arise from MHD waves or turbulence. In fact, a component ξ_{\parallel} parallel to the magnetic fields is often observed in on-disk ARs (e.g., [Brooks & Warren, 2016](#); [Prabhakar & Raju, 2022](#)), which cannot be simply explained by the Alfvénic waves because the perturbation is perpendicular to the local magnetic fields (e.g., [Shi et al., 2022](#)). For example, [Asgari-Targhi et al. \(2014\)](#) had to introduce a parallel component ξ_{\parallel} with the Alfvén wave turbulence model to reproduce the ξ observed by Hinode/EIS.

A few studies of the anisotropy of the nonthermal velocity confirm the existence of ξ_{\parallel} , but found different relationships between the two components ξ_{\parallel} and ξ_{\perp} , including $\xi_{\parallel} > \xi_{\perp}$ ([Hahn et al., 2023](#)) and $\xi_{\parallel} < \xi_{\perp}$ ([Hara & Ichimoto, 1999](#)). The possible candidates to create ξ_{\parallel} and the relatively constant nonthermal widths in closed fields include reconnections (e.g., jets and nanoflares) or slow mode waves ([Hahn et al., 2023](#)), but it is still difficult to have a firm conclusion ([Brooks & Warren, 2016](#)).

Additionally, [Singh et al. \(2002, 2006\)](#) proposed that the conduction between the warm and cold plasma within a single coronal loop could lead to a mixture of thermal and nonthermal motions below $1.3 R_{\odot}$. This conjecture is supported by observations showing a slight decrease in Fe XIV widths, an increase in Fe X width, and similar line widths between Fe X and Fe XIV from $1.2\text{--}1.3 R_{\odot}$ in the AR. Furthermore, other spectroscopic observations have suggested the existence of multi-strand (multi-thermal) loop cross-sections (e.g., [Aschwanden et al., 2013](#)). However, the scenario does not provide a clear explanation for the nature of the nonthermal motions and how they mix with each other within the multi-thermal plasma. A future study using coordinated spectroscopic observations in visible and EUV will provide new insights to explore this scenario.

5.5.2 Doppler Shifts in the Corona

Significant Doppler shifts greater than 5 km s^{-1} were only observed in Fe XIV 530.3 nm line in the northern and southern streamers, while the Fe X 637.4 nm line does not show any notable Doppler shifts. Interestingly, a redshift of approximately 10 km s^{-1} observed in the northeast region only appeared in Fe XIV, suggesting the presence of bulk motions in the 2 MK plasma. We argue that this redshift results from the plasma motions occurring at the boundary of open and closed-field structures, which is often suggested as the source region of the slow solar wind (e.g., [Antiochos et al., 2011](#)). Since the LOS component is approximately 10 km s^{-1} , the total outflow velocity may easily exceed 10 km s^{-1} . The upcoming 2024 TSE will be another unique opportunity to study the properties of these outflows, as the Solar Orbiter spacecraft ([Müller et al., 2020](#)) will be in quadrature with the Earth during the eclipse. The stereoscopic observations of plasma flows in the lower corona will provide new insights into their source regions and evolution.

CHAPTER 6

Conclusion and Future Works

6.1 Summary

This dissertation presents measurements of spectral line widths in closed- and open-field structures of the solar corona. The measured spectral line widths were used to estimate the nonthermal motions and ion temperatures in the corona. The nonthermal velocity provides constraints on the MHD wave amplitudes in the solar corona, while the ion temperature offers a probe into the ion cyclotron wave heating. Therefore, the dissertation provides new insights into the coronal heating problems, especially into the wave heating models.

However, it's important to note that these observations may be affected by instrumental stray light, LOS integration, and other instrumental limitations such as the wavelength coverage required to survey more ions or the FOV necessary to observe the open and closed fields simultaneously. To address these issues, this dissertation analyzes spectroscopic observations from various spectrographs, including eclipse observations with an extended FOV, and forward models the spectral line profiles using global MHD simulations.

To study line width variation in the open-field regions, Chapter 3 presents the Fe XII 192.4, 193.5, and 195.1 Å and Fe XIII 202.0 Å line widths in a polar coronal hole up to $1.5 R_{\odot}$ observed by Hinode/EIS. Observed line widths first increase between 1.0 – $1.05 R_{\odot}$ and then start to fluctuate within a range of approximately 0.05 – 0.1 Å, while the instrumental stray light does not significantly affect line widths measurements below $1.4 R_{\odot}$.

The LOS contamination is studied by the forward modeling of spectral line profiles using AWSoM and SPECTRUM. The synthetic line widths are much narrower by around 0.03 Å) below $1.3 R_{\odot}$ and increase monotonically from 0.03 to 0.07 Å between 1.0 and $1.5 R_{\odot}$. We suggest that the off-limb Fe XII emission in both simulations and observations is significantly contaminated by the emission from a streamer at the far side. The discrepancy between the model and observations may indicate that either AWSoM underestimates the nonthermal broadening in the streamer or AWSoM overestimates the contamination from the streamer.

To improve our knowledge of the preferential heating of heavy ions, Chapter 4 estimates possible T_i intervals $[T_{i,\min}, T_{i,\max}]$ at the polar coronal hole boundary observed by Hinode/EIS and SOHO/SUMER. The two instruments extend the Z/A coverage and allow us to study the dependence of T_i on Z/A between 0.125 and 0.37. Heavy ions with $0.12 < Z/A < 0.2$ and $0.33 < Z/A < 0.35$ are preferentially heated by a factor of 1.5 – 3 compared to electrons at the base of the coronal hole boundary. The T_i intervals show a nonmonotonic, U-shaped dependence on Z/A of heavy ions, which is inconsistent with the traditional cascade models of the ion-cyclotron resonance (Landi & Cranmer, 2009). These results are further validated with AWSoM-R simulations.

Besides, we found the EIS instrumental width is one of the most significant contributors to the uncertainty of the T_i measurement. We derived a narrower EIS instrumental width $\Delta\lambda_{\text{inst,EIS}} = 62.7 \text{ m\AA}$ by comparing the widths of O VI 184.1 Å and O VI 1032/1037 Å lines, which yields more consistent $[T_{i,\min}, T_{i,\max}]$ measurements between EIS and SUMER.

To provide simultaneous measurements of line widths in open and closed-field structures, Chapter 5 presents spectroscopic observations of the Fe x 637.4 nm and Fe XIV 530.3 nm visible forbidden lines during the 2017 TSE. Benefiting from the large FOV of 3PAMIS with its $4 R_\odot$ long slit, we analyzed the line intensity, Doppler shifts, and broadening across various corona structures at the east limb up to $1.5 R_\odot$, including an AR, streamers, and a polar CH. We found distinct behaviors of the line widths between open and closed-field regions. In the closed fields, the line widths are narrower, ranging from 20 to 30 km s^{-1} , and relatively constant. In contrast, the line widths in open fields are broader ($> 40 \text{ km s}^{-1}$) and increase with height between $1.0\text{--}1.3 R_\odot$.

Supplementary observations from Hinode/EIS and CoMP provide consistent measurements of the line widths and support our discoveries. The EIS observations extend our analysis of other heavy ion line widths in CH and QS regions. We discussed various underlying mechanisms, such as wave propagation, preferential heating, the LOS integration effect, and other nonthermal motions that may affect line widths in open- and closed-field structures. The wave-induced nonthermal velocity, which increases with the density drop in the solar corona, might contribute to the difference of line widths in open and closed structures.

This dissertation unveils the potential of combining various spectroscopic observations, particularly during TSEs, in combination with global MHD simulations to probe the wave heating of the solar corona via wave-induced non-thermal motions and the preferential heating of heavy ions probably due to the ion cyclotron resonance. The observed differences in the spectral line widths with distance in these distinct coronal structures indicate the predominance of wave heating in open structures versus localized heating in closed structures.

The findings of the nonthermal velocity variation from approximately 30 to 80 km s⁻¹, the preferential heating of heavy ions by a factor of 1.5 to 3 compared to electrons in open structures, as well as the relatively constant line widths in closed fields, provide crucial constraints on the wave heating models.

For future eclipse observations, improvements in the effective area of the spectrograph will empower us to measure Doppler shifts and line widths in the higher corona, for instance, the Fe x width variation above 1.3 R_{\odot} in CHs. Historically, this region was seldom explored by UV observations of lines forming at ~ 1 MK (see Figure 5.10e) due to the sharp decrease in line intensity and instrumental stray light. Therefore, it would be of great interest to continue the spectroscopic observations of Fe x 637.4 nm, and other visible forbidden lines during TSEs to shed light on the mysteries of the solar corona.

6.2 Ongoing and Future Plans

This section discusses several ongoing and future efforts to deepen our knowledge of line broadening in various coronal structures, also incorporating additional diagnostics, for instance, the coronal magnetic field.

6.2.1 AWSoM Simulation of the 2017 TSE

We continue to carry out the AWSoM simulation for the 2017 TSE. The forward modeling of Fe XIV 530.3 nm and Fe x 637.4 nm profiles discussed in Chapter 5 has been enriched by [Szente & Landi \(in prep\)](#) that added the photoexcitation into SPECTRUM. For the model setup, a GONG-ADAPT magnetogram on Aug 26 was utilized to properly model the off-limb AR emission when the AR rotated to the disk center. The Alfvén wave Poynting flux to field strength ratio S_A/B is $5 \times 10^5 \text{ W m}^{-2} \text{ T}^{-1}$ to create a typical AR temperature of 2–2.5 MK, which is slightly higher than observed values ([Boe et al., 2020](#)).

Figure 6.1 shows the synthetic line intensity to continuum ratio, Doppler shifts, and line widths of Fe XIV 530.3 nm and Fe x 637.4 nm, made by the new SPECTRUM module with photoexcitation. The white light continuum is calculated using a limb darkening factor $\mu = 0.5$. A substantial number of observed features in Fe XIV line profiles have been reproduced in AWSoM, such as the intensity enhancement in the off-limb AR and redshifts in the northeastern streamer regions. Most importantly, the narrower Fe XIV line widths in the AR and cusp streamers are accurately captured in the AWSoM simulation due to the low wave-induced nonthermal broadening, as previously suggested in Chapter 5.

Most of the Fe x emission in AWSoM forms close to the limb. Similar results were found

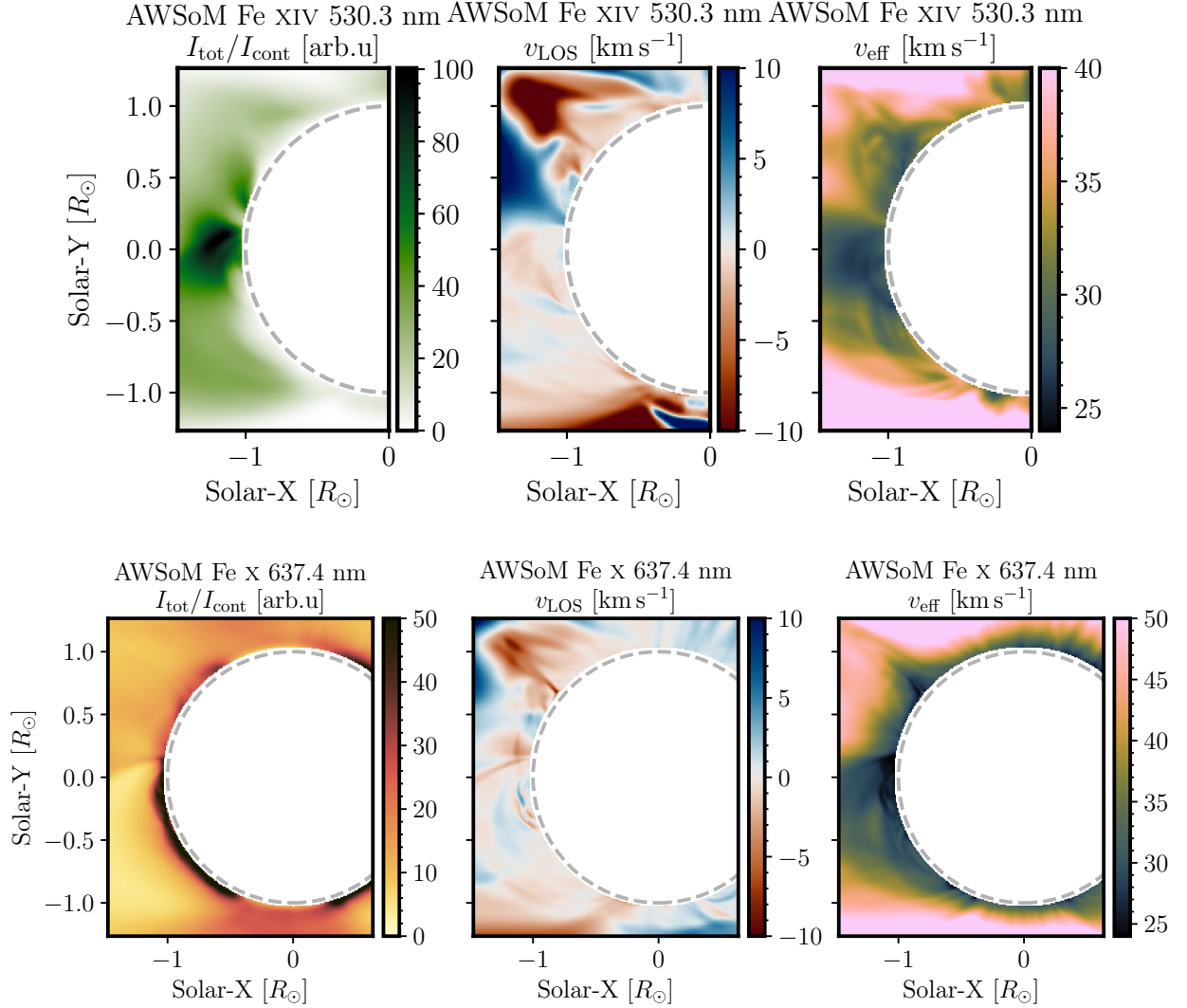


Figure 6.1: Synthetic intensity to continuum ratio, Doppler shifts, and line widths of Fe XIV 530.3 nm (top row) and Fe X 637.4 nm (bottom row).

in the MAS simulation of the 2019 TSE (Boe et al., 2022). AWSoM successfully predicted the Fe X emission at the bottom of cusp streamers shown in Fe XIV, narrower line widths in the closed fields, and an increase in Fe X line widths in polar CHs. Nevertheless, the Fe X line widths were narrower than observed at the base of polar CH, also found in Chapter 4 due to the lack of preferential heating of heavy ions in AWSoM.

The most prominent discrepancy between synthetic and observed emission is the enhancement of Fe X intensity at the edge of the off-limb AR. Although a fan-like structure can be identified in the synthetic Fe X intensity, it does not capture similar intense Fe X emission observed by 3PAMIS. This might be related to the limitation of spatial resolution and bot-

tom boundary conditions in AWSoM to reproduce the cool AR loops and outflow at AR edges.

Future studies, such as examining the distribution of emissivity and line widths along the LOS performed in Chapters 3 and 4 will be carried out to refine our insights into the diverse behavior of line widths in the open and closed fields.

6.2.2 Ion Temperature in Post-flare Active Regions

Beyond ion temperatures T_i in QS and CH studied by Landi (2007); Landi & Cranmer (2009), T_i in ARs are rarely investigated (e.g., Imada et al., 2009). We applied the same T_i diagnostic method introduced in Chapter 3 on a SOHO/SUMER observation (see Figure 6.2) of an off-limb post-flare AR to study ion temperatures of the post-flare plasma.

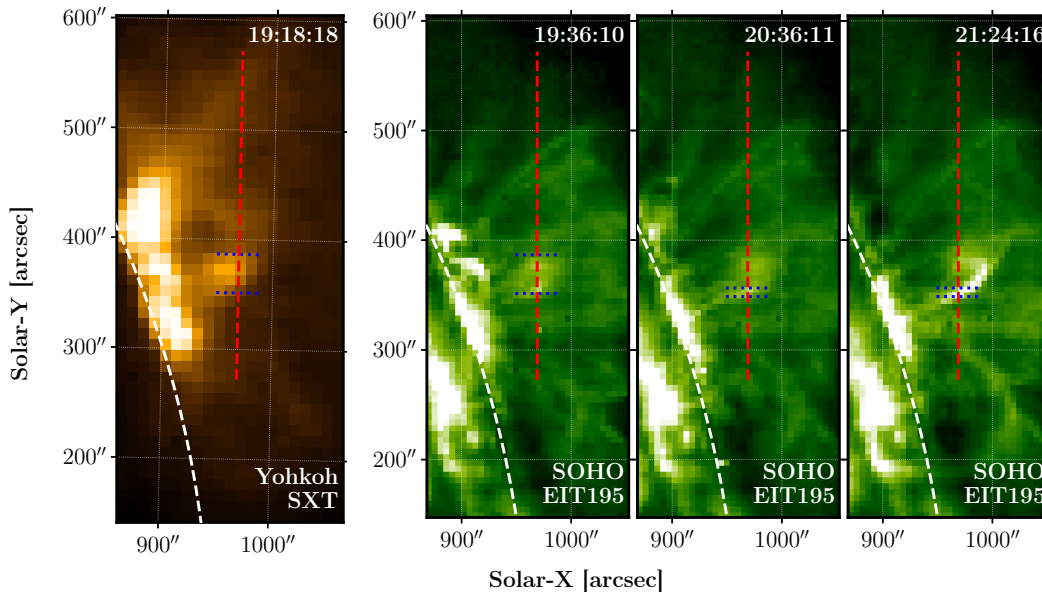


Figure 6.2: Yohkoh/Soft X-ray Telescope (SXT; Tsuneta et al., 1991) and EIT images of the post-flare AR. The red vertical line represents the SUMER slit position. The sections of the slit used to study the ion temperature in post-flare AR (left two) and coronal rain (right two) are highlighted by two blue parallel lines.

The results of ion temperature diagnostics are shown in Figure 6.3. No apparent dependence of T_i on Z/A of the heavy ions is observed. In particular, the proton temperature measured by the $\text{Ly}\beta$ line width is consistent with the inferred electron temperature. This suggests the absence of preferential heating of heavy ions in the post-flare ARs, or it might indicate frequent Coulomb collisions that result in $T_i \approx T_e$.

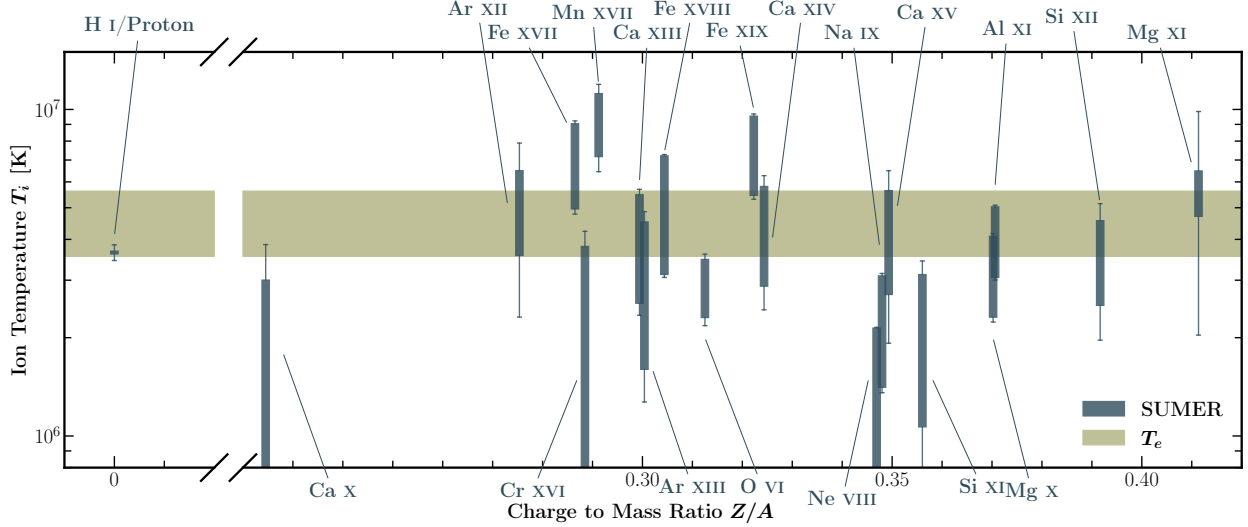


Figure 6.3: Estimated ion temperatures T_i vs. charge-to-mass ratios Z/A in the post-flare AR loops observed by SUMER. For each ion, the boxes show possible ion temperature intervals between $T_{i,\min}$ and $T_{i,\max}$, while the whiskers indicate the uncertainty in $T_{i,\min}$ and $T_{i,\max}$. The horizontal shaded area displays the measured electron temperature.

6.2.3 Line Widths in the Coronal Rain

Coronal rain is cold (10^4 – 10^5 K) and condensed plasma, forming during the drastic cooling events in the solar corona (De Groof et al., 2004; de Groof et al., 2005). The coronal rain is often observed in chromospheric and transition region lines, as the plasma clumps precipitate to the solar surface along the field lines like raindrops. The formation of the coronal rain is associated with the thermodynamic non-equilibrium cycle and thermal instability scenario (Kuin & Martens, 1982; Mok et al., 1990) to explain the periodic heating and cooling observed in the coronal loops and constrain the heating frequency (Klimchuk, 2019).

Within the SUMER dataset analyzed in Section 6.2.2, we identified a loop-brightening event followed by coronal rain after 15 minutes. Our analysis revealed a warm loop component at $\log T_e \approx 6.3$ and a cold coronal rain component at $\log T_e \approx 5.2$ (see Figure 6.4). The electron density within the coronal rain approaches $\log N_e \approx 9.8$, whereas $\log n_e \approx 8.7$ is measured in the warm loop, which suggests a gas pressure balance between the warm loop and the coronal rain plasma.

The measured effective temperature T_{eff} and nonthermal velocity ξ of the warm loop and cold rain are illustrated in Figure 6.5. The thermal broadening was removed by assuming the ion temperature is close to the maximum formation temperature of the ion $T_i = T_{\text{max}}$. We found that the nonthermal velocities ξ in the cold coronal rain, ranging from 20–30 km s $^{-1}$, are comparable to or even greater than ξ in the warm coronal loop. This might imply the

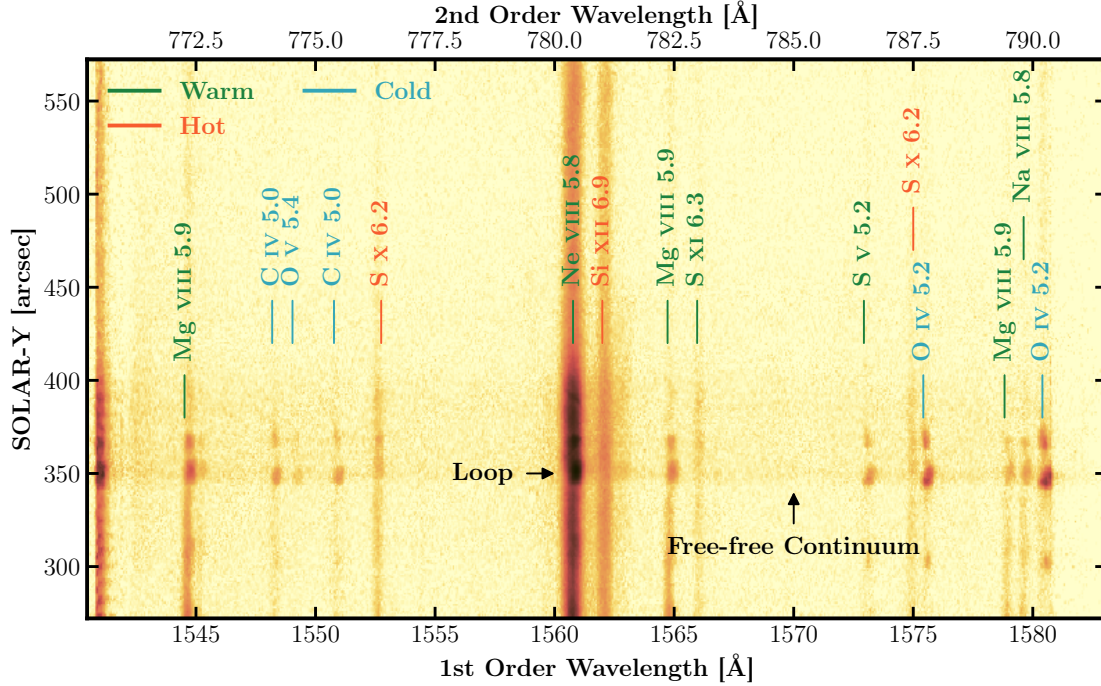


Figure 6.4: A SUMER exposure recording both the warm emission from the coronal loop (e.g., Ne VIII) and cold emission indicative of the coronal rain (e.g., C IV). A free-free continuum enhancement is also highlighted at the location where coronal rain occurred.

existence of unresolved turbulence and oscillations in the coronal rain plasma condensation.

6.2.4 Magnetic Field Diagnostics in the Solar Corona

The direct measurement of the coronal magnetic field provides crucial insight into the physical processes related to coronal heating and solar eruptions. We have proposed and designed an experiment to observe spectropolarimetric signals in the magnetic dipole transitions Fe XIII 1074.7 and 1079.8 nm in an off-limb active region using the Cryogenic Near-Infrared Spectropolarimeter (Cryo-NIRSP; [Fehlmann et al., 2023](#)) on DKIST. The proposal has been accepted in cycle 2 of the DKIST operation commission phase. Currently, we are still waiting for the observation to be executed.

We requested two spectropolarimetric scans, one in 1074.7 nm and the other in 1079.8 nm, across an AR with the $0.5'' \times 230''$ slit parallel to the limb. The scan starts at approximately $10''$ to $20''$ above the limb to skip the limb brightening. The total FOV is $60'' \times 230''$, as demonstrated in Figure 6.6.

In the data processing, a “single-point inversion” algorithm CLEDB ([Paraschiv & Judge, 2022](#)), assuming most emissions originate from one location along the LOS, will invert the

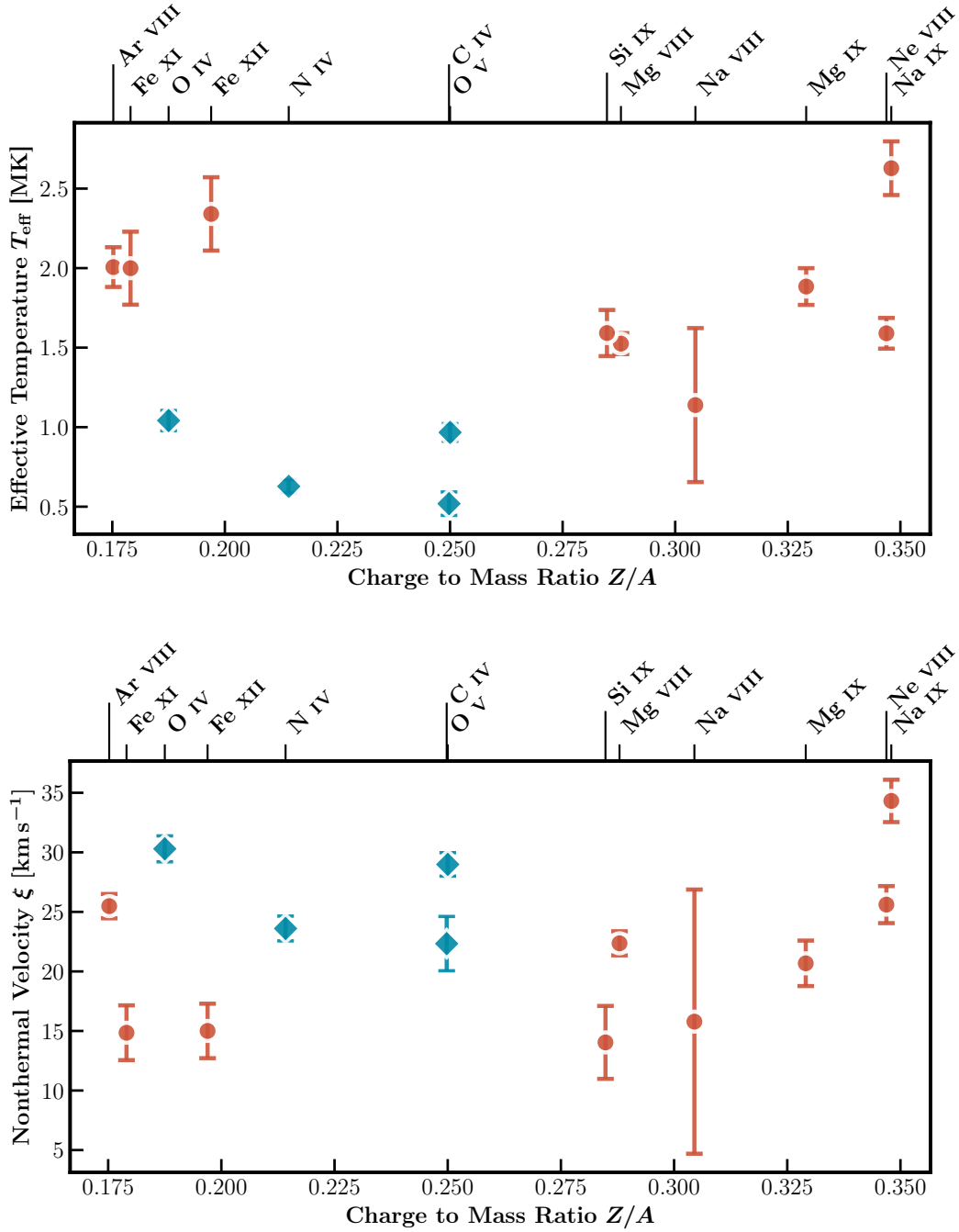


Figure 6.5: Effective temperature T_{eff} and nonthermal velocity ξ in the warm loop (red) and cold coronal rain (blue).

observed Stokes parameters to obtain the vector magnetic field, plasma properties, and the emitting position along the LOS. We plan to compare the coronal magnetic field reconstructed by the widely used PFSS model and Non-linear Force-Free Field (NLFFF) ex-

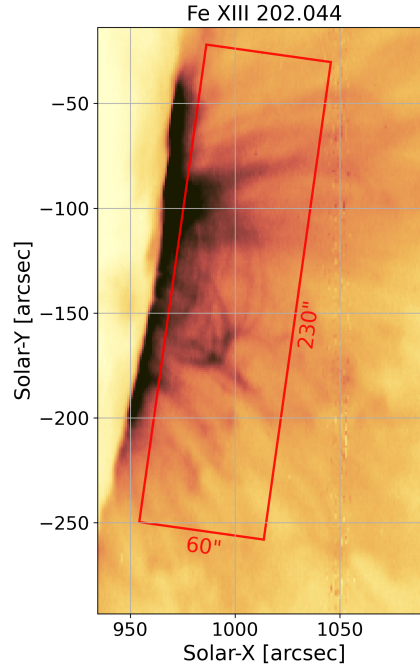


Figure 6.6: A schematic diagram of the proposed FOV of DKIST/Cryo-NIRSP in the spectropolarimetric scan of an AR.

trapolations at the emission position. Furthermore, the inverted magnetic field and plasma properties will be compared with the global steady-state corona simulated by AWSoM. This cross-model comparison will assess the capabilities of different models and improve the performance of field extrapolations.

6.2.5 Material Upflows in the Lower Corona

Ultimate solutions to the coronal heating problem also need to answer how the plasma in the lower atmosphere is transported into the solar corona. Previous studies confirmed upflows in coronal holes (e.g., [Hassler et al., 1999](#)), active region boundaries (e.g., [Hara et al., 2008](#)), and quiet Sun (e.g., [McIntosh & De Pontieu, 2009](#)). In my postdoc research, I plan to improve our understanding of the relation between upflow and coronal heating and solar wind acceleration. The instruments like the Spectral Imaging of the Coronal Environment (SPICE; [Spice Consortium et al., 2020](#)), EUI, and PHI on board the Solar Orbiter will provide unique observations to answer these questions.

To understand the nature of the flows in the solar corona, essential parameters like the intensity, Doppler shift, and line asymmetry should be measured at different heights (temperatures), from the lower transition region (TR) to the corona. With the capability to measure spectral lines forming between 0.05 to 1 MK simultaneously, SPICE will observe

the spatial and temporal variation of the line intensity (see Figure 6.7), and Doppler shifts at different heights, which will help us study both the long-term variation and the intermittent components of the upflows. The spatial correlation of the intensity and Doppler shift at different heights can be used to trace the expansion of upflow materials below the corona. EUV images of the corona (Fe x 174) and chromosphere/TR ($\text{Ly}\alpha$) will be used to study the dynamics of the upflow source region (e.g., loop, jet). Note that additional PSF corrections (e.g., [Plowman et al., 2023](#)) might be required for SPICE observations to measure the Doppler shifts correctly.

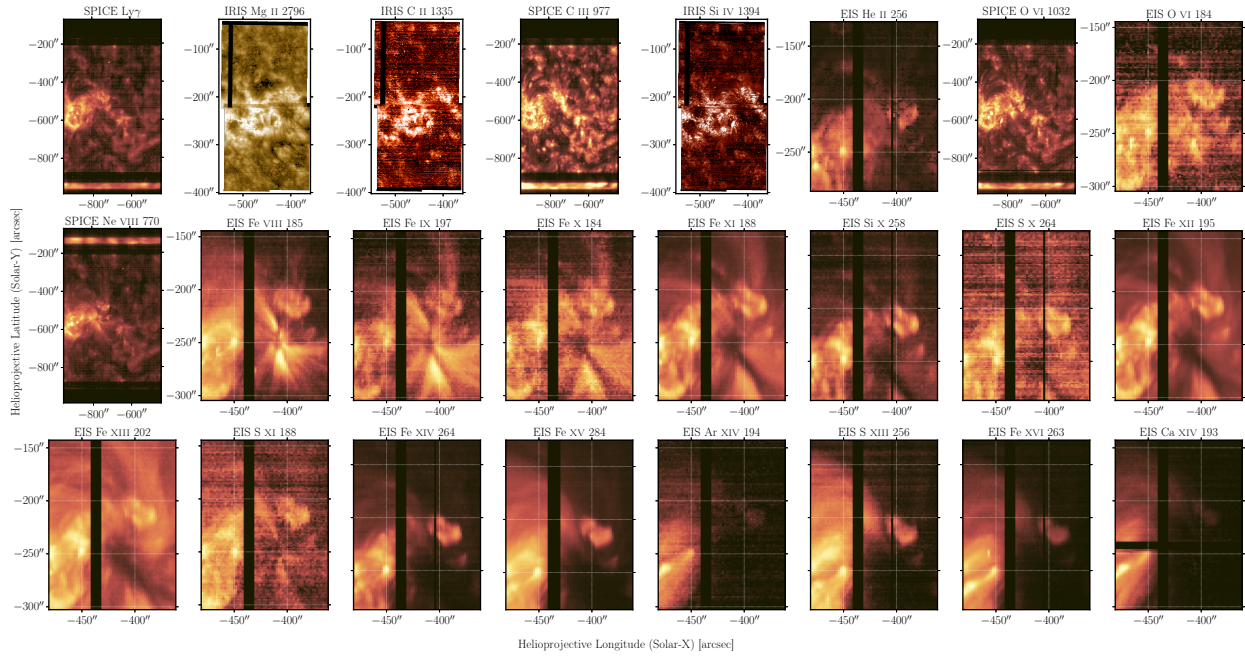


Figure 6.7: Emission originating from the chromosphere to solar corona in NOAA AR 12960 observed by IRIS, SoLo/SPICE, and Hinode/EIS.

Coordinated observations from other EUV images and spectrographs will provide additional insights into the upflows. Observations from IRIS will extend the temperature coverage to the upper chromosphere. Hinode/EIS will provide complementary diagnostics to the hotter plasma >1 MK. Observations from multiple vantage points using IRIS, EIS, and SPICE might help measure 3D velocity vectors and study their alignment with the local magnetic field (e.g., [Barczynski et al., 2023](#)).

Magnetic field measurements below the transition region contain critical information about the generation mechanism of the upflows, especially for upflows in the quiet Sun and AR close to the disk center. PHI magnetograms may show the possible flux cancellation or reconnection generating the upflows. Future coordinated observations from the Visible Spectro-Polarimeter (ViSP; [de Wijn et al., 2022](#)) on DKIST will provide high-resolution

photospheric (e.g., Fe I 630.1 nm) and chromospheric (e.g., Ca II 854.2 nm) magnetic field measurements to reveal the height-dependent magnetic structure that drives the plasma flows or waves in the source region.

APPENDIX A

Spicules, stray light, and Opacity Effects in SUMER and EIS Observations

In Chapter 4, we assumed that the spectral lines observed by SUMER and EIS are optically thin and are emitted by the plasma in the coronal hole. However, as we analyzed the observation between 1.01 and $1.04 R_{\odot}$, spicules might have contributed to the emission. To address the potential cold plasma along the LOS, we show the intensity distribution of the chromospheric and TR lines along the SUMER slit in Figure A.1. We found that the intensity of these cooler lines gradually decreases with height, like the common stray light found in other SUMER off-limb observations. The observed stray-light lines do not show significant enhancement at the bottom of the slit. And at the height we used for this work (pixels 0 to 30), the stray light is negligible. On the other hand, the intensities of hotter lines like N v and Ne VIII decrease drastically along the slit. Therefore, we conclude that the cold chromospheric and TR plasma, such as spicules, does not significantly contaminate the line profiles used for T_i diagnostics.

Del Zanna et al. (2019) found the anomalous variation of the Fe XII 195/192 ratio in the off-limb quiet-Sun corona. The Fe XII 195/192 ratio should not be sensitive to density or temperature. They suggested the reduction in Fe XII 195/192 ratio is caused by the optical thickness in the strongest Fe XII 195 Å. We measured $I_{195}/I_{192} = 3.25$ between 1.01 and $1.04 R_{\odot}$ using the GDZ calibration, which is fairly close to the optically thin limit $I_{195}/I_{192} = 3.15$ given by CHIANTI. Hence, we suggested that the optical thickness in Fe XII 195 Å is still negligible in our observations.

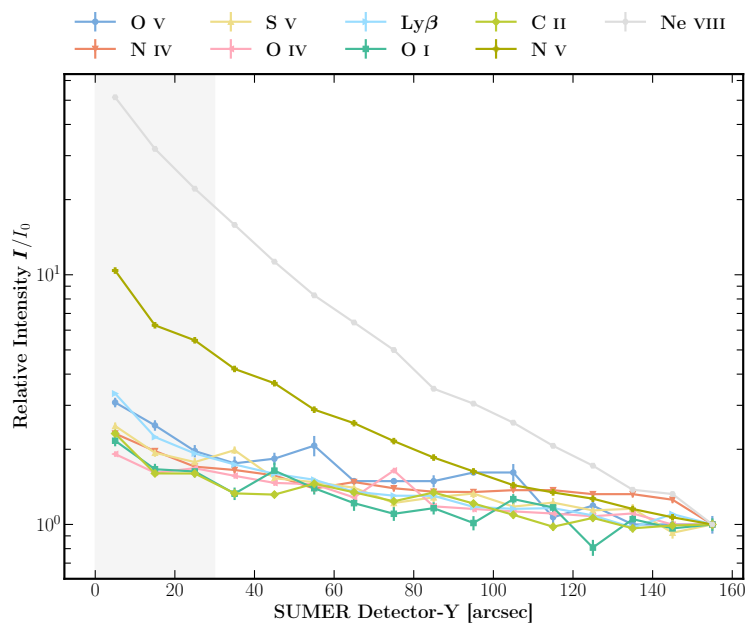



Figure A.1: Normalized intensity of the cooler stray light lines (O I, Ly β , C II, O IV, O v, N IV, and S v), and hotter lines (N v and Ne VIII) along the SUMER slit. The vertical shaded area represents the averaged 30 pixels. Link to the [Jupyter notebook](#) creating this figure .

APPENDIX B

Table of Ion Temperatures at the Coronal Hole Boundary

Table B.1: Estimated ranges of ion temperatures $T_{i,\min}$ and $T_{i,\max}$ from spectral line widths. The fitting of the individual spectral line can be found in the following [Jupyter notebooks](#): [EIS](#), [SUMER window 1](#), [SUMER window 2](#), [SUMER window 3](#), and [SUMER window 4](#).

Ion	Z/A	Inst.	Instrument Averaged Values				Individual Line Measurements			
			$\log T_{i,\min}$ [K]	$\log T_{i,\max}$ [K]	\bar{v}_{eff} [$\text{km} \cdot \text{s}^{-1}$]	λ [Å]	$\Delta\lambda_{\text{true}}$ [mÅ]	$\Delta\lambda_{\text{true}}$ [mÅ]	$\Delta\lambda_{\text{fit}}$ [mÅ]	
Fe VIII	0.125	EIS	$6.44^{+0.06}_{-0.08}$	32.0 ± 1.7	43.0 ± 1.5	185.213	31.4 ± 1.1	44.1 ± 0.8	76.48 ± 0.45
			$6.54^{+0.04}_{-0.05}$	$6.79^{+0.03}_{-0.03}$	186.598	38.8 ± 1.5	49.7 ± 1.1	79.79 ± 0.71
Mn VIII	0.127	EIS	$6.75^{+0.13}_{-0.19}$	43.4 ± 7.0	52.5 ± 5.8	185.455	44.7 ± 7.2	54.4 ± 5.9	82.8 ± 3.9
			$6.93^{+0.11}_{-0.15}$	191.206	33.1 ± 4.2	45.2 ± 3.1	77.1 ± 1.8
Fe IX	0.143	EIS	$6.08^{+0.08}_{-0.10}$	$6.67^{+0.02}_{-0.02}$	37.2 ± 1.0	46.3 ± 0.7	197.854	41.0 ± 0.7	51.3 ± 0.6	80.85 ± 0.35
			$6.86^{+0.01}_{-0.01}$	174.531	38.0 ± 3.1	49.0 ± 2.4	79.4 ± 1.5
Fe X	0.161	EIS	$6.06^{+0.08}_{-0.09}$	$6.66^{+0.02}_{-0.02}$	37.0 ± 0.9	47.4 ± 0.9	177.240	40.7 ± 1.3	51.2 ± 1.0	80.8 ± 0.6
			$6.88^{+0.02}_{-0.02}$	184.537	37.1 ± 0.6	48.4 ± 0.4	79.0 ± 0.3
Ar VIII	0.175	SUMER	$6.77^{+0.06}_{-0.06}$	$6.97^{+0.04}_{-0.04}$	52.7 ± 2.3	1028.053	301 ± 13	355 ± 11
			1028.082
Fe XI	0.179	EIS	$6.17^{+0.03}_{-0.03}$	$6.69^{+0.01}_{-0.01}$	38.3 ± 0.4	48.1 ± 0.3	713.801	197 ± 20	282 ± 14
			$6.89^{+0.01}_{-0.01}$	182.167	39.6 ± 3.0	50.3 ± 2.4	80.2 ± 1.5
Mg VI	0.206	EIS	$6.55^{+0.19}_{-0.36}$	$6.84^{+0.11}_{-0.15}$	45.6 ± 6.5	188.216	39.9 ± 0.7	50.5 ± 0.5	80 ± 0.3
			188.299	39.9 ± 0.7	50.5 ± 0.5	80 ± 0.3
Fe XII	0.197	EIS	$6.35^{+0.10}_{-0.14}$	$6.75^{+0.04}_{-0.05}$	41.1 ± 2.2	49.8 ± 1.8	192.627	42.7 ± 3.1	52.7 ± 2.5	81.7 ± 1.6
			$6.92^{+0.03}_{-0.03}$	202.424	51.4 ± 5.1	60.0 ± 4.3	86.6 ± 3.0
Mg VI	0.206	EIS	$5.63^{+0.62}_{-}$	$6.28^{+0.23}_{-0.35}$	36.3 ± 13.0	41.3 ± 11.4	1028.955	260 ± 37	322 ± 30
			$6.40^{+0.19}_{-0.35}$	$6.40^{+0.19}_{-0.35}$	$6.40^{+0.19}_{-0.35}$	192.394	41.9 ± 4.7	52.1 ± 3.7	81.3 ± 2.4
Mg VI	0.206	EIS	$5.63^{+0.62}_{-}$	$6.40^{+0.19}_{-0.35}$	36.3 ± 13.0	41.3 ± 11.4	193.509	40.4 ± 1.0	50.9 ± 0.8	80.6 ± 0.5
			$6.40^{+0.19}_{-0.35}$	$6.40^{+0.19}_{-0.35}$	$6.40^{+0.19}_{-0.35}$	195.119	47.5 ± 0.9	56.7 ± 0.8	84.4 ± 0.5

Table B.1 continued from previous page

Ion	Z/A	Inst.	Instrument Averaged Values				Individual Line Measurements					
			$\log T_{i,\min}$ [K]	$\log T_{i,\max}$ [K]	\tilde{v}_{eff} [km · s ⁻¹]	\tilde{v}_{eff} [km · s ⁻¹]	λ [Å]	$\Delta\lambda_{\text{true}}$ [mÅ]	$\Delta\lambda_{\text{true}}$ [mÅ]	$\Delta\lambda_{\text{fit}}$ [mÅ]		
Si VII	0.214	EIS	$5.94^{+0.02}_{-0.02}$	$6.41^{+0.01}_{-0.01}$	$6.42^{+0.10}_{-0.13}$	$6.64^{+0.06}_{-0.07}$	39.2 ± 0.3	43.7 ± 0.2	272.647	59.4 ± 2.3	66.5 ± 2.1	91.2 ± 1.5
		SUMER	$6.42^{+0.10}_{-0.13}$	$6.64^{+0.06}_{-0.07}$	50.8 ± 3.9	1049.153	296 ± 23	352 ± 19
Fe XIII	0.215	EIS	$6.21^{+0.13}_{-0.19}$	$6.70^{+0.05}_{-0.05}$	$6.61^{+0.06}_{-0.07}$	$6.88^{+0.03}_{-0.03}$	38.8 ± 2.2	47.4 ± 1.8	202.044	43.5 ± 2.5	53.4 ± 2.0	82.2 ± 1.3
		SUMER	$6.06^{+0.26}_{-0.77}$	$6.45^{+0.13}_{-0.18}$	41.7 ± 7.1	1053.996	244 ± 42	307 ± 33
Mg VII	0.247	EIS	$5.84^{+0.18}_{-0.32}$	$6.34^{+0.07}_{-0.08}$	$6.08^{+0.12}_{-0.16}$	$6.43^{+0.05}_{-0.06}$	38.7 ± 3.2	43.1 ± 2.9	276.154	59.3 ± 4.9	66.3 ± 4.4	91.1 ± 3.2
		EIS	$5.85^{+0.20}_{-0.39}$	$6.43^{+0.06}_{-0.07}$	$6.16^{+0.12}_{-0.16}$	$6.54^{+0.05}_{-0.06}$	37.3 ± 2.9	42.3 ± 2.7	259.496	61 ± 15	67.6 ± 14	92 ± 10
S X	0.281	SUMER	$6.86^{+0.19}_{-0.35}$	$6.97^{+0.16}_{-0.25}$	69.4 ± 15.0	776.373	299 ± 65	358 ± 54
		EIS	$5.55^{+0.92}_{-}$	$6.32^{+0.35}_{-}$	$6.04^{+0.52}_{-0.96}$	$6.46^{+0.28}_{-0.96}$	35.1 ± 21.5	41.1 ± 18.3	258.080	50 ± 31	59.1 ± 26.2	86 ± 18
Mg VIII	0.288	SUMER	$5.75^{+0.36}_{-}$	$6.36^{+0.12}_{-0.17}$	36.8 ± 5.9	694.686	142 ± 23	249 ± 13
		EIS	$6.32^{+0.05}_{-0.05}$	$6.55^{+0.03}_{-0.03}$	49.4 ± 1.7	689.641	187 ± 27	276 ± 18
Al IX	0.296	SUMER	$5.91^{+0.83}_{-}$	$6.39^{+0.46}_{-}$	39 ± 37	703.73	154 ± 143	256 ± 86
		EIS	$5.78^{+0.11}_{-0.15}$	$6.20^{+0.05}_{-0.05}$	$6.16^{+0.05}_{-0.06}$	$6.39^{+0.03}_{-0.03}$	40.6 ± 2.3	50.3 ± 1.9	184.117	41.5 ± 2.3	51.7 ± 1.9	81.1 ± 1.2
O VI	0.313	SUMER	$6.16^{+0.01}_{-0.01}$	$6.39^{+0.01}_{-0.01}$	50.3 ± 0.4	1031.912	294.4 ± 3.3	350.2 ± 2.8
		EIS	$5.76^{+0.12}_{-0.16}$	$6.36^{+0.03}_{-0.03}$	$6.09^{+0.06}_{-0.07}$	$6.48^{+0.03}_{-0.03}$	36.9 ± 1.4	42.1 ± 1.3	258.374	54.0 ± 4.2	61.7 ± 3.7	87.8 ± 2.6
Mg IX	0.329	SUMER	$6.24^{+0.17}_{-0.27}$	32.2 ± 7.5	624.694	112 ± 26	145 ± 20
		EIS	$6.53^{+0.03}_{-0.04}$	$6.69^{+0.02}_{-0.02}$	57.6 ± 1.6	706.060	228.5 ± 4.7	305.0 ± 3.5
Ne VIII	0.347	SUMER	$6.36^{+0.02}_{-0.02}$	$6.55^{+0.01}_{-0.01}$	53.8 ± 0.9	770.428	228.2 ± 2.3	302.3 ± 1.7
		EIS	$6.16^{+0.01}_{-0.01}$	$6.39^{+0.01}_{-0.01}$	50.3 ± 0.4	1037.613	288.8 ± 1.2	345.6 ± 1.0
Si X	0.320	SUMER	$6.24^{+0.17}_{-0.27}$	32.2 ± 7.5	624.694	112 ± 26	145 ± 20
		EIS	$5.76^{+0.12}_{-0.16}$	$6.36^{+0.03}_{-0.03}$	$6.09^{+0.06}_{-0.07}$	$6.48^{+0.03}_{-0.03}$	36.9 ± 1.4	42.1 ± 1.3	261.056	49.5 ± 8.1	57.8 ± 6.9	85.1 ± 4.7
Ne VIII	0.347	SUMER	$6.36^{+0.02}_{-0.02}$	$6.55^{+0.01}_{-0.01}$	53.8 ± 0.9	770.428	228.2 ± 2.3	302.3 ± 1.7
		EIS	$6.16^{+0.01}_{-0.01}$	$6.39^{+0.01}_{-0.01}$	50.3 ± 0.4	1037.613	288.8 ± 1.2	345.6 ± 1.0

Table B.1 continued from previous page

Ion	Z/A	Inst.	Instrument Averaged Values				Individual Line Measurements			
			$\log T_{i,\min}$ [K]	$\log T_{i,\max}$ [K]	\bar{v}_{eff} [$\text{km} \cdot \text{s}^{-1}$]	\bar{v}_{eff} [$\text{km} \cdot \text{s}^{-1}$]	λ [Å]	$\Delta\lambda_{\text{true}}$ [mÅ]	$\Delta\lambda_{\text{true}}$ [mÅ]	$\Delta\lambda_{\text{fit}}$ [mÅ]
Na IX	0.348	SUMER	$6.58^{+0.04}_{-0.04}$	$6.72^{+0.03}_{-0.03}$	61.4 ± 1.9	780.385	239.8 ± 3.9	311.0 ± 3.0
Mg x	0.370	SUMER	$6.17^{+0.11}_{-0.14}$	$6.48^{+0.06}_{-0.06}$	45.2 ± 3.1	681.719	232.5 ± 7.2	308.0 ± 5.4
							609.793	145.1 ± 2.6	171.4 ± 2.2
							624.941	170.6 ± 3.4	193.3 ± 3.0

APPENDIX C

Comparison between Different Spectral Orders in PaMIS

One of the advantages of PaMIS is its capability to work at multiple orders, allowing for measurements of line profiles multiple times. However, in this study, we have only adopted the most prominent order of Fe X and Fe XIV lines. To improve the S/N, a natural approach is to combine line profiles in different orders to make the best use of collected photons.

In Figure C.1, we present examples of Fe XIV line profiles at various orders obtained from different off-limb locations. In addition, we interpolated the line profiles at various orders to the same wavelength scale and summed these profiles together. This allows us to assess the performance of the instrument across different orders and examine the combined profiles.

In general, the fit results of Fe XIV line profiles at different orders are similar, especially when the S/N is high or after applying the 5-pixel average. In the brightest region of the AR, the differences in the Doppler shift and v_{eff} among various orders are typically less than 2 km s^{-1} , which might be caused by the uncertainty of the absolute wavelength calibration. However, in the regions where the S/N is low, such as the AR at $1.5 R_{\odot}$ and the fainter streamer, the Doppler velocity measurements in different orders may exceed $5\text{--}10 \text{ km s}^{-1}$.

The averaging along the slit and the summation of different orders greatly improve the S/N and result in more Gaussian-like profiles. The combination of various orders generally averages the Doppler shifts and line widths of individual profiles. We only used the strongest orders in the data analysis because the detectors were primarily focused on the strongest orders, which could potentially make the profiles asymmetric at weaker orders. However, the comparison highlights the potential of taking full advantage of multiple orders in future observations with caution, especially when the flatfield is properly made.

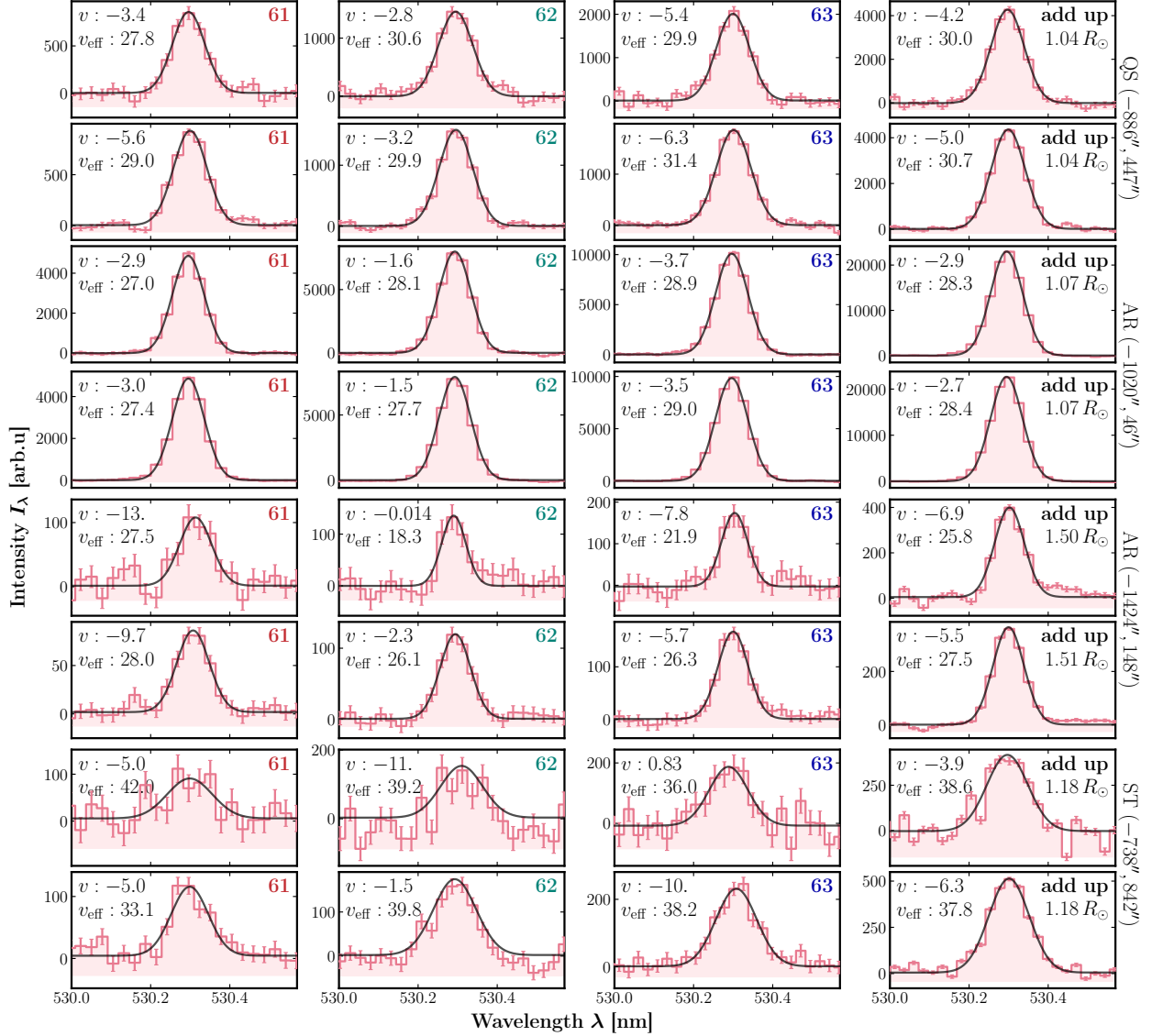


Figure C.1: Comparison between Fe XIV 530.3 nm profiles at the 61st, 62nd, and 63rd orders in various coronal structures and heights: the QS, AR, and streamer (ST). The profiles in each structure are depicted in two rows of subplots: the first row shows the original profiles, while the second row displays the 5-pixel averaged profiles. The last row shows the sum of three different orders. The fit Doppler velocity v and effective velocity v_{eff} are measured in the units of km s^{-1} . Link to the Jupyter notebook creating this figure: [🔗](#).

APPENDIX D

Photon Redistributions of Constant Continuum

The local emissivity $\epsilon(\nu, \hat{\mathbf{n}})$ at a frequency ν in the direction of $\hat{\mathbf{n}}$ caused by the incident emission is proportional to

$$\epsilon(\nu, \hat{\mathbf{n}}) \propto \frac{1}{4\pi} \int d\Omega' \int_0^\infty d\nu' R(\nu', \hat{\mathbf{n}}'; \nu, \hat{\mathbf{n}}) I(\nu', \hat{\mathbf{n}}') \quad (\text{D.1})$$

where the integral over differential solid angle $d\Omega'$ describes the scattering of incoming photons from different directions. $R(\nu', \hat{\mathbf{n}}'; \nu, \hat{\mathbf{n}})$ is the photon redistribution function in the observer's frame, which describes the probability to scatter an incoming photon at frequency ν' and along direction $\hat{\mathbf{n}}'$ to a new frequency ν and direction $\hat{\mathbf{n}}$, and $I(\nu', \hat{\mathbf{n}}')$ is the incoming photospheric radiation intensity. Consider the scattering from a constant (flat) continuum $I(\nu', \hat{\mathbf{n}}') = I(\hat{\mathbf{n}}')$, we have

$$\epsilon(\nu, \hat{\mathbf{n}}) \propto \frac{1}{4\pi} \int I(\hat{\mathbf{n}}') d\Omega' \int_0^\infty d\nu' R(\nu', \hat{\mathbf{n}}'; \nu, \hat{\mathbf{n}}) \quad (\text{D.2})$$

Let's first deal with the integral over the incident frequency

$$\mathcal{I}_1 = \int_0^\infty R(\nu', \hat{\mathbf{n}}'; \nu, \hat{\mathbf{n}}) d\nu' \quad (\text{D.3})$$

Assuming the scattering happens between two sharp energy levels, neglecting the natural broadening (Case I, [Mihalas, 1978](#)), the analytical form of the photon redistribution function can be written as ([Cranmer, 1998](#); [Gilly & Cranmer, 2020](#))

$$R(\nu', \hat{\mathbf{n}}'; \nu, \hat{\mathbf{n}}) = \frac{g(\Theta)}{\pi\beta(\Delta\nu)^2} \exp(-\zeta'^2) \exp\left[-\left(\frac{\zeta - \alpha\zeta'}{\beta}\right)^2\right] \quad (\text{D.4})$$

where $\Theta = \langle \hat{\mathbf{n}}', \hat{\mathbf{n}} \rangle$, $\alpha \equiv \cos \Theta$, and $\beta \equiv \sin \Theta$. $g(\Theta)$ is the angular distribution phase function. $\Delta\nu = \nu_0 v_{\text{eff}}/c$ represents the local effective velocity in frequency units, where ν_0 is the rest frequency of the spectral line. Additionally, ζ and ζ' are dimensionless frequency displacements defined by

$$\zeta \equiv \frac{\nu - \nu_0}{\Delta\nu} - \frac{\mathbf{u} \cdot \hat{\mathbf{n}}}{v_{\text{eff}}} = \frac{\nu - \nu_0 (1 + u_{\text{LOS}}/c)}{\Delta\nu} \quad (\text{D.5})$$

$$\zeta' \equiv \frac{\nu' - \nu_0}{\Delta\nu} - \frac{\mathbf{u} \cdot \hat{\mathbf{n}}'}{v_{\text{eff}}} \quad (\text{D.6})$$

where \mathbf{u} denotes the local bulk velocity and $\mathbf{u} \cdot \hat{\mathbf{n}}$ is the local LOS velocity u_{LOS} . Replacing $d\nu'$ with $\Delta\nu d\zeta'$, the integral in Equation (D.3) can be written as

$$\begin{aligned} \mathcal{I}_1 &= \frac{g(\Theta)}{\pi\beta\Delta\nu} \int_{-\nu_0/\Delta\nu - \mathbf{u} \cdot \hat{\mathbf{n}}'/v_{\text{eff}}}^{\infty} \exp(-\zeta'^2) \exp\left[-\left(\frac{\zeta - \alpha\zeta'}{\beta}\right)^2\right] d\zeta' \\ &\approx \frac{g(\Theta)}{\pi\beta\Delta\nu} \int_{-\infty}^{\infty} \exp(-\zeta'^2) \exp\left[-\left(\frac{\zeta - \alpha\zeta'}{\beta}\right)^2\right] d\zeta' \\ &= \frac{g(\Theta)}{\sqrt{\pi}\Delta\nu} \exp(-\zeta^2) \end{aligned} \quad (\text{D.7})$$

note that we also used $\nu_0 \gg \Delta\nu$ and $\alpha^2 + \beta^2 = 1$. Notably, \mathcal{I}_1 is a Gaussian profile, which does not depend on $\hat{\mathbf{n}}'$ anymore. Thus, the local emissivity is

$$\epsilon(\nu, \hat{\mathbf{n}}) \propto \frac{\mathcal{I}_1}{4\pi} \int I(\hat{\mathbf{n}}') d\Omega' \quad (\text{D.8})$$

where the integral over the solid angle is a scale factor due to the limb darkening. Therefore, the local emissivity is still a Doppler-shifted Gaussian function broadened by the local effective velocity v_{eff} . Physically, this is trivial because the flat continuum was scattered by a Gaussian absorption profile during the Case I scattering.

BIBLIOGRAPHY

- Akinari, N. 2007, *ApJ*, 660, 1660
- Alfvén, H. 1942, *Nature*, 150, 405
- . 1947, *MNRAS*, 107, 211
- Altschuler, M. D., & Newkirk, G. 1969, *SoPh*, 9, 131
- Anfinogentov, S. A., Nakariakov, V. M., & Nisticò, G. 2015, *A&A*, 583, A136
- Antiochos, S. K., Mikić, Z., Titov, V. S., Lionello, R., & Linker, J. A. 2011, *ApJ*, 731, 112
- Antolin, P., De Moortel, I., Van Doorselaere, T., & Yokoyama, T. 2016, *ApJL*, 830, L22
- Antolin, P., Pagano, P., Testa, P., Petralia, A., & Reale, F. 2021, *Nature Astronomy*, 5, 54
- Antolin, P., Yokoyama, T., & Van Doorselaere, T. 2014, *ApJL*, 787, L22
- Antonucci, E., Dodero, M. A., & Giordano, S. 2000, *SoPh*, 197, 115
- Antonucci, E., Dodero, M. A., Giordano, S., Krishnakumar, V., & Noci, G. 2004, *A&A*, 416, 749
- Arthanayaka, T., Beiersdorfer, P., Brown, G. V., et al. 2020, *ApJ*, 890, 77
- Aschwanden, M. J. 2005, *Physics of the Solar Corona. An Introduction with Problems and Solutions (2nd edition)* (Springer Berlin, Heidelberg)
- . 2019, *Astrophysics and Space Science Library*, Vol. 458, *New Millennium Solar Physics*
- Aschwanden, M. J., Boerner, P., Schrijver, C. J., & Malanushenko, A. 2013, *SoPh*, 283, 5
- Aschwanden, M. J., Fletcher, L., Schrijver, C. J., & Alexander, D. 1999, *ApJ*, 520, 880
- Aschwanden, M. J., Nightingale, R. W., Andries, J., Goossens, M., & Van Doorselaere, T. 2003, *ApJ*, 598, 1375
- Aschwanden, M. J., & Parnell, C. E. 2002, *ApJ*, 572, 1048
- Aschwanden, M. J., & Schrijver, C. J. 2011, *ApJ*, 736, 102
- Aschwanden, M. J., Tarbell, T. D., Nightingale, R. W., et al. 2000, *ApJ*, 535, 1047

- Aschwanden, M. J., & Wang, T. 2020, *ApJ*, 891, 99
- Aschwanden, M. J., Winebarger, A., Tsiklauri, D., & Peter, H. 2007, *ApJ*, 659, 1673
- Asgari-Targhi, M., van Ballegooijen, A. A., & Imada, S. 2014, *ApJ*, 786, 28
- Athay, R. G., & White, O. R. 1978, *ApJ*, 226, 1135
- Banerjee, D., Pérez-Suárez, D., & Doyle, J. G. 2009, *A&A*, 501, L15
- Banerjee, D., Teriaca, L., Doyle, J. G., & Wilhelm, K. 1998, *A&A*, 339, 208
- Barczynski, K., Harra, L., Schwanitz, C., et al. 2023, *A&A*, 673, A74
- Barkhudarov, M. R. 1991, *SoPh*, 135, 131
- Basu, S. 2016, *Living Reviews in Solar Physics*, 13, 2
- Bazin, C. 2013, *PhD thesis*, Aix-Marseille Université
- Belcher, J. W., & Davis, Leverett, J. 1971, *J. Geophys. Res.*, 76, 3534
- Bello González, N., Franz, M., Martínez Pillet, V., et al. 2010, *ApJL*, 723, L134
- Bemporad, A., & Abbo, L. 2012, *ApJ*, 751, 110
- Benz, A. O., & Krucker, S. 2002, *ApJ*, 568, 413
- Berghmans, D., Auchère, F., Long, D. M., et al. 2021, *A&A*, 656, L4
- Berghmans, D., Antolin, P., Auchère, F., et al. 2023, *A&A*, 675, A110
- Bevington, P. R., & Robinson, D. K. 2003, *Data reduction and error analysis for the physical sciences* (McGraw-Hill Education)
- Boe, B., Downs, C., & Habbal, S. 2023, *ApJ*, 951, 55
- Boe, B., Habbal, S., Downs, C., & Druckmüller, M. 2021, *ApJ*, 912, 44
- . 2022, *ApJ*, 935, 173
- Boe, B., Habbal, S., Druckmüller, M., et al. 2020, *ApJ*, 888, 100
- . 2018, *ApJ*, 859, 155
- Boland, B. C., Dyer, E. P., Firth, J. G., et al. 1975, *MNRAS*, 171, 697
- Bowen, T. A., Mallet, A., Huang, J., et al. 2020, *ApJS*, 246, 66
- Bowen, T. A., Chandran, B. D. G., Squire, J., et al. 2022, *PhRvL*, 129, 165101
- Brooks, D. H., & Warren, H. P. 2011, *ApJL*, 727, L13

- . 2016, *ApJ*, 820, 63
- Brooks, D. H., Warren, H. P., Williams, D. R., & Watanabe, T. 2009, *ApJ*, 705, 1522
- Brown, C. M., Feldman, U., Seely, J. F., Korendyke, C. M., & Hara, H. 2008, *ApJS*, 176, 511
- Brueckner, G. E., Howard, R. A., Koomen, M. J., et al. 1995, *SoPh*, 162, 357
- Cargill, P. J., De Moortel, I., & Kiddie, G. 2016, *ApJ*, 823, 31
- Chae, J., Schühle, U., & Lemaire, P. 1998, *ApJ*, 505, 957
- Chen, L., & Hasegawa, A. 1974, *J. Geophys. Res.*, 79, 1024
- Cheng, C. C., Doschek, G. A., & Feldman, U. 1979, *ApJ*, 227, 1037
- Chitta, L. P., Peter, H., Parenti, S., et al. 2022, *A&A*, 667, A166
- Chitta, L. P., Zhukov, A. N., Berghmans, D., et al. 2023, *Science*, 381, 867
- Cirtain, J. W., Golub, L., Lundquist, L., et al. 2007, *Science*, 318, 1580
- Cirtain, J. W., Golub, L., Winebarger, A. R., et al. 2013, *Nature*, 493, 501
- Coleman, Paul J., J. 1968, *ApJ*, 153, 371
- Contesse, L., Koutchmy, S., & Viladrich, C. 2004, *Annales Geophysicae*, 22, 3055
- Cowling, T. G. 1953, in *The Sun*, ed. G. P. Kuiper, 532
- Cranmer, S. R. 1998, *ApJ*, 508, 925
- . 2014, *ApJS*, 213, 16
- Cranmer, S. R., Field, G. B., & Kohl, J. L. 1999, *ApJ*, 518, 937
- Cranmer, S. R., van Ballegoijen, A. A., & Edgar, R. J. 2007, *ApJS*, 171, 520
- Cranmer, S. R., & Winebarger, A. R. 2019, *ARA&A*, 57, 157
- Culhane, J. L., Harra, L. K., James, A. M., et al. 2007, *SoPh*, 243, 19
- da Silva Santos, J. M., Danilovic, S., Leenaarts, J., et al. 2022, *A&A*, 661, A59
- Dammasch, I. E., Wilhelm, K., Curdt, W., & Hassler, D. M. 1999, *A&A*, 346, 285
- de Groof, A., Bastiaensen, C., Müller, D. A. N., Berghmans, D., & Poedts, S. 2005, *A&A*, 443, 319
- De Groof, A., Berghmans, D., van Driel-Gesztelyi, L., & Poedts, S. 2004, *A&A*, 415, 1141

- De Moortel, I., & Browning, P. 2015, [Philosophical Transactions of the Royal Society of London Series A](#), 373, 20140269
- De Moortel, I., Hood, A. W., & Arber, T. D. 2000, [A&A](#), 354, 334
- De Moortel, I., Hood, A. W., Ireland, J., & Arber, T. D. 1999, [A&A](#), 346, 641
- De Pontieu, B., Hansteen, V. H., Rouppe van der Voort, L., van Noort, M., & Carlsson, M. 2007a, [ApJ](#), 655, 624
- De Pontieu, B., McIntosh, S. W., Hansteen, V. H., & Schrijver, C. J. 2009, [ApJL](#), 701, L1
- De Pontieu, B., McIntosh, S. W., Carlsson, M., et al. 2007b, [Science](#), 318, 1574
- . 2011, [Science](#), 331, 55
- De Pontieu, B., Title, A. M., Lemen, J. R., et al. 2014, [SoPh](#), 289, 2733
- de Wijn, A. G., Casini, R., Carlile, A., et al. 2022, [SoPh](#), 297, 22
- DeForest, C. E., & Gurman, J. B. 1998, [ApJL](#), 501, L217
- Del Zanna, G. 2013, [A&A](#), 555, A47
- Del Zanna, G., Bromage, B. J. I., & Mason, H. E. 2003, [A&A](#), 398, 743
- Del Zanna, G., Dere, K. P., Young, P. R., & Landi, E. 2021, [ApJ](#), 909, 38
- Del Zanna, G., Gupta, G. R., & Mason, H. E. 2019, [A&A](#), 631, A163
- Del Zanna, G., & Mason, H. E. 2018, [Living Reviews in Solar Physics](#), 15, 5
- Del Zanna, G., Weberg, M., & Warren, H. P. 2023, [arXiv e-prints](#), arXiv:2308.06609
- Delaboudinière, J. P., Artzner, G. E., Brunaud, J., et al. 1995, [SoPh](#), 162, 291
- Dere, K. P., Bartoe, J. D. F., & Brueckner, G. E. 1989, [SoPh](#), 123, 41
- Dere, K. P., Del Zanna, G., Young, P. R., & Landi, E. 2023, [ApJS](#), 268, 52
- Dere, K. P., Del Zanna, G., Young, P. R., Landi, E., & Sutherland, R. S. 2019, [ApJS](#), 241, 22
- Dere, K. P., Landi, E., Mason, H. E., Monsignori Fossi, B. C., & Young, P. R. 1997a, [A&AS](#), 125, 149
- Dere, K. P., Brueckner, G. E., Howard, R. A., et al. 1997b, [SoPh](#), 175, 601
- Ding, A., & Habbal, S. R. 2017, [ApJL](#), 842, L7
- Dolla, L., & Solomon, J. 2008, [A&A](#), 483, 271
- . 2009, [Annales Geophysicae](#), 27, 3551

- Dolliou, A., Parenti, S., Auchère, F., et al. 2023, [A&A](#), 671, A64
- Domingo, V., Fleck, B., & Poland, A. I. 1995, [SoPh](#), 162, 1
- Doschek, G. A., & Feldman, U. 2000, [ApJ](#), 529, 599
- Downs, C., Lionello, R., Mikić, Z., Linker, J. A., & Velli, M. 2016, [ApJ](#), 832, 180
- Downs, C., Roussev, I. I., van der Holst, B., et al. 2010, [ApJ](#), 712, 1219
- Doyle, J. G., Teriaca, L., & Banerjee, D. 1999, [A&A](#), 349, 956
- Duda, R. O., & Hart, P. E. 1972, [Communications of the ACM](#), 15
- Dudík, J., & Dzifčáková, E. 2021, in *Astrophysics and Space Science Library*, Vol. 464, *Kappa Distributions; From Observational Evidences via Controversial Predictions to a Consistent Theory of Nonequilibrium Plasmas*, ed. M. Lazar & H. Fichtner, 53–87
- Dudík, J., Polito, V., Dzifčáková, E., Del Zanna, G., & Testa, P. 2017, [ApJ](#), 842, 19
- Edlén, B. 1943, [ZA](#), 22, 30
- Edwin, P. M., & Roberts, B. 1983, [SoPh](#), 88, 179
- Ellerman, F. 1917, [ApJ](#), 46, 298
- Elsasser, W. M. 1950, [Physical Review](#), 79, 183
- Esser, R., Fineschi, S., Dobrzycka, D., et al. 1999, [ApJL](#), 510, L63
- Esser, R., Holzer, T. E., & Leer, E. 1987, [J. Geophys. Res.](#), 92, 13377
- Fehlmann, A., Kuhn, J. R., Schad, T. A., et al. 2023, [SoPh](#), 298, 5
- Feldman, U., Doschek, G. A., Schühle, U., & Wilhelm, K. 1999, [ApJ](#), 518, 500
- Feng, X. 2020, [Magnetohydrodynamic Modeling of the Solar Corona and Heliosphere](#)
- Fludra, A., Del Zanna, G., Alexander, D., & Bromage, B. J. I. 1999, [J. Geophys. Res.](#), 104, 9709
- Foreman-Mackey, D. 2016, [The Journal of Open Source Software](#), 1
- Foreman-Mackey, D., Hogg, D. W., Lang, D., & Goodman, J. 2013, [PASP](#), 125, 306
- Fox, N. J., Velli, M. C., Bale, S. D., et al. 2016, [SSRv](#), 204, 7
- Gao, Y., Tian, H., Van Doorselaere, T., & Chen, Y. 2022, [ApJ](#), 930, 55
- Gilly, C. R., & Cranmer, S. R. 2020, [ApJ](#), 901, 150
- Gombosi, T. I., van der Holst, B., Manchester, W. B., & Sokolov, I. V. 2018, [Living Reviews in Solar Physics](#), 15, 4

- Gombosi, T. I., Chen, Y., Glocer, A., et al. 2021, *Journal of Space Weather and Space Climate*, 11, 42
- Goossens, M., Andries, J., & Aschwanden, M. J. 2002, *A&A*, 394, L39
- Goossens, M., Terradas, J., Andries, J., Arregui, I., & Ballester, J. L. 2009, *A&A*, 503, 213
- Goossens, M. L., Arregui, I., & Van Doorselaere, T. 2019, *Frontiers in Astronomy and Space Sciences*, 6, 20
- Gorman, J., Chitta, L. P., Peter, H., et al. 2023, *A&A*, 678, A188
- Grottrian, W. 1939, *Naturwissenschaften*, 27, 214
- Guennou, C., Auchère, F., Klimchuk, J. A., Bocchialini, K., & Parenti, S. 2013, *ApJ*, 774, 31
- Gupta, G. R. 2017, *ApJ*, 836, 4
- Gupta, G. R., Del Zanna, G., & Mason, H. E. 2019, *A&A*, 627, A62
- Habbal, S. R., Esser, R., & Arndt, M. B. 1993, *ApJ*, 413, 435
- Habbal, S. R., Morgan, H., Druckmüller, M., et al. 2013, *SoPh*, 285, 9
- Habbal, S. R., Morgan, H., Johnson, J., et al. 2007, *ApJ*, 663, 598
- Hahn, M., Asgari-Targhi, M., & Savin, D. W. 2023, *ApJ*, 953, 3
- Hahn, M., Bryans, P., Landi, E., Miralles, M. P., & Savin, D. W. 2010, *ApJ*, 725, 774
- Hahn, M., Landi, E., & Savin, D. W. 2012, *ApJ*, 753, 36
- Hahn, M., & Savin, D. W. 2013a, *ApJ*, 763, 106
- . 2013b, *ApJ*, 763, 106
- . 2013c, *ApJ*, 776, 78
- . 2014, *ApJ*, 795, 111
- Handy, B. N., Acton, L. W., Kankelborg, C. C., et al. 1999, *SoPh*, 187, 229
- Hansteen, V. H., De Pontieu, B., Rouppe van der Voort, L., van Noort, M., & Carlsson, M. 2006, *ApJL*, 647, L73
- Hara, H. 2019, *ApJ*, 887, 122
- Hara, H., & Ichimoto, K. 1999, *ApJ*, 513, 969
- Hara, H., Watanabe, T., Harra, L. K., et al. 2008, *ApJL*, 678, L67
- Harra, L. K., Mandrini, C. H., Brooks, D. H., et al. 2023, *A&A*, 675, A20

- Harrison, R. A. 1997, [SoPh](#), 175, 467
- Hart, A. B. 1956, [MNRAS](#), 116, 38
- Harvey, J. W., Hill, F., Hubbard, R. P., et al. 1996, [Science](#), 272, 1284
- Hassler, D. M., Dammasch, I. E., Lemaire, P., et al. 1999, [Science](#), 283, 810
- Hassler, D. M., & Moran, T. G. 1994, [SSRv](#), 70, 373
- Hassler, D. M., Rottman, G. J., Shoub, E. C., & Holzer, T. E. 1990, [ApJL](#), 348, L77
- Hassler, D. M., Wilhelm, K., Lemaire, P., & Schühle, U. 1997, [SoPh](#), 175, 375
- Heinemann, M., & Olbert, S. 1980, [J. Geophys. Res.](#), 85, 1311
- Henney, C. J., Toussaint, W. A., White, S. M., & Arge, C. N. 2012, [Space Weather](#), 10
- Heyvaerts, J., & Priest, E. R. 1983, [A&A](#), 117, 220
- Hollweg, J. V. 1978, [SoPh](#), 56, 305
- Hollweg, J. V. 1983, in NASA Conference Publication, Vol. 228, NASA Conference Publication, 0...5
- . 1984, [SoPh](#), 91, 269
- . 1986, [J. Geophys. Res.](#), 91, 4111
- Hollweg, J. V. 1991, in Mechanisms of Chromospheric and Coronal Heating, ed. P. Ulmschneider, E. R. Priest, & R. Rosner, 260
- Hollweg, J. V., & Isenberg, P. A. 2002, [Journal of Geophysical Research \(Space Physics\)](#), 107, 1147
- Hollweg, J. V., Jackson, S., & Galloway, D. 1982, [SoPh](#), 75, 35
- Hollweg, J. V., & Sterling, A. C. 1984, [ApJL](#), 282, L31
- Howard, R. A., Moses, J. D., Vourlidas, A., et al. 2008, [SSRv](#), 136, 67
- Hu, Y. Q., Esser, R., & Habbal, S. R. 2000, [J. Geophys. Res.](#), 105, 5093
- Hu, Y. Q., & Habbal, S. R. 1999, [J. Geophys. Res.](#), 104, 17045
- Huang, Z., Tóth, G., Sachdeva, N., et al. 2023a, [ApJL](#), 946, L47
- Huang, Z., Teriaca, L., Aznar Cuadrado, R., et al. 2023b, [A&A](#), 673, A82
- Hudson, H. S. 1991, [SoPh](#), 133, 357
- Imada, S., Hara, H., & Watanabe, T. 2009, [ApJL](#), 705, L208

- Inverarity, G. W., & Priest, E. R. 1995, *A&A*, 302, 567
- Ionson, J. A. 1978, *ApJ*, 226, 650
- Isenberg, P. A., & Hollweg, J. V. 1983, *J. Geophys. Res.*, 88, 3923
- Ishikawa, S.-n., Glesener, L., Krucker, S., et al. 2017, *Nature Astronomy*, 1, 771
- Ismayilli, R., Van Doorselaere, T., Goossens, M., & Magyar, N. 2022, *Frontiers in Astronomy and Space Sciences*, 8, 241
- Jeffrey, N. L. S., Hahn, M., Savin, D. W., & Fletcher, L. 2018, *ApJL*, 855, L13
- Jin, M., Manchester, W. B., van der Holst, B., et al. 2017, *ApJ*, 834, 173
- Joulin, V., Buchlin, E., Solomon, J., & Guennou, C. 2016, *A&A*, 591, A148
- Kahil, F., Hirzberger, J., Solanki, S. K., et al. 2022, *A&A*, 660, A143
- Kaiser, M. L., Kucera, T. A., Davila, J. M., et al. 2008, *SSRv*, 136, 5
- Kamio, S., Fredvik, T., & Young, P. 2019, EIS Software Note No. 5 - Orbital drift of the EIS wavelength scale, *EIS Wiki*, *MSSL*
- Kamio, S., & Mariska, J. T. 2012, *SoPh*, 279, 419
- Karampelas, K., & Van Doorselaere, T. 2018, *A&A*, 610, L9
- Kasper, J. C., Maruca, B. A., Stevens, M. L., & Zaslavsky, A. 2013, *PhRvL*, 110, 091102
- Kerr, G. S., Carlsson, M., Allred, J. C., Young, P. R., & Daw, A. N. 2019, *ApJ*, 871, 23
- Kim, I. S. 2000, in *Astronomical Society of the Pacific Conference Series*, Vol. 205, Last Total Solar Eclipse of the Millennium, ed. W. Livingston & A. Özgüç, 69
- Klimchuk, J. A. 2012, *Journal of Geophysical Research (Space Physics)*, 117, A12102
- . 2019, *SoPh*, 294, 173
- Klimchuk, J. A., & Bradshaw, S. J. 2014, *ApJ*, 791, 60
- Kobayashi, K., Cirtain, J., Winebarger, A. R., et al. 2014, *SoPh*, 289, 4393
- Kohl, J. L., Esser, R., Gardner, L. D., et al. 1995, *SoPh*, 162, 313
- Kohl, J. L., Noci, G., Antonucci, E., et al. 1997, *SoPh*, 175, 613
- . 1998, *ApJL*, 501, L127
- Kohutova, P., Verwichte, E., & Froment, C. 2020, *A&A*, 633, L6
- Kosugi, T., Matsuzaki, K., Sakao, T., et al. 2007, *SoPh*, 243, 3

- Koutchmy, S., Baudin, F., Abdi, S., Golub, L., & Sèvre, F. 2019, *A&A*, 632, A86
- Koutchmy, S., Contesse, L., Viladrich, C., Vilinga, J., & Bocchialini, K. 2005, in *ESA Special Publication, Vol. 11, The Dynamic Sun: Challenges for Theory and Observations*, ed. D. Danesy, S. Poedts, A. de Groof, & J. Andries, 26.1
- Krieger, A. S., Timothy, A. F., & Roelof, E. C. 1973, *SoPh*, 29, 505
- Krishna Prasad, S., Singh, J., & Banerjee, D. 2013, *SoPh*, 282, 427
- Krucker, S., & Benz, A. O. 1998, *ApJL*, 501, L213
- Kuin, N. P. M., & Martens, P. C. H. 1982, *A&A*, 108, L1
- Kumar, P., Karpen, J. T., Uritsky, V. M., et al. 2023, *ApJL*, 951, L15
- Laming, J. M., Feldman, U., Schühle, U., et al. 1997, *ApJ*, 485, 911
- Landi, E. 2007, *ApJ*, 663, 1363
- Landi, E., & Cranmer, S. R. 2009, *ApJ*, 691, 794
- Landi, E., & Feldman, U. 2003, *ApJ*, 592, 607
- Landi, E., Habbal, S. R., & Tomczyk, S. 2016, *Journal of Geophysical Research (Space Physics)*, 121, 8237
- Landi, E., Hutton, R., Brage, T., & Li, W. 2020, *ApJ*, 904, 87
- Landi, E., Raymond, J. C., Miralles, M. P., & Hara, H. 2010, *ApJ*, 711, 75
- Lazar, M., Fichtner, H., & Yoon, P. H. 2016, *A&A*, 589, A39
- Lee, K.-S., Imada, S., Moon, Y. J., & Lee, J.-Y. 2014, *ApJ*, 780, 177
- Leibacher, J. W., & Stein, R. F. 1971, *Astrophys. Lett.*, 7, 191
- Leighton, R. B. 1960, in *Aerodynamic Phenomena in Stellar Atmospheres*, ed. R. N. Thomas, Vol. 12, 321–325
- Leighton, R. B., Noyes, R. W., & Simon, G. W. 1962, *ApJ*, 135, 474
- Lemen, J. R., Title, A. M., Akin, D. J., et al. 2012, *SoPh*, 275, 17
- Lepri, S. T., Landi, E., & Zurbuchen, T. H. 2013, *ApJ*, 768, 94
- Li, D., & Long, D. M. 2023, *ApJ*, 944, 8
- Li, X., Habbal, S. R., Kohl, J. L., & Noci, G. 1998, *ApJL*, 501, L133
- Lionello, R., Linker, J. A., & Mikić, Z. 2001, *ApJ*, 546, 542
- . 2009, *ApJ*, 690, 902

- Lionello, R., Velli, M., Downs, C., Linker, J. A., & Mikić, Z. 2014, [ApJ](#), 796, 111
- Liu, W., Title, A. M., Zhao, J., et al. 2011, [ApJL](#), 736, L13
- Lockyer, J. N. 1868, Proceedings of the Royal Society of London Series I, 17, 131
- Long, D. M., Chitta, L. P., Baker, D., et al. 2023, [ApJ](#), 944, 19
- Lyot, B. 1931a, CR Acad. Sci. Paris, 193
- . 1931b, L’Astronomie, 45, 248
- Madjarska, M. S. 2019, [Living Reviews in Solar Physics](#), 16, 2
- Madjarska, M. S., Mackay, D. H., Galsgaard, K., Wiegmann, T., & Xie, H. 2022, [A&A](#), 660, A45
- Madjarska, M. S., Vanninathan, K., & Doyle, J. G. 2011, [A&A](#), 532, L1
- Magyar, N., & Van Doorselaere, T. 2016, [A&A](#), 595, A81
- Magyar, N., Van Doorselaere, T., & Goossens, M. 2017, [Scientific Reports](#), 7, 14820
- . 2019, [ApJ](#), 882, 50
- Manchester, W. B., I., van der Holst, B., & Lavraud, B. 2014, [Plasma Physics and Controlled Fusion](#), 56, 064006
- Mandal, S., Tian, H., & Peter, H. 2021, [A&A](#), 652, L3
- Mandal, S., Chitta, L. P., Antolin, P., et al. 2022, [A&A](#), 666, L2
- Mariska, J. T., Feldman, U., & Doschek, G. A. 1978, [ApJ](#), 226, 698
- . 1979, [A&A](#), 73, 361
- Markovskii, S. A., & Hollweg, J. V. 2004, [ApJ](#), 609, 1112
- Marsch, E., Goertz, C. K., & Richter, K. 1982, [J. Geophys. Res.](#), 87, 5030
- Martínez-Sykora, J., De Pontieu, B., Hansteen, V. H., et al. 2017, [Science](#), 356, 1269
- Massey, P., Valdes, F., & Barnes, J. 1992, IRAF User Guide, 2
- Matthaeus, W. H., Zank, G. P., Oughton, S., Mullan, D. J., & Dmitruk, P. 1999, [ApJL](#), 523, L93
- McIntosh, S. W., & De Pontieu, B. 2009, [ApJ](#), 707, 524
- McIntosh, S. W., de Pontieu, B., Carlsson, M., et al. 2011, [Nature](#), 475, 477
- Mierla, M., Schwenn, R., Teriaca, L., Stenborg, G., & Podlipnik, B. 2005, [Advances in Space Research](#), 35, 2199

- . 2008, [A&A](#), **480**, 509
- Mihalas, D. 1978, [Stellar atmospheres](#) (W. H. Freeman and Company)
- Mikić, Z., & Linker, J. A. 1996, in American Institute of Physics Conference Series, Vol. 382, Proceedings of the eighth International solar wind Conference: Solar wind eight, ed. D. Winterhalter, J. T. Gosling, S. R. Habbal, W. S. Kurth, & M. Neugebauer, 104–107
- Mikić, Z., Linker, J. A., Schnack, D. D., Lionello, R., & Tarditi, A. 1999, [Physics of Plasmas](#), **6**, 2217
- Mikić, Z., Downs, C., Linker, J. A., et al. 2018, [Nature Astronomy](#), **2**, 913
- Milano, L. J., Gómez, D. O., & Martens, P. C. H. 1997, [ApJ](#), **490**, 442
- Mok, Y., Drake, J. F., Schnack, D. D., & van Hoven, G. 1990, [ApJ](#), **359**, 228
- Molnar, M. E., Reardon, K. P., Cranmer, S. R., et al. 2021, [ApJ](#), **920**, 125
- Moran, T. G. 2003, [ApJ](#), **598**, 657
- Morton, R. J., Sharma, R., Tajfirouze, E., & Miriyala, H. 2023, [Reviews of Modern Plasma Physics](#), **7**, 17
- Morton, R. J., Tomczyk, S., & Pinto, R. 2015, [Nature Communications](#), **6**, 7813
- Morton, R. J., Tomczyk, S., & Pinto, R. F. 2016, [ApJ](#), **828**, 89
- Morton, R. J., Weberg, M. J., & McLaughlin, J. A. 2019, [Nature Astronomy](#), **3**, 223
- Müller, D., St. Cyr, O. C., Zouganelis, I., et al. 2020, [A&A](#), **642**, A1
- Muro, G. D., Gunn, M., Fearn, S., Fearn, T., & Morgan, H. 2023, [SoPh](#), **298**, 75
- Nakariakov, V. M., Anfinogentov, S. A., Nisticò, G., & Lee, D. H. 2016, [A&A](#), **591**, L5
- Nakariakov, V. M., & Kolotkov, D. Y. 2020, [ARA&A](#), **58**, 441
- Nakariakov, V. M., Ofman, L., Deluca, E. E., Roberts, B., & Davila, J. M. 1999, [Science](#), **285**, 862
- Nakariakov, V. M., Anfinogentov, S. A., Antolin, P., et al. 2021, [SSRv](#), **217**, 73
- Nechaeva, A., Zimovets, I. V., Nakariakov, V. M., & Goddard, C. R. 2019, [ApJS](#), **241**, 31
- Nisticò, G., Nakariakov, V. M., & Verwichte, E. 2013, [A&A](#), **552**, A57
- Noble, L. M., & Scarf, F. L. 1963, [ApJ](#), **138**, 1169
- Olbert, S. 1968, in Astrophysics and Space Science Library, Vol. 10, Physics of the Magnetosphere, ed. R. D. L. Carovillano & J. F. McClay, 641

- Oran, R., Landi, E., van der Holst, B., Sokolov, I. V., & Gombosi, T. I. 2017, [ApJ](#), 845, 98
- O’Shea, E., Banerjee, D., & Poedts, S. 2003, [A&A](#), 400, 1065
- Pagano, P., Pascoe, D. J., & De Moortel, I. 2018, [A&A](#), 616, A125
- Panesar, N. K., Hansteen, V. H., Tiwari, S. K., et al. 2023, [ApJ](#), 943, 24
- Panesar, N. K., Tiwari, S. K., Berghmans, D., et al. 2021, [ApJL](#), 921, L20
- Paraschiv, A. R., & Judge, P. G. 2022, [SoPh](#), 297, 63
- Parker, E. N. 1972, [ApJ](#), 174, 499
- . 1983, [ApJ](#), 264, 642
- . 1988, [ApJ](#), 330, 474
- Parnell, C. E., & De Moortel, I. 2012, [Philosophical Transactions of the Royal Society of London Series A](#), 370, 3217
- Parnell, C. E., & Jupp, P. E. 2000, [ApJ](#), 529, 554
- Patsourakos, S., Habbal, S. R., & Hu, Y. Q. 2002, [ApJL](#), 581, L125
- Pauluhn, A., Rüedi, I., Solanki, S. K., et al. 2001, [ApOpt](#), 40, 6292
- Pesnell, W. D., Thompson, B. J., & Chamberlin, P. C. 2012, [SoPh](#), 275, 3
- Peter, H. 2000, [A&A](#), 360, 761
- . 2001, [A&A](#), 374, 1108
- Peter, H., & Judge, P. G. 1999, [ApJ](#), 522, 1148
- Peter, H., Tian, H., Curdt, W., et al. 2014, [Science](#), 346, 1255726
- Peter, H., Chitta, L. P., Chen, F., et al. 2022, [ApJ](#), 933, 153
- Petralia, A., Reale, F., Orlando, S., & Klimchuk, J. A. 2014, [A&A](#), 567, A70
- Petrova, E., Magyar, N., Van Doorselaere, T., & Berghmans, D. 2023, [ApJ](#), 946, 36
- Plowman, J. E., Hassler, D. M., Auchère, F., et al. 2023, [A&A](#), 678, A52
- Powell, K. G., Roe, P. L., Linde, T. J., Gombosi, T. I., & De Zeeuw, D. L. 1999, [Journal of Computational Physics](#), 154, 284
- Prabhakar, M., & Raju, K. P. 2022, [ApJ](#), 931, 40
- Prabhakar, M., Raju, K. P., & Chandrasekhar, T. 2019, [SoPh](#), 294, 26
- Priest, E. R., Chitta, L. P., & Syntelis, P. 2018, [ApJL](#), 862, L24

- Priest, E. R., Heyvaerts, J. F., & Title, A. M. 2002, *ApJ*, 576, 533
- Purkhart, S., & Veronig, A. M. 2022, *A&A*, 661, A149
- Raju, K. P., Chandrasekhar, T., & Ashok, N. M. 2011, *ApJ*, 736, 164
- Raju, K. P., Desai, J. N., Chandrasekhar, T., & Ashok, N. M. 1991, *Journal of Astrophysics and Astronomy*, 12, 311
- Raouafi, N. E., Stenborg, G., Seaton, D. B., et al. 2023, *ApJ*, 945, 28
- Régnier, S., Alexander, C. E., Walsh, R. W., et al. 2014, *ApJ*, 784, 134
- Reid, J., Hood, A. W., Parnell, C. E., Browning, P. K., & Cargill, P. J. 2018, *A&A*, 615, A84
- Rimmele, T. R., Warner, M., Keil, S. L., et al. 2020, *SoPh*, 295, 172
- Rochus, P., Auchère, F., Berghmans, D., et al. 2020, *A&A*, 642, A8
- Sachdeva, N., van der Holst, B., Manchester, W. B., et al. 2019, *ApJ*, 887, 83
- Sachdeva, N., Tóth, G., Manchester, W. B., et al. 2021, *ApJ*, 923, 176
- Samanta, T., Tian, H., Yurchyshyn, V., et al. 2019, *Science*, 366, 890
- Scarf, F. L., & Noble, L. M. 1965, *ApJ*, 141, 1479
- Schad, T. A., Kuhn, J. R., Fehlmann, A., et al. 2023, *ApJ*, 943, 59
- Schatten, K. H., Wilcox, J. M., & Ness, N. F. 1969, *SoPh*, 6, 442
- Scherrer, P. H., Schou, J., Bush, R. I., et al. 2012, *SoPh*, 275, 207
- Schmelz, J. T., Asgari-Targhi, M., Christian, G. M., Dhaliwal, R. S., & Pathak, S. 2015, *ApJ*, 806, 232
- Schmelz, J. T., Kashyap, V. L., Saar, S. H., et al. 2009, *ApJ*, 704, 863
- Schrijver, C. J., Title, A. M., van Ballegoijen, A. A., Hagenaar, H. J., & Shine, R. A. 1997, *ApJ*, 487, 424
- Schrijver, C. J., Title, A. M., Berger, T. E., et al. 1999, *SoPh*, 187, 261
- Schühle, U. 2014, SUMER Data Cookbook
- Schwanitz, C., Harra, L., Mandrini, C. H., et al. 2023, *A&A*, 674, A219
- Schwarzschild, K. 1906, Nachrichten von der Königlichen Gesellschaft der Wissenschaften zu Göttingen. Math.-phys. Klasse, 195, 41
- Seaton, D. B., Berghmans, D., Nicula, B., et al. 2013, *SoPh*, 286, 43

Seely, J. F., Feldman, U., Schühle, U., et al. 1997, [ApJL](#), 484, L87

Shi, T., Manchester, Ward, I., Landi, E., et al. 2022, [ApJ](#), 928, 34

Shi, T., Manchester, W. B., Landi, E., et al. submitted to [ApJ](#)

Shibata, K., Nakamura, T., Matsumoto, T., et al. 2007, [Science](#), 318, 1591

Singh, J., Hasan, S. S., Gupta, G. R., Nagaraju, K., & Banerjee, D. 2011, [SoPh](#), 270, 213

Singh, J., Ichimoto, K., Imai, H., Sakurai, T., & Takeda, A. 1999, [PASJ](#), 51, 269

Singh, J., Sakurai, T., & Ichimoto, K. 2006, [ApJ](#), 639, 475

Singh, J., Sakurai, T., Ichimoto, K., & Muneer, S. 2003, [SoPh](#), 212, 343

Singh, J., Sakurai, T., Ichimoto, K., Suematsu, Y., & Takeda, A. 2002, [PASJ](#), 54, 793

Sokolov, I. V., van der Holst, B., Oran, R., et al. 2013, [ApJ](#), 764, 23

Sokolov, I. V., Holst, B. v. d., Manchester, W. B., et al. 2021, [ApJ](#), 908, 172

Solanki, S. K., del Toro Iniesta, J. C., Woch, J., et al. 2020, [A&A](#), 642, A11

Spice Consortium, Anderson, M., Appourchaux, T., et al. 2020, [A&A](#), 642, A14

Spruit, H. C. 1981, in *NASA Special Publication*, ed. S. Jordan, Vol. 450, 385–413

Sterling, A. C., Moore, R. L., Falconer, D. A., & Adams, M. 2015, [Nature](#), 523, 437

Stix, M. 2002, [The sun: an introduction](#)

Sturrock, P. A., & Uchida, Y. 1981, [ApJ](#), 246, 331

Szente, J., & Landi, E. in prep

Szente, J., Landi, E., Manchester, W. B., I., et al. 2019, [ApJS](#), 242, 1

Szente, J., Landi, E., & van der Holst, B. 2022, [ApJ](#), 926, 35

—. 2023, [ApJS](#), 269, 37

Terradas, J., Andries, J., Goossens, M., et al. 2008, [ApJL](#), 687, L115

Thompson, B. J., Plunkett, S. P., Gurman, J. B., et al. 1998, [Geophys. Res. Lett.](#), 25, 2465

Tian, H., Harra, L., Baker, D., Brooks, D. H., & Xia, L. 2021, [SoPh](#), 296, 47

Tian, H., McIntosh, S. W., Habbal, S. R., & He, J. 2011, [ApJ](#), 736, 130

Tian, H., McIntosh, S. W., Wang, T., et al. 2012, [ApJ](#), 759, 144

Tian, H., Tomczyk, S., McIntosh, S. W., et al. 2013, [SoPh](#), 288, 637

Tian, H., Young, P. R., Reeves, K. K., et al. 2016, [ApJL](#), 823, L16

Tian, H., DeLuca, E. E., Cranmer, S. R., et al. 2014, [Science](#), 346, 1255711

Titov, V. S., Török, T., Mikic, Z., & Linker, J. A. 2014, [ApJ](#), 790, 163

Tiwari, A. K., Morton, R. J., Régnier, S., & McLaughlin, J. A. 2019a, [ApJ](#), 876, 106

Tiwari, S. K., Alexander, C. E., Winebarger, A. R., & Moore, R. L. 2014, [ApJL](#), 795, L24

Tiwari, S. K., Hansteen, V. H., De Pontieu, B., Panesar, N. K., & Berghmans, D. 2022, [ApJ](#), 929, 103

Tiwari, S. K., Panesar, N. K., Moore, R. L., et al. 2019b, [ApJ](#), 887, 56

Tomczyk, S., & McIntosh, S. W. 2009, [ApJ](#), 697, 1384

Tomczyk, S., McIntosh, S. W., Keil, S. L., et al. 2007, [Science](#), 317, 1192

Tomczyk, S., Card, G. L., Darnell, T., et al. 2008, [SoPh](#), 247, 411

Török, T., Downs, C., Linker, J. A., et al. 2018, [ApJ](#), 856, 75

Tóth, G., van der Holst, B., Sokolov, I. V., et al. 2012, [Journal of Computational Physics](#), 231, 870

Träbert, E., Beiersdorfer, P., Brickhouse, N. S., & Golub, L. 2014, [ApJS](#), 215, 6

Tripathi, D., & Klimchuk, J. A. 2013, [ApJ](#), 779, 1

Tripathi, D., Mason, H. E., Del Zanna, G., & Young, P. R. 2010, [A&A](#), 518, A42

Tsuneta, S., Acton, L., Bruner, M., et al. 1991, [SoPh](#), 136, 37

Tu, C. Y., & Marsch, E. 1997, [SoPh](#), 171, 363

Tu, C. Y., Marsch, E., & Wilhelm, K. 1999, [SSRv](#), 87, 331

Tu, C. Y., Marsch, E., Wilhelm, K., & Curdt, W. 1998, [ApJ](#), 503, 475

Tu, C.-Y., Zhou, C., Marsch, E., et al. 2005, [Science](#), 308, 519

Ugarte-Urra, I. 2010a, EIS Software Note No. 12 - Stray light

—. 2010b, EIS Software Note No. 12 - Stray light

Ulrich, R. K. 1970, [ApJ](#), 162, 993

Uritsky, V. M., DeForest, C. E., Karpen, J. T., et al. 2021, [ApJ](#), 907, 1

van Ballegooijen, A. A. 1986, [ApJ](#), 311, 1001

- van Ballegooijen, A. A., Asgari-Targhi, M., Cranmer, S. R., & DeLuca, E. E. 2011, [ApJ](#), 736, 3
- van Ballegooijen, A. A., Asgari-Targhi, M., & Voss, A. 2017, [ApJ](#), 849, 46
- van Ballegooijen, A. A., & Cranmer, S. R. 2008, [ApJ](#), 682, 644
- van der Holst, B., Sokolov, I. V., Meng, X., et al. 2014, [ApJ](#), 782, 81
- van der Holst, B., Huang, J., Sachdeva, N., et al. 2022, [ApJ](#), 925, 146
- Van Doorselaere, T., Goossens, M., Magyar, N., Ruderman, M. S., & Ismayilli, R. 2021, [ApJ](#), 910, 58
- Van Doorselaere, T., Li, B., Goossens, M., Hnat, B., & Magyar, N. 2020a, [ApJ](#), 899, 100
- Van Doorselaere, T., Nakariakov, V. M., & Verwichte, E. 2008, [ApJL](#), 676, L73
- Van Doorselaere, T., Srivastava, A. K., Antolin, P., et al. 2020b, [SSRv](#), 216, 140
- Vasyliunas, V. M. 1968, [J. Geophys. Res.](#), 73, 2839
- Velli, M., Pucci, F., Rappazzo, F., & Tenerani, A. 2015, [Philosophical Transactions of the Royal Society of London Series A](#), 373, 20140262
- Vernazza, J. E., Avrett, E. H., & Loeser, R. 1981, [ApJS](#), 45, 635
- Vernazza, J. E., & Reeves, E. M. 1978, [ApJS](#), 37, 485
- Verth, G., Terradas, J., & Goossens, M. 2010, [ApJL](#), 718, L102
- Wang, H., Tang, F., Zirin, H., & Wang, J. 1996, [SoPh](#), 165, 223
- Wang, T. 2011, [SSRv](#), 158, 397
- Wang, T., Ofman, L., Davila, J. M., & Su, Y. 2012, [ApJL](#), 751, L27
- Wang, T., Ofman, L., Sun, X., Provornikova, E., & Davila, J. M. 2015, [ApJL](#), 811, L13
- Wang, T. J., Solanki, S. K., Curdt, W., et al. 2003a, [A&A](#), 406, 1105
- Wang, T. J., Solanki, S. K., Innes, D. E., Curdt, W., & Marsch, E. 2003b, [A&A](#), 402, L17
- Warren, H. P., Brooks, D. H., Ugarte-Urra, I., et al. 2018, [ApJ](#), 854, 122
- Warren, H. P., Ugarte-Urra, I., & Landi, E. 2014, [ApJS](#), 213, 11
- Warren, H. P., Ugarte-Urra, I., Young, P. R., & Stenborg, G. 2011, [ApJ](#), 727, 58
- Warren, H. P., Winebarger, A. R., & Brooks, D. H. 2012, [ApJ](#), 759, 141
- Wedemeyer-Böhm, S., Lagg, A., & Nordlund, Å. 2009, [SSRv](#), 144, 317

- Wendeln, C., & Landi, E. 2018, [ApJ](#), 856, 28
- Westfall, J., & Sheehan, W. 2015, *Celestial shadows: Eclipses, transits, and occultations* (Springer)
- Wilhelm, K. 1999, [Ap&SS](#), 264, 43
- Wilhelm, K., Dammasch, I. E., Marsch, E., & Hassler, D. M. 2000, [A&A](#), 353, 749
- Wilhelm, K., Dwivedi, B. N., & Teriaca, L. 2004, [A&A](#), 415, 1133
- Wilhelm, K., Fludra, A., Teriaca, L., et al. 2005, [A&A](#), 435, 733
- Wilhelm, K., Marsch, E., Dwivedi, B. N., et al. 1998, [ApJ](#), 500, 1023
- Wilhelm, K., Curdt, W., Marsch, E., et al. 1995, [SoPh](#), 162, 189
- Winebarger, A. R., Schmelz, J. T., Warren, H. P., Saar, S. H., & Kashyap, V. L. 2011, [ApJ](#), 740, 2
- Withbroe, G. L., & Noyes, R. W. 1977, [ARA&A](#), 15, 363
- Yang, Z., Bethge, C., Tian, H., et al. 2020, [Science](#), 369, 694
- Yeates, A. R., Amari, T., Contopoulos, I., et al. 2018, [SSRv](#), 214, 99
- Young, C. A. 1870, [Nature](#), 1, 532
- Young, P. 2010, EIS Software Note No. 4 - Slit tilts, [EIS Wiki](#), [MSSL](#)
- . 2011a, EIS Software Note No. 3 - Spatial Y-offsets between different wavelengths (spectrum tilt and CCD offset), [EIS Wiki](#), [MSSL](#)
- . 2011b, EIS Software Note No. 7 - Instrumental line widths for the narrow slits of EIS, [EIS Wiki](#), [MSSL](#)
- Young, P. R. 2022, Calibrating EIS data: the EIS_PREP routine, 3.8, [Zenodo](#)
- Young, P. R., Watanabe, T., Hara, H., & Mariska, J. T. 2009, [A&A](#), 495, 587
- Young, P. R., Del Zanna, G., Mason, H. E., et al. 2007, [PASJ](#), 59, S857
- Zajtsev, V. V., & Stepanov, A. V. 1975, *Issledovaniia Geomagnetizmu Aeronomii i Fizike Solntsa*, 37, 3
- Zhao, L., Sokolov, I., Gombosi, T., et al. 2023, [arXiv e-prints](#), arXiv:2309.16903
- Zhong, S., Nakariakov, V. M., Kolotkov, D. Y., et al. 2023a, [Nature Communications](#), 14, 5298
- Zhong, S., Nakariakov, V. M., Miao, Y., Fu, L., & Yuan, D. 2023b, [Scientific Reports](#), 13, 12963

Zhu, Y., Sente, J., & Landi, E. 2021, [ApJ](#), 913, 74

—. 2023, [ApJ](#), 948, 90

Zimovets, I. V., & Nakariakov, V. M. 2015, [A&A](#), 577, A4